Collins, Jonathan A. (2021) *Development of nanobridge based Josephson junction electronics for the readout of superconducting photon sensor arrays.* PhD thesis.

https://theses.gla.ac.uk/82550/

Copyright and moral rights for this work are retained by the author

A copy can be downloaded for personal non-commercial research or study, without prior permission or charge

This work cannot be reproduced or quoted extensively from without first obtaining permission in writing from the author

The content must not be changed in any way or sold commercially in any format or medium without the formal permission of the author

When referring to this work, full bibliographic details including the author, title, awarding institution and date of the thesis must be given

Enlighten: Theses
https://theses.gla.ac.uk/
research-enlighten@glasgow.ac.uk

DEVELOPMENT OF NANOBRIDGE BASED JOSEPHSON JUNCTION ELECTRONICS FOR THE READOUT OF SUPERCONDUCTING PHOTON SENSOR ARRAYS

Jonathan A. Collins

Submitted in Fulfilment of the Requirements for the Degree of Doctor of Engineering

University of Glasgow
College of Science and Engineering
James Watt School of Engineering

October 2021

The copyright in this thesis is owned by the author. Any quotation from the thesis or use of any of the information contained in it must acknowledge this thesis as the source of the quotation or information.

Abstract

Superconducting nanowire single photon detectors (SNSPDs) have been shown to have unrivalled performance for single photon detection. However, scaling up to a large scale detection array which maintains the single pixel performance has proven to be challenging. Several solutions have been demonstrated, but no single readout scheme has to date proven to be capable of meeting all of the required specifications.

One promising solution is for a low temperature digital signal processing scheme based on the generation and transmission of voltage pulses with an area corresponding to a single flux quantum (SFQ), $V \approx 2.07$ mV$\cdot$ps. Conventional SFQ technology use superconducting tunnel junctions (STJ) as the active element, which require a multistep fabrication process which has so far proven difficult to integrate with SNSPD fabrication. To overcome this we propose the use of bridge-type weak links as the active element, known as nanobridges, to replace the STJ. Such a nanobridge based SFQ scheme could be integrated with an SNSPD detector array on-chip.

In this work the feasibility of using nanobridges as active weak link elements is investigated. To do this, a fabrication process was developed which can be used to produce nanobridges with the physical dimensions required to exhibit the Josephson effect, in a scalable and reproducible process. The electrical properties of nanobridges have been measured and show that the switching parameters can be reproduced in a scalable way. Finally, evidence of the Josephson effect in nanobridges is presented and used to derive the current-phase relationship (CPR) in nanobridges. It was found that the CPR of the nanobridge is multivalued, and deviates from the standard sinusoidal relationship. This CPR was then used to simulate SFQ circuitry where nanobridges are used as the active element, showing that nanobridges can be used in SFQ circuitry.

Acknowledgements

I would first like to thank my supervisor Alessandro Casaburi for his support, encouragement and guidance over the last four years. I also thank my industrial supervisor at NPL, Jane Ireland in supporting me throughout my travels between Glasgow and London.

At the university I would like to thank Robert Hadfield for making it possible for me to undertake this work. I would also like to thank former group members Rob Heath for establishing most of the Python scripts that are used in the lab, Kleanthis Erotokritou and Umberto Nasti for getting me started with fabrication, and Jharna Paul and Koran Jackson who provided me with extra hands when I was unable to physically be in the JWNC.

At NPL I have to thank Connor Shelly, who provided essential assistance with the measurement set up, and for explaining the same component to me every time I returned to NPL after more than a few weeks. Jonathan Williams also provided support, and Patrick See who provided essential information in the early part of the project which was used to develop the fabrication process.

Working amongst the JWNC community has been an excellent part of the last four years, and I would like to thank Stephen Thoms and Paul Reynolds for their tireless patience in fixing my markers. This work would not have been possible without many members of JWNC staff, in particular Laura McGlynn, James Grant and Dave Gourlay have provided assistance over the course of the project. Haiping Zhou provided vital discussion which proved to be the point at which the fabrication process began to come together, and many users who freely shared their knowledge over the course of the project.

I would also like to thank Martin Weides for the loan of an RF signal generator, and members of his team Sergey Danilin and Valentino Seferai, who are always helpful when sharing fabrication notes, or when facing the arduous task of conducting repairs on the deposition system.

Finally, I would like to thank my friends and family. To my parents, who have supported me despite not understanding when I discuss what I've been doing at work, and the parents of my wife who have provided encouragement. Also to my friends Kristy, Steve and Dan who have each kept me going. I am forever grateful to the support of my wife Meg who has been indispensible to me throughout, not only during this project but for the last eight years. And the patience and tolerance of my son, Finn, who will undoubtedly demand I honour the promises I made to him while writing this thesis tomorrow morning.

Declaration

I declare that, except where explicit reference is made to the contribution of others, that this dissertation is the result of my own work and has not been submitted for any other degree at the University of Glasgow or any other institution.

Jonathan A. Collins

Contents

1 Introduction **1**

2 Motivation **5**

2.1 Single Photon Detection Technologies 5

2.2 SNSPD Arrays and Readout Schemes 7

2.2.1 Row-Column Readouts 8

2.2.2 Pulse Amplitude Multiplexing 9

2.2.3 Frequency Division Multiplexing 11

2.2.4 Time-Domain Multiplexing 12

2.2.5 Single Flux Quantum Electronics 14

2.2.6 Summary 15

3 Background **16**

3.1 Josephson Effect 16

3.1.1 The Zero Voltage State 17

3.1.2 Josephson Junctions in the Resistive State 21

3.1.3 Response to Driving Sources 28

3.2 Rapid Single Flux Quantum 32

3.2.1 Generation of SFQ pulses 33

3.2.2 Typical Operating Parameters of RSFQ Devices 35

3.3 Types of Josephson Junction 37

3.3.1 Superconducting Tunnel Junctions 38

3.3.2 Nanobridge Weak Links 39

4 Fabrication **54**

4.1 Film Deposition 55

4.2 Electron Beam Lithography 58

4.2.1 Electron Beam Resists 58

4.2.2 Electron Beam Exposure and Dosing 62
4.3 Etching 66
4.3.1 Reactive Ion Etching 66
4.3.2 Wet Etching 67
4.4 Process Development 68
4.4.1 Adaptation of SNSPD Fabrication Process 68
4.4.2 PMMA Single Step Process 72
4.4.3 Multistep PMMA and ZEP mixed process 76

5 Results **81**

5.1 Experimental Setups 81
5.1.1 Current Voltage Characteristic Measurements 81
5.1.2 Switching Current Statistics Measurements 83
5.1.3 Experimental Setup at NPL 85
5.1.4 Experimental Set Up at University of Glasgow 87
5.2 Nanobridge Scale Up and Repeatability 89
5.2.1 Effect of Physical Geometry on Critical Current 92
5.2.2 Effect of Electrode Angle on Critical Current 96
5.2.3 Comparison with Theoretical Models for Critical Current 98
5.2.4 Effect of Film Thickness on Critical Current 99
5.2.5 Nanobridge Switching Characteristics 100
5.2.6 Nanobridge Repeatability 102
5.3 Thermal Hysteresis in Nanobridges 103
5.3.1 Effect of Film thickness on the return current in nanobridges 103
5.3.2 Effect of the addition of Al Thermal Channel on Nanobridge Behaviour 105
5.3.3 Effects of Nanobridge Geometry on Thermal Hysteresis 107
5.4 Investigations of the Current-Phase Relationship in Nanobridge type weak links 108
5.4.1 Derivation of Current Phase Relationship in Nanobridges 110
5.5 Evidence of Josephson Effect in Nanobridges based on Shapiro Steps 112
5.5.1 IVC Response to Increasing RF Power 116
5.6 Simulated RSFQ Circuitry with Derived Nanobridge CPR 120

6 Conclusion and Future Work **123**
6.1 Summary of Results 123
6.2 Outlook and Future Work 124

A Fabrication Processes **127**
A.1 Deposition Process 127
A.2 Fabrication Process 128

Bibliography **130**

Bibliography **130**

List of Tables

2.1 Comparison of photon detection technologies, including the semiconducting technologies photomultiplier tube (PMT) and single photon avalanche diode (SPAD), and the superconducting technologies superconducting tunnel junction (STJ), transition edge sensor (TES) and SNSPD. 6

4.1 A comparison of the parameters of the ebeam resists used over the course of this project. 59
4.2 Measurement of mask undercutting as a function of the applied RF power during the etch showing that the undercut increased in severity as increasing RF power was applied. 70
4.3 The average measurements from each array over a sample with one hundred and sixty nanobridges. Many of the nanobridges with electrode angles of 60° were broken or physically inconsistent. It can be seen that while the accuracy of the nanobridges here was poor, the variance across each array showed good consistency. 74

5.1 The average physical dimensions of the nine measured nanobridges for each of the three arrays which were fabricated with $\theta = 15°$. 93
5.2 The average physical dimensions of each of the three arrays which were fabricated with $\theta = 30°$. 95
5.3 A comparison of values of the I_cR_n product for nanobridges which were fabricated in each of the three film thicknesses used over the course of the project. The values of I_c and R_n were determined from a four point contact IVC measurement to negate the lead resistance. 99
5.4 The calculated values of the T_H, for two arrays, where the sample was measured with the normal metal Al layer added on top, and again after the Al layer had been stripped. 106
5.5 The hysteretic crossover temperature, T_H, occurs at approximately the same point independent of the electrode angle. 107

5.6 The parameters used for each thickness of film to numerically calculate the step size. The values of I_c and R_n were obtained from measurement, the values of ξ were calculated for $f = 20$ GHz and φ_c was obtained from the IVC fitting described in Section 5.4. 116

List of Figures

1.1 A standard readout scheme for an individual detector, where the detector is biased from room temperature with a DC source and a bias resistor. When a photon is detected the resulting pulse is transmitted through the RF branch of the bias tee to an oscilloscope or counter with a matched 50 Ω. 2

2.1 (a) An example of a meandered nanowire structure with a width of around 100 nm in a NbN film with thickness of 8 nm. The bend of the wire is fabricated at least three times wider than the nanowire width to account for current crowding [55]. The active detection area is marked by the red dashed line. Image recreated from Reference [56]. (b) An example of the typical pulse shape produced during a detection event, the fast rise time on the order of $\sim$ 500 ps shown in red reaches a maximum amplitude of around 0.9 mV, the much longer delay time of $\sim$ 30 ns in blue shows the time required before the device is ready to detect another photon [57]. 7

2.2 (a) An example of a segment of the detector array, each detector is represented by the circle. Bias current is supplied to each row and shunted by the column inductor L_c. When a pixel is triggered, as shown by the red circle, current is diverted out of the pixel on triggering resulting in a positive row pulse and a corresponding negative column pulse. Pixel discrimination is achieved by cross-referencing the row and column pulses. (b) The equivalent circuit of the detector, composed of the normal state resistance, R_n, of the SNSPD, the intrinsic inductance of the SNSPD L_p and an integrated 50 Ω impedance R_p. Image adapted from Allman et al (2015) [18] 8

2.3 A PAM scheme in which the detectors are connected in series. The normal state resistance of the nanowire is much greater than the parallel resistance R_{n}. When the detector is triggered the current redistributed into R_{n} generates a voltage pulse which is used to discriminate the detectors. 10

2.4 Unlike the scheme shown in Figure 2.3, each detector is biased in parallel. The discrimination mechanism remains the same however, with the current redistribution into R_n producing a voltage pulse which is used for pixel discrimination. 11

2.5 (a) The equivalent circuit for a RF-SNSPD. The capacitor C_p and inductor L_p form the resonant circuit, L_c represents the kinetic inductance of the SNSPD. (b) An example of the transmission against the frequency, the loss in transmission corresponds to the resonant frequency of the LC resonator 11

2.6 A schematic of a time-tagged readout scheme, showing a nanowire meandered over a detection area. The meander is coupled to room temperature through a Klopfenstein taper at both ends to allow for impedance matching of the circuit. When a photon is detected the output pulses, P_1 and P_2, at each end of the wire arrive at the readout with time delays of τ_1 and τ_2. The photon arrival time is calculated using the equation $t_p = ((\tau_2 + \tau_1) - L/v)/2$. From this time the position of the detection event along the length of the wire, x_p, can be calculated. Image adapted from Zhao et al [37] 13

3.1 It can be seen that the driving current changes the shape of the Josephson energy. At $I = 0$ the Josephson energy has a purely sinusoidal relationship, while at $I = 0.5I_c$ the tilted washboard shape becomes evident. At $I > I_c$ the local gradient between maxima and minima is removed and the phase can be continually driven. 19

3.2 The total junction current, I, can be divided into four current components, each of which is represented by one branch of the equivalent circuit. The supercurrent, I_s is represented by a barrier B. The normal current is represented by a resistance which is equivalent to the normal state resistance, R_n. The displacement current is represented by a capacitance, C. Additional random current fluctuations are represented by an additional current source I_F. 21

3.3 The superconducting band gap forms around the Fermi energy, at values of $\pm\Delta(T)$, with the energy state of all Cooper pairs in the system positioned at the Fermi energy. To break a Cooper pair requires both electrons to be excited by an energy of Δ, this action can occur either through thermal excitation or due to the energy provided by a driving external voltage. 22

3.4 The IVC of a typical Josephson junction showing the time averaged voltage $< V >$, where (a) shows a junction driven by a current source, and (b) shows a junction driven by a voltage source. The condition $T < T_c$ is represented by the blue line, and $T > T_c$ by the red dashed line. 23

3.5 The superconducting voltage and current oscillations corresponding to $I_{\text{app}}/I_c = 1.2, 1.8$ and 2.4, normalised in time corresponding to $\tau = \hbar/2eI_cR_n$. (a) Due to the oscillation of the normal and superconducting currents in the normal state, the junction voltage will vary depending on the applied current. (b) The supercurrent oscillations change with the applied current. Reproduced from Reference [82]. 28

3.6 Where the junction is strongly damped, $\beta_c << 1$, in the presence of a combination of RF and DC sources the equivalent circuit can be considered as a combination of the parallel I_s and I_n channels due to the negligibly small capacitance. 30

3.7 With an RF source, the Josephson junction when switched to the normal state will exhibit Shapiro steps at voltages which correspond to $V = hf_{\text{rf}}/2e$. The magnitude of the step current on the Ohmic relationship, shown by the blue line, corresponds to the applied RF power as described by Equation 3.53. Adapted from Enss and Hunklinger [84]. 31

3.8 A schematic for a simple SFQ pulse generator, where the inductance L and the critical current of the junction J are set such that the dimensionless parameter $2 < \lambda < 6$ then a DC pulse at the input of the circuit will produce a train of SFQ pulses at the output which can then be supplied to another circuit. 33

3.9 (a) Ramping the input shows that no SFQ pulses are produced while the input pulse is less than the critical current. Only once the threshold of the critical current is reached will the Josephson junction begin to produce SFQ pulses. As the input is ramped up the rate at which the junction switches is increased. (b) The switching rate of the Josephson junction which is driven by a DC input, shown in (a) is dependent on the amplitude of the driving input pulse, as well as the critical current of the junction. It can be seen that the switching rate is proportional to I_cR_n. 33

3.10 The schematic of a DC-SFQ converter, when a triggering DC input pulse arrives the SFQ pulse is produced by the J2-J3 interferometer loop. The falling edge of the DC pulse then triggers J1 which causes the converter to reset, the frequency of pulses corresponds to the level of input pulse. The junction begins to switch as the critical current threshold is reached, and the switching frequency increases as the pulse amplitude is increased. 34

3.11 In (a) the result of a JSIM simulation [93] showing that for a DC pulse applied to the input a single SFQ pulse will be triggered, at the falling edge of the pulse a transient can be seen which comes from the switching of J1 resetting the device. In (b) the phase change in the junctions of the circuit shows how the DC pulse rising edge triggers junctions J2 and J3 simultaneously which produce the SFQ pulse at the output, the circuit is reset by the DC falling edge triggering J1. 34
3.12 The energy consumption of SFQ technologies compared with standard CMOS electronics [95]. The SFQ-based schemes can operate with reduced energy consumption and clock cycle, much closer to the quantum limit than is currently possible with room temperature CMOS electronics, which allows low-power, high operating frequency low temperature electronics. 36
3.13 Josephson junctions can take a variety of forms, some of these include (a) superconducting tunnel junctions (STJ), which make use of an oxide barrier layer, (b) sandwich-type junction, where the barrier is formed of another material, such as a semiconductor or metal, (c) proximity effect junction, (d) ion-implanted bridge, (e) continuous thickness bridge, (f) variable thickness bridge, (g) point contact and (h) blob type junction. The devices shown in (a) - (d) are barrier type junctions, and (e) - (h) are weak links. This work makes use of the bridge type continuous thickness weak links shown in (e). 37
3.14 The two electrodes of the terminal can be seen, in fabrication the first electrode is deposited and oxidised, before the second electrode is added on top. In large scale circuits this results in an uneven surface. The associated shunting resistor is not shown in this image. 38
3.15 In the Volkov model the nanobridge is bounded by hyperbola, the centres of which are separated by a distance of $2a > L_{\text{eff}}$. The current density in the nanobridge is reduced as the length increases, reaching the minimum at the centre of the nanobridge. 40
3.16 If the current flowing through the nanobridge is large a magnetic field can be generated which can suppress the switching current. The direction of the magnetic field is perpendicular to the current flow, which is represented by the dashed lines. In this representation the magnetic field occurs in the z direction. 41
3.17 The physical size of the weak link determines the operating regime of the Josephson junction. Where the effective length is less than $3.49\xi(T)$ the weak link can show Josephson effects. At a bridge width greater than $4.44\xi(T)$ the nanobridge can exhibit Josephson vortice behaviour. 42

3.18 The thermal energy generated by Joule heating in the nanobridge can be dissipated through three channels: heat can flow through the film, heat can flow into the substrate, and where the sample is submerged in a cryogen heat can flow into the cryogen. 43

3.19 Skocpol et al [105] defined the behaviour of the nanobridge dependent on the relationship between the thermal healing length, η, and the length of the bridge L. In the context of the thermal behaviour of nanobridges "long" bridges are those where $\eta < L$, as shown in (a), while "short" bridges are those there the thermal hotspot extends into the electrodes as shown in (b), which occurs where $\eta > L$. 45

3.20 As the current is increased from zero the nanobridge remains in the superconducting state until the critical current value is reached, at which point the nanobridge switches to the normal state. On sweeping the current back to zero the nanobridge remains in the normal state at currents less than the critical current, and only once the return current value is reached does the nanobridge switch back to the superconducting state. 46

3.21 The IVC of nanobridges typically resembles the RSM model [108], where the IV relation shown in blue asymptotically approaches an Ohmic relation which has gradient of R_n and an offset of $0.5I_cR_n$, shown in red. 47

3.22 (a) The current dependent on the phase for several values of intrinsic inductance. $L_1 = 0$, showing the purely sinusoidal relationship, $L_2 = \Phi_0/2\pi I_c$, $L_3 > \Phi_0/2\pi I_c$ and $L_4 > L_3$. Adapted from Deaver 1972 [101] (b) The equivalent circuit for this model, with the intrinsic inductance L, and a Josephson junction B, in parallel with the normal state resistance, R_n. The nanobridge capacitance is considered to be very small and so the displacement current negligible. 47

3.23 The RCSJ model of the nanobridge corresponds to the physical layout as shown. The superconducting current and resistive current branches represent the current flowing through the nanobridge. An inductance is generated by the superconducting material in the electrodes up to the magnetic penetration depth λ. The displacement current channel generated due to the capacitive coupling of the inductances between the two electrodes. 50

4.1 (a) An example of the cross-section of the type of layout of SFQ circuits which utilise STJs, the fabrication process required is complex and involves many stages. The SNSPD layer must be placed either on top of the final layer where the surface is uneven and will likely result in lower quality SNSPDs, or on the substrate before fabrication of the SFQ circuit which requires many layers of processing on top of the SNSPD. (b) An example of a nanobridge scheme that eliminates this issue by having the SNSPD and SFQ layer fabricated adjacent on the same sample. The output from the SNSPD layer is fed through an on-chip amplifier and into the SFQ readout, which then produces a DC pulse which can be transmitted to room temperature. 54

4.2 DC Magnetron Sputtering System (a) The Ar ions are directed toward the target by the magnetic field generated by the cathode, and cause clusters of atoms to be dislodged. These clusters will then become vaporised in the main chamber and condense onto the surfaces, including the substrate. (b) an image of the main chamber of the sputter system during deposition, the chamber is lit by the Ar plasma used in the deposition. 55

4.3 (a) The crystallographic structure of the substrate onto which the Nb film is grown effects the structure of the thin film, adapted from Wildes (2001) [122] (b) The conditions in the chamber result in differences in the type of crystallisation which occurs during film growth depending on the deposition temperature T^* and deposition energy E^*. In Zone 1 the film is composed of porous, tapered crystallites separated by voids, the film is under tensile stress. In Zone T the film transitions to compressive stress, in Zone 2 the growth regime is that of tight grain boundaries between columnar growth and in Zone 3 the film growth is dominated by isotropic and equiaxed grains. As the deposition energy is increased the process enters the ion etching regime, where the sputtered particles have an energy large enough to remove material from the sample surface. Figure adapted from Anders (2010) [123]. 56

4.4 (a) A schematic of the measurement setup used to determine the critical current. Current is applied through the film. In the superconducting state all of the supplied current will flow through the sample to ground, and so $V_2 \sim 0$. As the sample transitions into the normal state the resistance is increased and the current is redirected to the V_2 path. The resistance can then be determined by calculation. (b) Two measurements undertaken on the same device over a thirteen-month period show comparable T_c and resistance of the film. Between measurements the sample was stored under vacuum. The slight discrepancy in the total resistance between the two measurements is likely caused by the different placement of wirebonds in each measurement in a two wire measurement setup. A four point contact measurement was not used as only T_c was being measured. This sample with a Nb film with thickness of $d = 150$ nm, onto a 10 μm × 10 μm Si substrate. 57

4.5 After exposure the pattern is produced by development, where the unwanted resist is removed from the surface. For negative tone resists the exposed area is hardened and remains after development, while in the positive tone resist the exposed area is removed and the unexposed areas are left behind after development 58

4.6 (a) The polymer structure of the PMMA molecule. (b) To improve the lift-off performance a bilayer of PMMA can be used. (i) A bilayer is formed of a thicker bottom layer is spun onto the sample and baked, before a second, typically thinner layer of heavier PMMA is spun on top. (ii) When exposed the more sensitive bottom layer will result in a larger area of exposure, creating an overhang of the upper layer and preventing the deposited metal from forming a continuous layer, allowing the deposited metal to be removed. (iii) The PMMA bilayer can then be removed with a solvent, which also removes the metal layer on top of the resist, and (iv) the metal layer is left behind to produce the desired pattern according to the lithography exposure. 60

4.7 The cage-like structure of the HSQ molecule. When the resist is exposed the hydrogen atoms are removed and the molecules become cross-linked. 61

4.8 The polymer-chain structure of ZEP. 61

4.9 A gradation curve for the exposure of a 350 nm thick layer of ZEP520A. The clearing dose can be seen at $\sim$ 300 μC/cm^2, at which point the resist is almost completely cleared during the development step. Resist residues can often remain which can be removed by an oxygen etching process known as ashing. 62

4.10 Electrons from the ebeam which are directed into the resist layer can be transmitted (blue), elastically scattered (red) by interactions with the material in the stack or produce secondary scattering due to electrons in the resist layer becoming excited (green). 63
4.11 Three examples of electron beams at varying of the acceleration voltage. The forward scattered electrons are represented in blue, and the backscattered and secondary electrons in red. For a stack with 750 nm PMMA, 150 nm Nb on bulk Si, with a beam width of 5 nm. (a) shows a 20 keV beam, (b) shows a 50 keV and (c) shows a 100 keV beam. The higher energy beams experience less scattering as the higher energy electrons can maintain their trajectory without losing energy to collisions. Images were made using the EISS software package [139]. 64
4.12 Looking at a larger cross-sectional area of a stack with the same parameters as in Figure 4.11, the higher energy beams can penetrate deeper into the stack which reduces the proximity effect in the resist as more of the electrons can be dissipated into the substrate. 65
4.13 (a) An example of a RIE process. The chamber is flooded with a mixture of CHF_3 and SF_6 gas which is then ionised. The two plates of the etching tool generate an electric field to direct the ions toward the sample (b) for large features, ions which have been deflected are likely to reach the thin film to contribute to the etching process. In the smaller features there are fewer paths to reach the thin film, so the number of ions which contribute to the etching process is reduced which results in a longer etch time. 66
4.14 The ionised etchants are directed by the applied field, but radicals can be produced during the etching process which are not directed and can result in isotropic component to the etch and an undercut of the mask. 67
4.15 Diagram of two typical etch processes. (a) the result of an isotropic etch, where the mask has been undercut and the sidewalls of the sample are not uniform, typical of wet etching (b) an anisotropic process, where the etchant has been directed, typical of dry etch. 67

4.16 (a) The first step of the fabrication process is to deposit a Nb film onto a Si substrate by sputter deposition. (b) Au markers and contacts are patterned by ebeam, using PMMA as the resist. After an Au gold layer is deposited onto the sample the gold markers are defined through a lift-off process. (c) An Al layer is patterned with a PMMA lift-off process to mark out the electrical contacts and microwires, and (d) the sample is etched to produce the layout of Nb wires. (e) A final ebeam step is used to define the nanobridges in the microwire and is etched. After the completion of this etch step the ZEP resist can be removed and the sample is ready to be used. 68

4.17 (a) The layout of the test samples, ten nanobridges are fabricated on a microwire with physical dimensions 4 μm $\times$ 160 μm, each nanobridge in the array is connected to four of the 200 μm $\times$ 200 μm contact pads to allow for four wire measurement of any single nanobridge in the array. (b) An example of a fabricated sample where the nanobridge was completed removed during the etch process, creating a break between the two electrodes of the nanobridge. 69

4.18 (a) A nanobridge fabricated with physical dimensions on the order of 200 nm which was found to be the smallest intact nanobridge, and (b) using the same design layout included into a test structure the nanobridge was removed during etching. 70

4.19 A schematic of the Nb film during etching showing the issues which caused the removal of the nanobridges. The sidewall profile of the ZEP causes the etching ions to deflect, which causes material under the mask to become removed. The proximitisation of the resist which is to form the nanobridge will result in either a bridge with reduced thickness, or the complete removal of the nanobridge during the etching process. . . . 71

4.20 (a) An example of a test pattern in ZEP resist. It was found that the proximity effect from patterning large area exposures adjacent to small resist columns with sizes comparable to that used to mask the nanobridge resulted in a partial exposure of the resist. (b) After the etch process it can be seen that the nanobridge is mostly removed, with only a small strip of material remaining. This is the result of the partially exposed nanobridge resist, which is removed during the etching process and allows the nanobridge to become partially etched. 71

4.21 (a) An example of a nanobridge fabricated with an included proximity effect correction, the width of the nanobridge is reduced while the length is increased from the designed dimensions. The nanobridge has been partially etched such that the film thickness of the nanobridge is less than that of the electrodes. (b) In another example of a nanobridge, fabricated with a later sample than in (a) with included proximity effect, where the electrodes are connected by the bridge, but the overexposure has increased the length and reduced the width from the designed parameters. 72
4.22 Two examples of successfully fabricated nanobridges made using a PMMA process with an Al hard mask. In (a) a top down view of a Nb nanobridge, the roughness at the edge of the Al mask can be seen, and in the side view (b) it is shown how this is transferred into the Nb during the etch process. In this sample the Al mask has been removed. 73
4.23 A nanobridge with an Al mask after the lift-off process, where a piece of Al has not been removed by flushing as shown in the upper part of the image. 75
4.24 (a) Despite not being fabricated to the desired length and width, the nanobridges in each array had physical dimensions which could be used to compare length to width. (b) Comparing like nanobridges with different electrode angles, it was found that the 0°, 15° and 30° nanobridges were similar in size, while the 45° was significantly different and 60° could not be measured. This is an example of the small fabrication tolerance in this single step PMMA method. 75
4.25 (a) An optical microscope image of a ten nanobridge array after the first etch step where the microwire has been etched into the Nb prior to patterning any nanobridges, and (b) the same sample after the nanobridge etch step where the separation between the electrodes can be seen. 76
4.26 An example of a nanobridge fabricated using a multistep ebeam process. In (a) the sidewalls of the nanobridges are seen to be much smoother, and without the poor line edge roughness as seen in the devices fabricated with an Al mask. (b) The end of the trench separating the two electrodes was found to be shorted when the distance between the electrodes was < 150 nm. This was resolved by including a widening of the separation toward the end of the electrodes. An area of the Si substrate at the end of the electrode gap, where the substrate has been etched during both etch steps, however this does not interfere with the operation of the nanobridge. 77

4.27 (a) A nanobridge with designed width of 60 nm and length of 80 nm, and physical dimensions which approximately match this as measured by SEM. (b) A completed nanobridge, the first ebeam exposure defines the microwire and the second exposure used to define the nanobridge within the microwire can clearly be seen. Some additional residual material from the first etch step can also be seen, which does not affect the behaviour of the nanobridge. 77
4.28 (a) An example of a nanobridge designed with width 50 nm and length 100 nm, which is tilted at 30° to show the clean sidewall of the nanobridge. (b) A similar nanobridge, fabricated on the same sample with a width 50 nm and length 110 nm, showing the control this fabrication process has over the physical dimensions. 78
4.29 Differences between the physical and measured dimensions of the nanobridge fall within the measuring resolution of the SEM. The lengths are consistently greater, and widths consistently smaller than designed, which is a frequently seen result of the proximitisation of resist, as the dimensions of the electrode gap are increased. This can be further reduced through optimisation of the fabrication parameters. 79
4.30 (a) The number of nanobridges fabricated compared to the number of nanobridges which were designed on the sample is shown. Early in the project, while attempting to use a single step ebeam process with ZEP as the resist there were almost no nanobridges successfully fabricated. The single step PMMA process improved the nanobridge yield, but issues with the lift-off process resulted in losses of $\sim$ 10 - 20 %. In the final three samples, all fabricated with the multistep PMMA and ZEP process it can be seen that only two of 120 nanobridges were not successfully fabricated, which was due to the small bridge width. (b) It can be seen the best performance of the single step PMMA process yielded $\sim$ 90 % of the nanobridges successfully fabricated, in the multistep PMMA and ZEP process the fabrication yield is approaching 100 %. 80

5.1 Measurement setup for electrical characterisation of nanobridges, current is supplied by the NPL DAC and an in-series bias resistor. The sample is bonded in such a way to allow the current to pass through the entire array and the IVC for each is produced by measuring the voltage across individual nanobridges, which are represented by the barrier symbol. 82
5.2 A schematic of the measurement set up used to measure the IVC of the nanobridges under RF irradiation. The RF line was terminated on the sample with a 50 Ω impedance, and the nanobridges were then wirebonded in series to provide the RF bias. 83

5.3 The measurement setup for measuring the switching currents of a nanobridge array. The bias is provided by an AWG, which also produces a concurrent pulse to trigger the start of the timer. The ramped bias current passes through the bias resistor R_B until the device is switched into the resistive state. The amplified voltage pulse from the nanobridge is used to stop the AWG and the timer. The time on the counter corresponds to the switching current due to the linearly ramped bias current. 84
5.4 (a) A He dip dewar with a probe inserted, the electrical connections to the sample are fed through the probe, which also allows the He gas to vent. The probe is held in place by a probe clamp. (b) A schematic of the Helium dip dewar, showing the sample at the bottom of the probe which can reach the He. The He vapour provides a gradient in temperature from 4.2 K just above the liquid He to room temperature at the neck of the dewar. 85
5.5 An image of a sample mount with a nanobridge sample fixed in place. The Al wire-bonds connecting the sample to the measurement setup can be seen. A 1 kΩ resistor is used to heat the sample, the temperature is measured by thermometer which provides feedback to a PID which controls the current supply to the heater. 86
5.6 A schematic of the measurement setup at NPL. The sample is connected to the probe through a D-connector, which allows the sample to be easily removed for wirebonding. The D-connector is connected to the breakout box through a manganin loom which terminates with SMA connectors which connects to the measurement equipment. The measurement is controlled by a current bias and PID which are controlled by the measurement PC, and an amplifier is used to read the voltages from the device. . . . 86
5.7 The sample mount used in the cryogen free refrigeration system, which was a modified PCB designed at NPL for low temperature measurements fixed to a sample mount used for SNSPD measurements designed and fabricated at UoG. The bolt which fixed the PCB sample mount to the copper mounting plate can be seen. The RF connection provided by a SMP connection, is also shown. The sample was mounted to minimise the length of the RF wirebond. 88
5.8 A schematic of the measurement set up at UoG. The sample is placed in thermal contact with a 2 K mounting rod, and heat control is provided by a 1 kΩ resistor on the upper stage. The heater current source, RF source and SIM900 used to control the DC measurements are each connected to the controlling PC, where control software is written in Python by the author. 88

5.9 Sweeping the current from -3 mA to $+3$ mA it can be seen that the nanobridge transitions to the superconducting state at the return current, I_R and returns to the normal state once the value of I_c is reached. As the temperature is reduced the value of both I_R and I_c increase at different rates, which can result in hysteretic behaviour. 89

5.10 Two examples of IVC of the same nanobridge at different temperatures, where $T_c =$ 8.65 K. (a) The non-hysteretic behaviour which can be seen at temperature 8.6 K. (b) When the temperature is reduced to 7.2 K the hysteretic behaviour of the nanobridge can be seen, where $I_R < I_\mathrm{c}$. 90

5.11 The layout of the sample, showing the electrode angle, the designed dimensions and the average physical dimensions of the array in nanometres. Four arrays were placed on each 5 mm $\times$ 5 mm segment. The sample was fabricated as a single piece and then cleaved along the dashed lines. 91

5.12 Measuring the T_c of the sample it was found that the $T_\mathrm{c} \approx 8.6$ K, which was defined as being the point at which the resistance reached $1/2R_\mathrm{n}$. R_n is the point at which the gradient of $R(T) \approx 0$, shown here at 140 Ω. 91

5.13 The average critical current plotted over a range of temperatures from 4.2 K to T_c of the sample, which occured at 8.5 K for nanobridges with $\theta = 0°$. The Y-axis error bars shown represent the standard deviation in the critical currents across the sample for each temperature,. The dashed line shows the best fit achieved using Equation 5.2, the fitting parameters are shown in the legend. 93

5.14 The critical current against temperature for arrays with nanobridges fabricated with $\theta = 15°$ over the temperature range 4.2 K to T_c, which occured at ~ 8.4 K. Equation 5.2 was used to determine the values of $I_c(0)$ and T_c, and the fitting parameters used in each case are included in the legend. 94

5.15 The critical current against temperature for nanobridge arrays with $\theta = 30°$, ... 95

5.16 Three arrays of nanobridges for which L and W are similar, with varying θ. The average critical current over the temperature range from 4.2 K to $T_c = 8.4$ K is plotted. 96

5.17 (a) The calculated critical current densities in the arrays with nanobridges where $\theta = 0°$, assuming uniform current density throughout the cross sectional area. (b) The ratio of the current densities shown in (a) which at low temperature takes on a value close to the average value, 0.64, where the standard deviation of the I_c in the array is $\sigma = 0.08$. 97

5.18 Fitting the measured critical current for an array with d = 150 nm, θ = 15°, L = 18 nm and W = 30 nm to the calculated theoretical values for AB, KO-I and KO-II. The fitting parameters used are shown in the legend, $I_c(0)$ was found by fitting Equation 5.2, while R_n was determined from the measured IVC of the nanobridge. . . 98
5.19 Fitting the measured critical current for an array with d = 20 nm, θ = 0°, L = 70 nm and W = 50 nm to the calculated theoretical values for AB, KO-I and KO-II. The fitting parameters are shown in the legend. 99
5.20 The switching currents of six identically fabricated nanobridges were each measured fifty thousand times at temperatures from 4.2 K to the critical temperature, shown at (a) T = 4.75 K and (b) T = 7.50 K. It can be seen that the switching current forms a Gaussian curve. It can be seen that as the temperature changes the critical current distributions vary at different rates. For example, it can be seen that Bridge 6, which has the greatest critical current at 4.75 K has the lowest critical current at 7.50 K. . . 100
5.21 The switching distributions across the range of temperatures, where each distribution curve corresponds to a single nanobridge. It can be seen that the switching currents vary at different rates over the temperature range. 101
5.22 Looking at the standard deviation of nanobridges in all arrays as a percentage of the average switching current it can be seen that as the temperature is reduced the variation between the switching currents in the nanobridges is also reduced. Below 6 K the standard deviation of all arrays has reduced to less than 15 %. At higher temperatures the instability of the temperature creates larger variations in the I_c, at lower temperature where the I_c becomes more stable the variation across the nanobridge becomes significantly smaller. 102
5.23 The averaged values of the return current across an entire array. In (a) the film thickness was 20 nm, while in (b) the film thickness was 50 nm. The calculated line shown in blue was calculated using Equation 3.72, using the measured parameters for the nanobridge. 104
5.24 When measured in a He dip dewar, where heat can flow into the He as an additional thermal channel, it was found that the values of the return current were consistently greater than predicted by Equation 3.72. For both films with thicknesses 50 nm, shown in (a), and 150 nm, shown in (b), the measured values of the return current were consistently greater than expected. 105

5.25 The average values of I_c and I_R for eight nanobridges in two arrays, where in (a) the electrode angle is 0°, and in (b) the electrode angle is 15°. In both cases, the value of T_H showed minimal change due to the additional Al layer, and the critical temperature appeared to be reduced when the Al was removed. The values of I_c were fitted using Equation 5.2, and the values of I_R were fitted with 3.72. T_H was calculated as the point of intersect between these two fitted curves. 106

5.26 The measured values of I_R for three arrays with similar values of L, W and d, and the value of θ is varied. 108

5.27 The equivalent circuit for constant thickness bridges used by Deaver and Pierce [101]. The bridge capacitance is considered to be small such that the displacement current is negligible, and the nanobridge can be represented by only the superconducting branch composed of an in-series inductance L_{ex} and constriction B, with a purely sinusoidal CPR, and a resistive branch composed of the normal state resistance R_n. 109

5.28 In (a) the experimental data from a nanobridge with parameters $d = 150$ nm, $L = 30$ nm, $W = 33$ nm and $\theta = 15°$, measured at $T = 7.8$ K $= 0.92T_c$. In (b) the experimental data from a nanobridge with parameters $d = 50$ nm, $L = 65$ nm, $W = 60$ nm and $\theta = 0°$, measured at $T = 4.5$ K $= 0.89T_c$. 110

5.29 (a) The IVC of a nanobridge with parameters $d = 20$ nm, $L = 70$ nm, $W = 50$ nm at $T = 3.2$ K $= 0.52T_c$. (b) The derived values of φ_c at temperatures 3 K to 5.6 K. . . . 111

5.30 By fitting the measured IV data to the Jackel model the CPR was determined for a range of temperatures. It was expected that the CPR would be approximately sinusoidal at temperatures close to T_c and deviate with reduced temperature, however it was found that the smallest φ_c occurred at the lowest temperature. This can be explained by the inductance of the nanobridge increasing as the temperature approaches T_c. 112

5.31 The derived CPR of the nanobridge was calculated using Equation 5.11, however this is not suitable to mathematically describe the CPR in the JSim software. Instead, an approximation was made, shown in blue, where the CPR could be described using 5.16. It was assumed that at $\varphi > \varphi_c$ a phase slip would occur, and the system would jump to the curve which was offset by 2π, which is represented here by the dashed arrows. 113

5.32 (a) The parameters of the nanobridge $d = 50$ nm, $\theta = 0°$, $L = 65$ nm and $W = 60$ nm. The applied RF frequency was 20 GHz, and the sample was measured at 5.4 K. From the fitting function the nanobridge was found to have $I_c = 226.75$ μA, $I_{\mathrm{rf}} = 58$ μA and $R_n = 6.2\ \Omega$. In (b) the parameters of the nanobridge $d = 150$ nm, $\theta = 0°$, $L = 50$ nm and $W = 35$ nm. The applied RF frequency was 20 GHz, and the sample was measured at $T = 8.1$ K. From the fitting function the nanobridge was found to have $I_c = 251.6$ μA, $I_{\mathrm{rf}} = 86$ μA and $R_n = 0.35\ \Omega$. 114
5.33 In the return current branch of the IVC in a nanobridge with parameters $L = 80$ nm, $W = 55$ nm, $d = 150$ nm and $\theta = 0$ Shapiro steps can be observed. The measurement was made at $T = 7.75$ K with $f = 18.1$ GHz. 115
5.34 The approximated functions used as CPR 2 for each film thickness are shown, with the associated colour corresponding to the function used for each film thickness. The sinusoidal function, shown as a dashed grey line, was used as CPR 1 in each case. . . 117
5.35 (a) The step size of the zeroth step in the current domain, plotted against the applied RF power. (b) The IVC of the nanobridge is shown for several values of the applied RF power. 117
5.36 The measured values of the step width, shown in green, compared with the values for CPR 1, CPR 2 and the Bessel calculation. In (a) the first step is shown, and in (b) the second step is shown. 118
5.37 (a) The step height with increasing RF power, plotted with the numerically calculated values for CPR 1 and CPR 2, as well as the Bessel calculated values. (b) The IVC for a nanobridge with $d = 50$ nm calculated using CPR 1. 119
5.38 In the IVC of nanobridges with film thickness (a) 20 nm and (b) 50 nm it can be seen that the width of the zeroth order step oscillates as the RF power is increased. 119
5.39 The simple circuit which can produce a train of SFQ pulses from a DC input. The parameters were set based on the experimentally obtained parameters for the nanobridge: $I_{\mathrm{c}} = 150$ μA and biased at $0.7 I_{\mathrm{c}}$, the inductance L was set to 8.8 pH which corresponded to $\lambda \approx 4$. 120
5.40 It can be seen that when simulating the circuit where the Josephson junctions have a non-sinusoidal CPR that the device operates as intended to. The input pulse produces a single SFQ pulse just as it does in the standard case, with a greater pulse amplitude. 121
5.41 The schematic of the DC-SFQ converter which was simulated, showing the parameters of each of the components. 121

5.42 (a) The rising edge of the input pulse triggers junctions J2 and J3, as shown in Figure 5.41, and generates a SFQ pulse at the output. The DC-SFQ converter is reset by the falling edge of the input pulse, which triggers J1 and resets the J2 - J3 loop. It is shown in (b) that when driven by a periodic input that J2 and J3 undergo a 2π phase change at the rising edge of the pulse and J1 will be driven by 2π at the falling edge of the pulse. 122

6.1 An example SEM image of the fabricated SFQ circuit, which makes use of nanobridges as the active element. The first stages of the fabrication process were completed in February 2020, prior to the JWNC closure in March 2020. 124

6.2 An example of a nanobridge which was fabricated as part of an investigation on making variable thickness nanobridges. A trench can be seen in the rightmost electrode showing the misalignment of the final patterning step. The trench etched into the sample should be patterned directly over the gap between the two electrodes, in this case there has been a misalignment of $\sim$ 220 nm in the $x-$direction. 125

Chapter 1

Introduction

Superconducting nanowire single photon detectors (SNSPDs) offer unrivalled performance in single photon detection over a wide spectral range, from ultraviolet to infrared[1, 2]. SNSPDs have been demonstrated to show detection efficiency of 93 % [3], dark count rate of 10 Hz [4], timing jitter as low as 2.7 ps [5], and reset time on the order of tens of ps [6]. Quantum technologies capable of providing single photon sensitivity have become increasingly important in a variety of fields, including quantum key distribution (QKD) [7, 8], quantum information processing [9], single photon imaging [10] and ground-to-space optical communication [11]. SNSPDs are now offered by several companies around the world as plug-and-play systems opening up the commercially viability of the technology [12, 13, 14]. There has been recent interest in applying the properties of SNSPDs to fields such as single photon LiDAR [15], dark-matter detection [16], space-based astronomy [17] which could take advantage of the sensitivity to mid-infrared wavelengths, the low dark count rate and short period of timing jitter. For many applications which could benefit from the properties of SNSPDs large scale arrays consisting of many pixels and increased detection area are required.

The most frequently used readout scheme for individual SNSPDs or small-scale array readout connects the detector to room temperature electronics via a 50 Ω coax line, where the SNSPD pulse is amplified and digitised, as shown in Figure 1.1. To realise a large-scale detection area capable of high temporal resolution an array of many SNSPDs is required. Individual readout for each detector quickly becomes unfeasible due to the demands on the cooling power of the refrigeration system for each coax line, and the large physical footprint required to connect to each individual detector. Realisation of a large-scale detector array therefore requires a readout architecture capable of multiplexing the detector array signals without increasing the number of cables, and simplifying the readout electronics at room temperature which can maintain SNSPD performance. However when designing a readout scheme the small amplitude of the output pulse of the SNSPD must be considered. SNSPDs can be fabricated from a variety of materials, and the characteristics of the

output pulse varies greatly. A typical SNSPD output pulse has an amplitude in the range of $\sim 10\ \mu$A which will result in an output of ~ 0.5 mV across a 50 Ω load. In the resisitive state the nanowire typically has a large impedance which causes latching effects, where the applied current must be reduced to restore the superconducting state. These factors have prevented the realisation of a room temperature multiplexing readout scheme.

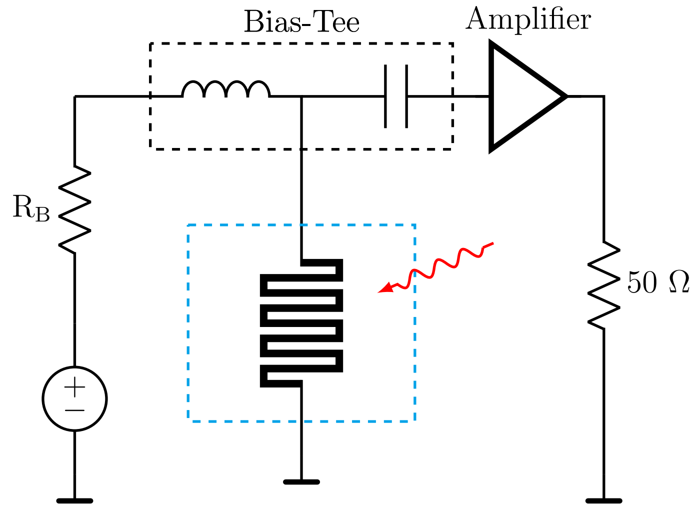

Figure 1.1: A standard readout scheme for an individual detector, where the detector is biased from room temperature with a DC source and a bias resistor. When a photon is detected the resulting pulse is transmitted through the RF branch of the bias tee to an oscilloscope or counter with a matched 50 Ω.

A number of methods capable of the readout of multiple pixels while reducing the number of cables have been demonstrated, including row-column multiplexing [18], pulse amplitude multiplexing [19, 20], and frequency division multiplexing [21]. A recent record number of pixels was achieved, with an array of 1024 pixels which is read out on 64 data lines [22]. Despite this, to date none of the proposed solutions have achieved a large-scale array which maintains the performance qualities seen in individual SNSPDs.

An alternative solution for low temperature digital signal processing is to use Josephson junction based superconducting digital electronics which is based on the generation, transmission and processing of voltage pulses with the quantised area of a single flux quantum (SFQ) [23]. Unlike CMOS which uses transistors to control currents and voltages the active element in the SFQ family of electronics is the Josephson junction. The standard junction used in SFQ electronics is composed of two superconducting electrodes which are separated by a thin oxide barrier, through which the current must tunnel. The switching of a Josephson junction will produce a pulse of $\int V(t)dt = \Phi_0 \approx 2\ \text{mV} \cdot \text{ps}$, which allows SFQ electronics to be operated with very low power consumption and with an operating frequency in excess of hundreds of GHz. These properties allow for a readout scheme which can be integrated with an SNSPD array, can be interfaced without complex amplification and operates at

the same temperature as the detector, and can maintain the temporal performance of the SNSPD.

SFQ electronics have also become an increasingly promising approach for other digital logic applications. Due to the ability to provide a low noise scheme for the control and readout of superconducting qubits, SFQ architectures have found use in quantum computing as an intermediary stage between the quantum circuit and room temperature electronics. It has been shown that qubits can successfully be controlled using SFQ pulse trains to bias [24, 25], and SFQ based readout schemes are now being investigated as a method for providing digital readout of superconducting qubits [26].

The low power consumption and high operating frequencies have also seen superconducting digital computing become a leading solution to the issue of post-Silicon classical computing. SFQ based electronics have been demonstrated to operate at frequencies of 770 GHz [27] and despite requiring cooling to reach the low temperatures required for superconductivity have also been shown to have a Joule/bit cost much lower than current semiconducting computing [28]. However, an open challenge in this field is that there is currently no means of scalable superconducting memory, and as a result attempts to realise a superconducting digital computer were hindered due to the requirement to interface between low temperature superconducting devices and room temperature data storage. The subject of superconducting memory systems has recently become a more active area of research, with several proposed solutions ranging from hybrid superconductor-semiconductor schemes, to more novel approaches such as the vortex-transition memory [29] and superconducting spintronics [30].

Superconducting tunnel junctions (STJs) are the most established type of Josephson junction, having been used in the initial experimental confirmation of the Josephson effect [32] and with complete theories of the zero-voltage state [33] and voltage state [34, 35] developed in 1963 and 1966, respectively. The theoretical model of STJ provides an accurate description of the behaviour of these junctions, and as a result have become the standard for use in Josephson junction electronics. STJs are typically fabricated using a multistep Nb trilayer process [36], and it has proven difficult to integrate an additional layer into the fabrication process to include SNSPDs or superconducting qubits. This has forced the use of separate samples which must be connected through wirebonding [37] or coaxial cables [38] which reduces the operational frequency and causes degradation of the signal at high frequency.

A possible solution is to use continuous thickness bridge-type weak links, which is commonly now referred to as a nanobridge, as the active element in an SFQ electronics scheme. There was significant interest in these structures during the 1970s, when the bridge structure was most commonly fabricated by cutting into a thin film with a razor blade, which could produce bridges with dimensions as small as hundreds of nanometres. However, this method was not repeatable or scalable, and the required physical dimension for nanobridges were beyond the capabilities of contemporary fabrication

technology. With the widespread adoption of electron beam lithography for nanofabrication, it is now possible to repeatably produce nanobridges at the required scale. These superconducting electronics can be fabricated in a single lithography step, using techniques comparable to those of the SNSPD and in a manner which is easily integrable with a SNSPD array layer. The dynamics of nanobridges is less well understood and more complex than in STJs, and one potential issue is with the generation of SFQ pulses for use in electronics. It is well understood that the Josephson junction dynamics in STJs will generate SFQ pulses independent of temperature, and in nanobridges it is not clear if nanobridges can generate SFQ pulses, and how this is affected by the operating temperature of the device.

This thesis describes an investigation by the author into the suitability of using nanobridge type weak links as Josephson elements for use in these superconducting digital logic schemes, focusing on the development of a readout array for an SNSPD scheme. Chapter 2 begins with a review of superconducting nanowire single photon detectors, and the state of the art in readout schemes. Chapter 3 provides the theoretical background of the Josephson effect, the basic principles of Rapid Single Flux Quantum (RSFQ) electronics and the types of Josephson junctions. Chapter 4 describes the methods which were used in the fabrication of the nanobridge type weak links used in this work, and an explanation of the experimental set-ups used for characterisation of the devices at the National Physical Laboratory (NPL) and at the University of Glasgow (UoG) where this work was conducted. Chapter 5 discusses the results, beginning with the repeatability of the nanobridges which were fabricated, and a discussion on the thermal properties of the nanobridges

Chapter 2

Motivation

This chapter first discusses the single photon detection technologies and the requirements in scaling up to large area arrays, followed by a brief discussion of the competing readout schemes which have been developed to multiplex large area SNSPD arrays.

2.1 Single Photon Detection Technologies

SNSPDs are type of a single-photon detector [39] which have been used in applications for optical and near-infrared wavelengths, although recent studies suggest that these devices are sensitive to wavelengths up to 5 μm [2]. Single photon detection technologies are defined by a number of performance metrics:

- Spectral Range: the wavelength range to which the detector is sensitive. Only photons which are within the spectral range will cause a detection event to be registered by the detector.
- Detection Efficiency: the percentage of incident photons which cause a detection event.
- Dark Count Rate: the rate at which the detector registers a count without an incident photon.
- Timing Jitter: the time delay between the arrival of the photon and the pulse being registered by the detector.
- Maximum Count Rate: the maximum number of counts per second which can be registered by the detector.

SNSPDs offer unrivalled performance in single photon detection, the operating parameters are shown in comparison to rival photon detecting technologies in table 2.1. For many imaging applications the type of detector which is used is determined by a single crucial parameter, for example TES can offer large detection areas which operate with low count rate, or semiconducting detectors where low temperature cooling is not possible.

Table 2.1: Comparison of photon detection technologies, including the semiconducting technologies photomultiplier tube (PMT) and single photon avalanche diode (SPAD), and the superconducting technologies superconducting tunnel junction (STJ), transition edge sensor (TES) and SNSPD.

Detector	Spectral Range	Detection Efficiency (1550nm)	Dark Count Rate	Timing Jitter	Count Rate
PMT	1.7 μm [40]	2 % [40]	200 kHz [41]	30 ps [42]	10 MHz [41]
SPAD	1.7 μm [43]	40 % [44]	58 kHz [45]	240 ps [45]	1 MHz [45]
STJ	500 nm [46]	-	-	10 ps	10 kHz [47]
TES	4 μm [48]	95 % [49]	-	100 ns [50]	1 MHz [51]
SNSPD	5 μm [2]	93 % [3]	varies	2.7 ps [5]	10 GHz [52]

An SNSPD is formed of a wire around 100 nm wide and with a length in the range of hundreds of microns, with a film thickness $<$ 10 nm, and can be meandered over an area to form a pixel, an example of which is shown in Figure 2.1(a). When the SNSPD detects a photon the wire is driven into a resistive state. The resistance of the wire is much greater than the 50 Ω impedance of the readout scheme and so the current is redistributed in the system which generates an output current pulse, an example of which is shown in Figure 2.1(b). The SNSPD pulse has a fast rise time, which is shown in red, and a slower relaxation time as the detector returns to the superconducting state. The relaxation time is determined by the kinetic inductance of the nanowire, which is linearly proportional to the physical properties of the wire as $L_k \propto l/A$, where l is the length of the wire and A is the cross sectional area [53]. Simply increasing the length of the wire to increase the detection area will therefore result in an increase in the reset time of the nanowire [54].

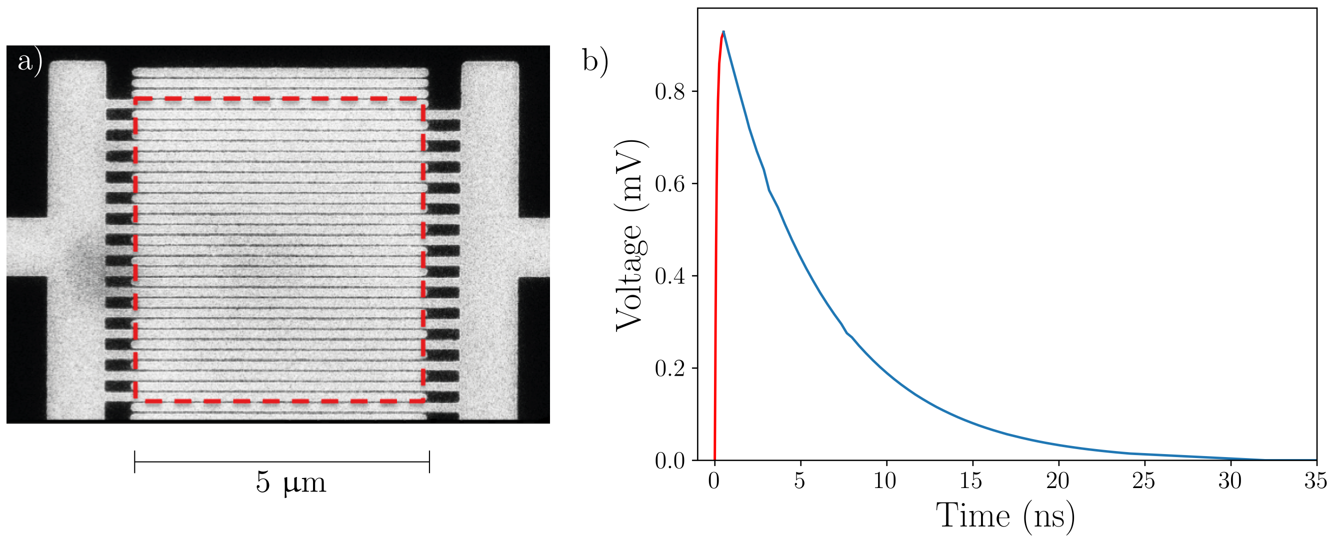

Figure 2.1: (a) An example of a meandered nanowire structure with a width of around 100 nm in a NbN film with thickness of 8 nm. The bend of the wire is fabricated at least three times wider than the nanowire width to account for current crowding [55]. The active detection area is marked by the red dashed line. Image recreated from Reference [56]. (b) An example of the typical pulse shape produced during a detection event, the fast rise time on the order of $\sim$ 500 ps shown in red reaches a maximum amplitude of around 0.9 mV, the much longer delay time of $\sim$ 30 ns in blue shows the time required before the device is ready to detect another photon [57].

When a photon is detected by the SNSPD a pulse of < 1 mV will be produced in the 50 Ω load of the readout electronics. For single detectors this is typically read out by individually biasing each detector and connecting to a 50 Ω coax line to room temperature, where the pulse can then be amplified as shown in Figure 1.1. To achieve a large-scale array with this type of readout scheme would require a single coax line for each detector, and each detector uses a dedicated bias-tee and amplifier chain, with the additional room temperature electronics required to multiplex the SNSPD pixels. The increased heat load placed on the cryostat and complexity of the room temperature electronics makes scaling up to an array of many detectors impractical.

2.2 SNSPD Arrays and Readout Schemes

The excellent performance metrics of SNSPD detectors makes them a very promising technology for a number of applications. Many of these applications require detector arrays which have a large detection area and are comprised of a greater number of detectors than is currently available, while maintaining the imaging capability of a single SNSPD. Such an array would be useful for applications such as dark matter detection [16] and astronomical observation [17], which require low dark count rates and mid-infrared wavelengths, for single photon LiDAR where the response time of the detector is crucial, and would benefit from a larger detection area to reduce the measurement time [10] and

for on-chip photonics for quantum computing [58].

To achieve a large-scale array of SNSPDs there have been several suggested methods of multiplexing and reading out the signals at room temperature. These can be separated into two categories, those which use on-chip superconducting electronics to provide low temperature digital signal processing, and those which multiplex on-chip by some analogue means and are processed at room temperature. The former offers a more integrated solution with less room temperature overhead, at the cost of increasing on-chip complexity while the latter allows a reduction in on-chip complexity with much greater demands on the external hardware required.

2.2.1 Row-Column Readouts

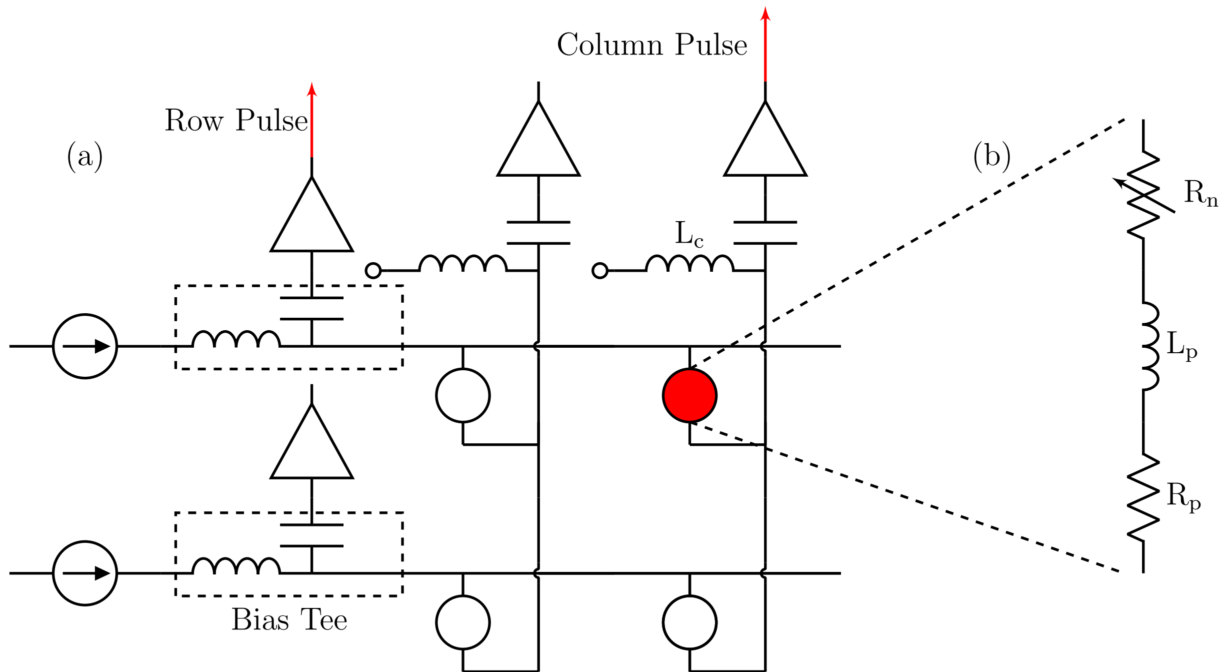

Figure 2.2: (a) An example of a segment of the detector array, each detector is represented by the circle. Bias current is supplied to each row and shunted by the column inductor L_c. When a pixel is triggered, as shown by the red circle, current is diverted out of the pixel on triggering resulting in a positive row pulse and a corresponding negative column pulse. Pixel discrimination is achieved by cross-referencing the row and column pulses. (b) The equivalent circuit of the detector, composed of the normal state resistance, R_n, of the SNSPD, the intrinsic inductance of the SNSPD L_p and an integrated 50 Ω impedance R_p. Image adapted from Allman et al (2015) [18]

In a row-column readout scheme [18], an array consists of an $N \times N$ grid of detectors, shown in figure 2.2. Each individual detector is composed of an SNSPD with kinetic inductance $L_p \sim 8$ μH and an integrated 50 Ω resistor. The detectors in each row are connected together in parallel and share a common DC bias which is connected through the DC port of a bias tee, and each column of detectors is then combined in parallel and grounded through the DC port of a bias tee. When a photon is detected, the SNSPD switches to the resistive state and a positive pulse is transmitted

through the RF port of the row SNSPD, and a negative pulse is transmitted through the RF port of the column bias tee.

The current splitting technique is capable of multiplexing and providing pixel discrimination while the number of coaxial cables is reduced, for an $N \times N$ array the reduction is from N^2 to $2N$. An array of 1024 pixels, with a 32×32-pixel array which is read out along 64 DC lines has been produced as part of a joint project with MIT and NASA [22].

This array has a large static power dissipation generated by the resistor R_p which is integrated into each of the detectors. This increases the power consumption of the detector array, and the heat load on the cryostat, which scales with the number of detectors.

The maximum count rate of the detector is given as 4.6 MHz, although the count rate is limited by the reset time of the detector. The detector array cannot multiplex multi-photon events which restricts the capability of the array to make time-of-flight measurements, as the reset time is determined by the nanowire relaxation time rather than from the detector jitter.

This scheme is restricted by relatively high jitter, operated with a bias current of 3 μA the jitter was found to be 400 ps, and at 4 μA while the jitter was reduced to 250 ps this increased the number of failed pixels. The high jitter is the result of current redistribution, when a single pixel is switched into the resistive state the current flows into the still superconducting detectors, not into the amplifier chain where it can be detected and increases the effect of the amplifier noise. This effect becomes more pronounced when the number of elements in the detector is increased. Recent work [59] with this method has included an attempt to integrate this technique with an SFQ based architecture which can reduce the effect of the amplifier noise without a corresponding increase in the jitter of the system.

2.2.2 Pulse Amplitude Multiplexing

Pulse Amplitude Multiplexing (PAM) requires a single coaxial cable to read out multiple SNSPDs and does not require the use of complex postprocessing. The scheme consists of detector elements composed of an SNSPD with a resistance in parallel, which can then be combined together either in series or in parallel [20] as shown in Figures 2.3 and 2.4. The device is fabricated in such a way that the resistance R_n is much smaller than the normal state resistance of the SNSPD. When a photon is detected the SNSPD will turn resistive and the current is forced through the parallel resistor, creating a voltage pulse proportional to the resistance of R_n. By varying the sizes of the resistances, the amplitudes of the voltage pulses can be used to determine which SNSPD corresponds to each detection event.

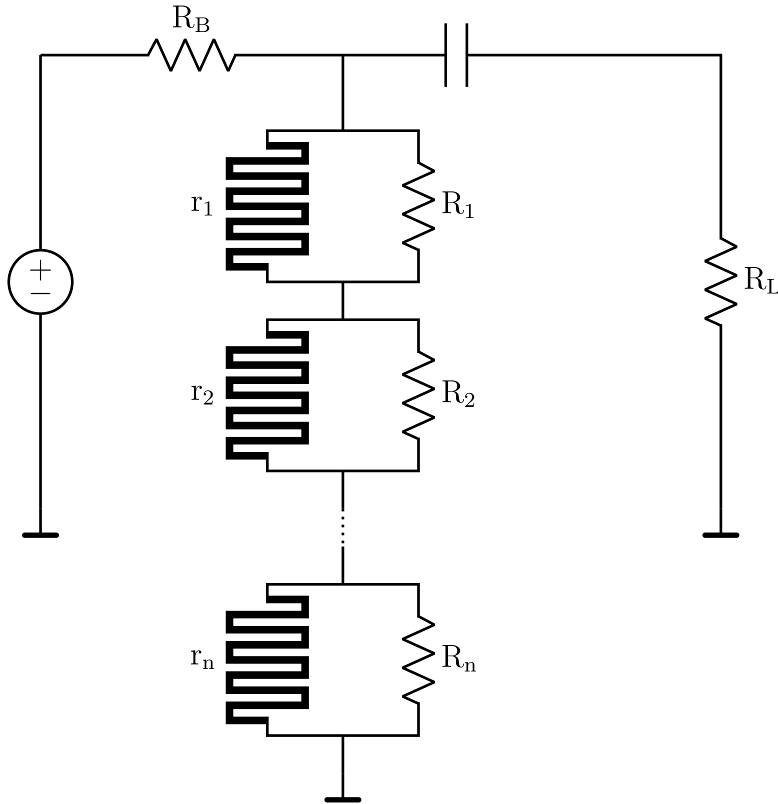

Figure 2.3: A PAM scheme in which the detectors are connected in series. The normal state resistance of the nanowire is much greater than the parallel resistance R_{n}. When the detector is triggered the current redistributed into R_{n} generates a voltage pulse which is used to discriminate the detectors.

PAM provides a means of photon number counting with an architecture which is relatively simple and does not require extensive room temperature electronics or complex low temperature processing, although this comes at the cost of additional fabrication steps to include the parallel resistance that is integrated with each SNSPD. The signal can be read out with a single coax line, and the electronics required at room temperature are reasonably simple as only the pulse amplitude is required for pixel discrimination.

The architectures shown in Figure 2.3 and 2.4 are restricted in scaling up by the number of resistors which can be used to provide pixel discrimination. Furthermore, each additional pixel limits the operational performance of the device, and when an SNSPD is triggered the current in each of the subsequent detectors is affected. In the parallel scheme shown in Figure 2.4 the detectors are biased with a total current $N \times I_{\mathrm{bias}}$, and this will be redistributed when one detector is switched into the resistive state. For both cases this results in sub-optimal operation and can cause an increase in dark counts or reduced efficiency due to reduced bias current.

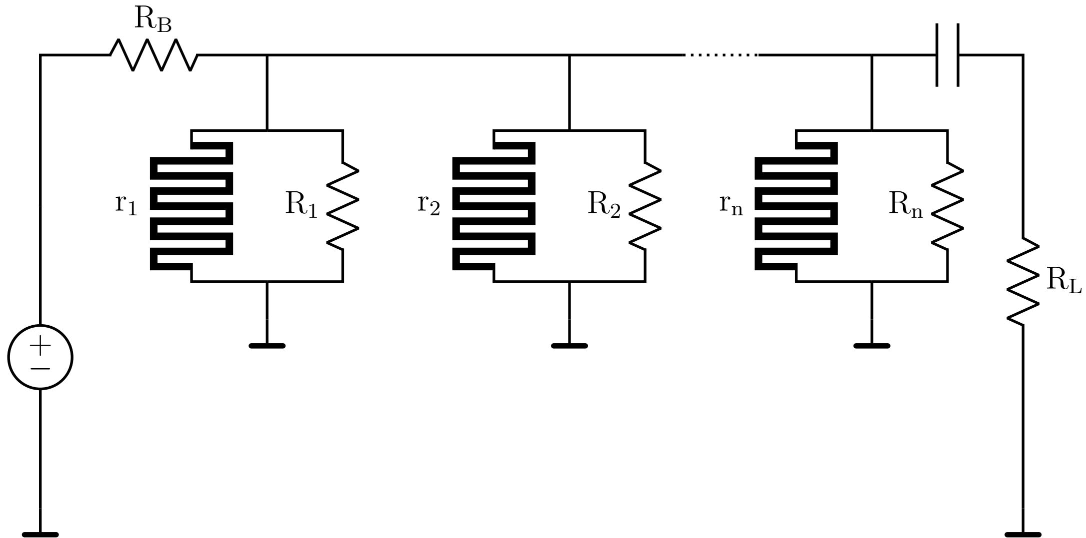

Figure 2.4: Unlike the scheme shown in Figure 2.3, each detector is biased in parallel. The discrimination mechanism remains the same however, with the current redistribution into R_n producing a voltage pulse which is used for pixel discrimination.

As SNSPDs require to be biased close to the critical current the redistribution of current could result in detectors switching due to a cascade effect similar to that in three terminal superconducting amplifiers [60] or in superconducting nanowire avalanche photodetectors [61]. To prevent the cascade effect from driving the detectors into the normal state each SNSPD must be biased below the threshold bias current, which limits their operational performance.

2.2.3 Frequency Division Multiplexing

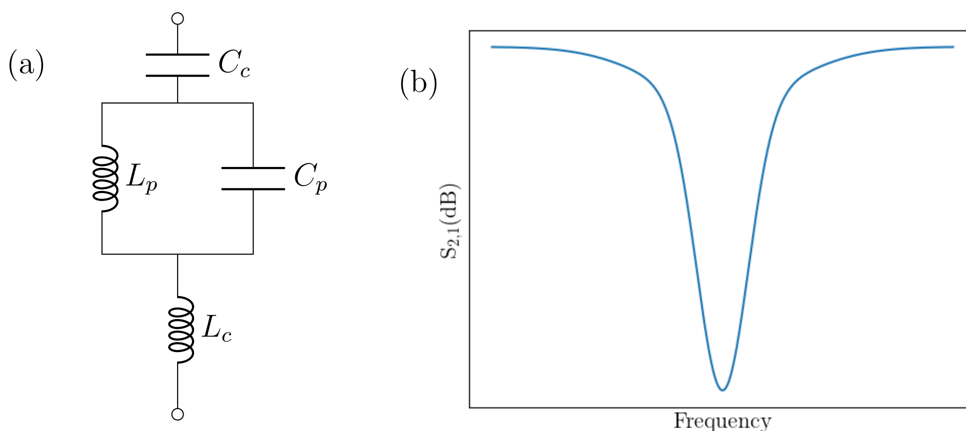

Figure 2.5: (a) The equivalent circuit for a RF-SNSPD. The capacitor C_p and inductor L_p form the resonant circuit, L_c represents the kinetic inductance of the SNSPD. (b) An example of the transmission against the frequency, the loss in transmission corresponds to the resonant frequency of the LC resonator

Frequency-division multiplexing (FDM) is a technique commonly used in telecommunications where a single transmission line is shared by multiple independent signals with different frequencies. This technique has been applied to SNSPDs to allow a number of detectors to be read out along a single coax line and for each detector to be multiplexed in the frequency domain (in a similar manner to the operation of a microwave kinetic inductance detector [62]), which can transmit the spatial and temporal information of each detector to room temperature.

Each detector contains a parallel LC circuit, with inductance L and capacitance C, as shown in Figure 2.5 which prevent a change in the resonant frequency of the device as the bias is varied. The SNSPD has inductance $L_c << L$ and capacitance C_c which defines the quality factor of the device.

When a photon is detected by the SNSPD the value of L_c is changed by the SNSPD being driven into the normal state, and a shift in the resonant frequency is detected at room temperature as a voltage pulse in a load resistor.

The FDM method can be scaled up to larger number of pixels although this architecture requires more processing at room temperature than other readout electronics. The technique has shown to be capable of photon number resolution and maintains the time resolution of a standard SNSPD [21, 63]. An FDM scheme can also be used to multiplex other types of superconducting sensors, and has been used with a TES array [64]. However, scaling up to large numbers of pixels could be restricted by the need for complex room temperature electronics to provide the readout for the detection scheme.

2.2.4 Time-Domain Multiplexing

A time-domain multiplexed (TDM) architecture is achieved with a single continuous nanowire which is meandered to create a detection area [37], shown in Figure 2.6. The nanowire is terminated at each end with a Klopfenstein taper designed such that the entire device is impedance matched to 50 Ω which allows the detector to be efficiently coupled with a microwave readout circuit. When a photon is detected by the nanowire the signal is transmitted as a pair of pulses with opposite polarities and constant velocity through the meandered nanowire and into the Klopfenstein tapers at each end. The pulse pair is then detected by the readout electronics, and the delay time between the arrival of the first and second pulses corresponds to the position of the detection event in the wire. The velocity of the pulse within the wire, v, is known, and the arrival time of each pulse can be calculated as $\tau_1 = t_p + (L - x_p)/v$ and $\tau_2 = t_p + x_p/v$, where L is the length of the wire, t_p is the pulse travelling time and x_p is the pulse position on the wire. The position of the pulse on the wire can be determined by resolving these equations.

The timing of the pair of pulses produced by a photon absorption event is subject to the electrical

noise, which will introduce some error into the timing and therefore the position. Slowing the velocity of signal will reduce the error in the detection and provide a more precise spatial resolution, at the cost of a reduced count rate. This scheme shows a maximum count rate of 4.8 MHz and jitter of 56 ps.

Despite the trade-off between operating frequency and spatial resolution time-tagged readouts have been demonstrated with < 20 μm spatial resolution and 50 ps timing resolution in a wire 19 mm long, resulting in almost 600 individual "pixels", with a count rate < 5 MHz. The count rate was maximised by reducing the signal to noise ratio, it is not possible with this configuration of detector to improve the count rate to that seen in other detection systems.

To improve the signal to noise and the detection area an optimised device was fabricated which contained sixteen detectors formed of two parallel superconducting nanowires [65] which were placed in series and joined with 300 nm delay lines. The detector used a two-element design which improves the signal to noise ratio of the device which made use of a cascade effect on the nanowires. For single photon detection this scheme operates with a detection mechanism which is similar to that described for the scheme shown in Figure 2.6. When detecting multiple photons simultaneously only the first pulse will be detected from each end, preventing the system from fully resolving the position of both events. This limits the use of this detector to applications where the initial detection time is known, for example where pulsed photon sources are used.

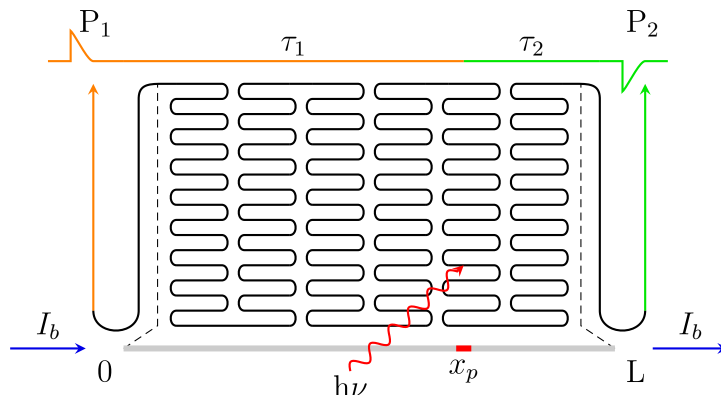

Figure 2.6: A schematic of a time-tagged readout scheme, showing a nanowire meandered over a detection area. The meander is coupled to room temperature through a Klopfenstein taper at both ends to allow for impedance matching of the circuit. When a photon is detected the output pulses, P_1 and P_2, at each end of the wire arrive at the readout with time delays of τ_1 and τ_2. The photon arrival time is calculated using the equation $t_p = ((\tau_2 + \tau_1) - L/v)/2$. From this time the position of the detection event along the length of the wire, x_p, can be calculated. Image adapted from Zhao et al [37]

This detector scheme also requires that each pixel is isolated by a transmission line, which significantly reduces the fill factor. The jitter of this device was 20 ps, with a timing delay between pixels of 87 ps, and the maximum count rate of the scheme showed no improvement over the

previous design, at 4.8 MHz.

2.2.5 Single Flux Quantum Electronics

SFQ electronics based on Josephson junctions have been demonstrated as a readout scheme for SNSPDs [66, 67]. The SFQ circuitry is used to digitise the SNSPD outputs at low temperature and transmitting the data directly to room temperature. SFQ electronics have successfully been used to combine the signals for four SNSPDs simultaneously, which allowed the entire detection area to operate as a single large area pixel without the loss of performance due to the increase in size [68]. A simple SFQ combiner was used as a proof of principle to demonstrate that SFQ electronics could be used to provide readout for SNSPD arrays. This system used the SFQ circuitry as a signal combiner without any pixel discrimination, which allowed the SNSPD array to act as a single large scale pixel which maintained the properties of the single SNSPDs. A more complex design was used to multiplex a four pixel array which is capable of single pixel discrimination [69], while also demonstrating that SFQ circuitry was capable of time-resolution on the order of 10 ps. A recent result has shown that a combination of SFQ electronics schemes can be implemented to provide individual pixel discrimination and maintaining the count rate seen in individual SNSPDs [38]. Using this scheme to read out a four pixel SNSPD array, it was found that the maximum count rate was 10 MHz, and the jitter of the SNSPD was maintained when integrated with the SFQ electronics readout scheme.

To date the largest array of SNSPDs to use an SFQ scheme for readout had 64 individual pixels, although only 8 pixels could be read at each cooldown [70]. Such a scheme requires full on-chip integration between the SFQ readout electronics and SNSPD detection area. SFQ devices also require dedicated input and output devices to integrate with standard semiconducting room temperature electronics, although a simple means of integration can be achieved through the use of superconducting amplifiers, such as three-terminal amplifiers [60, 71] and nanocryotrons [72, 37], which are easily integrated into the fabrication process. Circuits which can convert between DC and SFQ pulses have been demonstrated [73], and can be used with any SFQ scheme.

Standard SFQ electronics uses superconducting tunnel junctions (STJs) as Josephson junctions, and these devices require a multilayer fabrication process which is difficult to integrate with the fabrication of SNSPDs. Integrating in this manner eliminates the need for complex amplification and allows a low power electronics which can operate at temperatures comparable to the operation of the SNSPD. To date however, it has proven difficult to integrate the SNSPD array with an STJ-based SFQ scheme, due to the fabrication process and physical layout.

2.2.6 Summary

Each of the multiplexing schemes presented here have demonstrated successful readout of SNSPDs.

Some schemes have shown more viability for large-scale arrays, for example the row-column readout, although the demonstrated 1024−pixel array [22] cannot maintain the peformance of individual SNSPDs in terms of the detection efficiency, max count rate and jitter. It has been demonstrated that the FDM scheme can be scaled up to large numbers of pixels, although this scheme is not capable of providing low temperature digital signal processing and requires complex room temperature electronics.

SFQ electronics offer a solution to large array SNSPD which can maintain the performance metrics of single pixel devices described in Table 2.1, beyond the capabilities of the alternative schemes. With an SFQ readout scheme each pixel can be integrated with a dedicated readout line, which prevents the detector reset time being determined by adjacent pixels as in the row-column readout. Using SFQ electronics it is possible to achieve a "plug and play" system, which can be read out without the need for complex room temperature electronics or a skilled user. This would provide a low power, high speed readout scheme which could be integrated on-chip with the SNSPD detector array.

For STJ-based SFQ circuits the fabrication process is based on a multilayer Nb process, which has proven to be difficult to integrate with the SNSPD detector layer. This could be overcome by implementing an SFQ scheme based on bridge-type weak link Josephon junctions, which can be fabricated on-chip using similar processes to those required to produce SNSPDs.

This work is an investigation into the possibility of using bridge-type weak links as the active element in an SFQ-based readout scheme. We begin with a discussion of the theoretical description of the Josephson effect as it occurs in Josephson junctions.

Chapter 3

Background

This section begins with a discussion of the Josephson Effect, covering the superconducting state where a Josephson current flows across the junction with no associated voltage drop, and the voltage state where the current in the Josephson junction can be approximately described by Ohm's law. This is typically modelled as an equivalent circuit composed of multiple current branches each represented by a single lumped element. This description of the current dynamics in the Josephson junction is then used to discuss the response of the Josephson junction to various driving sources. Following this the principles of single flux quantum electronics are introduced, and a description of the types of Josephson junctions which can be used for SFQ electronics.

3.1 Josephson Effect

The Josephson Effect is the phenomenon of a current flowing between two superconducting electrodes, which contains a supercurrent component, I_s. The existence of the phenomenon was theoretically predicted by Brian D. Josephson in 1962 [74], and experimentally confirmed the following year [32].

Devices which exhibit this effect, Josephson junctions, are classified as either tunnel junctions, or weak links [75]. In tunnel junctions, if the barrier thickness, d, is sufficiently thin then the supercurrent component can flow through the barrier layer by quantum mechanical tunnelling [76]. For weak links the superconducting current flows by direct conductivity. Where the weak link is formed by a normal metal, the Josephson current is the result of proximitisation of the normal metal by the superconducting electrodes. The Cooper pairs of the supercurrent can conserve the amplitude and phase of the order parameter, Ψ, over a distance of the coherence length ξ_{N} into the normal metal. As the weak link is formed of two superconducting electrodes coupled by the normal metal weak link it is possible to maintain the supercurrent over several lengths of ξ_{N}.

The "classical" theoretical description of Josephson junctions is typically valid for STJs. In this

case the superconducting current across the junction is described by the equation

$$I_s = I_c \sin \varphi \tag{3.1}$$

where I_c is the critical current of the Josephson junction, the maximum current that can flow across the junction with no voltage drop. The phase difference across the junction, φ is related to the number density of Cooper pairs in each electrode, $n_{1,2}$, through the relationship

$$\Psi_1 = \sqrt{n_1} \exp\left(i\varphi_1\right) \tag{3.2}$$

$$\Psi_2 = \sqrt{n_2} \exp\left(i\varphi_2\right) \tag{3.3}$$

where $\Psi_{1,2}$ is the the wavefunction of the Cooper pair condensate in the electrodes [77]. The phase difference across the junction is $\varphi = \varphi_1 - \varphi_2$.

The voltage across the junction is described by the equation

$$\frac{d\varphi}{dt} = \frac{2e}{\hbar} V \ . \tag{3.4}$$

Together, Equations 3.1 and 3.4 are commonly described as the Josephson equations, which describe the basic behaviour of the Josephson tunnel junction.

3.1.1 The Zero Voltage State

Where the current flowing through the junction is less than the critical current I_c the junction will operate in the zero-voltage state. In this state the current flowing through the junction can flow entirely as supercurrent I_s, without any associated voltage drop across the junction.

3.1.1.1 Josephson Coupling Energy

In the superconducting state there is no voltage across the junction, and so it follows that there will also be no power dissipation across the junction. However, there is a stored finite energy which can be determined by considering a junction for which an external current is applied from zero to a finite value over time t, while maintaining the condition $I < I_c$. This ramping current produces a corresponding change in the phase over time according to Equation 3.1, and from Equation 3.4 it can be seen that this will result in a voltage across the junction. As the electrons in a superconductor experience no resistance there can be no power dissipated as a result of this voltage and current,

instead the potential energy of the current source is converted into kinetic energy of the electrons in the supercurrent.

This kinetic energy can be calculated by integrating the energy supplied by the current source, over time, t,

$$E_J = \int_0^t I_s V dt \ . \tag{3.5}$$

Substituting the current and voltage for those described by the Josephson Equations 3.1 and 3.4 into the equation results in an energy,

$$\begin{aligned} E_J &= \int_0^t I_c \sin\varphi \cdot \frac{\Phi_0}{2\pi}\frac{d\varphi}{dt} dt & (3.6) \\ &= \frac{I_c \Phi_0}{2\pi} \int_0^\varphi \sin\varphi d\varphi & (3.7) \\ &= E_{J0} \left(1 - \cos\varphi\right) \ , & (3.8) \\ \text{where } E_{J0} &= \frac{I_c\Phi_0}{2\pi} \ . & (3.9) \end{aligned}$$

The energy, E_J, is the Josephson coupling energy and $\Phi_0 = h/2e$ is the single flux quantum. From Equation 3.8 it can be seen that the Josephson energy of a junction will be at the lowest value when the cosine term is at the maximum, which occurs for values of $\varphi = 2n\pi$, where n is an integer. In some cases the minimum in Josephson energy can occur at $\varphi = (2n + 1)\pi$, and the Josephson junctions which exhibit this behaviour are known as π-junctions [31].

3.1.1.2 The Superconducting State

If a constant DC current is applied to the junction, it can be seen from Equation 3.1 that this will result in a constant phase. Rearranging this equation to find an expression for the phase

$$\varphi = \varphi_n = \arcsin\left(\frac{I_{\text{app}}}{I_c}\right) + 2n\pi \tag{3.10}$$

$$\varphi = \widetilde{\varphi}_n = \pi - \arcsin\left(\frac{I_{\text{app}}}{I_c}\right) + 2n\pi \ , \tag{3.11}$$

where φ_n corresponds to the minima and $\widetilde{\varphi}_n$ to the maxima. This is limited to the zero-voltage state where the magnitude of the applied current is less than the critical current, $|I_{\text{app}}| < I_c$. As the time derivative of the phase will be static, $d\varphi/dt = 0$, in the case of a constant applied current, then it can be seen from Equation 3.4 that there will be zero-voltage across the junction in this condition.

$$E_p(\varphi) = E_(\varphi) - I\left(\frac{\Phi_0}{2\pi}\varphi + c\right) \tag{3.12}$$

$$= E_{J0}(1 - \cos\varphi) - \left(\frac{\Phi_0}{2\pi}\varphi + c\right) \tag{3.13}$$

$$= E_{J0}\left(1 - \cos\varphi - \frac{I}{I_c}\varphi\right) + c\ . \tag{3.14}$$

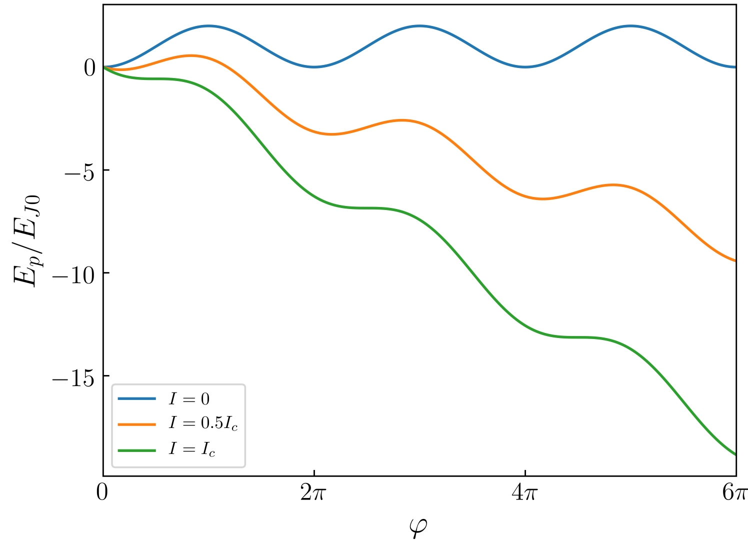

Figure 3.1: It can be seen that the driving current changes the shape of the Josephson energy. At $I = 0$ the Josephson energy has a purely sinusoidal relationship, while at $I = 0.5I_c$ the tilted washboard shape becomes evident. At $I > I_c$ the local gradient between maxima and minima is removed and the phase can be continually driven.

The potential energy of the Josephson junction in this condition can be found by considering that

$$G = E - Fx, \tag{3.15}$$

where G is the Gibb's energy, and E is the intrinsic free energy. In the Josephson junction the external applied force, F, corresponds to the applied current I, and the coordinate x can be chosen such that the product $F\dot{x}$ corresponds to the power flowing into the subsystem. As this power is equal to $P = IV$, it follows that x should be described as the time integral of the voltage,

$$x = \int V dt = \frac{\hbar\varphi}{2e} + \mathrm{c}\ . \tag{3.16}$$

where c is an integration constant.

This produces a potential energy function with the shape known as a "tilted washboard" potential,

an example of which is shown in Figure 3.1.

The tilted washboard has minima which occur at Equation 3.10 and maxima at Equation 3.11, and a general slope which is dependent on the ratio of the applied current to the critical current, I/I_c.

The difference between the local maxima and minima of the potential function,

$$U_0 = E_p(\varphi_n) - E_p(\tilde{\varphi}_n) \tag{3.17}$$

can be determined by considering the curvature of the slope between the local minimum and maximum

$$k = \frac{\partial^2 E_p}{\partial \varphi^2} k = E_{J0} \sqrt{1 - \left(\frac{I}{I_c}\right)^2} \,, \tag{3.18}$$

and it can be seen that as the applied current, I, approaches the critical current, I_c both the difference between the maxima and minima, and the slope $dE_P/d\varphi$ approach zero. In this situation the barrier to overcome is continually reduced, and the phase can be continually increased more easily, and where $d\varphi/dt$ takes a finite value it follows that the Josephson junction will have a voltage described by Equation 3.4. This is often described with the analogue of the motion of a particle moving along the potential, which is described in Section 3.1.2.1.

3.1.1.3 Josephson Inductance

The stored energy described in Section 3.1.1.1 suggests that the Josephson junction can be described as a non-linear reactance. It is possible to determine the inductance of the Josephson junction by considering a small increament in current which is generated by a small deviation in phase from the current-phase relationship Equation 3.1,

$$I_s + \delta_I = I_c \sin\left(\varphi_0 + \delta_\varphi\right) \;. \tag{3.19}$$

If the phase change δ_φ is sufficiently small the right-hand side can be expanded by Taylor expansion to

$$\delta_I = I_c \cos(\varphi_0) \delta_\varphi \;. \tag{3.20}$$

Combining this with the Josephson voltage Equation 3.4 produces an expression for the voltage,

$$V = \frac{\Phi_0}{2\pi} \left(\frac{d\varphi_0}{dt} + \frac{d\delta_\varphi}{dt} \right) = \frac{\Phi_0}{2\pi} \frac{\delta_I}{I_c \cos\left(\varphi_0\right)} \;. \tag{3.21}$$

Substituting these values into the equation for the voltage across a standard inductor an expression for the Josephson inductance is found

$$L_J = \frac{\Phi_0}{2\pi I_c \cos(\varphi)} \ . \tag{3.22}$$

One unusual property is that in the range $\pi/2+2\pi n < \varphi < 3\pi/2+2\pi n$ the Josephson inductance can take negative values, which is not the case for a typical non-linear reactance. When a constant voltage is applied to a non-linear reactance the current typically increase linearly. In the Josephson junction, as the voltage is increased the current will oscillate according to the Josephson oscillations, which is further discussed in Section 3.1.3.2.

3.1.2 Josephson Junctions in the Resistive State

Where the current flowing through the junction exceeds the critical current, the Josephson junction switches from the zero-voltage state to the finite voltage state. In this state the current can be considered to be a combination of parallel current channels in addition to the previously described supercurrent. At temperatures greater than 0 K a finite number of Cooper pairs are broken by thermal excitation into electrons which will generate a normal component of the total current, I_n. A further current component is generated by the finite capacitance of the Josephson junction, known as the displacement current, I_D. The final component to the current is a fluctuation current I_F, which can be used to account for random current fluctuations in the system.

3.1.2.1 Resistively and Capacitively Shunted Junction Model

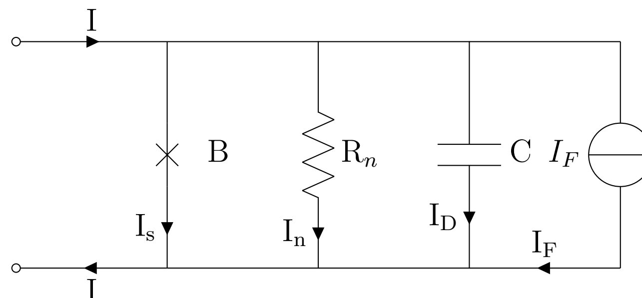

Figure 3.2: The total junction current, I, can be divided into four current components, each of which is represented by one branch of the equivalent circuit. The supercurrent, I_s is represented by a barrier B. The normal current is represented by a resistance which is equivalent to the normal state resistance, R_n. The displacement current is represented by a capacitance, C. Additional random current fluctuations are represented by an additional current source I_F.

The Josephson junction can be modelled as an equivalent circuit, shown in Figure 3.2. By applying Kirchoff's law, each of the current components can be represented by a parallel branch, where the

supercurrent passes through a barrier, B, the normal current I_n, passes through a resistance R_n and the displacement current I_D passes through a capacitance C. An additional parallel current source I_F is included to model the random fluctuations that occur in the total junction current.

3.1.2.2 The Normal Current, I_n

At finite temperatures Cooper pairs will be broken by thermal excitations, which produces a finite density of normal electrons [78]. The Cooper pairs occupy a single energy level at the Fermi energy, E_F, and the energy levels within $E_F \pm \Delta$, where Δ is the superconducting band gap, become unavailable, which results in the superconducting energy gap as shown in Figure 3.3. Due to the nature of the Cooper pair condensate the properties of the excited state electrons differ slightly from the normal electrons, and so to differentiate from the normal electrons the excited electrons are known as "quasiparticles".

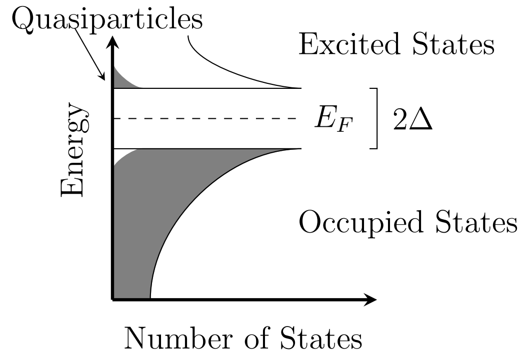

Figure 3.3: The superconducting band gap forms around the Fermi energy, at values of $\pm\Delta(T)$, with the energy state of all Cooper pairs in the system positioned at the Fermi energy. To break a Cooper pair requires both electrons to be excited by an energy of Δ, this action can occur either through thermal excitation or due to the energy provided by a driving external voltage.

Quasiparticles are formed at finite temperatures by the thermally induced breaking of Cooper pairs. There is no contribution to the junction current from the quasiparticles unless the junction phase changes with time, which produces a non-zero junction voltage according to Equation 3.4. In this case the quasiparticles provide a current contribution known as the normal current, I_n.

The magnitude of Δ is temperature dependent, and close to the critical temperature of the superconductor, $T \lesssim T_C$ the gap energy becomes small enough, $\Delta < k_B T$, that almost all of the Cooper pairs are broken by thermal excitation. In the junction IVC this produces an approximately Ohmic relation

$$I = \frac{V}{R_n} \ . \tag{3.23}$$

Cooper pairs are broken by an external voltage which provides sufficient energy to excite the

electrons by the gap voltage,

$$V_g = \frac{\Delta_1(T) + \Delta_2(T)}{e} \ , \tag{3.24}$$

where $\Delta_{1,2}$ are the superconducting energy gaps of each of the two electrodes. A Cooper pair is broken in one of the junction electrodes, and one of the two newly formed quasiparticles can tunnel across the junction barrier to contribute to I_n.

It can be seen in Figure 3.4, that the junction is in the zero-voltage state when both $T < T_C$ and $|V| < V_g$. At $T > T_c$ the IVC will become Ohmic regardless of the junction voltage, however at $T < T_c$ and $|V| < V_g$ the IVC is dependent on the type of driving source, and whether the sweep is driven in the positive or negative direction.

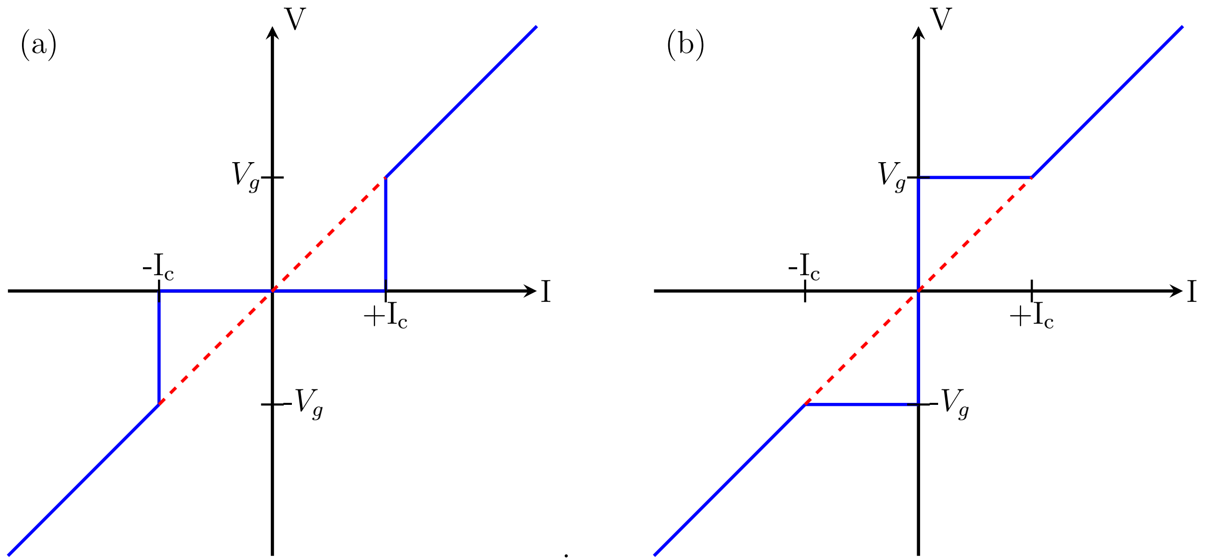

Figure 3.4: The IVC of a typical Josephson junction showing the time averaged voltage $< V >$, where (a) shows a junction driven by a current source, and (b) shows a junction driven by a voltage source. The condition $T < T_c$ is represented by the blue line, and $T > T_c$ by the red dashed line.

When the junction is driven by an external current the total current must be constant, and as the superconducting current varies sinusoidally according to Equation 3.1 then the normal current must vary in response. This produces a varying junction voltage, based on the relation $V = IR_n$, and so the voltage which is recorded in the IVC is a time averaged voltage, $< V >$.

The thermally excited quasiparticles which are formed at finite temperatures can tunnel across the junction at $|V| < V_g$, and generate a temperature dependent finite resistance known as the sub-gap resistance, $R_{sg}(T)$. This resistance is dependent on the number of thermally excited quasiparticles at a given temperature,

$$R_{sg}(T) = \frac{n_{\rm tot}}{n(T)} R_n \ , \tag{3.25}$$

where $n(T)$ is the density of excited quasiparticles at temperature T and n_{tot} is the total density of normal state electrons.

The normal current channel is defined by the sub gap resistance at $|V| < V_g$, and by the normal resistance at $|V| > V_g$. Additionally, as the gap voltage of the superconductor is dependent on the temperature this results in a nonlinear resistance which is dependent on both the temperature and the junction voltage which defines the normal current I_n.

3.1.2.3 The Displacement Current, I_D

The displacement current is defined as the current in a capacitor

$$I_D = C\frac{dV(t)}{dt} , \tag{3.26}$$

where C is the capacitance, which is the same for both the superconducting and normal states. The junction capacitance is dependent on the physical layout of the junction. For superconducting tunnel junctions (STJs) which are formed by two superconducting plates coupled by insulating material, the junction capacitance can be described by the same equations as in a standard parallel-plate capacitor. The capacitance of the STJ can therefore be written in the form

$$C = \frac{\epsilon A}{d} \tag{3.27}$$

where d is the barrier thickness, A is the junction area and ϵ is the dielectric constant of the barrier material. In bridge type weak links, a finite capacitance between the two parallel electrodes does exist, however due to the presence of the bridge structure this becomes difficult to determine. The capacitance of the nanobridge is typically very small in comparison to the capacitance of a STJ with comparable I_c.

3.1.2.4 The Fluctuation Current, I_F

The current also includes a contribution from random fluctuations which occur in the Josephson junction. There are three types of noise fluctuations: thermal noise, shot noise and $1/f$ noise.

The thermal noise, or Johnson-Nyquist noise can be described as a power spectral density

$$S_I(f) = \frac{4k_BT}{R_N} , \tag{3.28}$$

is valid for an an Ohmic resistor at temperatures high enough that $k_BT \gg eV, \hbar\omega$ is satisfied.

The relative intensity of the thermal noise is described by the dimensionless parameter

$$\gamma = \frac{k_B T}{E_J} = \frac{2ek_B T}{\hbar I_c} \tag{3.29}$$

where E_J is the Josephson energy [79]. For values of $\gamma > 1$ the Josephson effect is destroyed by the thermal fluctuations in the system.

The shot noise is the effect of random current fluctuations caused by the charge carriers in a conductor. The power spectral density of shot noise current fluctuations is given by the Schottky formula

$$S_I(f) = 2eI_N \tag{3.30}$$

and follows a Poissonian distribution where the amplitude of the current fluctuations is expressed by the variance of the current I,

$$\Delta I^2 = \left\langle (I - \langle I \rangle)^2 \right\rangle \ . \tag{3.31}$$

The $1/f$ noise is inversely dependant on frequency and can be considered negligible at frequencies greater than 1 kHz for Josephson junctions, which is typically well below the operating frequency of RSFQ circuitry.

3.1.2.5 Stewart-McCumber Parameter

When driven by a fixed, non-zero DC voltage the superconducting current of the Josephson junction will oscillate with a frequency

$$\omega_J = \frac{2e}{\hbar} V \ . \tag{3.32}$$

The characteristic voltage of the Josephson junction is described as

$$V_c = I_c R_n \ . \tag{3.33}$$

This voltage defines a corresponding frequency, which describes the relaxation time in a Josephson junction where only the superconducting and normal current channels contribute to the total current. This frequency, ω_c is the characteristic frequency of the Josephson junction and can be described as

$$\omega_c = \frac{R_n}{L_J} = \frac{2e}{\hbar} V_c = \frac{2\pi}{\Phi_0} V_c \tag{3.34}$$

where the inductance is the Josephson inductance which was derived in Equation 3.22. The Josephson junction will operation will be determined by the characteristic frequency, ω_c, where the total current is composed of only normal and supercurrent contributions. Where the junction voltage is less than the characteristic voltage $V < V_c$ the operating frequency of the junction will be smaller than the characteristic frequency, $\omega << \omega_c$.

The junction behaviour can also be defined by the plasma frequency, ω_p, which can be described as

$$\omega_p = \frac{1}{\sqrt{L_J C}} = \sqrt{\frac{2eI_c}{\hbar C}} \ . \tag{3.35}$$

The Stewart-McCumber parameter [80][81] is introduced when characterising the effect these parameters have on the Josephson junction up to the characteristic frequency ω_c,

$$\beta_c = \frac{\omega_c^2}{\omega_p^2} = \frac{2e}{\hbar} I_c R_n^2 C \ . \tag{3.36}$$

The Stewart-McCumber parameter corresponds to the quality factor of a parallel LRC circuit as

$$Q = \sqrt{\beta_c} = R_n \sqrt{\frac{C}{L_{\mathrm{J}}}} \ . \tag{3.37}$$

The quality factor Q determines the rate of damping of an oscillator. In the case of a Josephson junction where the capacitance and resistance are small, resulting in the Stewart-McCumber parameter $\beta_c < 1$ the junction is considered to be overdamped and the Josephson junction IVC will exhibit non-hysteretic behaviour. In the reverse case, where the junction has a large capacitance and $\beta_c > 1$ the junction will be underdamped and exhibit hysteretic behaviour.

3.1.2.6 Basic Junction Equation

As shown by Figure 3.2 the total current passing through the junction can be described by the equation

$$I = I_s + I_n + I_D + I_F \tag{3.38}$$

and substituting for the expressions of the current components with the Equations 3.1, 3.23 and 3.26 results in the expression

$$I = I_c \sin\varphi + \frac{V}{R_n(V)} + C\frac{dV}{dt} + I_F(t) \ . \tag{3.39}$$

By replacing the voltages with the Josephson voltage from Equation 3.4 this equation can be

rewritten as

$$I = I_c \sin\varphi + \frac{\Phi_0}{2\pi R_n(V)}\frac{d\varphi}{dt} + C\frac{\Phi_0}{2\pi}\frac{d^2\varphi}{dt^2} + I_F \ , \tag{3.40}$$

which is the basic equation which describes the nonlinear behaviour of the STJ.

3.1.2.7 Underdamped and Overdamped Josephson Junctions

When a current is applied to the Josephson junction the washboard potential becomes tilted corresponding to the magnitude of the current as was described in Section 3.1.1.2. For applied currents $I_{\text{app}} > I_c$ the gradient between the local maximum and minimum allows the phase to be continually driven by the current, and the junction will be in the voltage state. When $I_{\text{app}} < I_c$ local minima in the washboard potential prevent the phase from changing in time. This creates a barrier in the washboard potential which the particle cannot overcome, and prevents the particle from escaping the local minima. When the particle is trapped the phase becomes constant and so the junction is in the zero-voltage state.

The change of the phase can be understood by considering the movement of a particle with mass M corresponding to the junction capacitance C, which experiences some damping η corresponding to the resistance as $1/R_n$, where the phase φ corresponds to the position of the particle x. In the case of strong damping, where $\beta_c << 1$, the particle mass is small and the damping is large. It follows that for the case of weak damping the opposite is the case: the particle will have large mass and experience small damping.

When the current is increased from zero in both cases the junction remains in the zero-voltage state while $I_{\text{app}} < I_c$. In the analogue this is because the particle is trapped in a local minimum and has no kinetic energy driving it forward. Once the driving current reaches the critical current the local maximum will disappear and the particle is able to move continuously, this results in continuous driving of phase φ and the junction is in the voltage state.

A distinction in the behaviour can be made between the strongly and weakly damped cases where the junction is being driven by an applied current $I_{\text{app}} > I_c$. Where $\beta_c << 1$, once the applied current is reduced to the critical current and local minima appear in the washboard potential the strong damping η causes the particle to become immediately trapped, returning it to the zero-voltage state. For the weak damping case, where $\beta_c >> 1$, the momentum of the particle is large enough that the damping cannot trap it in a local minimum, and the particle can overcome the barrier to continue moving. Only by reducing the applied current further, and increasing the barrier height, can the particle become trapped. The value of current at which this happens is known as the return current I_R, and in the IVCs of the junctions this can be seen as a hysteretic behaviour in weakly

damped Josephson junctions.

3.1.3 Response to Driving Sources

The behaviour of a Josephson junction in the finite voltage state varies depending on the driving source. How the junction reacts to each driving source can be determined by using the RCSJ model.

3.1.3.1 Response to DC Current Source

In the voltage state the superconducting current of a Josephson junction biased with a constant voltage will oscillate sinusoidally according to Equation 3.1. Taking the time averaged voltage over this oscillation period, T,

$$\langle V \rangle = \frac{1}{T}\int_0^T V(t)dt \tag{3.41}$$

$$= \frac{1}{T}\int_0^T \frac{\hbar}{2e}\frac{d\varphi}{dt}dt \tag{3.42}$$

$$= \frac{1}{T}\frac{\hbar}{2e}\left(\varphi(T) - \varphi(0)\right) \ . \tag{3.43}$$

When the junction is being driven by a DC current source the total junction current must be continuous and equal to the applied current I_{app}. In the resistively and capacitively shunted junction (RCSJ) model the total current through the junction is given by Equation 3.40, and so where $I_{\text{app}} > I_c$ some of the current must be carried by the normal and displacement currents.

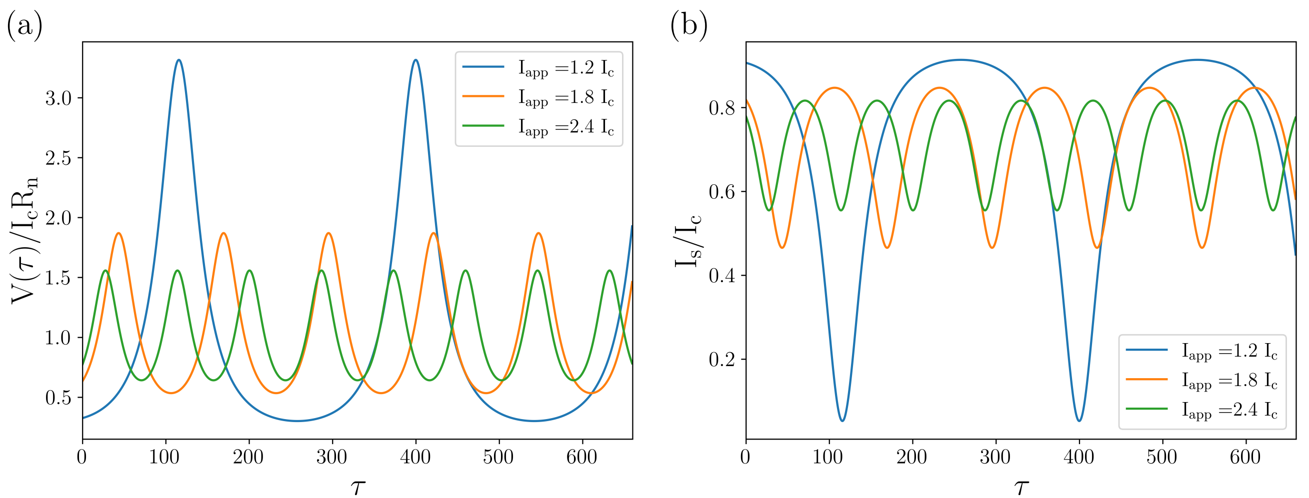

Figure 3.5: The superconducting voltage and current oscillations corresponding to $I_{\text{app}}/I_c = 1.2, 1.8$ and 2.4, normalised in time corresponding to $\tau = \hbar/2eI_cR_n$. (a) Due to the oscillation of the normal and superconducting currents in the normal state, the junction voltage will vary depending on the applied current. (b) The supercurrent oscillations change with the applied current. Reproduced from Reference [82].

The total current through the junction must sum to the applied current, $I_{\text{app}} = I_s + I_n + I_D$, and since the superconducting current will oscillate according to Equation 3.1 the other current components must oscillate to compensate in response. This complex sum of the three current component which produces a complex non-sinusoidal Josephson current oscillation, an example of this is shown in Figure 3.5.

In the IVC of a hysteretic Josephson junction which is driven by a DC current there will be a return current I_R, which is the current at which the junction will transition from the voltage state to the zero-voltage state. This current is determined by the evolution of the phase from one minima of the Josephson potential to the next, and so is dependent on the Stewart-McCumber parameter β_c.

3.1.3.2 Response to DC Voltage Sources

When a DC voltage, V_{dc}, is applied to the junction the phase φ can be calculated using Equation 3.4,

$$\varphi = \int \frac{2e}{\hbar} V_{\text{dc}} dt \tag{3.44}$$

$$= \frac{2e}{\hbar} V_{\text{dc}} t \ . \tag{3.45}$$

This equation can be substituted into Equation 3.1 to give an expression where the current is dependent on the voltage across the junction

$$I_s = I_c \sin\left(\frac{2e}{\hbar} V_{\text{dc}} t\right) \tag{3.46}$$

showing that the current oscillates with frequency per volt,

$$\frac{f}{V} = \frac{2e}{\hbar} \tag{3.47}$$

$$= 483.6 \text{ MHz}/\mu\text{V} \ , \tag{3.48}$$

and consequently, Josephson junctions exhibit high sensitivity to electromagnetic effects.

A Josephson junction which is driven by a constant voltage must necessarily have a time derivative of that voltage $dV_{\text{dc}}/dt = 0$, and as a result there is no contribution from the displacement current.

The current is therefore carried by the normal channel, resulting in a current across the junction

$$I = \frac{V_{\rm dc}}{R_n} \tag{3.49}$$

when the junction is in the voltage state.

3.1.3.3 Response to RF Voltage Sources

To understand the response of the Josephson junction to an RF source it is mathematically convenient to consider the junction in the presence of a voltage bias, although for practical applications the device must be biased with a current source. For a junction which exhibits strong damping, where $\beta_c << 1$, with applied voltage

$$V(t) = V_{\rm dc} + V_{\rm rf}\cos(\omega_{\rm rf} t)\ , \tag{3.50}$$

the current contribution from the displacement current will be negligible due to the small capacitance, and only the Josephson current and normal current need to be considered, as shown in the equivalent circuit Figure 3.6.

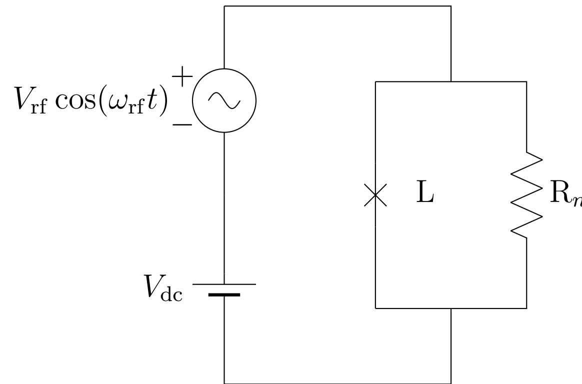

Figure 3.6: Where the junction is strongly damped, $\beta_c << 1$, in the presence of a combination of RF and DC sources the equivalent circuit can be considered as a combination of the parallel I_s and I_n channels due to the negligibly small capacitance.

The phase difference across the junction can be written as

$$\varphi(t) = \varphi_0 + \frac{2\pi}{\Phi_0} V_{\rm dc} t + \frac{2\pi}{\Phi_0}\frac{V_{\rm rf}}{\omega_{\rm rf}}\sin(\omega_{\rm rf})t \tag{3.51}$$

where φ_0 emerges from the integration constant. This can be directly substituted into Equation 3.1, and so for a Josephson junction driving by both a DC and RF source the current-phase

relationship can be expressed as

$$I_s(t) = I_c \sin\left[\varphi_0 + \frac{2\pi}{\Phi_0}V_{\text{dc}}t + \frac{2\pi}{\Phi_0}\frac{V_{\text{rf}}}{\omega_{\text{rf}}}\sin(\omega_{\text{rf}})t\right] . \tag{3.52}$$

The frequency of the Josephson current oscillations in this case is a combination of both the DC voltage frequency $\omega_{\text{dc}} = 2\pi/\Phi_0 V_{\text{dc}}$, and a sinusoidally varying phase generated by the driving RF voltage source. These current oscillations are therefore not equal only to the frequency of the RF voltage source which is an effect of the fact that the current-phase relation can also couple additional driving frequencies.

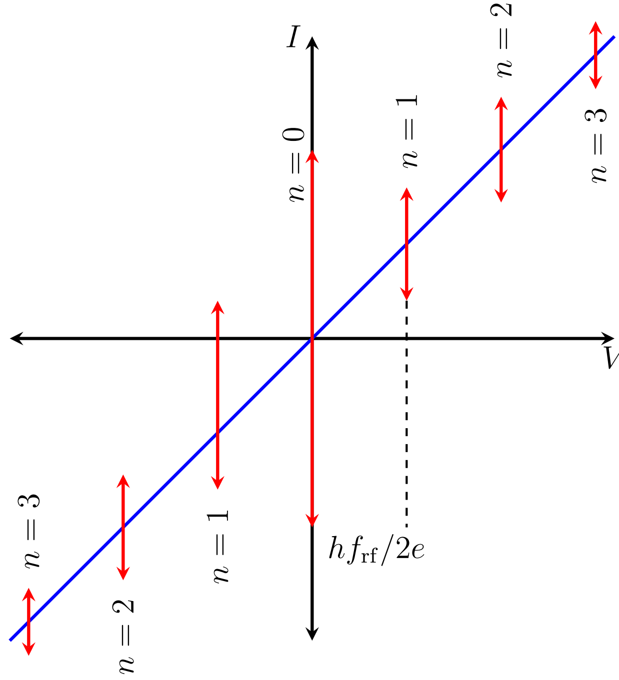

Figure 3.7: With an RF source, the Josephson junction when switched to the normal state will exhibit Shapiro steps at voltages which correspond to $V = hf_{\text{rf}}/2e$. The magnitude of the step current on the Ohmic relationship, shown by the blue line, corresponds to the applied RF power as described by Equation 3.53. Adapted from Enss and Hunklinger [84].

The current-phase relationship of the Josephson junction when driven by an RF source, Equation 3.52, can also be written as the Fourier-Bessel function of the form [83]

$$I_s(t) = I_c \sum_{n=-\infty}^{\infty} -1^n \jmath_n\left(\frac{2\pi V_{\text{rf}}}{\Phi_0\omega_{\text{rf}}}\right)\sin\left([\omega_{\text{dc}} - n\omega_{\text{rf}}]t + \varphi_0\right) . \tag{3.53}$$

Here $\jmath_n$ is the nth order Bessel function of the first kind.

Steps induced by RF signal occur at values where the DC driving voltage

$$V_{\text{dc}} = n\frac{hf_{\text{rf}}}{2e} , \tag{3.54}$$

an example of this is shown in Figure 3.7. These steps, known as "Shapiro steps" [85] occur where the sine term of Equation 3.53 resolves to zero due to the interaction between DC and RF biases. As the amplitude of the RF source is increased the switching current will decrease, following a zeroth order Bessel function while the higher order steps emerge from the resistive branch.

3.2 Rapid Single Flux Quantum

Rapid single flux quantum (RSFQ) is a type of low temperature digital electronics which makes use of strongly damped Josephson junctions as the active element [23][86]. Unlike CMOS where binary data is represented by DC voltage levels, rapid single flux quantum instead uses SFQ pulses, which have a quantised area corresponding to

$$\Phi_0 = \int V(t)dt \tag{3.55}$$

$$= \sim 2 \text{ mV} \cdot \text{ps}. \tag{3.56}$$

This small pulse duration and amplitude of the pulses generated by Josephson junctions allows RSFQ circuitry to operate at frequencies beyond 100 GHz and with low power dissipation. For CMOS devices a relatively large current must be used to represent a single bit, which typically requires an energy in the range of 10^{-16} J/bit. In comparison to the SFQ pulses which are used to represent data in the SFQ scheme require energy of $\sim 2 \times 10^{-19}$ J/bit [28].

RSFQ pulses can only be generated by an input signal which provides sufficient voltage gain to switch the junction into the normal state, any pulse less than this threshold value will fail to trigger the junction and so in this way RSFQ circuitry acts as an inherent noise discriminator.

The standard design philosophy used for RSFQ is to implement elementary "cells" which receive and transmit RSFQ pulses based on much of the early work conducted by the research group of Likharev [87][88][89][73]. To maintain timing between these circuits each cell is accompanied by a timing circuit which requires a clock pulse from the timing circuit of the previous cell, and an acknowledgement from the subsequent cell [90]. Only once both of these pulses are received will the clock pulse be transmitted. In this way RSFQ circuits maintain local self-timing and maintain global timing based on the operation of the slowest cell.

3.2.1 Generation of SFQ pulses

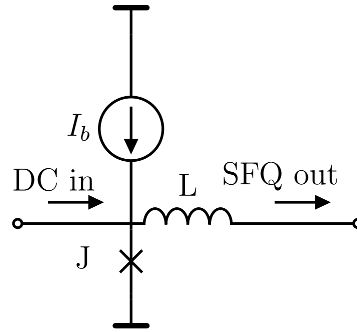

Figure 3.8: A schematic for a simple SFQ pulse generator, where the inductance L and the critical current of the junction J are set such that the dimensionless parameter $2 < \lambda < 6$ then a DC pulse at the input of the circuit will produce a train of SFQ pulses at the output which can then be supplied to another circuit.

Generating an SFQ pulse from a single junction requires that an input pulse with a duration on the order of ps [23]. A much simpler method of pulse generation can be achieved with the simple addition of an inductor, as shown in the circuit in Figure 3.8. The inductance of the circuit, L, should be designed such that the dimensionless parameter $2 < \lambda < 6$, where $\lambda = 2\pi I_c L/\Phi_0$ [91][92].

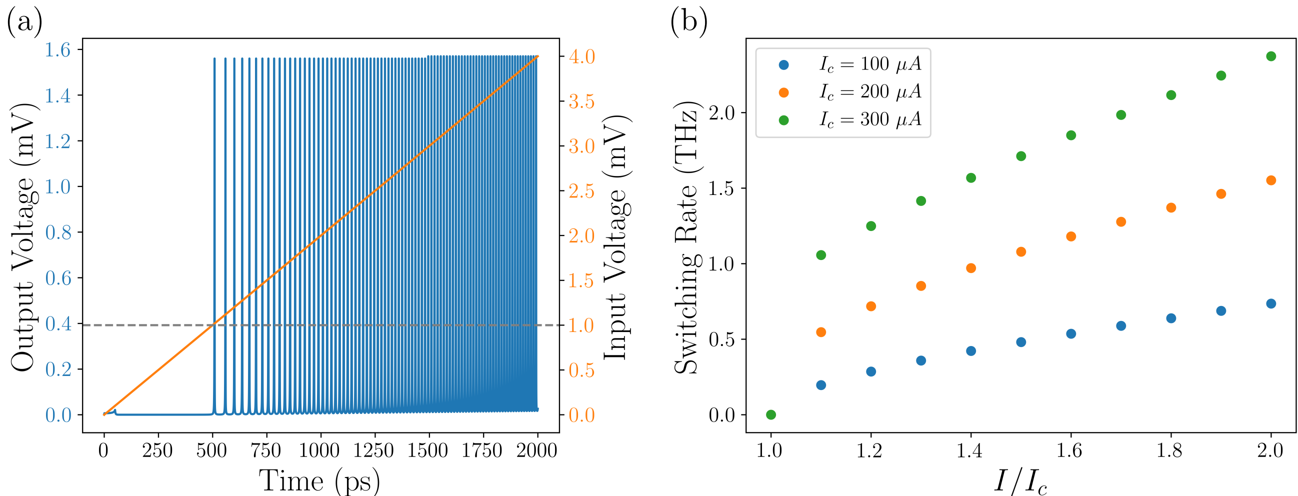

Figure 3.9: (a) Ramping the input shows that no SFQ pulses are produced while the input pulse is less than the critical current. Only once the threshold of the critical current is reached will the Josephson junction begin to produce SFQ pulses. As the input is ramped up the rate at which the junction switches is increased. (b) The switching rate of the Josephson junction which is driven by a DC input, shown in (a) is dependent on the amplitude of the driving input pulse, as well as the critical current of the junction. It can be seen that the switching rate is proportional to $I_c R_n$.

When an input pulse which can trigger the junction by exceeding the critical current is passed into the circuit a train of pulses is produced at the output, and the rate of switching is determined by amplitude of the triggering pulse. This is shown in Figure 3.9 where the frequency of pulses increases as the amplitude of the input pulse is ramped.

This calculation was achieved using the JSim software package [93] which is used to simulate circuits containing Josephson junctions using a network analysis process to determine the currents, voltages, and in the case of Josephson junctions, the phase, of each of the components.

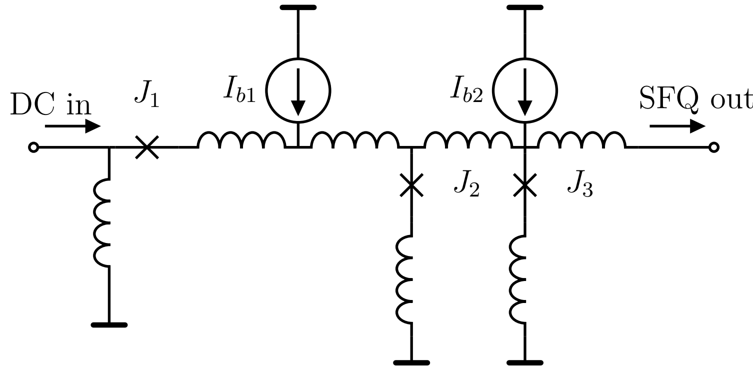

Figure 3.10: The schematic of a DC-SFQ converter, when a triggering DC input pulse arrives the SFQ pulse is produced by the J2-J3 interferometer loop. The falling edge of the DC pulse then triggers J1 which causes the converter to reset, the frequency of pulses corresponds to the level of input pulse. The junction begins to switch as the critical current threshold is reached, and the switching frequency increases as the pulse amplitude is increased.

For most circuitry applications a train of pulses is not suitable, and a square input pulse which produces a single corresponding SFQ pulse representing one bit is needed. This can be achieved with a three junction DC-SFQ circuit, an example of which is shown in Figure 3.10.

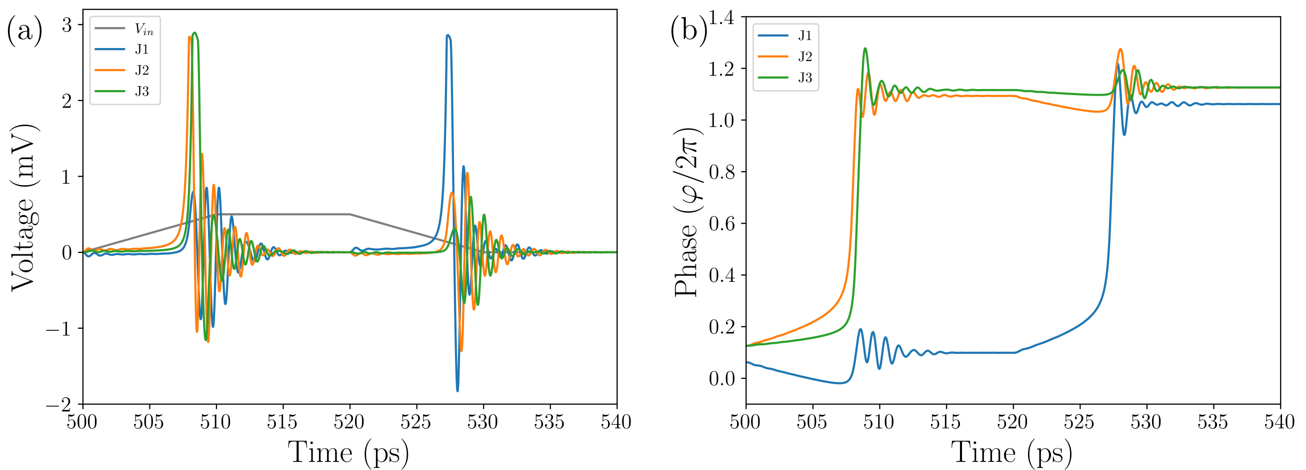

Figure 3.11: In (a) the result of a JSIM simulation [93] showing that for a DC pulse applied to the input a single SFQ pulse will be triggered, at the falling edge of the pulse a transient can be seen which comes from the switching of J1 resetting the device. In (b) the phase change in the junctions of the circuit shows how the DC pulse rising edge triggers junctions J2 and J3 simultaneously which produce the SFQ pulse at the output, the circuit is reset by the DC falling edge triggering J1.

If the DC input exceeds the threshold value, I_{on}, the J2-J3 loop is triggered, both junctions switch almost simultaneously, and an SFQ pulse is produced at the output. The input current will not trigger any additional SFQ pulses to be transmitted during the input pulse period. The circuit is

reset by the input pulse falling below a certain value I_{off}, which causing J1 to switch and the circuit is ready to receive another DC input pulse. The results of a JSim simulation of this circuit are shown in Figure 3.11.

3.2.2 Typical Operating Parameters of RSFQ Devices

A well-known early effort to realise a computer using Josephson junctions was attempted by IBM in the late 1970s [94]. For this project STJs fabricated from Pb were used as the Josephson junction, which is not resistant to thermal cycling causing degradation of the junction barrier over time. These junctions are underdamped and operate in the hysteretic regime. The logic scheme chosen represented '0' by the superconducting state, and a '1' by a Josephson junction latched in the resistive state. To reset the junction it was required to reduce the bias current to less than I_R, which restricted the operating frequency to $\sim$ 1 GHz [23]. After IBM had abandoned the project having failed to demonstrate a benefit over semiconducting devices, a group based at Moscow State University led by Prof. K. K. Likharev suggested that rather than to represent the binary data as IBM had done using latching logic, to use SFQ pulses which could naturally be generated by overdamped Josephson junctions [86]. It was this paradigm shift which led to the development of SFQ electronics.

The SFQ pulses used in RSFQ circuitry are generated by strongly damped Josephson junctions, where the junction operates in the non-hysteretic regime. From Equation 3.4 it can be seen that a voltage pulse corresponding to $\Phi_0 = h/2e$ will result in a phase change of 2π

$$d\varphi = \frac{\hbar}{2e}\Phi_0 dt \tag{3.57}$$

$$= 2\pi \ . \tag{3.58}$$

The 2π phase change corresponds to the movement between adjacent minima of the Josephson potential seen in Equation 3.14.

The pulse duration is related to the characteristic voltage and characteristic frequency of the junction, as described in Section 3.1.2.5. The maximum switching frequency of the Josephson junction is approximately described by the characteristic frequency, introduced in Equation 3.36

$$\omega_c = \frac{\hbar}{2e} V_c \tag{3.59}$$

where V_c is the characteristic voltage of the junction, which is often described as the $I_c R_n$ product. A Josephson junction with $I_c = 100\mu\text{A}$ and $R_n = 50\ \Omega$ produces pulses with a duration of $\sim$ 2.6 ps,

and a maximum operating frequency in the range of ~ 350 GHz.

The pulse amplitude produced will correspond to $V_{\text{amp}} \approx 2V_c$, and so a junction with the same characteristics as previously described will produce a pulse with an amplitude of ~ 10 mV.

The power dissipation in the production of each pulse can be written as $\Delta E = I_c\Phi_0$, if thermal effects are not considered. For a junction with critical current $I_c = 100$ μA this corresponds to a power dissipation of $\sim 2\times10^{-19}$ J each time an SFQ pulse is generated by the Josephson junction. In the early work done on the development of RSFQ circuitry the bias currents were distributed with a network of bias resistors resulting in a high static power dissipation. A more recently developed type of RSFQ known as efficient RSFQ (eRSFQ) has resolved this problem by using Josephson junctions to distribute the bias currents [28].

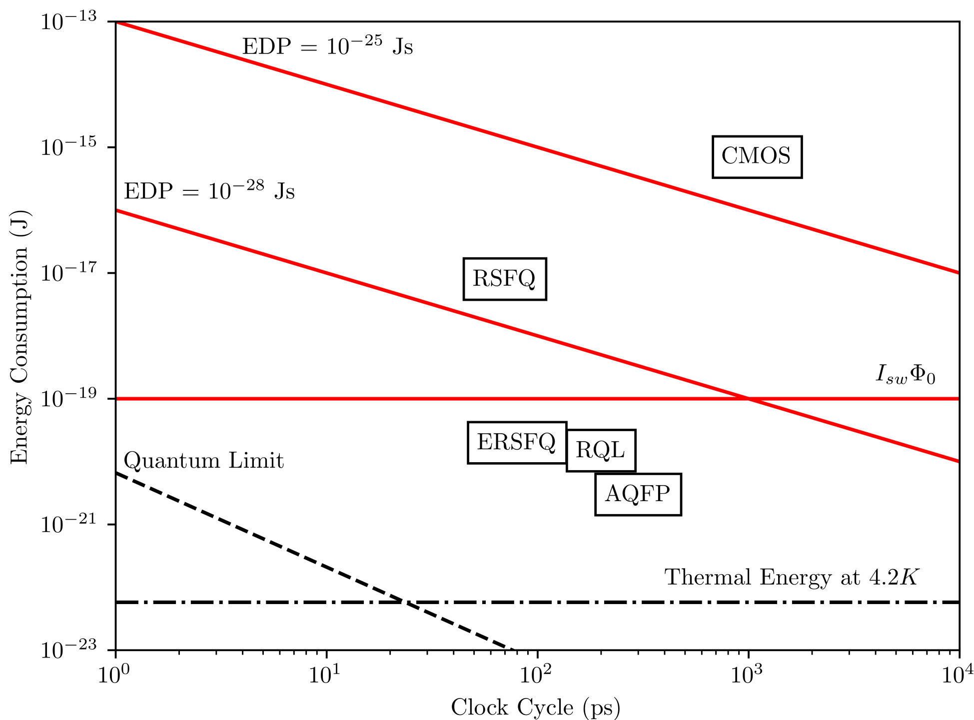

Figure 3.12: The energy consumption of SFQ technologies compared with standard CMOS electronics [95]. The SFQ-based schemes can operate with reduced energy consumption and clock cycle, much closer to the quantum limit than is currently possible with room temperature CMOS electronics, which allows low-power, high operating frequency low temperature electronics.

In comparison with other digital logic technologies, SFQ schemes offer low dynamic power consumption. Figure 3.12 shows the energy consumption against the clock speed for a variety of digital logic families. It can be seen that SFQ based schemes can operate closer to the quantum limit than standard CMOS technologies, due to the high clock frequency and low energy per bit as a consequence of the SFQ pulse shape.

3.3 Types of Josephson Junction

Josephson junctions are composed of two superconducting electrodes which are connected by an area of reduced critical current across which Cooper pairs can flow. There are two types of Josephson junction. Barrier type Josephson junctions are those where the critical current density, J_c is reduced compared to the electrodes, where the Cooper pairs must tunnel between the electrodes. The second junction type is weak links, where current flows with direct connectivity. The normal material between the two superconducting electrodes is proximitised, allowing the phase and amplitude of the order parameter Ψ to be maintained over several times the coherence length ξ_{N}. Shown in Figure 3.13 is a variety of the types of Josephson junctions which have been realised.

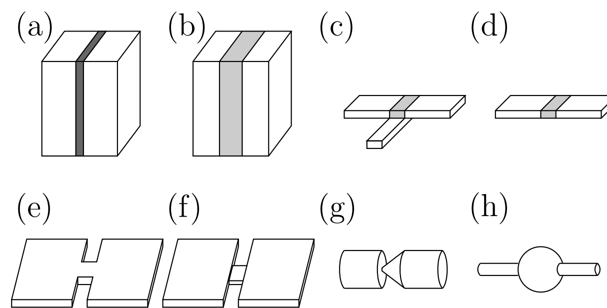

Figure 3.13: Josephson junctions can take a variety of forms, some of these include (a) superconducting tunnel junctions (STJ), which make use of an oxide barrier layer, (b) sandwich-type junction, where the barrier is formed of another material, such as a semiconductor or metal, (c) proximity effect junction, (d) ion-implanted bridge, (e) continuous thickness bridge, (f) variable thickness bridge, (g) point contact and (h) blob type junction. The devices shown in (a) - (d) are barrier type junctions, and (e) - (h) are weak links. This work makes use of the bridge type continuous thickness weak links shown in (e).

Each of type of junction has different physical properties and offers advantages and disadvantages for specific purposes. The earliest research into the Josephson effect used point contact and blob-type junctions, which were easily produced without modern fabrication techniques but offered poor repeatability. STJs have been most commonly used type of Josephson junction for SFQ applications [96]. The early work which used bridge-type weak links used a rudimentary fabrication process which mechanically cut the bridge out of a film using a razor blade [97][83]. With the advent of electron beam lithography, it has become possible to achieve continuous thickness bridge type weak links (often called Dayem bridges in literature) with physical dimensions in the range of tens of nanometres. While these devices - commonly referred to as nanobridges - have not yet seen widespread adoption for SFQ electronics there has been recent interest in nanobridge field-effect transistors [98][99].

This section describes the physics of the STJ and the nanobridge as they relate to the generation of SFQ pulses for superconducting electronics purposes.

3.3.1 Superconducting Tunnel Junctions

STJs are formed of two superconducting electrodes which are separated by an insulating layer, the layout of which is shown in Figure 3.14. This junction is typically produced by a multi-layered structure, for superconducting electronics STJs are most commonly fabricated using a Nb-trilayer process, where a bottom electrode of Nb is covered with an Al layer which can be oxidised in a controlled manner to produce the barrier. A top Nb electrode can then be added to complete the junction.

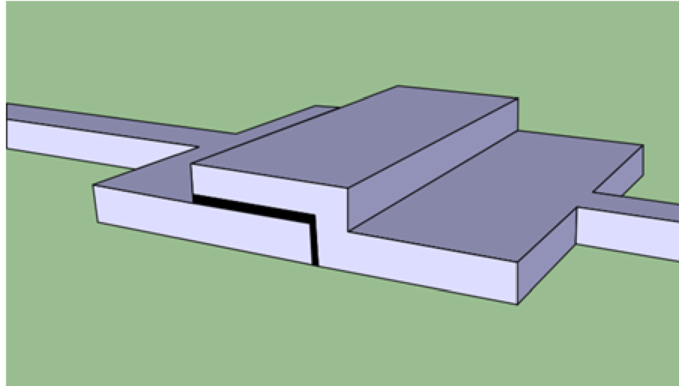

Figure 3.14: The two electrodes of the terminal can be seen, in fabrication the first electrode is deposited and oxidised, before the second electrode is added on top. In large scale circuits this results in an uneven surface. The associated shunting resistor is not shown in this image.

STJs can be accurately described by microscopic theory under two conditions

- the thickness of the barrier is less than the characteristic length scales of the superconductor, in particular the superconducting coherence length, $\xi(T)$.
- the transparency factor of the barrier, $\mathcal{T}$, is sufficiently small that the critical current of the barrier is much less than the critical current of the junction electrodes.

This makes it possible to ignore contributions to the superconducting current from tunnelling normal electrons, and so the current through the barrier layer can be approximately described by Equation 3.1. It can also be considered, using the small junction approximation [75], that the phase and voltage are uniform throughout the barrier. The characteristic voltage of the STJ can be written as

$$V_c = \frac{\pi}{2}\frac{\Delta(T)}{e}\tanh\frac{\Delta(T)}{2k_BT} \ . \tag{3.60}$$

It was shown by Likharev [75] that this characteristic voltage of the junction was dependant only on the critical temperature of the superconducting banks.

As the STJ is formed by two superconducting electrodes coupled by an insulating barrier the junction will have a significant capacitance. This capacitance can be written as

$$C = \frac{\epsilon A}{d} \tag{3.61}$$

where ϵ is the permittivity of the barrier, A is the junction area and d is the barrier thickness. For a typical junction with parameters $I_c = 100$ µA and $R_n = 50\ \Omega$, using a Nb-trilayer process where the critical current density is in the range of $j_c = 1$ kA/cm^2, it is found bt applying these values to Equation 3.36 that this junction has a Stewart-McCumber parameter in the range of $\beta_c \sim 1000$. STJs are typically underdamped Josephson junctions, and unsuitable for use in SFQ electronics.

It is clear by looking at Equation 3.36 that the Stewart-McCumber parameter can be reduced in three ways:

- reducing the critical current, I_c, although this is usually restricted by the operating parameters of the device.
- reducing the normal state resistance, R_n. In STJs this is usually achieved by including a shunt resistor, if the example junction is shunted by a 1 Ω resistor $\beta_c \sim 0.3$ and the junction will operate in the overdamped regime.
- increasing the barrier thickness, d, without reducing the critical current density. This can be achieved by replacing the oxide barrier with a normal metal or semiconductor [100].

3.3.2 Nanobridge Weak Links

A weak link type Josephson junction is one in which the current flowing through the junction is equal to the current flowing in the electrodes, and there is no barrier which the Cooper pairs must tunnel across. Weak links can take a variety of forms, some of which are shown in Figure 3.13. A weak link can be formed in a similar manner to a STJ, replacing the insulating barrier with a normal metal or semiconducting material. Alternatively, a superconducting strip can have a barrier induced by ion implantation. The reduction of I_c can also be achieved geometrically, by creating a constriction where the critical current will be reduced with respect to the electrodes.

Nanobridge differs from STJs in both geometry and the fundamental physical properties of the device. The current-phase relationship (CPR) of STJ which can typically be described by $I_s = I_c \sin(\varphi)$, in nanobridges the CPR can deviate from this relation and produce a “non-ideal” Josephson

effect where phase-slips and anharmonic Shapiro steps can form. The nanobridge can display self-consistent heating behaviour which is not observed in STJs.

This work focuses on bridge-type weak link structures where the film is a constant thickness, historically known as Dayem bridges and referred to hereafter as nanobridges due to the physical dimensions of the structure.

The nanobridge has a width, W, and a film thickness, d, which define the cross sectional area of the bridge, and the current flow through the bridge. The length of the bridge, L, describes the physical separation between the electrodes, but the electrical characteristics of the bridge are determined by the effective length $L_{\text{eff}} > L$, which is the length scale at which the electrodynamic processes of the nanobridge extend into the electrodes [75]. These non-linear processes in the nanobridge can lead to variations in the order parameter of the electrodes. In addition, Equation 3.1 is approximately applicable where $L_{\text{eff}} \leqslant \xi$, and diverges from this as the effective length increases [101].

3.3.2.1 Nanobridge Lengths and Widths

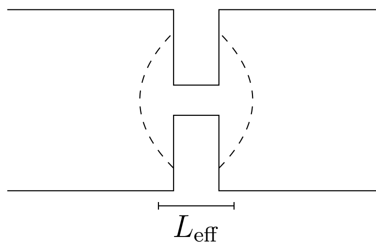

Figure 3.15: In the Volkov model the nanobridge is bounded by hyperbola, the centres of which are separated by a distance of $2a > L_{\text{eff}}$. The current density in the nanobridge is reduced as the length increases, reaching the minimum at the centre of the nanobridge.

The simplest model for evaluating the effect of the nanobridge physical lengths and widths on the electronics properties of the nanobridge is the One-Dimensional Structure with Electrodes in Equilibrium (ODSEE) model [102]. This model requires two approximations about the nanobridge.

- The cross section of the weak link is smaller than λ^2, where λ is the magnetic penetration depth, and is constant in the direction of the current flow.

- The non-linear processes are restricted to the physical area of the nanobridge. This is to say that the effective length $L_{\text{eff}} = L$, and that the order parameter in the electrodes remains unchanged.

In nanobridges the first restriction is satisfied, the current concentration is uniform over the constant thickness of the nanobridge. However, the second restriction is not necessarily true as $L_{\text{eff}} \approx \max[L, W]$, the non-linear processes can extend into the electrodes. In the work of Volkov

[103] the bridge was allowed to extend into the electrodes as a hyperbola separated by a distance of $2a$, shown in Figure 3.15.

This Volkov model gives an expression for the critical current

$$I_c = \frac{V_c}{R_n(\xi)} \tag{3.62}$$

where the normal state resistance

$$R_n(\xi) = 2R_\square \ln(\xi/L_{\text{eff}}) \tag{3.63}$$

is the resistance of the bridge inside a radius of ξ, where the $R_\square$ is the normal state resistance of the film per square.

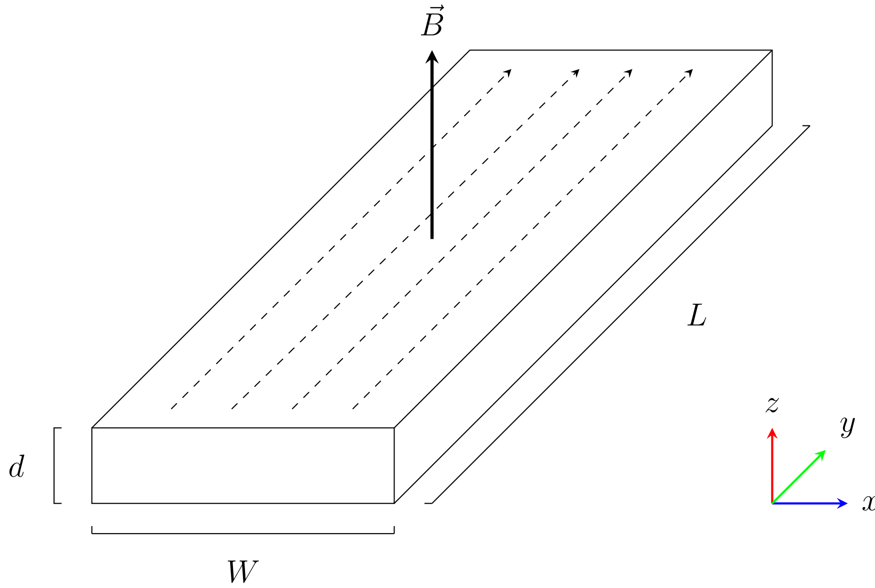

Figure 3.16: If the current flowing through the nanobridge is large a magnetic field can be generated which can suppress the switching current. The direction of the magnetic field is perpendicular to the current flow, which is represented by the dashed lines. In this representation the magnetic field occurs in the z direction.

The physical geometry of the nanobridge determines the operating regime of the nanobridge. The length of the nanobridge must be sufficiently small to maintain coherence between the two electrodes, but does not require any additional properties [75]. As the length of the nanobridge is increased beyond the size of the coherence length there will be an associated reduction in the critical current, until at $L \approx 10\xi(T)$ the critical current of the nanobridge reaches a constant value. This occurs as the order parameter of the nanobridge, Δ, scales with the nanobridge length. For short

nanobridges the ratio of Δ to Δ_0, is $\Delta/\Delta_0 < 1$, where Δ_0 is the order parameter at a $T = 0$ K [75]. At $L = 3.49\xi(T)$ the order parameter reaches a value of $\Delta/\Delta_0 = 1$, and beyond this length the Josepson effect can no longer be maintained across the bridge.

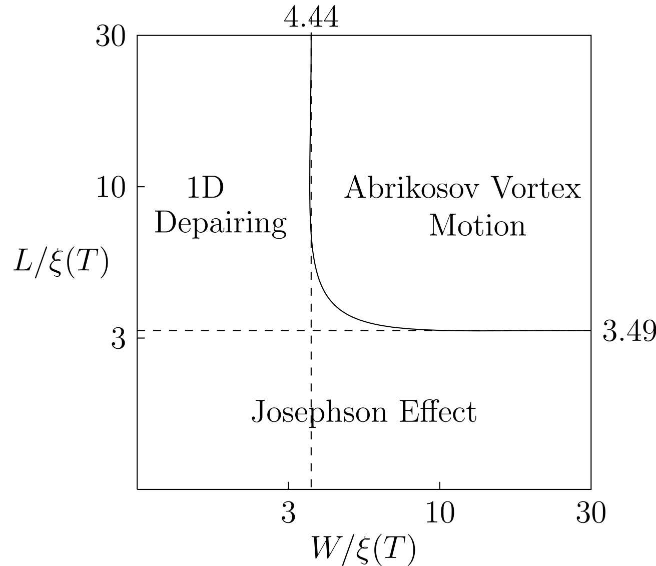

Figure 3.17: The physical size of the weak link determines the operating regime of the Josephson junction. Where the effective length is less than $3.49\xi(T)$ the weak link can show Josephson effects. At a bridge width greater than $4.44\xi(T)$ the nanobridge can exhibit Josephson vortice behaviour.

The restriction on the width of the bridge occurs due to the effect of high current densities in the bridge in the superconducting state. For constant superconducting electron density, which is dependent on the cross-sectional area of the bridge as

$$j_s = \frac{I_s}{Wd} , \tag{3.64}$$

there will be an induced magnetic field which emerges from the centre of the bridge and propagates perpendicular to the direction of the current flow, $\vec{B}\mu_0 j_s \hat{z}$. The volume of current which contributes to this effect is proportional to a length with is roughly proportional to the bridge width W. When the flux which is generated in this process is equal to, or exceeds $\Phi_0/2$ then the current through the bridge can be described by a spatially varying current density,

$$\int_0^{w/2} \vec{B} W d\hat{z} = \frac{\mu_0 I_c W^2}{8d} > \frac{\Phi_0}{2} , \tag{3.65}$$

which can also be expressed as a minimum superconducting current in the nanobridge

$$I_c > \frac{2hd}{eW^2\mu_0} \; . \tag{3.66}$$

This results in a modulated current density due to the formation of these Josephson vortices.

A bridge where the physical features of the bridge $W > 4.4\xi(T)$ and $L > 3.49\xi(T)$ will operate in the region where the current density in the bridge is modulated due to the formation of Abrikosov vortices [104].

3.3.2.2 Joule Heating in Nanobridges

When the nanobridge is switched into the superconducting state the current applied to the junction will generate Joule heating, with thermal power of

$$P_{\text{Joule}} = I_{\text{app}}^2 R_n \; , \tag{3.67}$$

which can result in the formation of a self-consistent hotspot in the nanobridge [105]. Even when the level of the current is reduced to $|I| < I_c$, the hotspot can continue to drive the nanobridge into the normal state, and the current level must be reduced to a value of the return current, I_R, to restore the superconducting state. The thermal hotspot is able to self-consistently maintain itself in this way because the critical current of the superconductor is temperature dependent, and the Joule heating reduces the critical current of the nanobridge.

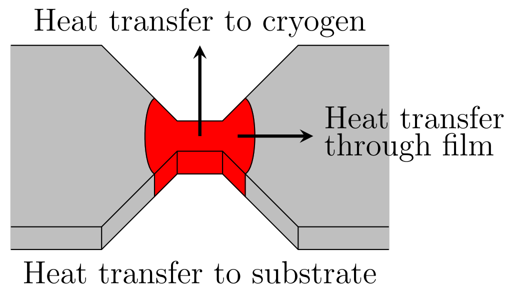

Figure 3.18: The thermal energy generated by Joule heating in the nanobridge can be dissipated through three channels: heat can flow through the film, heat can flow into the substrate, and where the sample is submerged in a cryogen heat can flow into the cryogen.

There are three possible channels for the thermal energy to flow away from the resistive hotspot, as shown in Figure 3.18.

- The rate of heat flow through the thin film is determined by the thermal conductivity of the film, K.

- Heat flows into the substrate at a rate which is determined by the heat transfer coefficient of the substrate α, and the temperature of the substrate T_{sub}. It is generally assumed that T_{sub} is fixed at the temperature of the He bath or cryocooler, as the volume of the substrate is much greater than the volume of the nanobridge.

- In cryocooler systems the nanobridge is operated in a vacuum, and the effects of blackbody radiation are generally considered to be negligible. Cryogen cooled systems however include a channel through which the cryogenic liquid or gas in contact with the nanobridge includes another channel for heat flow.

The heat flow in a nanobridge can be described by the equation [105]

$$J^2\rho + \kappa\frac{\partial^2 T}{\partial x^2} - \frac{\alpha}{d}\left(T - T_{\text{sub}}\right) = T\frac{\partial c}{\partial t}\ , \tag{3.68}$$

where J is the current density flowing through the nanobridge, x is the position along a one-dimensional wire, ρ is the resistivity, d is the film thickness, c is the specific heat capacity of the film per unit volume, α is the heat transfer coefficient per unit area into the substrate which has temperature T_{sub}, κ is the thermal conductivity of the film, and ∂t is the time step. The $J^2\rho$ term is the thermal energy generated by the Joule heating, and in the superconducting state as the resistance of the nanobridge is zero this term only contributes in the normal state. The second term on the left-hand side describes the heat flow into the thin film, and generally it is assumed that the term κ is constant for both the normal and superconducting states. The final term on the left-hand side describes the heat flow into the substrate, where the substrate is at a fixed temperature T_{sub}.

The length scale over which the heating effects occur is known as the self-healing length [105], and is defined as

$$\eta = \left(\frac{Kd}{\alpha}\right)^{1/2}\ , \tag{3.69}$$

where K is the thermal conductivity of the film, d is the thickness of the film and α is the heat transfer coefficient per unit area into the substrate.

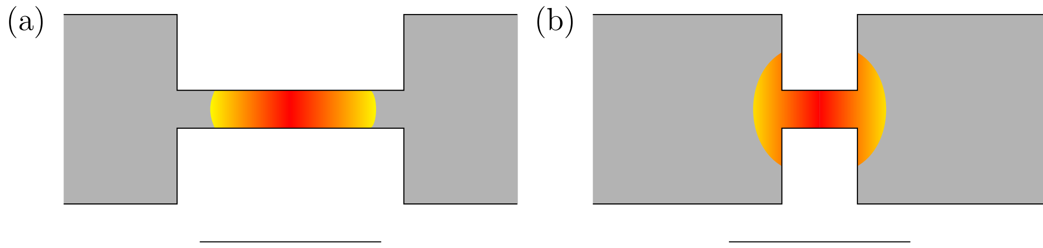

Figure 3.19: Skocpol et al [105] defined the behaviour of the nanobridge dependent on the relationship between the thermal healing length, η, and the length of the bridge L. In the context of the thermal behaviour of nanobridges "long" bridges are those where $\eta < L$, as shown in (a), while "short" bridges are those there the thermal hotspot extends into the electrodes as shown in (b), which occurs where $\eta > L$.

The type of nanobridge is defined by whether the physical length of the bridge is longer or shorter than η. For the Nb films used in this project the thermal healing length [106][107]

$$\eta = \left(\frac{53.7 \times 150 \times 10^{-9}}{8 \times 10^{-5}} \right) \tag{3.70}$$

$$\approx 3\ \mu\text{m}\ , \tag{3.71}$$

which is much greater than the length of the nanobridges, and so the devices used in this work are considered "short" for the purposes of the thermal model, such that the thermal hotspot extends into the electrodes by a distance a, as shown in Figure 3.19.

The value of the return current $I_R(T)$ can be calculated depending on the type of bridge, for short bridges this expression is [105]

$$I_R = \left(\kappa d^2 \frac{T_c - T_{\text{sub}}}{\rho} \right)^{1/2} \ . \tag{3.72}$$

The nature of the heating effect can be defined by the relationship of the physical bridge length to the self-healing length, with "long" bridges, where $\eta < l$ and by "short" bridges where $\eta > l$. In the case of long bridges, the thermal hotspot is completely contained within the bridge itself, and the return current can be determined by the equation [105].

$$I_R = \left[\frac{\alpha w^2 d (T_c - T_{\text{sub}})}{\rho} \right]^{1/2} \ . \tag{3.73}$$

In "short" bridges, where the healing length is greater than the physical bridge length the hotspot can extend into the electrodes to form a semi-circle hotspot at each end of the nanobridge. The

expression for the return current in this instance differs from Equation 3.73 by a factor of η/W, and can therefore be written as

$$I_R = \left[\frac{\alpha K d^2(T_c - T_{\text{sub}})}{\rho}\right]^{1/2} . \tag{3.74}$$

Hysteretic behaviour in nanobridges is seen when $I_R < I_c$, which occurs where the thermal energy generated by the hotspot cannot be reduced sufficiently to restore the superconducting state, shown in Figure 3.20. As the critical current density is temperature dependent the thermal hotspot can suppress the local critical current to values less than the switching current, and so even when the applied current is reduced to a value less than the original value of switching current used to drive the nanobridge from the normal state into the superconducting state the hotspot can remain.

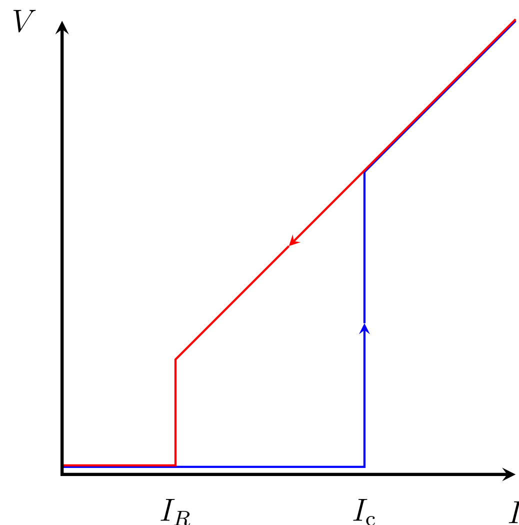

Figure 3.20: As the current is increased from zero the nanobridge remains in the superconducting state until the critical current value is reached, at which point the nanobridge switches to the normal state. On sweeping the current back to zero the nanobridge remains in the normal state at currents less than the critical current, and only once the return current value is reached does the nanobridge switch back to the superconducting state.

For the purposes of electronics this will significantly reduce the operating time of any device which uses hysteretic nanobridges, as the current must be ramped down to I_R after each switching event to restore the superconducting state.

3.3.2.3 Current-Voltage Characteristics of Nanobridges

The RCSJ model, described in Section 3.1.2.1 provides a reasonably good approximation of STJ behaviour, but fails to completely describe the experimental measurements of nanobridges. The IVC of nanobridges resembles that of the Rieger, Scalapino and Mercerau (RSM) model [108] which was

developed as a description for phase slips, and can be interpreted as an IVC which approaches a shifted Ohmic current-voltage relationship asymptotically at large currents. This shifted current is known as the excess current, shown in Figure 3.21.

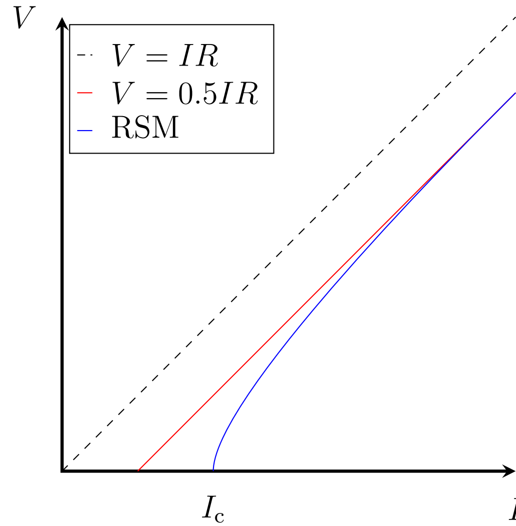

Figure 3.21: The IVC of nanobridges typically resembles the RSM model [108], where the IV relation shown in blue asymptotically approaches an Ohmic relation which has gradient of R_n and an offset of $0.5I_cR_n$, shown in red.

It has been proposed that the existence of the excess current generated by the intrinsic inductance of bridge-type weak links can be accounted for by modifying the RCSJ model to include an inductance, L_{ex} in series with the constriction in the superconducting current branch [101] which is described by the Josephson current phase relationship model described in Equation 3.1. In this model the CPR of the nanobridge becomes skewed, the magnitude of which is dependent on the intrinsic inductance and examples of the resultant CPRs are shown in Figure 3.22(a).

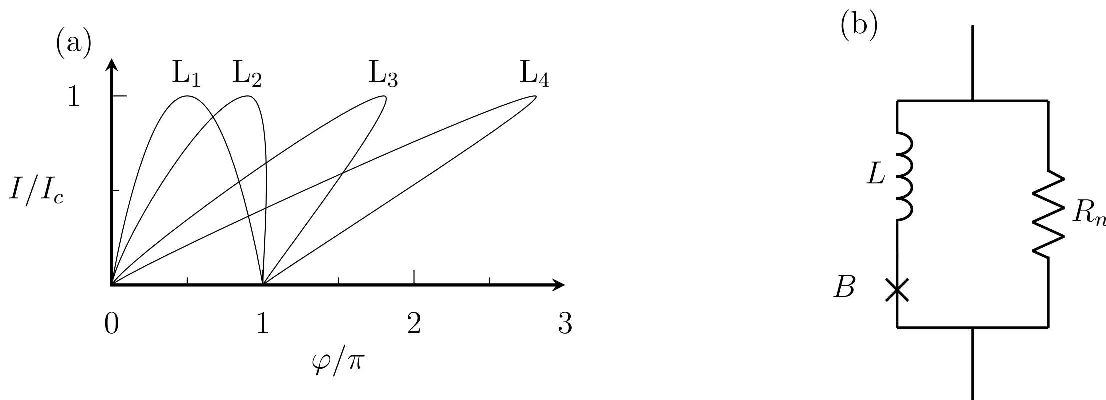

Figure 3.22: (a) The current dependent on the phase for several values of intrinsic inductance. $L_1 = 0$, showing the purely sinusoidal relationship, $L_2 = \Phi_0/2\pi I_c$, $L_3 > \Phi_0/2\pi I_c$ and $L_4 > L_3$. Adapted from Deaver 1972 [101] (b) The equivalent circuit for this model, with the intrinsic inductance L, and a Josephson junction B, in parallel with the normal state resistance, R_n. The nanobridge capacitance is considered to be very small and so the displacement current negligible.

In this model the phase and voltage of the nanobridge are described by the equations

$$\varphi = \varphi_{\text{bridge}} + \varphi_L = \arcsin\left(\frac{I_s}{I_c}\right) + \frac{2\pi L}{\Phi_0} I_s \tag{3.75}$$

$$V = \frac{\Phi_0}{2\pi}\frac{d\varphi}{dt} = (I - I_s)R_n \tag{3.76}$$

where I_s is the superconducting current in the combined inductor-constriction branch of the circuit shown in Figure 3.22(b). At $L = 0$ the CPR agrees with that described by Equation 3.1, and as L increases the CPR deviates from this relation. At $L = \Phi_0/2\pi I_c$ the value of $\varphi(\pi)$ becomes singular with an infinitely large voltage corresponding to $d\varphi/dt$. For $L > \Phi_0/2\pi I_c$, the phase becomes multivalued at values of $\varphi > \pi$ and likely results in a 2π phase slip. If the inductance is greater still, and the inflection point of the CPR occurs a value of $\varphi > 2\pi$ then phase slips of $n2\pi$ can occur.

Jackel et al [109] showed that the CPR of the nanobridge when $L > \Phi_0/2\pi I_c$ could be described as approximately sawtooth shaped due to the distortion from the simple sinusoidal relation, and the phase slip which occurs at the inflection point of the CPR. The point at which the phase slip occurs is known as the critical phase, φ_c. The voltage of the nanobridge can be described as

$$V = -\frac{2\pi R_n I_c}{\varphi_c}\left[\ln\left(\frac{I/I_c - 1}{I/I_c - 1 + 2\pi/\varphi_c}\right)\right]^{-1} . \tag{3.77}$$

The superconducting current branch, which is described as

$$I_s = I_c \sin\left(\varphi + I_s \frac{2\pi L_{\text{ex}}}{\Phi_0}\right) , \tag{3.78}$$

where L_{ex} defines the in-series inductance used to account for the excess current, and the normal current branch is described as

$$I_n = V R_n , \tag{3.79}$$

both of which are defined by the parameters of the nanobridge itself.

While the Jackel model provides a useful method for evaluating the behaviour of the nanobridge, the complete analytical solution is found by solving the Usadel equations.

The Usadel equations can be expressed in the φ parameterisation[110], by making the substitu-

tions

$$F = \frac{\varphi}{\sqrt{\omega_n^2 + |\varphi|}} \tag{3.80}$$

$$G^2 = 1 - |F|^2 \ , \tag{3.81}$$

where G and F are the anomalous Green's functions. ω_n is the Matsubara frequency,

$$\omega_n = \frac{\pi k_B T(2n+1)}{\hbar} \ , \tag{3.82}$$

where k_B is the Boltzmann constant, T is the temperature and n is an integer.

The Ambegaokar-Baratoff (AB) model [33] generalised the original tunnelling calculations made by Josephson in his seminal paper using the Green's method function described in Equation 3.80. This results in the expression

$$\frac{eI_s(\varphi)R_n}{2\pi T_c} = \frac{T}{T_c} \sum_{\omega_n > 0} \frac{\Delta_1 \Delta_2}{\sqrt{(\omega_n^2 + \Delta_1^2)(\omega_n^2 + \Delta_2^2)}} \ . \tag{3.83}$$

The AB model describes a SIS tunnel junction under constant voltage bias. The CPR of the Josephson junction is restricted to a purely sinusoidal relation.

In weak links the stationary properties can be described using the Usadel equations [111]. Using the Green's functions described by Equation 3.80 the Usadel equation can be written as

$$2\omega_n F - D(\nabla - i\frac{2e}{\hbar c}\mathbf{A}) \left[G \left(\nabla - i\frac{2e}{\hbar c}\mathbf{A} \right) F - F\nabla G \right] = \frac{2}{\hbar}\Delta G \ . \tag{3.84}$$

For a sufficiently small weak link, which is one where $l << \xi(T)$, Equation 3.84 can be simplified to the gradient term. Unlike the AB model which describes a STJ with a purely sinusoidal CPR, the Kulik-Omelyanchuk model in the dirty limit (KO-I) [112] considered a diffusive quasi-one-dimensional wire connecting two superconducting banks. This one-dimensional wire has length $d << \sqrt{\xi_0 l}$, where $\xi_0 = \hbar \nu_F / 2\pi T_c$ and ℓ is the electron mean free path, where $\ell << \xi_0$.

An expression for the supercurrent can be derived by neglecting the non-gradient terms [110], and assuming that the superconducting electrodes, resulting in the CPR

$$I_s(\varphi) = \frac{4\pi T}{eR_n}\sigma_{\omega_n>0}\frac{2\Delta\cos(\varphi/2)}{\partial}\arctan\left(\frac{\Delta\sin(\varphi/2)}{\partial}\right) . \tag{3.85}$$

Solving this equation for arbitrary temperatures results in a CPR which is non-sinusoidal at lower temperatures, and more closely resembles the Aslamazov-Larkin model as $T \to T_c$.

For a ballistic case, where $\xi_0 << ell$, Kulik and Omelyanchuk proposed a theoretical model, known as KO-II [113]. In this model the Equation 3.84 can be solved to give an expression for the supercurrent

$$I_s(\varphi) = \frac{\pi\Delta}{eR_n}\sin(\varphi/2)\tanh\frac{\Delta\cos(\varphi/2)}{2T} . \tag{3.86}$$

Similar to the KO-I model, at temperatures $T \to T_c$ the KO-II model calculates an approximately sinusoidal CPR. At low temperatures the weak link CPR can be described as a multivalued function where the intrinsic inductance $L >> \Phi_0/2\pi I_c$, similar to the CPRs described in Figure 3.22(a).

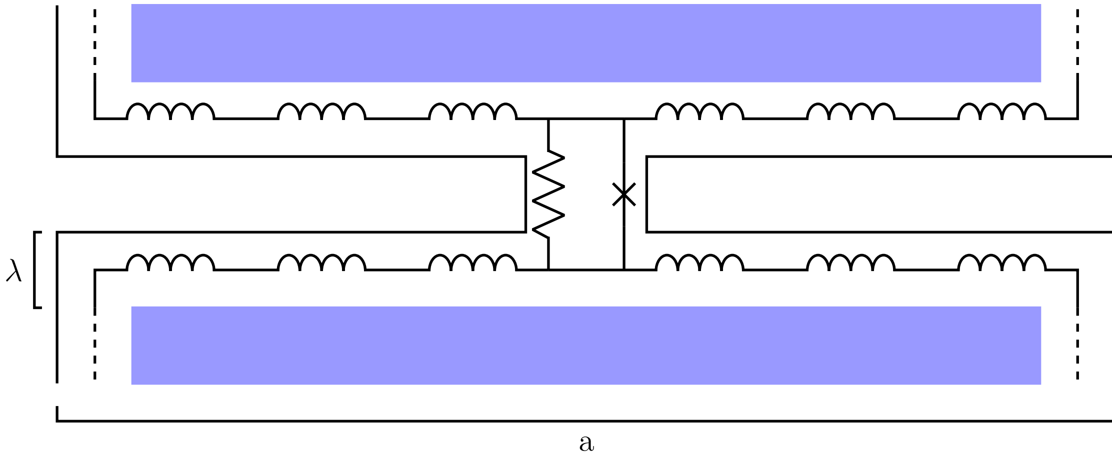

Figure 3.23: The RCSJ model of the nanobridge corresponds to the physical layout as shown. The superconducting current and resistive current branches represent the current flowing through the nanobridge. An inductance is generated by the superconducting material in the electrodes up to the magnetic penetration depth λ. The displacement current channel generated due to the capacitive coupling of the inductances between the two electrodes.

The nanobridge capacitance, which results from the fact that the current flows along the surface of the superconducting film at a depth corresponding to the penetration depth $\lambda = \lambda_L/d^2$. The capacitance of the nanobridge results from the current flowing through the inductance in the parallel electrodes. This nanobridge capacitance generates a displacement current through the nanobridge, however due to the magnitude of the capacitance this current component can be considered negligible. The inductance of the electrodes can be estimated along the length of the gap between the electrodes

[114], which is shown in Figure 3.23.

In nanobridges the constriction of the superconducting current branch and resistance of the normal current branch used in the RCSJ model represent the nanobridge itself, as shown in Figure 3.23. These active components which contribute to the behaviour of the bridge must physically be in the immediate proximity of the constriction, at a distance of $\sim$ 100 nm.

The intrinsic inductance used in the RSM model is included due to the inductance of the electrodes within a distance of the magnetic penetration depth λ,

$$L = \frac{\mu_0 a}{2}\left(\ln\frac{4a}{\lambda} - 0.75\right) , \tag{3.87}$$

where a is the length of the electrodes from the nanobridge as shown in Figure 3.23. The capacitance can also be estimated [114] using the equation

$$C = \frac{2\pi\epsilon_r\epsilon_0 a}{\ln(2l/\lambda)} , \tag{3.88}$$

where ϵ_r and ϵ_0 are the permeability of the gap material and of free space respectively, and l is the length of the gap between the electrodes. For the nanobridges used in this project the typical capacitance calculated with this equation is on the order of fF.

3.3.2.4 Noise in Nanobridges

Noise can be generated either in the nanobridge itself, or from the external bias source, and can result in an IVC which significantly differs from that predicted by the RCSJ model [115]. If the noise from both sources is due to thermal effects then the noise can be described by the parameter

$$\Gamma = \frac{2ek_BT^*}{\hbar I_c} , \tag{3.89}$$

where T^* is the effective noise temperature. This parameter represents the ratio of the thermal energy of the noise, k_BT, to the nanobridge coupling energy $\hbar I_c/2e$, and where $\Gamma > 1$ the Josephson effect in the nanobridge will be completely overcome, for $\Gamma < 1$ the noise will affect the superconducting current and produce a finite voltage for currents $|I| < I_c$. The noise as it occurs in nanobridges is described by the processes discussed in Section 3.1.2.4.

The thermal noise can be understood with the analogy of a particle in a potential well [115, 116]

and this method has been verified in STJs [117] and in point-contact structures [118]. The effects of this noise can also be seen in Shapiro steps when the nanobridge is biased with an RF source.

Low-frequency noise, which is observed at low voltage, can also be described using the RCSJ model. As nanobridges operate in the overdamped regime of $\beta_c << 1$, the IVC can be described by the equation [80, 81].

$$\left(\frac{V}{V_c}\right)^2 = \left(\frac{I_{\text{app}}}{I_c}\right)^2 - 1 \ . \tag{3.90}$$

Driving a strongly damped Josephson junction where the noise current fluctuates with a frequency which is less than the Josephson frequency, $f = 2eV/h$, the measured voltage can be recorded as the average of the instantaneous junction voltage. This occurs under the condition that $1/(R_{\text{vm}}^2 C_{\text{vm}}^2) <<$ ν_{noise}, where R_{vm} and the C_{vm} are the resistance and capacitance of the voltmeter, and ν_{noise} is the frequency limit of the noise current.

The IVC of the Josephson junction, considering this additional low frequency voltage, can be written as

$$\begin{aligned} V = &\frac{V_c}{I_n\sqrt{2\pi}} \left(\int_{I_c}^{\infty} \left[\left(\frac{I}{I_c}\right)^2 - 1 \right]^{1/2} \exp\left[-\frac{(I - I_{\text{app}})^2}{2I_n^2} \right] dI \right. \\ &\left. - \int_{-\infty}^{-I_c} \left[\left(\frac{I}{I_c}\right)^2 - 1 \right]^{1/2} \exp\left[-\frac{(I - I_{\text{app}})^2}{2I_n^2} \right] dI \right) \ , \end{aligned} \tag{3.91}$$

where I_n is the noise current and I_{app} is the current supplied by the source.

It has been shown that the low-frequency noise at low voltages can dominate over the high-frequency thermal noise in the IVC of Josephson junctions [118].

3.3.2.5 Nanobridge Response to RF Driving Source

For nanobridges which have an applied RF signal in addition to a DC bias the excess current will affect the behaviour of the device, and in this case the current flowing through the bridge can be described as

$$I_{\text{rf}} \sin(2\pi f_{\text{rf}} t) + I_{\text{dc}} = I_c \sin\varphi + \frac{\hbar}{2eR_n}\frac{d\varphi}{dt} \ , \tag{3.92}$$

and the voltage can be written as the Josephson voltage equation,

$$V = \frac{\hbar}{2e}\frac{d\varphi}{dt} \ . \tag{3.93}$$

I_{rf} and f_{rf} are the current amplitude and frequency from the applied RF source. In the solution to these equations it can be seen that the voltage steps occur at values corresponding to $hf_{\mathrm{rf}}/2e$ as described in Section 3.1.3.3.

As the applied RF bias is increased the magnitude of the current steps will vary according to the applied RF power as described by Equation 3.53. This has been experimentally verified in nanobridges by Gregers-Hansen and Levinsen (1971) [97], where it was demonstrated that in addition to steps which occurred at integer multiples of the voltage. It was also observed by Gregers-Hansen and Levinsen that non-integer steps obeyed the same Bessel function like behaviour.

Chapter 4

Fabrication

This chapter is comprised of two sections, the first provides a brief overview of each of the methods used in the fabrication process. The second section describes the iterative stages toward the development of a scalable fabrication process to allow the repeatability production of nanobridges with desired physical dimensions.

Producing complex, large scale SFQ circuitry composed of thousands of Josephson junctions has been successfully achieved using STJs [119]. However, such a scheme requires a multi-layer fabrication process, involving a number of patterning and deposition steps which makes integration with an SNSPD array difficult. Either the SFQ must be fabricated on top of the detector layer and risks damaging the detectors during processing, or the SNSPD must be fabricated on the uneven SFQ layer as shown in Figure 4.1(a), which can compromise the quality of the fabricated SNSPD.

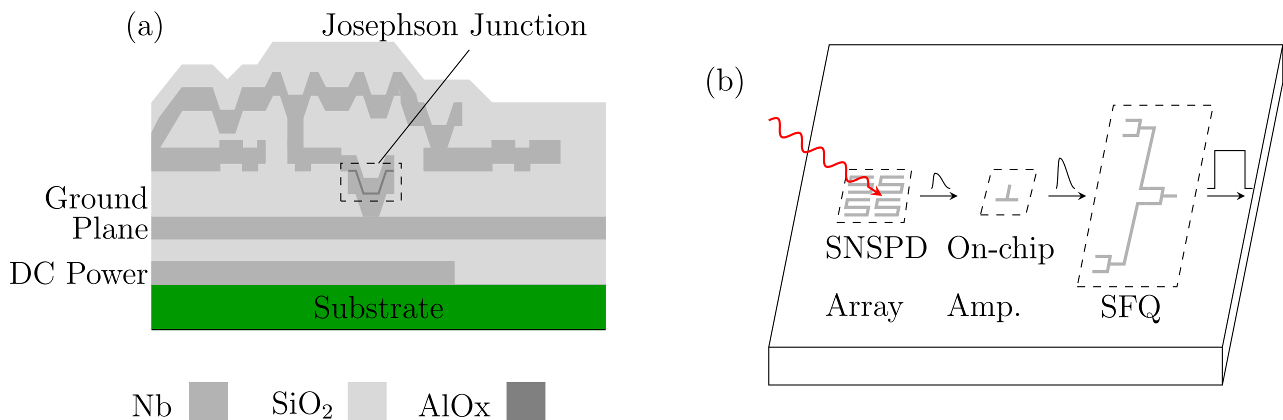

Figure 4.1: (a) An example of the cross-section of the type of layout of SFQ circuits which utilise STJs, the fabrication process required is complex and involves many stages. The SNSPD layer must be placed either on top of the final layer where the surface is uneven and will likely result in lower quality SNSPDs, or on the substrate before fabrication of the SFQ circuit which requires many layers of processing on top of the SNSPD. (b) An example of a nanobridge scheme that eliminates this issue by having the SNSPD and SFQ layer fabricated adjacent on the same sample. The output from the SNSPD layer is fed through an on-chip amplifier and into the SFQ readout, which then produces a DC pulse which can be transmitted to room temperature.

Using nanobridges as the active element for SFQ electronics allows the use of a planar design, where the SFQ circuitry can be implemented adjacent to the SNSPD array, as shown in Figure 4.1(b).

To achieve large scale SFQ circuitry based on nanobridges it was necessary to develop a scalable fabrication process which could achieve physical nanobridge dimensions corresponding to the limits described in Section 3.3.2, which for Nb nanobridges requires bridge dimensions of $L, W \lesssim 100$ nm.

In the early 1970s nanobridges were fabricated using the ”double-scratch” technique [83, 97], where a trench was scratched into the substrate, the superconducting film deposited and a sharp tool used to scratch the film perpendicular to the direction of the trench which formed the weak superconducting connection. With this process it was possible to produce variable thickness bridges with minimum length and width of $\sim$ 200 nm $-$ 500 nm. More recently focused ion beam (FIB) nanobridges have been developed [120] which can produce the physical dimensions required to operate in the Josephson regime, but requires that each nanobridge is individually milled and can result in contamination of the superconducting film due to the ions.

4.1 Film Deposition

Superconducting Nb films were deposited using a DC magnetron sputter system based at the James Watt Nanofabrication Centre (JWNC) at the University of Glasgow.

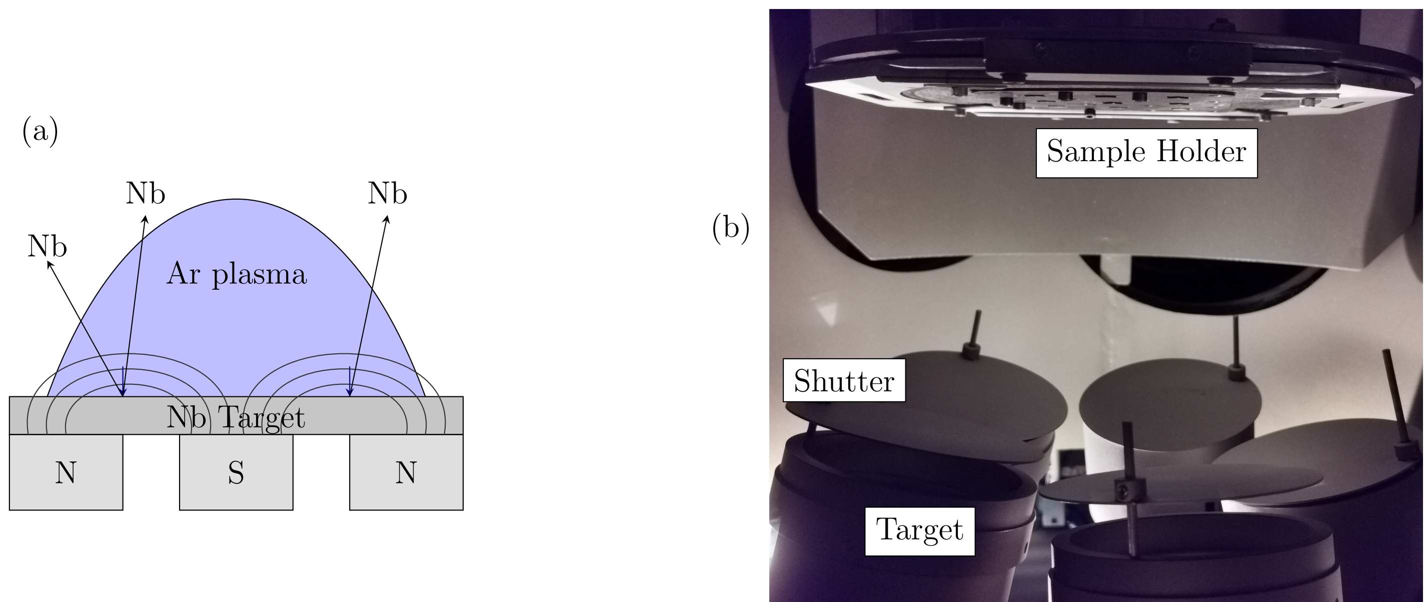

Figure 4.2: DC Magnetron Sputtering System (a) The Ar ions are directed toward the target by the magnetic field generated by the cathode, and cause clusters of atoms to be dislodged. These clusters will then become vaporised in the main chamber and condense onto the surfaces, including the substrate. (b) an image of the main chamber of the sputter system during deposition, the chamber is lit by the Ar plasma used in the deposition.

DC magnetron sputtering is a method of thin film deposition where a target material is vaporised

by bombarding ions and condenses onto a substrate to produce the thin film [121]. Sputtering is typically easier to control and is generally cheaper than alternative methods, such as epitaxial growth and atomic layer deposition.

Sputtering is achieved in ultra-high vacuum (UHV) conditions, at a main chamber pressure less than 1×10^{-6} Pa. Ar gas is then pumped into the chamber at a constant flow rate and controlled by a throttle valve on the main chamber to stabilise the flow. The Nb target is set within a gun that contains a cathode, when power is applied to the cathode the inert Ar gas is positively ionised to produce an Ar plasma. The positively charged Ar ions are attracted to the negatively charged cathode, and collide with the Nb target at high velocity, which "sputters off" some of the Nb particles. A schematic diagram of this process can be seen in Figure 4.2. These Nb particles will cross the deposition chamber and deposit themselves on the surface of the substrate to form the thin film.

The deposition rate is controlled by setting a fixed cathode current and varying the deposition time to control the film thickness. The film deposition was optimised to achieve the highest possible T_c.

After optimising the critical temperature of the film the deposition rate of Nb was ~ 10 nm/min.

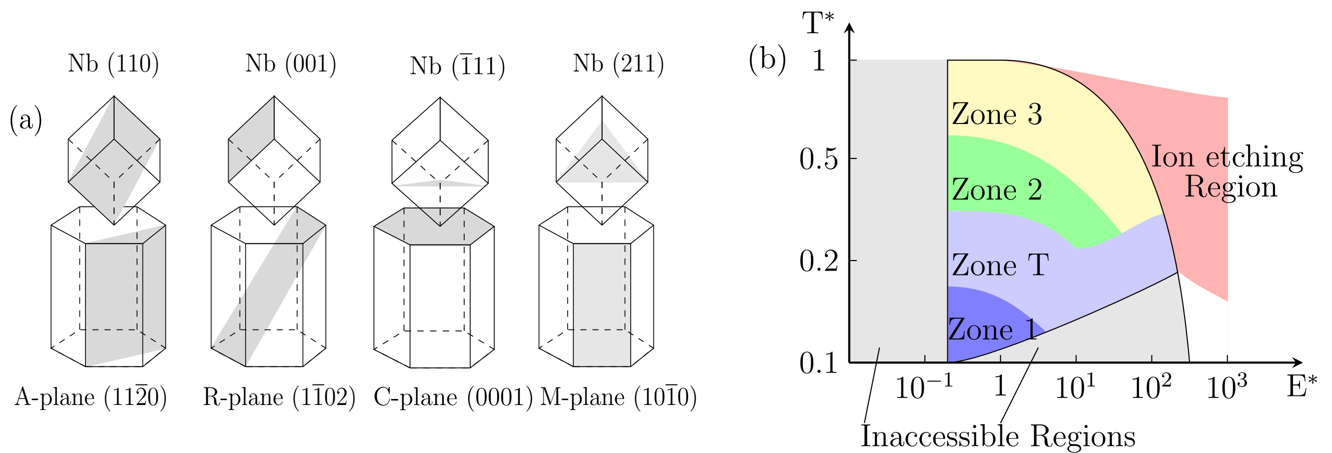

Figure 4.3: (a) The crystallographic structure of the substrate onto which the Nb film is grown effects the structure of the thin film, adapted from Wildes (2001) [122] (b) The conditions in the chamber result in differences in the type of crystallisation which occurs during film growth depending on the deposition temperature T^* and deposition energy E^*. In Zone 1 the film is composed of porous, tapered crystallites separated by voids, the film is under tensile stress. In Zone T the film transitions to compressive stress, in Zone 2 the growth regime is that of tight grain boundaries between columnar growth and in Zone 3 the film growth is dominated by isotropic and equiaxed grains. As the deposition energy is increased the process enters the ion etching regime, where the sputtered particles have an energy large enough to remove material from the sample surface. Figure adapted from Anders (2010) [123].

The crystallographic properties of the film are defined by the substrate onto which the thin film is grown [122], as shown in Figure 4.3 (a). A lattice mismatch between the substrate and thin film can induce stress or strain in the film [124, 125]. During the deposition process, the structure is

determined by the relationship between the temperature of the substrate, the kinetic energy of the ions and the deposition rate, which determines the growth regime of the film [123], and a schematic of the different growth regimes are shown in Figure 4.3 (b). This film structure will affect the electron mean free path which is a critical factor of the superconducting properties of the film.

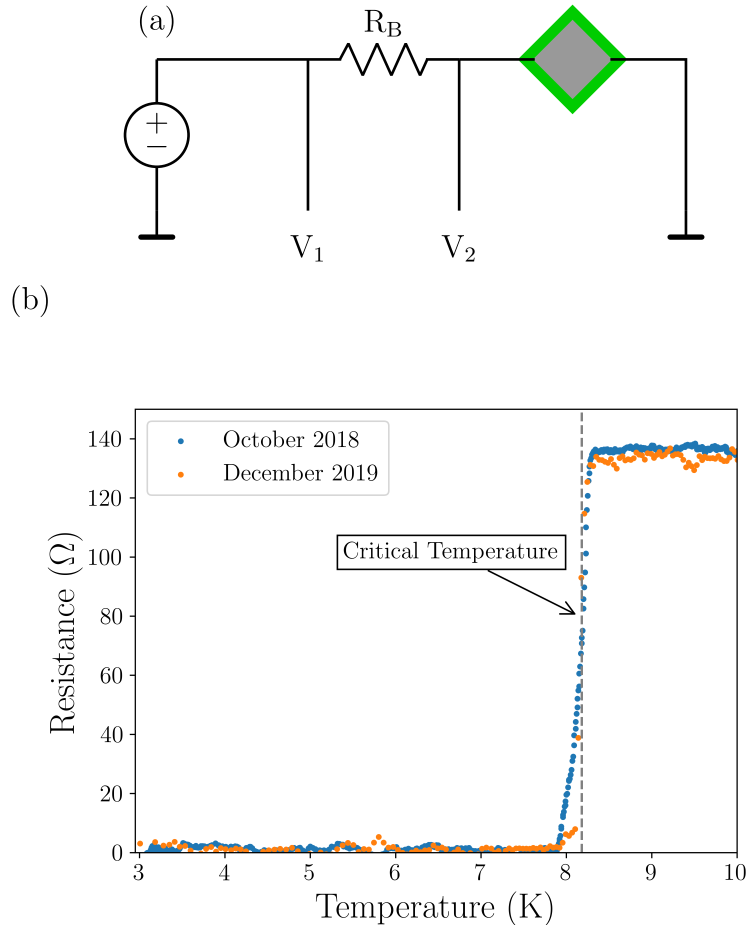

Figure 4.4: (a) A schematic of the measurement setup used to determine the critical current. Current is applied through the film. In the superconducting state all of the supplied current will flow through the sample to ground, and so $V_2 \sim 0$. As the sample transitions into the normal state the resistance is increased and the current is redirected to the V_2 path. The resistance can then be determined by calculation. (b) Two measurements undertaken on the same device over a thirteen-month period show comparable T_c and resistance of the film. Between measurements the sample was stored under vacuum. The slight discrepancy in the total resistance between the two measurements is likely caused by the different placement of wirebonds in each measurement in a two wire measurement setup. A four point contact measurement was not used as only T_c was being measured. This sample with a Nb film with thickness of d = 150 nm, onto a 10 μm × 10 μm Si substrate.

Nb films with thicknesses of 20 nm, 50 nm and 150 nm were grown on Silicon substrates, to be patterned to produce nanobridges. The film deposition process used in this growth can be found in Appendix A.1.

Once deposited, samples are stored under vacuum until required for device fabrication. Films have been held under these conditions for periods greater than one year without any notable degradation of the superconducting properties, an example of a comparison made on one sample can be seen in Figure 4.4.

4.2 Electron Beam Lithography

Electron beam (ebeam) lithography is a nanofabrication technique which is capable of patterning features with sub-10 nm resolution [126]. In ebeam lithography a focused beam of electrons is used to directly write the pattern into an electron-sensitive resist surface, the pattern is then developed to remove the unwanted resist which can then be used either as an etch mask, or to produce a hard mask through a lift-off process. This section outlines the principle points of ebeam lithography and how these were applied to the development of nanobridges.

4.2.1 Electron Beam Resists

Resists are electron sensitive materials, which are spun onto the sample to produce a layer into which the ebeam pattern can be written. A resist can be either positive tone, where exposure to the ebeam will break the molecular links and remove this resist during development, or negative tone, where the exposed resist is hardened and will remain after development, as shown in Figure 4.5. The ebeam will change the properties of the resist depending on the current dose applied to the resist during the exposure.

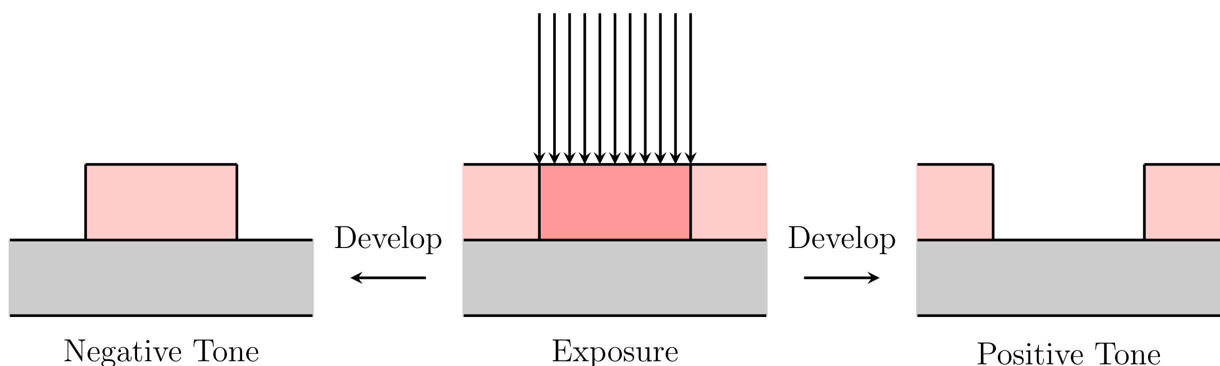

Figure 4.5: After exposure the pattern is produced by development, where the unwanted resist is removed from the surface. For negative tone resists the exposed area is hardened and remains after development, while in the positive tone resist the exposed area is removed and the unexposed areas are left behind after development

The usage of each resist is dependent on the resist properties, the most important of which for the purposes of nanobridge fabrication are:

- Sensitivity, which determines the dose required to expose the resist. Highly sensitive resists can be patterned in shorter exposure times and will result in less accumulated charging in the sample but are more susceptible to proximity effects [127].

- Etch resistance, the capability of the resist to provide an etch mask. This is generally determined by the selectivity, which is the ratio of the etch rate of the thin film to the resist layer, which varies for materials and etch processes. Resists with low selectivity can be patterned to produce hard masks for etching.

- Thermal stability, which is the ability of the resist to withstand high temperature processing.

These parameters can be generally summed up as the ease of processing, which can be used to describe the complexity of application, patterning, development, etching and resist stripping.

There are three resists which are most commonly used in nanofabrication processes at the JWNC: Polymethyl Methacrylate (PMMA) [128], Hydrogen Silsesquioxane (HSQ) [129] and ZEP520A (ZEP) [130].

Table 4.1: A comparison of the parameters of the ebeam resists used over the course of this project.

Resist	Resolution	Tone	Sensitivity	Selectivity	Developer	Thermal Stability
PMMA	4 nm [131]	Positive	Intermediate [128]	Low [132]	MIBK or IPA	Low [133]
ZEP	12 nm [134]	Positive	High [130]	High [132]	Xylenes	Intermediate [135]
HSQ	5 nm[136]	Negative	Low [129]	High [137]	TMAH	High [138]

4.2.1.1 Polymethyl Methacrylate

PMMA is a long chain, organic polymer, as shown in Figure 4.6 which can be used to achieve sub-10 nm feature sizes. During exposure the PMMA chain is broken down by the electron beam and dissolved when exposed to the developer.

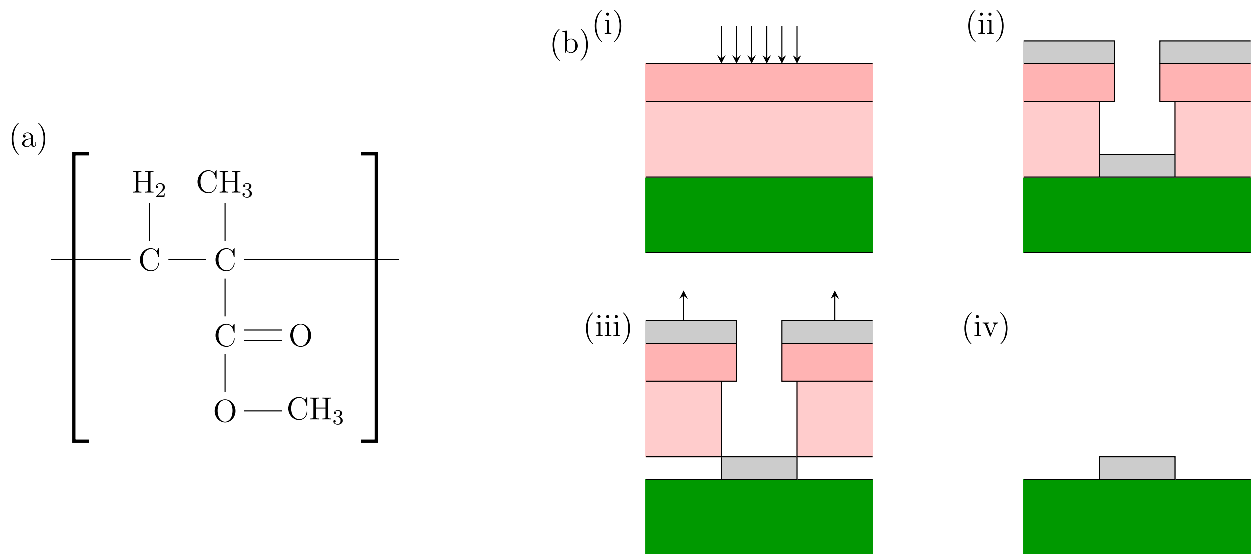

Figure 4.6: (a) The polymer structure of the PMMA molecule. (b) To improve the lift-off performance a bilayer of PMMA can be used. (i) A bilayer is formed of a thicker bottom layer is spun onto the sample and baked, before a second, typically thinner layer of heavier PMMA is spun on top. (ii) When exposed the more sensitive bottom layer will result in a larger area of exposure, creating an overhang of the upper layer and preventing the deposited metal from forming a continuous layer, allowing the deposited metal to be removed. (iii) The PMMA bilayer can then be removed with a solvent, which also removes the metal layer on top of the resist, and (iv) the metal layer is left behind to produce the desired pattern according to the lithography exposure.

PMMA can be etched by Cl, F and O plasmas, and as a result typically has poor etch resistance and can often see poor repeatability, although PMMA bilayers can be used in a lift-off process , shown in Figure 4.6(b) which can be used to produce metal hard masks, or to define features without etching the sample. The lift-off process is unsuitable for refractory metals which require high temperature evaporation and can damage the PMMA layer. In comparison with ZEP and HSQ resists, PMMA is simple to develop and can be easily and cleanly removed by flushing with acetone.

4.2.1.2 Hydrogen Silsequioxane

More recently developed than PMMA and ZEP, hydrogen silsequioxane (HSQ) can provide 5 nm resolution and has excellent etch resistance and minimal line edge roughness.

HSQ is a negative tone resist which is formed of eight $(HSiO)_{(3/2)}$ monomers, the structure of which is shown in Figure 4.7. During exposure adjacent molecules are cross linked by the breaking of Si - O bonds linking with the broken Si - H bond for a neighbouring molecule which produces a strong network of Si-O-Si bonds, and a hydrogen gas by-product.

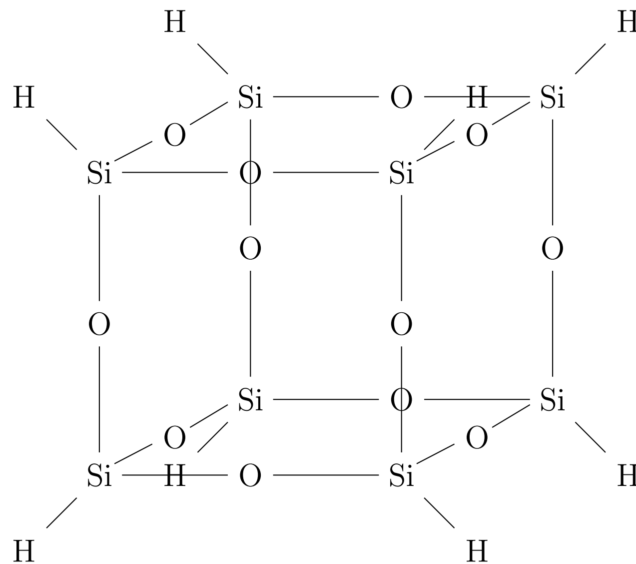

Figure 4.7: The cage-like structure of the HSQ molecule. When the resist is exposed the hydrogen atoms are removed and the molecules become cross-linked.

However, HSQ requires development in alkaline hydroxide developers and is etched with HF, which are hazardous substances not required when using PMMA or ZEP resists. HSQ also requires additional pre-patterning and post-patterning processing, which is not required for ZEP and PMMA resists, and so it was decided to avoid the use of HSQ for this project.

4.2.1.3 ZEP520A

ZEP resists are a -chloromethyl acrylate and methyl styrene copolymer dissolved in an anisole solvent, the chemical structure of which is shown in Figure 4.8. These resists are developed by xylenes, although amyl-acetate is also a suitable developer. The selectivity of ZEP in Fl and Cl etching when etching Nb is sufficiently high that it can act as a mask for film thicknesses in the range of 500 nm. When using high acceleration voltages the ZEP resist will develop a sloped sidewall, which makes it unsuitable for lift-off processes.

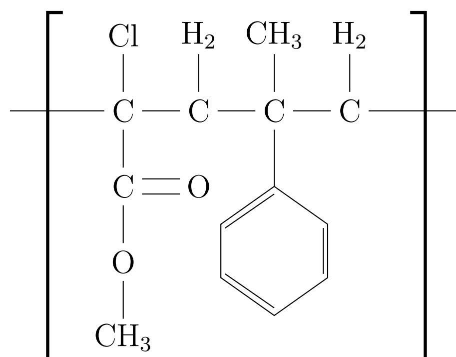

Figure 4.8: The polymer-chain structure of ZEP.

ZEP resists offer a high etch resistance, which allows the resist to be used as an etching mask. When patterning ZEP, its high sensitivity allows it to be exposed in a short time but can also result in unwanted exposure due to the proximity effect, particularly where there are small features in a large exposure field. ZEP can also be difficult to remove and without a suitable removal procedure can leave a residue which creates adhesion issues when applying further ebeam resist layers.

4.2.2 Electron Beam Exposure and Dosing

During the ebeam patterning process the resist layer is exposed to a focused electron beam to transfer the desired pattern. This pattern can then be etched into the film using the resist as a etch mask, or for a lift-off process. The current of the ebeam emitter is typically fixed, and the dose is accumulated in the sample due to the exposure time. To fully expose the ebeam resist there is a minimum dose, known as the clearing dose.

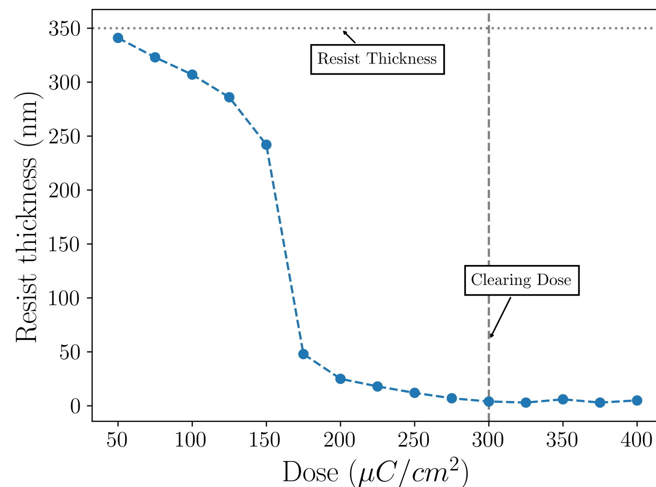

Figure 4.9: A gradation curve for the exposure of a 350 nm thick layer of ZEP520A. The clearing dose can be seen at $\sim$ 300 μC/cm^2, at which point the resist is almost completely cleared during the development step. Resist residues can often remain which can be removed by an oxygen etching process known as ashing.

The clearing dose can be determined by repeated patterning of a test structure, with incremental increases in dose each time. After the sample is developed the thickness of the removed resist can be evaluated using a height profilometer to produce a gradation curve for the resist, an example of which is shown in Figure 4.9.

The required dose to clear is dependent on the material properties of the layers of resist, film and substrate of the sample which is to be patterned, which is commonly referred to as the stack. The resist can be exposed either by electrons emitted directly from the electron source, by scattered electrons or from secondary scattered electrons as shown in Figure 4.10.

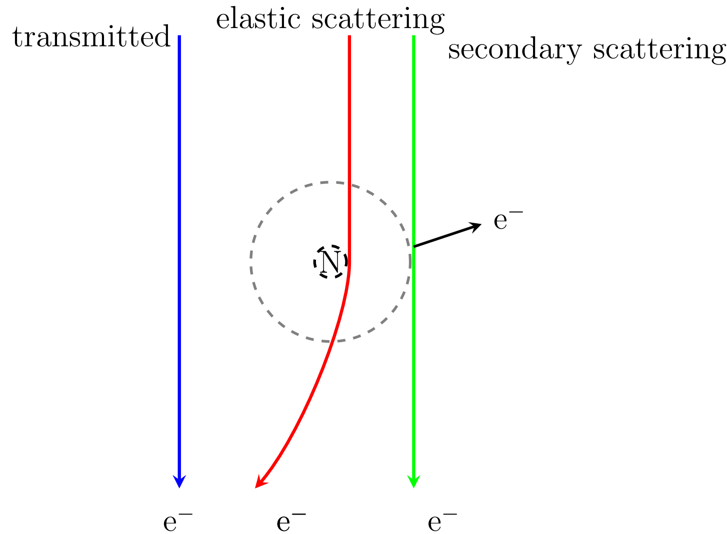

Figure 4.10: Electrons from the ebeam which are directed into the resist layer can be transmitted (blue), elastically scattered (red) by interactions with the material in the stack or produce secondary scattering due to electrons in the resist layer becoming excited (green).

These scattered electrons can be deflected outside the area which is intended to be exposed or can induce secondary electrons to scatter outside of the exposure, resulting in the widening of the pattern, or complete removal features for certain patterns.

4.2.2.1 Electron Scattering and Proximity Effect

The proximity effect in electron beam lithography is the phenomenon of dose extending beyond the designed limits of the pattern due to electron scattering. This causes the ebeam resist outside the area of the scanned pattern to receive a non-zero dose during the exposure.

As electrons are emitted the electron-electron interaction causes the beam to broaden. Once the electrons enter the resist the scattering effects can cause further dispersion, and electrons can be backscattered back into the resist layer due to scattering with the film and substrate. The scattering of electrons can be seen in Figures 4.11 and 4.12.

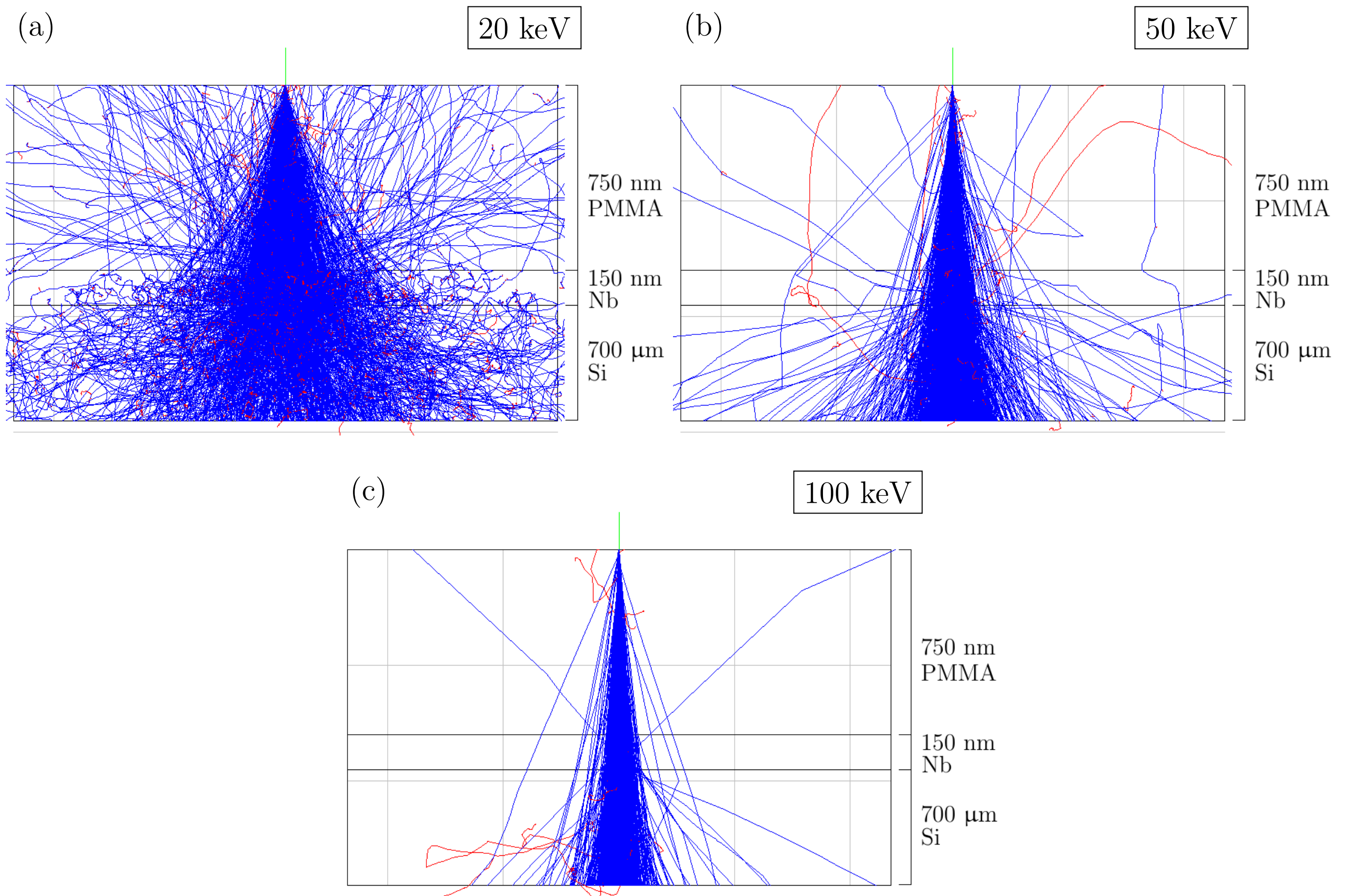

Figure 4.11: Three examples of electron beams at varying of the acceleration voltage. The forward scattered electrons are represented in blue, and the backscattered and secondary electrons in red. For a stack with 750 nm PMMA, 150 nm Nb on bulk Si, with a beam width of 5 nm. (a) shows a 20 keV beam, (b) shows a 50 keV and (c) shows a 100 keV beam. The higher energy beams experience less scattering as the higher energy electrons can maintain their trajectory without losing energy to collisions. Images were made using the EISS software package [139].

Using higher acceleration voltage beams during exposure can reduce the proximity effect during patterning by reducing both forward scattered and back scattered electrons. The effect of the electron beam broadening is reduced for higher acceleration voltage beams [140], as shown in Figure 4.11. This also results in the electrons penetrating deeper into the stack, reducing the probability of the electron being reflected back into the resist and improving the line edge roughness [141], this is shown in Figure 4.12.

Increasing the acceleration voltage of the electron beam does not completely eliminate the over-exposure due to the proximity effect. A more complete method is to use a mathematical technique known as the proximity effect correction (PEC) [142] which can be applied to the exposure. There are two techniques for implementing a PEC to a pattern, these are by modification of the dose of the electron beam across the pattern, or by changing the shape of the pattern such that it will result in the correct physical dimensions after patterning and development.

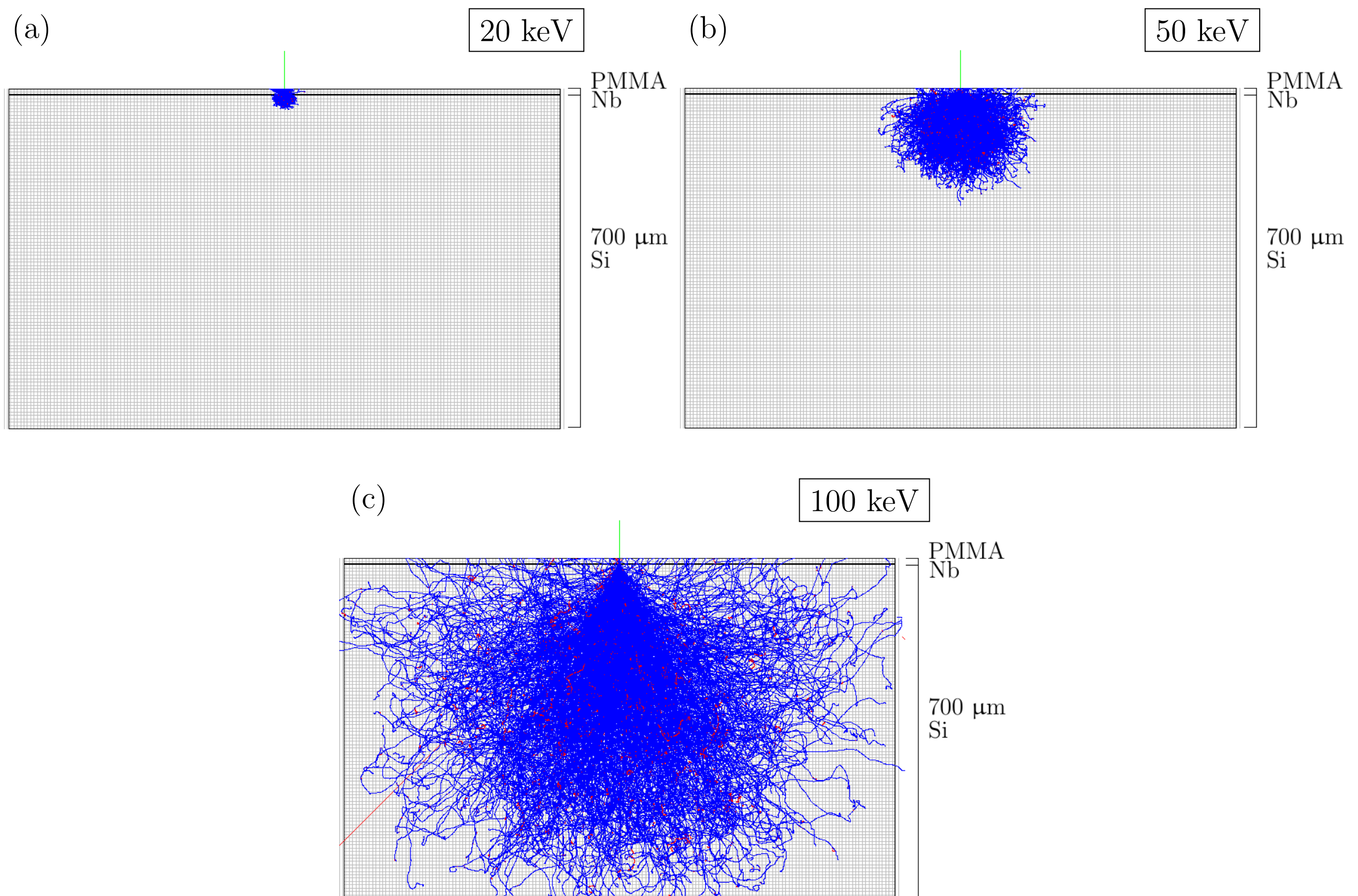

Figure 4.12: Looking at a larger cross-sectional area of a stack with the same parameters as in Figure 4.11, the higher energy beams can penetrate deeper into the stack which reduces the proximity effect in the resist as more of the electrons can be dissipated into the substrate.

The dose modification technique is a mathematical solution which requires only information about the point spread function (PSF) - a radial symmetric function which describes the spread of the electron beam - of the material which is being exposed to correct any arbitrary shape. However, this requires a computationally expensive calculation to be completed to evaluate the PSF. The shape modification is a simpler method which does not require complex dose adjustment across the sample, however this method also requires a similarly computationally expensive calculation to evaluate the correction and cannot provide as accurate a correction as the dose modification method. A hybrid method which combines both dose modification and shape modification is typically capable of producing greater accuracy then either of single method.

In the Beamer software package, which is used to prepare the pattern for ebeam exposure shape corrections, proximity effect corrections and hybrid functions can be included as part of the job preparation. The shape PEC correction was implemented onto the nanobridge samples to improve the accuracy of the fabrication.

4.3 Etching

In nanofabrication etching is the process of removing layers from the surface of a sample to produce a desired pattern in a thin film. An etch mask is used to reproduce a pattern into a thin film, the mask is usually a sacrificial layer of resist or material which is resistant to the etchant. There are two etching processes: liquid etching, which is also known as wet etching, where the sample is submerged into a liquid etchant, and plasma etching, or dry etching which makes use of ionised plasma to physically and chemically etch the thin film layer.

Etching processes are either isotropic, where the etching occurs in all directions, or anisotropic, where etching process is directed to preferentially etch in one direction.

4.3.1 Reactive Ion Etching

Reactive ion etching (RIE) is a type of dry etching in which a chemically reactive plasma is directed toward the sample to remove excess material and retain the desired pattern. An applied, directional RF field ionises the etchant which is then directed toward the sample, as shown in Figure 4.13(a). The positively charged ions then react chemically and physically with the thin film and substrate which causes the sample to be etched. The ratio of etch rate between each of the layers is known as the selectivity, with high selectively the layers to be removed will be etched much faster than the layers which are to remain. It is also important to consider the ratio of the mask height to the size of the features, as the etchant ions can be deflected and collide with the sidewalls which reduces the etch rate. To minimise this effect the resist height should ideally be kept within $\sim 3\times$ the size of the smallest feature, although this is a general guide rather than an explicit rule.

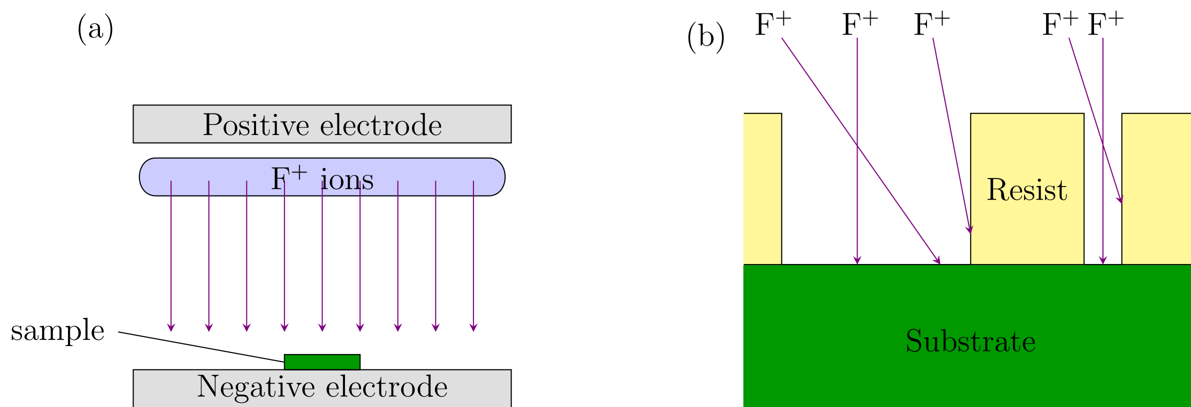

Figure 4.13: (a) An example of a RIE process. The chamber is flooded with a mixture of CHF_3 and SF_6 gas which is then ionised. The two plates of the etching tool generate an electric field to direct the ions toward the sample (b) for large features, ions which have been deflected are likely to reach the thin film to contribute to the etching process. In the smaller features there are fewer paths to reach the thin film, so the number of ions which contribute to the etching process is reduced which results in a longer etch time.

RIE is a primarily anisotropic process, with the etching primarily being directed downwards onto the sample surface. Some portion of the etchant gases will form radicals, which chemically etch isotropically and can cause undercutting of the mask as shown in Figure 4.14.

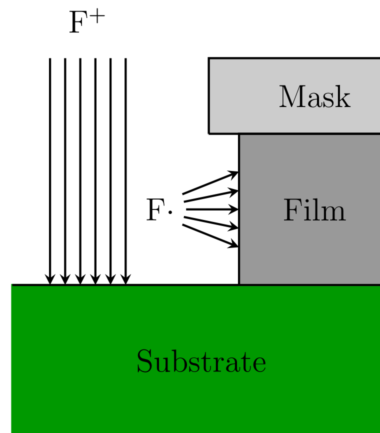

Figure 4.14: The ionised etchants are directed by the applied field, but radicals can be produced during the etching process which are not directed and can result in isotropic component to the etch and an undercut of the mask.

The ratio of radicals to ions is controlled by the applied RF power, and the anisotropicity of the etch can be reduced by increasing the power to reduce the number of ions. However, this also increases the etch rate and makes the process more difficult to control, particularly for very thin films $\lesssim$ 10 nm. The parameters of the etching process can be optimised to minimise the line edge roughness and maintain a controllable process.

4.3.2 Wet Etching

Wet etching uses a bath of liquid etchant into which the sample is submerged, allowing the etchant to chemically remove the unwanted material. This process is less controllable than dry etching, as the liquid etchant will etch isotropically as shown in Figure 4.15, and requires that the etchant is chemically stopped, which can result in variations in the etch across the sample.

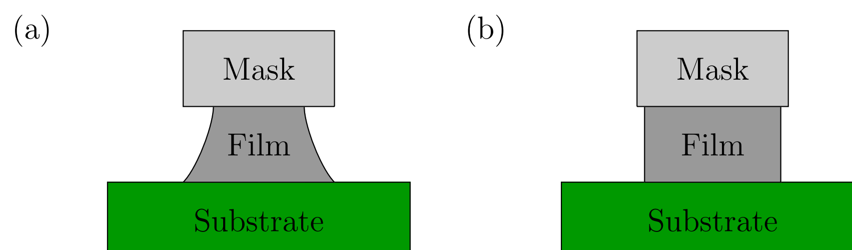

Figure 4.15: Diagram of two typical etch processes. (a) the result of an isotropic etch, where the mask has been undercut and the sidewalls of the sample are not uniform, typical of wet etching (b) an anisotropic process, where the etchant has been directed, typical of dry etch.

Wet etching is typically cheaper than dry etching, as it does not require any complex equipment, and is preferred where there is high selectivity and isotropic etching is not a significant issue, for example in the removal of an etch mask to complete a sample.

4.4 Process Development

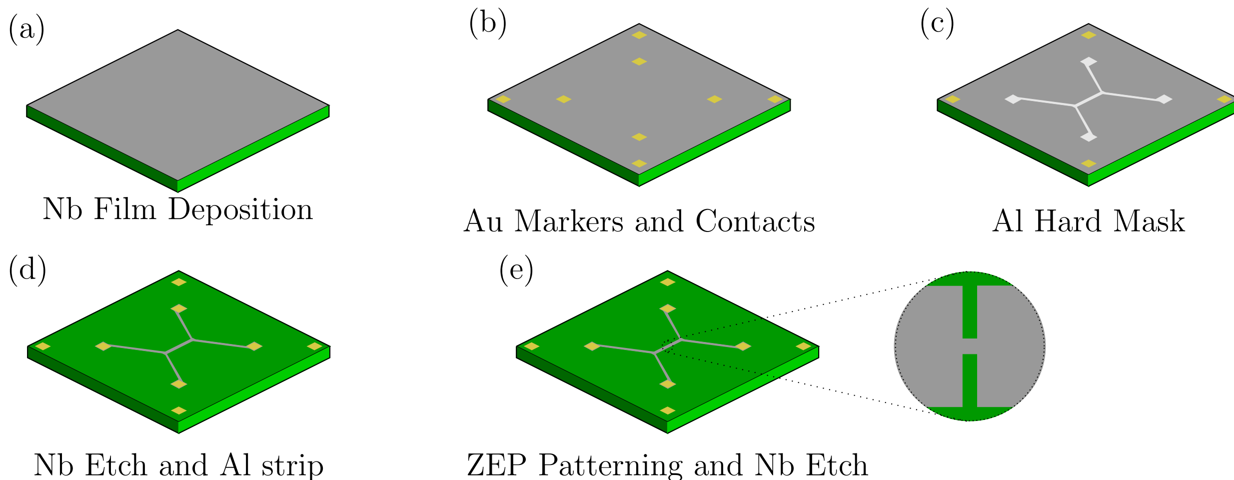

Figure 4.16: (a) The first step of the fabrication process is to deposit a Nb film onto a Si substrate by sputter deposition. (b) Au markers and contacts are patterned by ebeam, using PMMA as the resist. After an Au gold layer is deposited onto the sample the gold markers are defined through a lift-off process. (c) An Al layer is patterned with a PMMA lift-off process to mark out the electrical contacts and microwires, and (d) the sample is etched to produce the layout of Nb wires. (e) A final ebeam step is used to define the nanobridges in the microwire and is etched. After the completion of this etch step the ZEP resist can be removed and the sample is ready to be used.

The techniques for fabrication which have been outlined were used to develop a robust fabrication process for the production of nanobridges for use in this work. This section outlines the iterative steps which were taken to realise the fabrication of nanobridges. A schematic of the final fabrication process is shown in Figure 4.16. The superconducting Nb film of the desired thickness is first deposited, and then Au contacts and markers are added to the sample. A lift-off method is used to produce a hard Al mask to etch all micro-scale features into the film. Following from this a ZEP resist layer is spun onto the sample, into which the nanobridge structures are patterned. The ZEP is then used as a etch mask to produce the completed device.

4.4.1 Adaptation of SNSPD Fabrication Process

The process used in the first batch of samples was based on the method of fabrication for SNSPDs developed at the JWNC by Dr. Alessandro Casaburi, the details of which are thoroughly described in the thesis of former group member Dr. Rob Starkwood [56]. It was decided that the nanobridges

would be fabricated from films with 150 nm film thickness to increase the chance that the film was superconducting, and so the resist thickness was increased from 120 nm which was used in the fabrication of SNSPDs to 500 nm. An abbreviated description of the process is as follows,

- ZEP resist spun to thickness of 500 nm
- Single ebeam pattern step
- Develop with o-Xylene
- RIE with CF_4 etchant gas.
- Resist stripping and sample testing

The single ebeam step was divided into two components which were patterned sequentially, the 'large' features used a 128 nm beam size where the resolution was less important and the nanobridge patterning used a 3 nm beam size, which was completed over a single exposure. After etching the samples it was found that the nanobridges had been removed creating a break between the two electrodes, as shown in Figure 4.17(b).

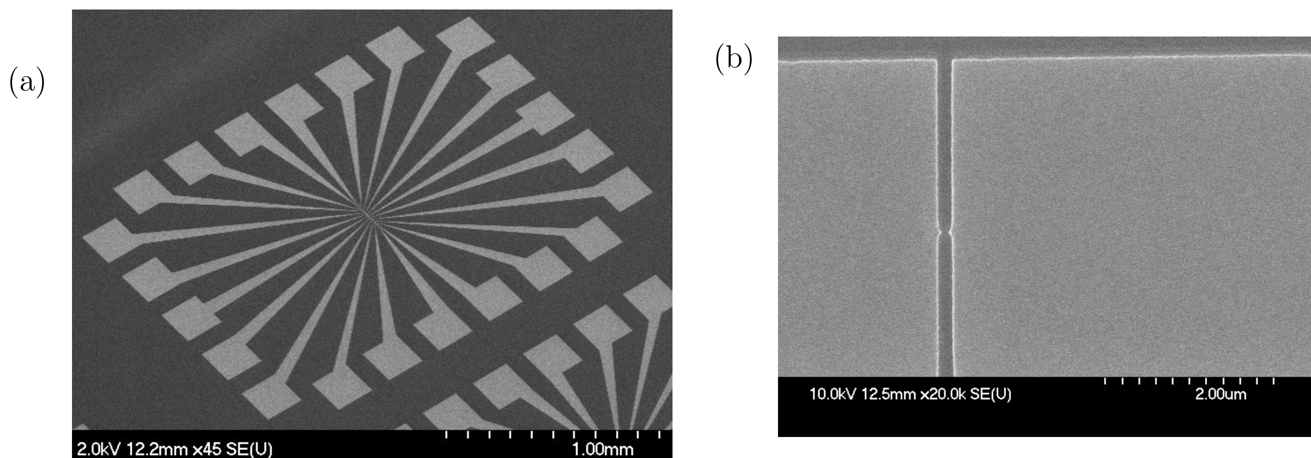

Figure 4.17: (a) The layout of the test samples, ten nanobridges are fabricated on a microwire with physical dimensions 4 μm × 160 μm, each nanobridge in the array is connected to four of the 200 μm × 200 μm contact pads to allow for four wire measurement of any single nanobridge in the array. (b) An example of a fabricated sample where the nanobridge was completed removed during the etch process, creating a break between the two electrodes of the nanobridge.

Nanobridges with varying geometries were fabricated to investigate the effect which the variation of the electrode geometry had on the electrical behaviour of the nanobridge, and if a consistent offset could be found between the designed and fabricated dimensions. It was found that the smallest nanobridges that could be produced with this method had a width of $\sim$ 200 nm where the nanobridge was designed at 500 nm, and example of this is shown in Figure 4.18(a). Where the dimensions were

reduced resulted in the complete removal of the nanobridge, although it was noted that some material remained behind as shown in Figure 4.18(b).

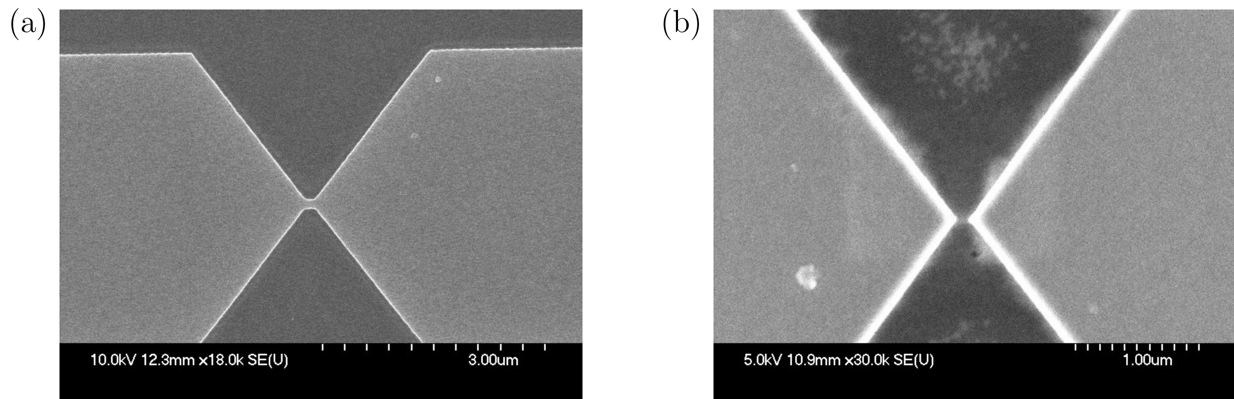

Figure 4.18: (a) A nanobridge fabricated with physical dimensions on the order of 200 nm which was found to be the smallest intact nanobridge, and (b) using the same design layout included into a test structure the nanobridge was removed during etching.

It was suspected that the ZEP mask was being undercut during the etching process resulting in the removal of the nanobridge, and so the RF power applied during the etching was varied in an attempt to reduce the extent of this undercutting. Increasing the RF power will result in a reduction in the number of free radicals in the etchant gas, which should reduce the isotropicity of the etch. However the results as shown in Table 4.2 suggested that increasing the power resulted in an increase in the undercutting of the mask.

Table 4.2: Measurement of mask undercutting as a function of the applied RF power during the etch showing that the undercut increased in severity as increasing RF power was applied.

Power (W)	Undercut (nm)
80	20
150	35
180	30
200	45
220	110

It was suggested [143] that the increase of the undercut as the power was increased indicates that this issue originates in the lithography step rather than as a result of the etch parameters. ZEP resists will develop a sloped sidewall proportional to the acceleration voltage of the ebeam system and the exposure. The system at the JWNC exposes with a fixed 100 keV electron beam, which produces a sloped sidewall in this resist. During the etching step the ions directed toward the sample can be deflected when they collide with this sloped surface to cause the mask to be undercut which

will increase with increasing RF power as shown in Figure 4.19.

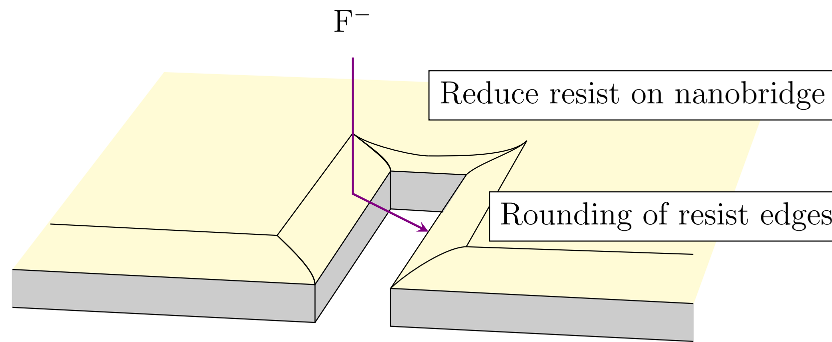

Figure 4.19: A schematic of the Nb film during etching showing the issues which caused the removal of the nanobridges. The sidewall profile of the ZEP causes the etching ions to deflect, which causes material under the mask to become removed. The proximitisation of the resist which is to form the nanobridge will result in either a bridge with reduced thickness, or the complete removal of the nanobridge during the etching process.

In addition to sloped profile of the resist, ZEP resists have high sensitivity which can cause issues when exposing small features in large exposure areas. When exposing the entire pattern in a single step the nanobridge will become partially exposed due to the proximity effect. Test structures, an example of which are shown in Figure 4.20(a), were written to investigate if the patterned ZEP could be patterned into a structure which could be used to mask the nanobridge sufficiently for etching.

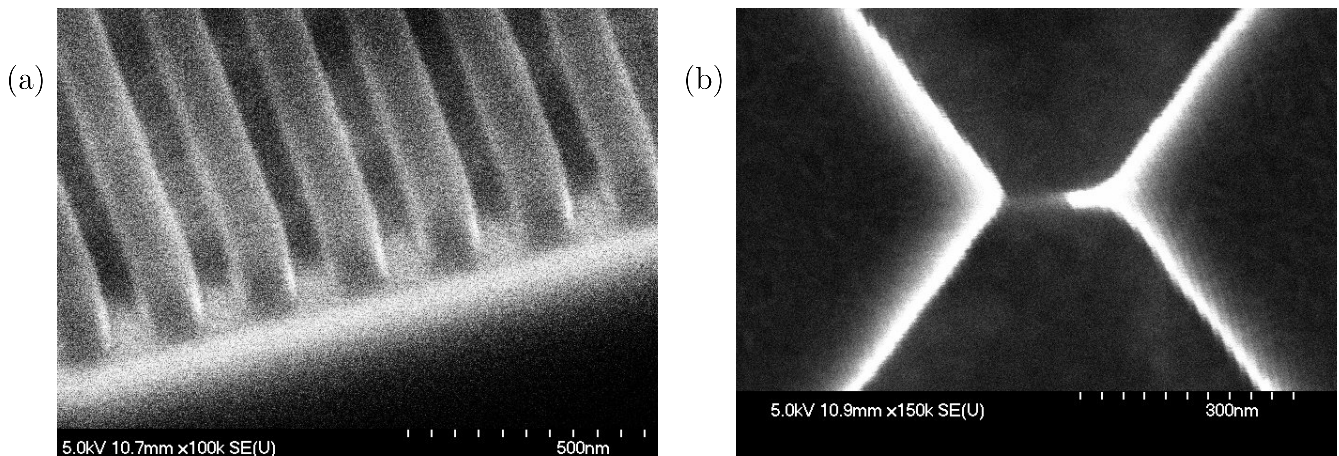

Figure 4.20: (a) An example of a test pattern in ZEP resist. It was found that the proximity effect from patterning large area exposures adjacent to small resist columns with sizes comparable to that used to mask the nanobridge resulted in a partial exposure of the resist. (b) After the etch process it can be seen that the nanobridge is mostly removed, with only a small strip of material remaining. This is the result of the partially exposed nanobridge resist, which is removed during the etching process and allows the nanobridge to become partially etched.

It was found that isolated ZEP columns could be correctly patterned, but when placed between large exposed areas of 4 μm × 4 μm the proximitisation of the resist reduced the thickness of the column. In some cases the column was completely removed during the exposure. In the nanobridges this is seen by the reduction of the thickness of the resist which is used to mask the nanobridge

during the etching process. The remaining resist is then removed during the etching process and the nanobridge becomes exposed, resulting in a nanobridge which is partially etched through, an example of this is shown in Figure 4.20(b).

Attempts were made to improve the proximitisation of the nanobridge area by reducing the area which was patterned changing the geometry of the surrounding contacts and connecting wires to increase the distance from the large exposure to the nanobridges but these were ultimately unsuccessful.

In an attempt to reduce the effect of the proximisation on the nanobridge during exposure the width of the microwire was increased from 4 μm to 16 μm. This moved the large exposure area which was used to pattern the electrical contacts and wirebonding pads further away from the nanobridge, although this did not have a significant effect on the overexposure of the nanobridge resist. Proximity corrections in the pattern improved the lithography and allowed wire structures to be produced, and yielded nanobridges with a length > 150 nm or where the film was partially etched leaving a nanobridge with reduced thickness as shown in Figure 4.21.

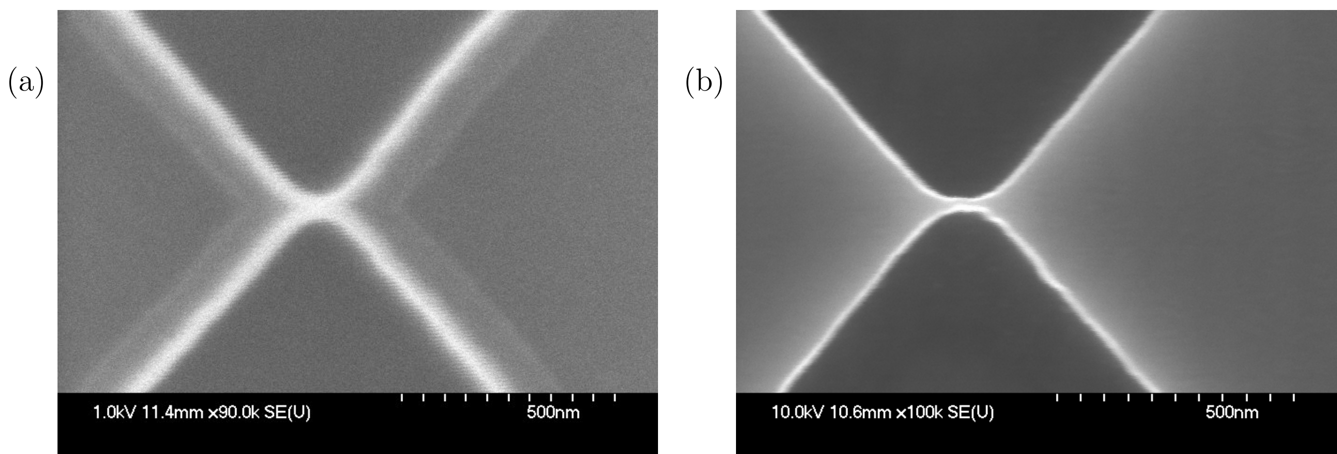

Figure 4.21: (a) An example of a nanobridge fabricated with an included proximity effect correction, the width of the nanobridge is reduced while the length is increased from the designed dimensions. The nanobridge has been partially etched such that the film thickness of the nanobridge is less than that of the electrodes. (b) In another example of a nanobridge, fabricated with a later sample than in (a) with included proximity effect, where the electrodes are connected by the bridge, but the overexposure has increased the length and reduced the width from the designed parameters.

It was concluded from the results yielded by this process that fabricating these samples in a single step with this resist was unfeasible.

4.4.2 PMMA Single Step Process

As an alternative to ZEP it was decided to use PMMA as the ebeam resist. This resist forms a much less effective etch mask, so the pattern was written as a negative tone and used a lift-off process to

produce an Al hard mask for etching. By exploiting the lower sensitivity, with a clearing dose around four times that of ZEP, and the smaller patterning area of the negative tone pattern the intention was to reduce the effect of proximitisation on the resist, while the Al hard mask would prevent the mask undercutting which was seen with ZEP.

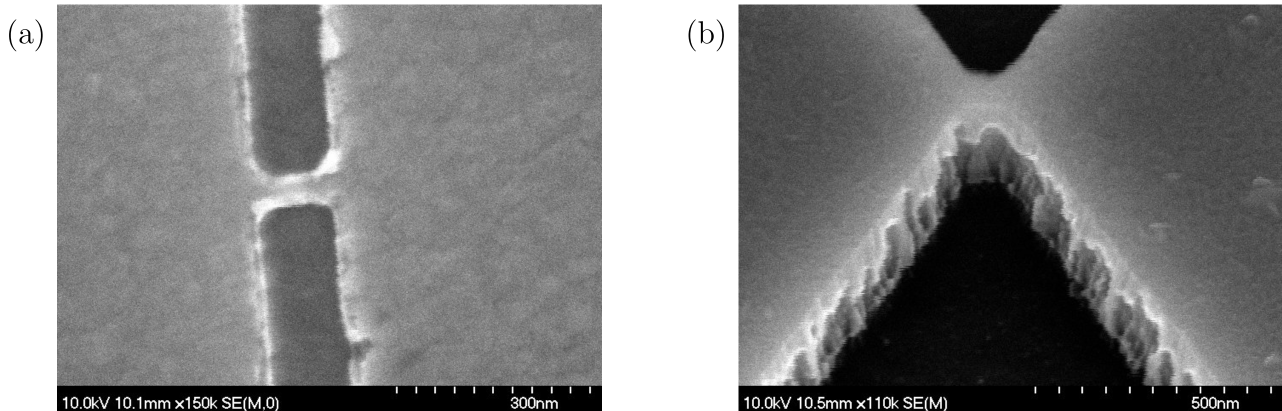

Figure 4.22: Two examples of successfully fabricated nanobridges made using a PMMA process with an Al hard mask. In (a) a top down view of a Nb nanobridge, the roughness at the edge of the Al mask can be seen, and in the side view (b) it is shown how this is transferred into the Nb during the etch process. In this sample the Al mask has been removed.

A PMMA bilayer with a 200 nm bottom layer of Elvisite 2010 PMMA and a 100 nm top layer of Elvisite 2041 PMMA was used, and this was exposed with a negative tone pattern. After development an Al layer was deposited onto the sample with ebeam evaporation and lifted off to produce the etch mask. The samples were then etched with a F based RIE process and the Al mask layer was wet etched using CD26 photodeveloper.

Test structures of straight 10 μm long lines with varying widths were fabricated and showed negligible undercut of the mask during the etch process. It can also be seen in this sample that the edges of the samples show irregularity. This is due to the Al hard mask: Al forms a granular structure with grain sizes in the range of $5 - 10$ nm, and during the etch process this is transferred into the Nb. This is clearly visible on inspection with SEM, as shown in Figure 4.22.

Despite successfully yielding superconducting nanobridges this fabrication process produced two issues which effected the quality of samples. Firstly, the physical parameters did not match the designed parameters, the difference between the designed and measured physical differences can be seen in Table 4.3.

Table 4.3: The average measurements from each array over a sample with one hundred and sixty nanobridges. Many of the nanobridges with electrode angles of 60° were broken or physically inconsistent. It can be seen that while the accuracy of the nanobridges here was poor, the variance across each array showed good consistency.

Electrode Angle (nm)	Designed Width (nm)	Designed Length (nm)	Average Width (nm)	Average Length (nm)	σ Width (nm)	σ Length (nm)
0	50	80	broken	broken	-	-
0	50	100	29.7	33.2	0.8	1.7
0	70	100	36.8	36.9	2.1	3.0
15	50	80	17.6	30.2	1.5	3.4
15	50	100	33.2	30.5	1.8	0.8
15	70	100	41.4	31.4	1.2	0.8
30	50	80	33.0	29.7	1.6	1.2
30	50	100	31.1	40.7	1.4	2.0
30	70	100	43.4	44.8	1.5	1.0
45	50	80	67.5	78.2	5.4	6.7
45	50	100	64.2	93.2	2.1	2.3
45	70	100	83.4	96.4	1.7	2.2

The tolerance on the physical dimensions of the nanobridges were found to be extremely difficult to control, with a variation in exposure dose of 10 μC cm^{-2} resulting in changes of tens of nanometres in the nanobridge length and width. Differences were noted between samples which had been fabricated with the same process, suggesting that environmental factors had a significant effect of the physical parameters of the nanobridges.

The results of a completed sample made using the PMMA method are shown in Table 4.3, showing how the designed and physical parameters of the nanobridges across the sample vary. Despite this, it can be seen that the physical dimensions are consistent for identically designed nanobridges.

variance of the nanobridge dimensions across the sample are small. The length and width of the nanobridges was found to be much shorter than designed dimensions, this is due to the small tolerance range of the dose in the ebeam patterning step.

The second issue was that during the lift-off step the Al mask could not always be completely removed as shown in Figure 4.23, resulting in a structure with a width of half the microwire. This was most noticeable where the nanobridge had the smallest separation between the electrodes, with an electrode angle of 0°. The Al layer was reduced from an initial 100 nm to 20 nm, as the etch rate of the Al was measured at $<$ 5 nm, with a resist thickness of 300 nm, which failed to eliminate

this issue. Increasing the thickness of the resist would limit the nanobridge dimensions which the process could produce. Several samples were briefly sonicated in acetone in an attempt to remove the extraneous Al, however this very often resulted in destruction of the nanobridges.

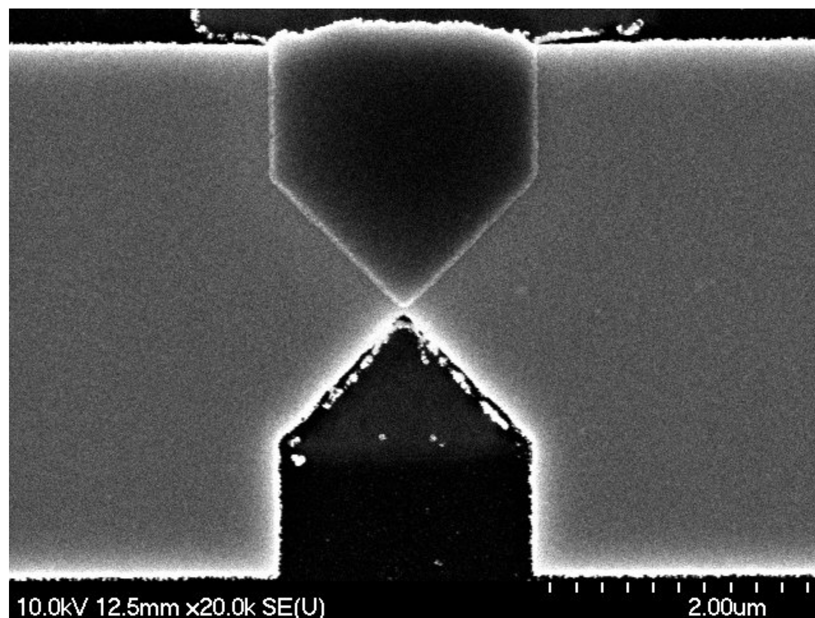

Figure 4.23: A nanobridge with an Al mask after the lift-off process, where a piece of Al has not been removed by flushing as shown in the upper part of the image.

It was also found that the standard deviation of the parameters was very small, suggesting that despite the lack of accuracy with the designed parameters that the process is repeatable and can be used to consistently produce large numbers of nanobridges.

Measured Length and Widths of Nanobridges with Electrode Angle 15°

Measured Lengths and Widths of Nanobridges With Varying Electrode Angles

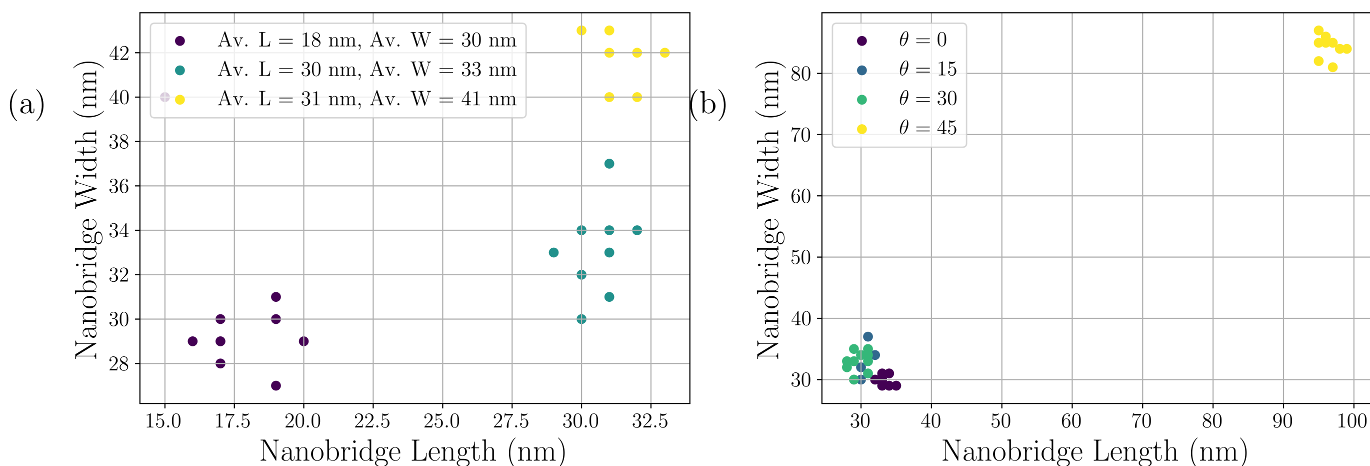

Figure 4.24: (a) Despite not being fabricated to the desired length and width, the nanobridges in each array had physical dimensions which could be used to compare length to width. (b) Comparing like nanobridges with different electrode angles, it was found that the 0°, 15° and 30° nanobridges were similar in size, while the 45° was significantly different and 60° could not be measured. This is an example of the small fabrication tolerance in this single step PMMA method.

The aim of fabricating this sample was to compare length and widths over three arrays, and it is evident from Figure 4.24(a) that the physical measurements of the nanobridges in each array are clustered together, allowing direct comparison between the lengths and widths. In Figure 4.24(b) it can be seen that for arrays with designed identical nanobridge width and length the electrode angle has an effect on the nanobridge physical dimensions. This was observed in several samples, where the physical dimensions of the nanobridge are much greater for the array where the electrode angle was 45°. The nanobridges in this case were much closer to the designed dimensions of width 70 nm and length 100 nm, despite each array being fabricated in the same fabrication run. This effect was consistently observed over several samples, and suggests that the proximitisation of the nanobridge area of the resist during the ebeam lithography causes the overexposure of the PMMA resist before the Al hard mask is added.

4.4.3 Multistep PMMA and ZEP mixed process

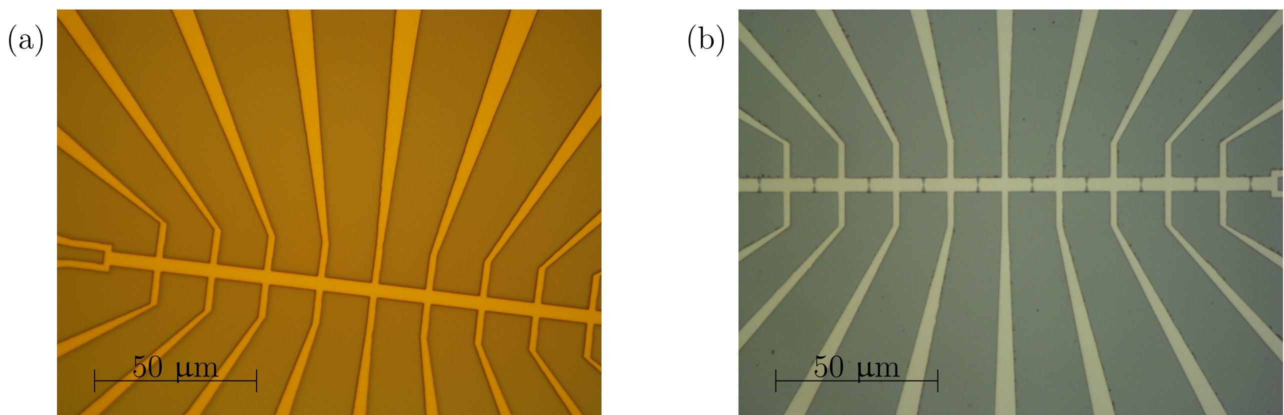

Figure 4.25: (a) An optical microscope image of a ten nanobridge array after the first etch step where the microwire has been etched into the Nb prior to patterning any nanobridges, and (b) the same sample after the nanobridge etch step where the separation between the electrodes can be seen.

To improve the yield and quality of the samples several alternative fabrication options were considered. As the JWNC userbase has extensive knowledge of HSQ resist this was one possible candidate, and can reliably achieve < 5 nm resolution. It was decided against using HSQ due to the additional preparation required prior to ebeam exposure, and the requirement of hazardous chemical etchant and developer. Use of PMMA by either double baking to improve the etch resistance, or to use PMMA as a negative tone resist which can be achieved by increasing the exposure dose. This was not pursued as it would increase the exposure times and become more difficult to remove the PMMA, without being capable of achieving the necessary resolution.

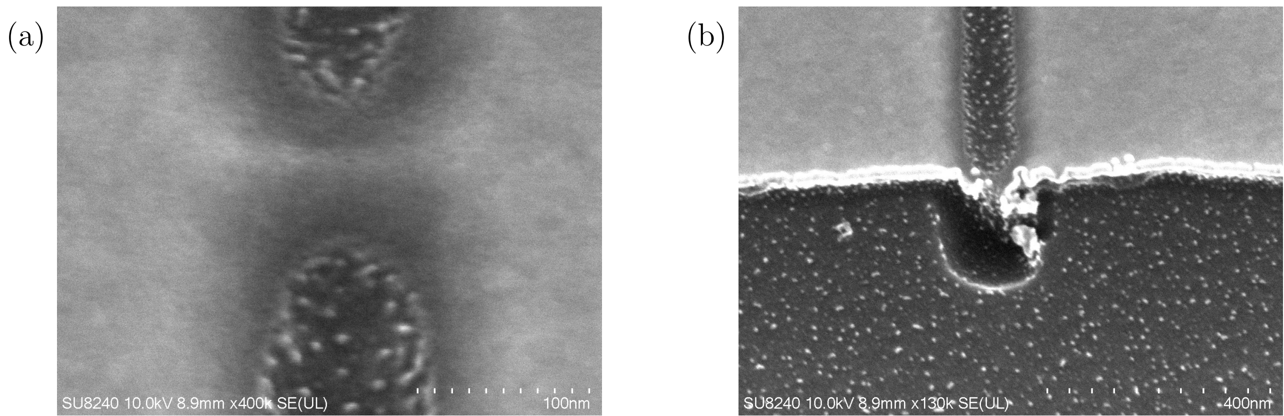

Figure 4.26: An example of a nanobridge fabricated using a multistep ebeam process. In (a) the sidewalls of the nanobridges are seen to be much smoother, and without the poor line edge roughness as seen in the devices fabricated with an Al mask. (b) The end of the trench separating the two electrodes was found to be shorted when the distance between the electrodes was < 150 nm. This was resolved by including a widening of the separation toward the end of the electrodes. An area of the Si substrate at the end of the electrode gap, where the substrate has been etched during both etch steps, however this does not interfere with the operation of the nanobridge.

The method that was chosen was a multi-step ebeam process where the structures which are > 1 μm are produced with lift-off, and the nanobridges are then patterned in a second exposure. This method was developed to make use of the low sensitivity and ease with which PMMA can be removed from the sample, and the precision and high etch resistance of ZEP.

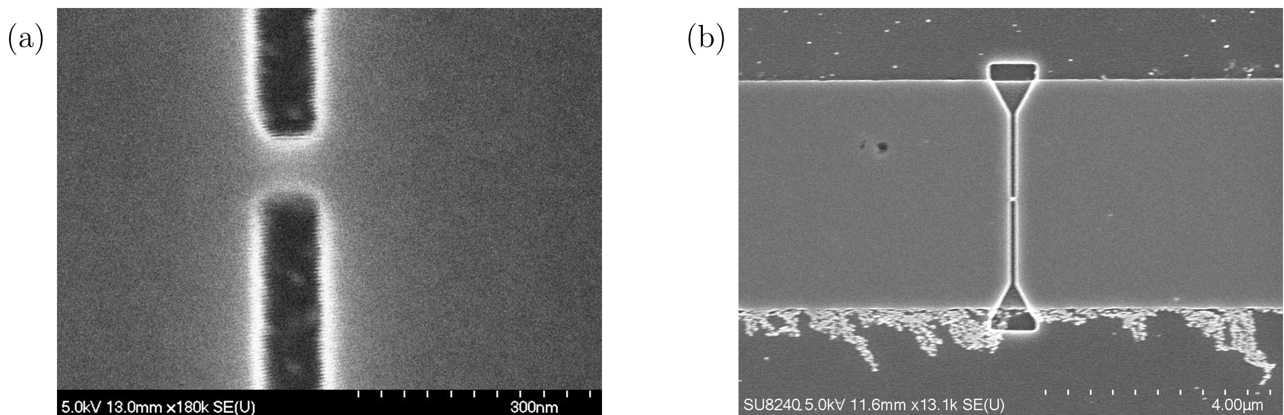

Figure 4.27: (a) A nanobridge with designed width of 60 nm and length of 80 nm, and physical dimensions which approximately match this as measured by SEM. (b) A completed nanobridge, the first ebeam exposure defines the microwire and the second exposure used to define the nanobridge within the microwire can clearly be seen. Some additional residual material from the first etch step can also be seen, which does not affect the behaviour of the nanobridge.

The first ebeam step is used to pattern the microwire structures and the contact pads, which uses PMMA bilayer as the ebeam resist and an Al hard mask, an optical microscope image of the completed microwire array is shown in Figure 4.25(a). A layer of ZEP is then spun onto the sample and a second ebeam step is used to expose the nanobridge pattern, a completed sample where the nanobridges have been etched into the sample is shown in Figure 4.25(b). After development this was

then etched to produce the nanobridge and the ZEP was removed from the sample. This resulted in a nanobridge with physical dimensions within ±5 nm of the design value, and with much smoother edges than was achieved with the single step PMMA and Al process, as shown in 4.26.

It was noted that this sample contains sloped sidewall in the Nb, though to be a result of the ZEP slope transferring into the Nb. At the edges of the microwire the nanobridges which had parallel electrodes often had a short created by material not fully removed by the etching process, which can be seen in Figure 4.26(b), although this was rectified by simply including a widening gap at the edge, an example of which can be seen in Figure 4.27(b).

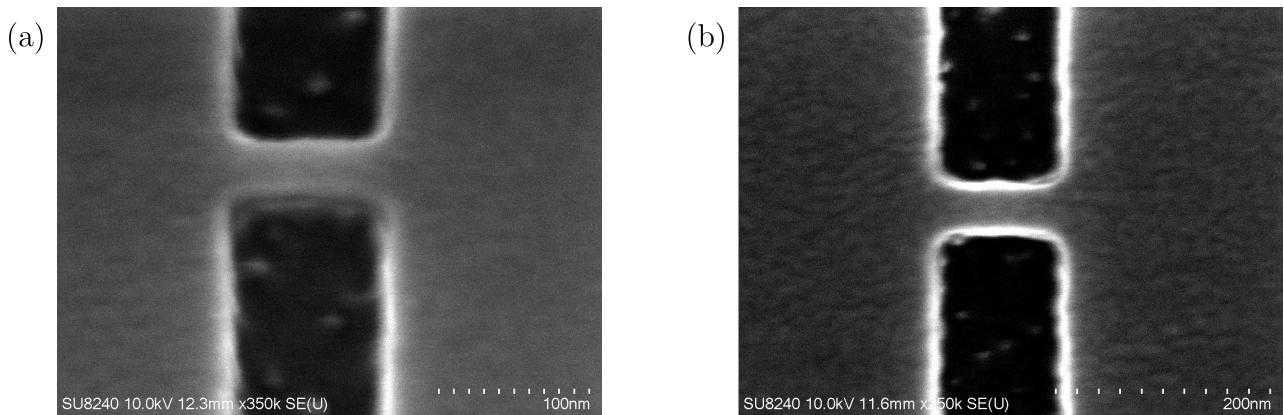

Figure 4.28: (a) An example of a nanobridge designed with width 50 nm and length 100 nm, which is tilted at 30° to show the clean sidewall of the nanobridge. (b) A similar nanobridge, fabricated on the same sample with a width 50 nm and length 110 nm, showing the control this fabrication process has over the physical dimensions.

After measuring the resist thickness and updating the PSF data used in the proximity effect correction and refining the ZEP exposure step dose it was found that the nanobridges could be fabricated with clean edges, without significant sloped sidewalls and with improved LER, as shown in Figure 4.28.

As the thickness of the ZEP was reduced it was no longer capable of providing an etch mask for the thickest films, $d \sim 150$ nm. It was also found that the sample could be improved by including a Cl etch step to etch through the Al, before removing the ZEP and etching the Nb. The Al can then be removed with the standard Al wet etch, as shown in Figure 4.27. A well-defined nanobridge with a sample yield close to 100 %, an example of which is shown in Figure 4.27. A detailed list of the fabrication steps used in this process can be found in Appendix A.2.

Measuring the physical dimensions of the nanobridges, it becomes clear that this fabrication process can produce nanobridges with great consistency and accuracy. Shown in Figure 4.29 are the differences between the designed and measured physical parameters of a sample on which 40 nanobridges were fabricated, with a variety of physical dimensions. Although the measurements of these nanobridges were made using SEM, where the spot size is $\sim 5 - 10$ nm, it is clear that the

multistep fabrication process is capable of fabricating nanobridges with physical dimensions within ~ 10 nm of the designed dimensions.

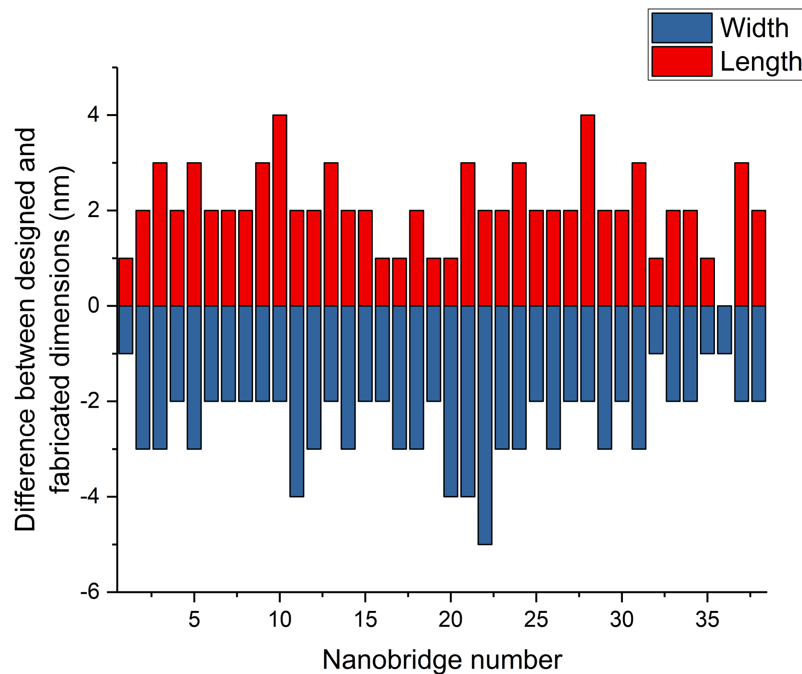

Figure 4.29: Differences between the physical and measured dimensions of the nanobridge fall within the measuring resolution of the SEM. The lengths are consistently greater, and widths consistently smaller than designed, which is a frequently seen result of the proximitisation of resist, as the dimensions of the electrode gap are increased. This can be further reduced through optimisation of the fabrication parameters.

On this sample there were two nanobridges which were completely etched through, which had a designed bridge width of 10 nm, however the adjacent nanobridges with width 20 nm being successfully fabricated. This is likely caused by the sloped sidewall effect seen in ZEP resists, which increases with the ebeam acceleration voltage. The sloped sidewalls on each side of the nanobridge can overlap and cause a reduction of the thickness of the resist on the nanobridge. During the etch process this can cause this resist to become completely removed and begin to etch the nanobridge area. To resolve this either the parameters of the ebeam lithography step used to pattern the nanobridges could be optimised, or by using a resist for the second lithography step to one which does not exhibit the same sloping sidewall effects.

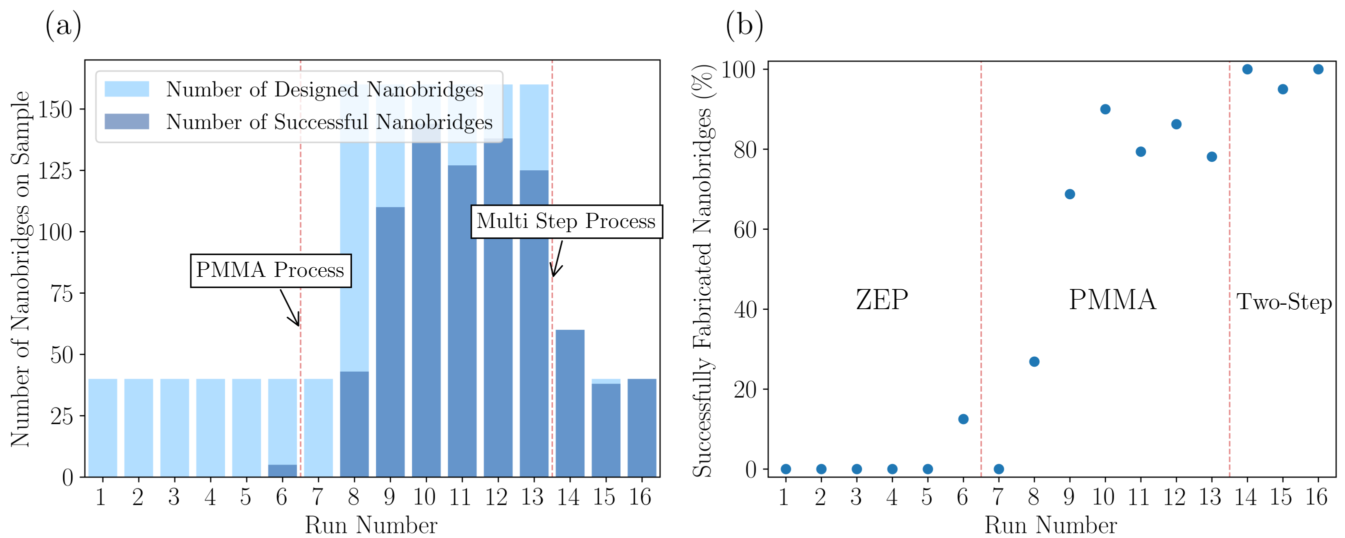

Figure 4.30: (a) The number of nanobridges fabricated compared to the number of nanobridges which were designed on the sample is shown. Early in the project, while attempting to use a single step ebeam process with ZEP as the resist there were almost no nanobridges successfully fabricated. The single step PMMA process improved the nanobridge yield, but issues with the lift-off process resulted in losses of $\sim$ 10 - 20 %. In the final three samples, all fabricated with the multistep PMMA and ZEP process it can be seen that only two of 120 nanobridges were not successfully fabricated, which was due to the small bridge width. (b) It can be seen the best performance of the single step PMMA process yielded $\sim$ 90 % of the nanobridges successfully fabricated, in the multistep PMMA and ZEP process the fabrication yield is approaching 100 %.

It can be seen in Figure 4.30(a) that the yield of fabrication is now approaching 100 %. In Figure 4.30(b) the percentage of successfully fabricated bridges in each fabrication process is shown. In the single step ZEP process the nanobridges were consistently etched through due to the proximity effect. On changing to a single step ebeam process, using PMMA as the ebeam resist and an Al hard mask for etching, the fabrication yield was improved, although due to the issues outlined the maximum yield achieved was in the range of 90 %. Samples fabricated with the multistep fabrication process show yield close to 100 %, in nanobridges which are consistent and more accurate than in previous processes.

Chapter 5

Results

This section describes the results obtained from the measurement of nanobridges over the course of the project. First, an overview of the experimental set up and measurement techniques used is provided. This is followed by the measurement results, which is divided into two main parts. The first of these describes the results of measurements made to investigate the engineering challenges in reliably fabricating large numbers of nanobridges for use in SFQ electronics. This is composed of an evaluation of the electronics properties and switching currents of nanobridges, and the nature of the hysteresis seen in nanobridges. The second section describes the physics of the nanobridge for use as an SFQ element, which comprises an investigation into the effect of low voltage noise on the IVC of the nanobridge, followed by evidence of the Josephson effect and derivation of the nanobridge CPR. This section concludes with JSim simulations of SFQ circuitry which uses Josephson junctions where the CPR has been modified to match that derived from experimental measurements of Nb nanobridges.

5.1 Experimental Setups

Experimental measurements were undertaken between the National Physical Laboratory (NPL) and the University of Glasgow (UoG). In this section are described the experimental set ups and basic principles of measurement techniques used in this project.

5.1.1 Current Voltage Characteristic Measurements

To electrically characterise the nanobridges measurements of the IVC were conducted at NPL. The samples were cooled in a He dip dewar with a base temperature of 4.2 K, and could be varied by lifting the probe into the He vapour for $T > 4.2$ K and maintained with a PID controller. A schematic of the measurement set up, shown in Figure 5.1, shows how the current is supplied across the entire

array by an optically isolated measurement unit, which was designed at NPL for use in high precision metrology [144].

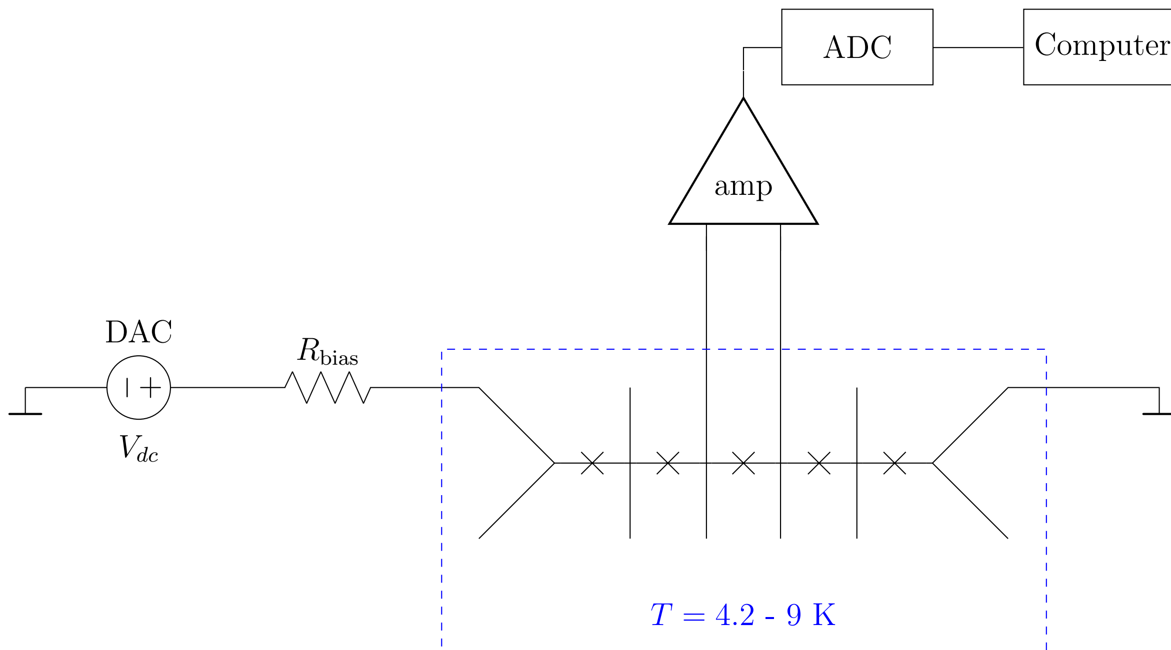

Figure 5.1: Measurement setup for electrical characterisation of nanobridges, current is supplied by the NPL DAC and an in-series bias resistor. The sample is bonded in such a way to allow the current to pass through the entire array and the IVC for each is produced by measuring the voltage across individual nanobridges, which are represented by the barrier symbol.

This unit provided a bias voltage in the range of −10 V to +10 V, and includes a variety of resistors which can be used to set a suitable bias current range. The voltage was measured across each nanobridge individually, and amplified at room temperature by a Stanford Research Systems SR560 Low-noise voltage preamplifier and then recorded by computer via an NPL analogue to digital converter (ADC). The measurement was controlled and the data recorded by LabView control software.

5.1.1.1 Current Voltage Measurements with RF Bias

To measure the response of the Josephson junction in the presence of an RF bias, a signal generator was connected to the experimental set up shown in Figure 5.1. The RF signal was supplied to the sample through a coaxial cable which has an impedance of 50 Ω, which was wirebonded to the sample onto the contact used to supply DC current.

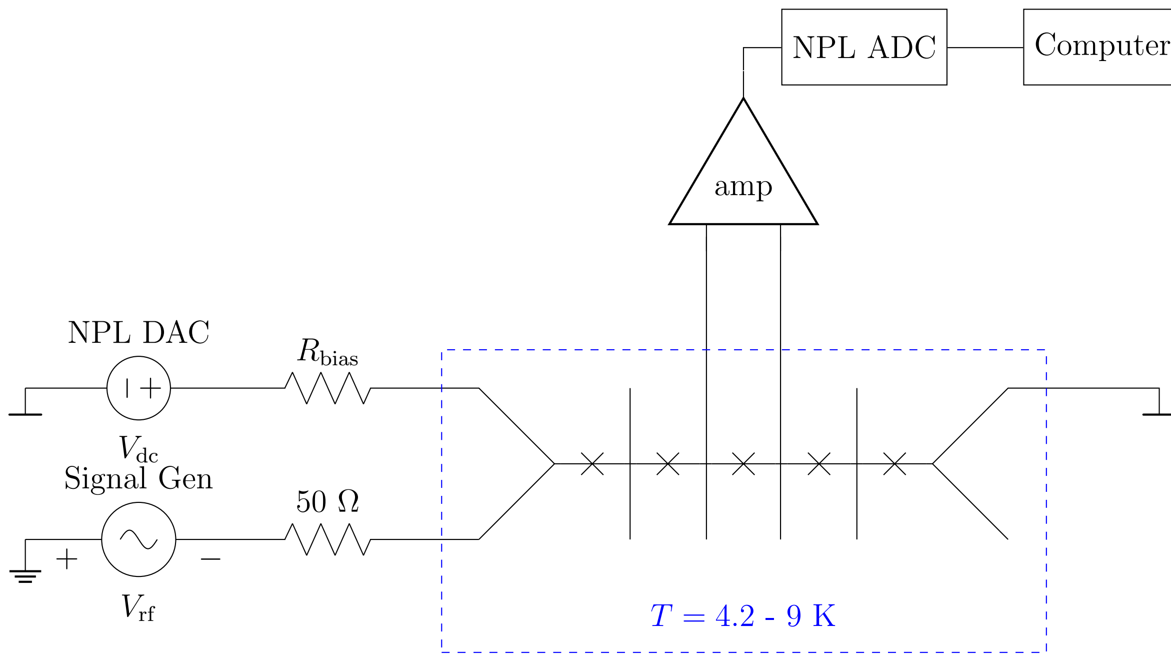

Figure 5.2: A schematic of the measurement set up used to measure the IVC of the nanobridges under RF irradiation. The RF line was terminated on the sample with a 50 Ω impedance, and the nanobridges were then wirebonded in series to provide the RF bias.

The signal generators used over the course of this project had a maximum frequency of 20 GHz. The RF properties of the circuit were not optimised and the attenuation of the line was not considered important. The response of the nanobridge during a sweep of the frequencies was used to calibrate the frequency used. It was found that at f = 20 GHz the nanobridges showed a suitable response in the nanobridge and that this setup provided a suitable RF bias.

5.1.2 Switching Current Statistics Measurements

The variance of switching currents became so small at lower temperature that the measurement resolution of the NPL DAC became comparable to the magnitude of the difference between the switching current of the nanobridges. In addition, measuring a complete IVC of the nanobridge was a time-consuming process, both in the length of time to complete the current switch and to set up the measurement system to measure each nanobridge, which required each cable to be manually transferred between the connections of the breakout box.

To overcome these issues a measurement was designed to increase the number of switching events and determine the probability distribution of the switching event. The schematic of the experimental set up is shown in Figure 5.3. The experiment is timed by a 10 MHz timing pulse from the PID temperature controller, to eliminate crosstalk between the nanobridge measurement and the heater and thermometer. The timing pulse is received by a Zurich Instruments HD Arbitrary Waveform Generator (AWG), and two waveforms are output simultaneously: a square pulse which starts the

timer of a Stanford Research Systems SR620 Time Interval Counter, and a linear voltage ramp which is sent to the bias resistor R_B to bias the device. The bias current is passed through a Data Proof 160A Low Thermal Scanner which is used to switch the current between each nanobridge, and the voltage across the entire array is measured through a Stanford Research Systems SR560 Low-noise Voltage Preamplifier. The nanobridge is driven by the bias current until it switches to the normal state, at which point the bias current produces a voltage corresponding to $V = I_{\text{bias}}R_{\text{n}}$ which is used to turn off the ramping bias current to prevent the nanobridge from heating, and to stop the counter.

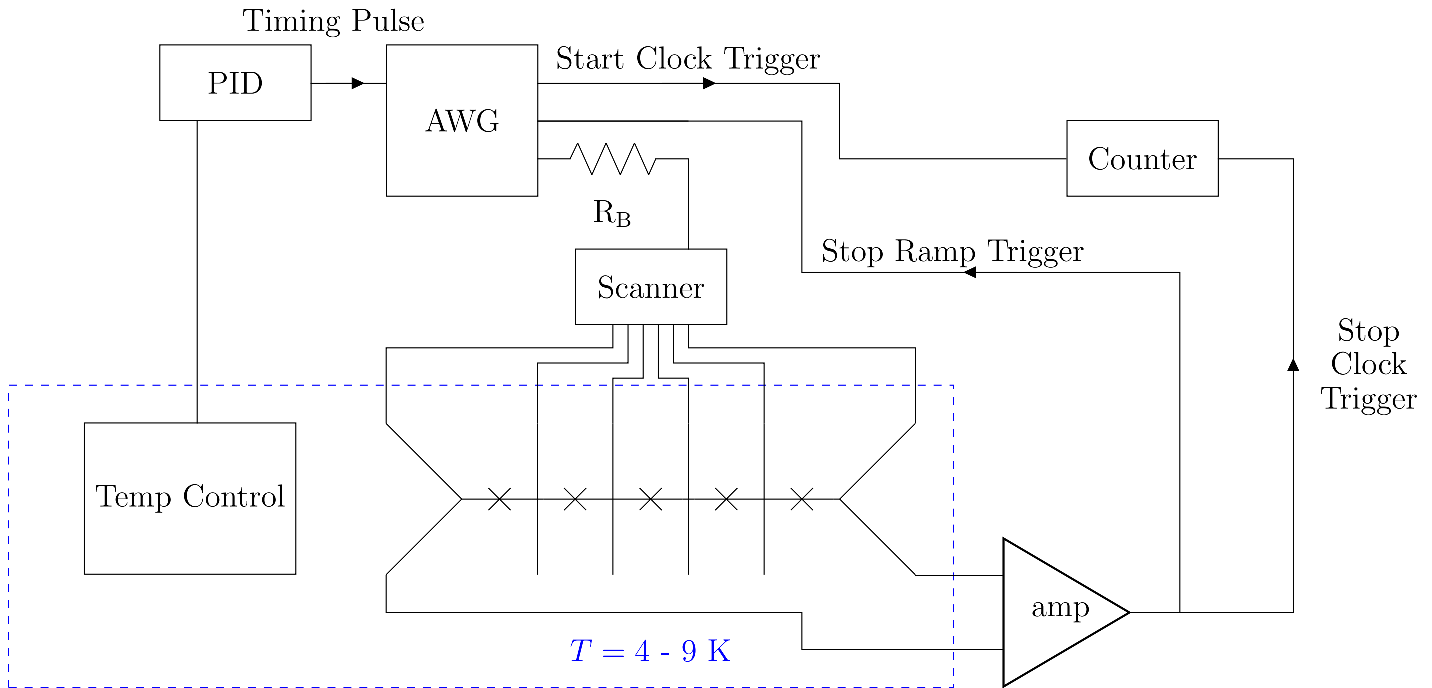

Figure 5.3: The measurement setup for measuring the switching currents of a nanobridge array. The bias is provided by an AWG, which also produces a concurrent pulse to trigger the start of the timer. The ramped bias current passes through the bias resistor R_B until the device is switched into the resistive state. The amplified voltage pulse from the nanobridge is used to stop the AWG and the timer. The time on the counter corresponds to the switching current due to the linearly ramped bias current.

The time measured by the counter was then used to calculate the current at which the nanobridge switching from the superconducting to normal state, using the equation

$$I_c = \frac{\delta t V_{\text{ramp}}}{R_B} \, , \tag{5.1}$$

where δt is the time between the start counter pulse and the stop trigger from the nanobridge, V_{ramp} is the linear ramp rate of the bias voltage source and R_B is the bias resistance.

5.1.3 Experimental Setup at NPL

Measurements at NPL were conducted using a He dip dewar. Samples were fixed to a sample mount which was fixed in place onto a He dip probe, and a cryoperm was used to provide the sample with magnetic shielding. The probe was lowered into the dewar which was partially filled with liquid He to cool the sample to a temperature of 4.2 K. The He vapour above the liquid has a temperature gradient from 4.2 K to room temperature, as shown in Figure 5.4, and for temperatures of 4.2 K $< T < T_c$ the sample was raised above the liquid He into the vapour, the probe was then fixed in place with the clamp and a PID controlled heater was used to prevent temperature drift during the measurement. This allowed temperature control to within ±0.1 K.

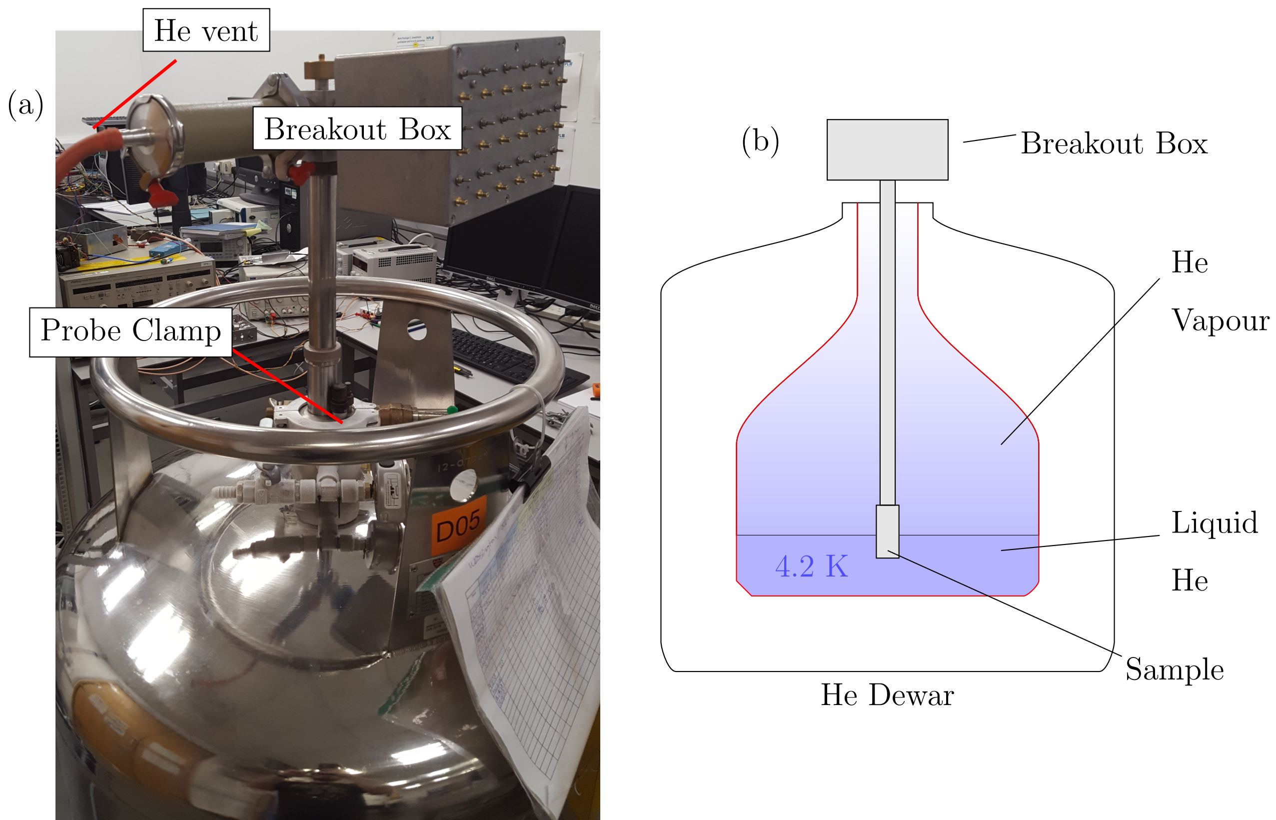

Figure 5.4: (a) A He dip dewar with a probe inserted, the electrical connections to the sample are fed through the probe, which also allows the He gas to vent. The probe is held in place by a probe clamp. (b) A schematic of the Helium dip dewar, showing the sample at the bottom of the probe which can reach the He. The He vapour provides a gradient in temperature from 4.2 K just above the liquid He to room temperature at the neck of the dewar.

The sample was mounted onto a printed circuit board (PCB), shown in Figure 5.5, with an isolated metal area for the sample to be mounted to improve the thermal contact between the sample and heater. Once fixed in place with silver paste, each sample was electrically connected to contact pads with Al wire with an ultrasonic wirebonder, which were connected to the pins of the sample mount.

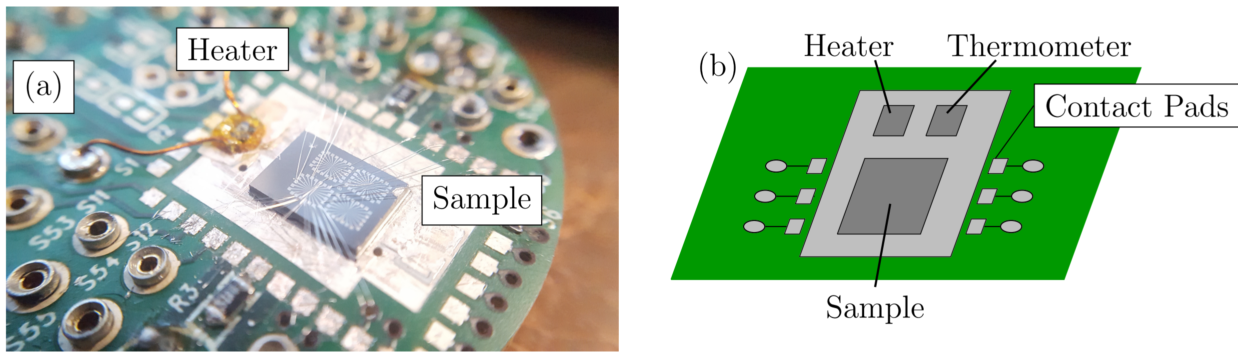

Figure 5.5: An image of a sample mount with a nanobridge sample fixed in place. The Al wirebonds connecting the sample to the measurement setup can be seen. A 1 kΩ resistor is used to heat the sample, the temperature is measured by thermometer which provides feedback to a PID which controls the current supply to the heater.

The pins were connected with manganin [145] wire to the room temperature breakout box via a D-connector, which allowed for easy removal of the sample holder for mounting samples and wirebonding. The breakout box allowed each line to be connected with a SMA connector, and each line could be independently grounded to reduce the risk of damage to the sample by electrostatic discharge during cooldown or while the experimental setup was modified.

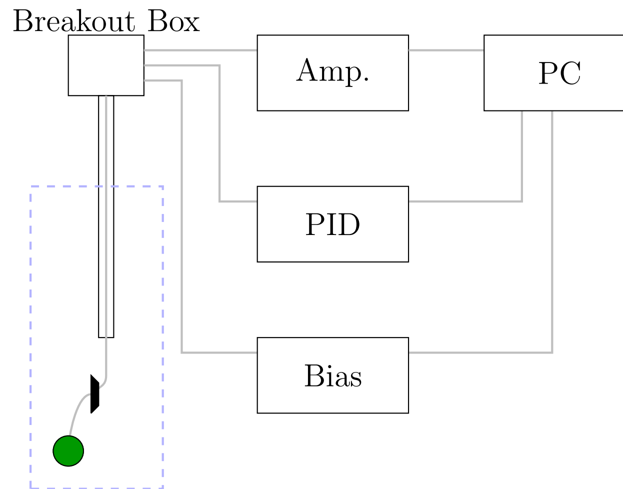

Figure 5.6: A schematic of the measurement setup at NPL. The sample is connected to the probe through a D-connector, which allows the sample to be easily removed for wirebonding. The D-connector is connected to the breakout box through a manganin loom which terminates with SMA connectors which connects to the measurement equipment. The measurement is controlled by a current bias and PID which are controlled by the measurement PC, and an amplifier is used to read the voltages from the device.

The breakout box also included an RF connection which was connected to the sample mount by an SMP connector. The sample was wirebonded such that the central line of the RF coax cable was connected to the same on-chip contact as the DC current in, and the RF ground line to the same contact as the DC current out. The RF ground line of the sample was connected to the ground of the coax cable.

Data was recorded using LabView software on a PC which was connected to the measurement setup. The temperature control was maintained using a PID to supply a current to the heater, which was controlled by a LabView script written by Dr. George Long. A schematic of the measurement setup is shown in Figure 5.6.

5.1.4 Experimental Set Up at University of Glasgow

Low temperature measurements were undertaken at the University of Glasgow using a cryogen-free refrigeration system. Cooling power is provided by a Sumitomo RDK101D cold head and an air-cooled HC-4A Zephyr compressor. Components for radiation shielding, thermal anchoring of the system and flanges for electrical feedthroughs composing the cryostat body were designed and machined at the University of Glasgow. The cryostat can reach a base temperature of 2.2 K. The cold-head is housed in a 34 litre vacuum can which is pumped to a pressure in the range of 10^{-5} mbar. The vacuum is pumped by an Adixen ATP80 turbo molecular pump, backed by an ACP15 Roots roughing pump, and the pumping station also contains a He leak detector system which can be used to check the vacuum seals of the cryostat.

The original design of the cryostat included eight coaxial connections, with SMA connections at room temperature and SMP connections to the sample. To allow the refrigerator to measure multiple nanobridge devices in each cooldown a Fischer connector with eleven manganin DC lines was added by the author. The DC lines terminated in a D-connector on the 2 K stage of the cryostat, which allowed the sample mount to be easily removed to allow the sample to be fixed in place and wirebonded.

With the addition of the Fischer connector to increase the number of DC lines two of the coaxial cables were re-purposed to allow the addition of a heater and RF line. Heating is provided by a 1 kΩ high power resistor which is fixed in place on the 2 K stage, and capable of heating the lower stage to $\sim$ 20 K. A Keithley 238 Source-Measure Unit was used to provide the heater with up to 50 mA of current, which produced 2.5 W of power. The 2 K stage of the cryostat was then warmed by Joule heating, and the thermometer of this stage used for temperature control. The previously installed coaxial cables were unsuitable for RF transmission due to the poor bandwidth. These were replaced with an RF line which was composed of solid steel RF cables, with $\sim$ 80 dB loss, and was connected to the sample with an SMP connector.

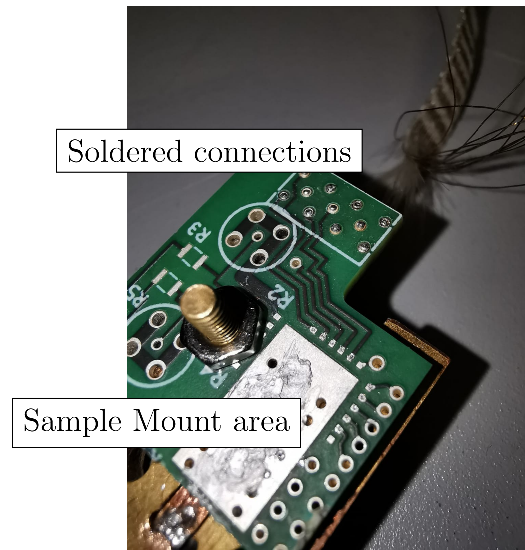

Figure 5.7: The sample mount used in the cryogen free refrigeration system, which was a modified PCB designed at NPL for low temperature measurements fixed to a sample mount used for SNSPD measurements designed and fabricated at UoG. The bolt which fixed the PCB sample mount to the copper mounting plate can be seen. The RF connection provided by a SMP connection, is also shown. The sample was mounted to minimise the length of the RF wirebond.

The sample mount was a modified PCB developed by Dr. Jonathan Williams and Dr. Connor Shelly at NPL, shown in Figure 5.7. The PCB was fixed to a copper sample holder used for low temperature testing of SNSPDs, held in place by a bolt and connected with thermal paste to ensure thermal contact between the cryocooler and the sample.

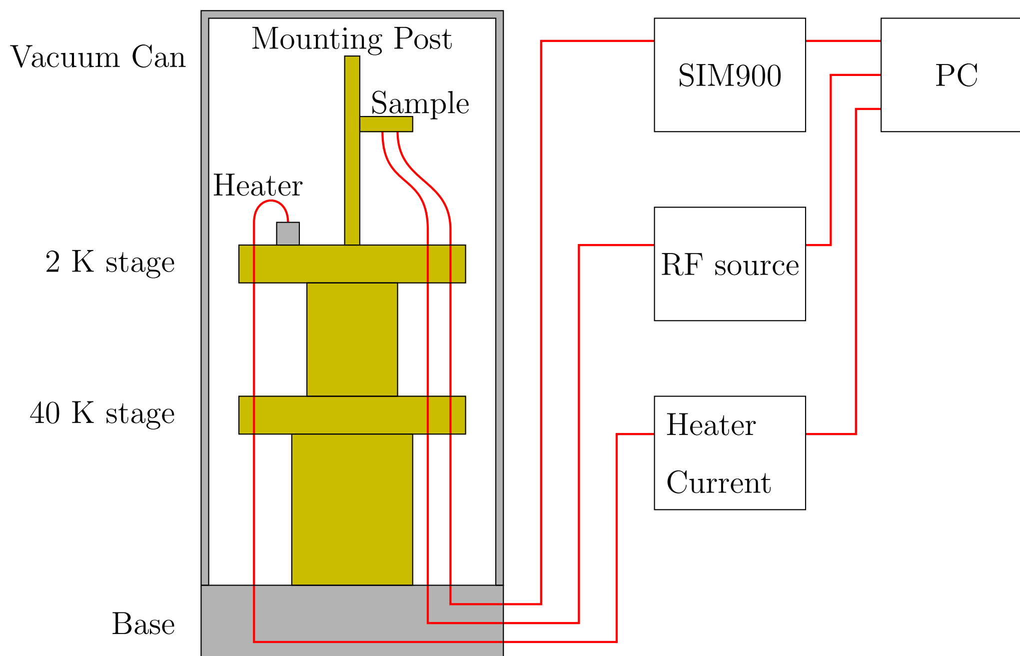

Figure 5.8: A schematic of the measurement set up at UoG. The sample is placed in thermal contact with a 2 K mounting rod, and heat control is provided by a 1 kΩ resistor on the upper stage. The heater current source, RF source and SIM900 used to control the DC measurements are each connected to the controlling PC, where control software is written in Python by the author.

The cryostat was controlled by software written by the author. Measurements were undertaken

using a Stanford Research Systems Simple Instrumentation Model (SIM900) mainframe fitted with a SIM928 Isolated Voltage Source, a SIM 970 Quad Voltmeter and a SIM922 Diode Temperature Monitor. Where required a Stanford Research Systems SR560 Low-noise voltage preamplifier was used to amplify the voltage which was measured across each of the nanobridges.

The temperature was set by monitoring the temperature and controlling the current from the Keithley 238 Source-Measure Unit. The temperature was found to oscillate with a frequency of ~ 1 Hz due to the pumping of the cold-head. To compensate for this a Python script was written to record the temperature over a time period of 30 s and calculate the oscillation. This variation was then applied to the heater supply current which reduced the temperature oscillations.

The automation software first sets the temperature, which must be stable within a range of ± 0.1 K for 2 s. Next, the IVC measurement is taken. First the system measures through the current range with a small number of data points to give rough measurement. This measurement is then checked by the software to ensure that a normal state resistance and the transitions between normal state and superconducting state can be detected. If this is true the IVC is then measured a second time in greater detail, with the number of data points around the expected values of the transitions. Once the measurement is completed the desired temperature can be incremented and the process is repeated. Once the maximum temperature is reached the heater and bias current are turned off and the user is notified that the measurement is complete.

5.2 Nanobridge Scale Up and Repeatability

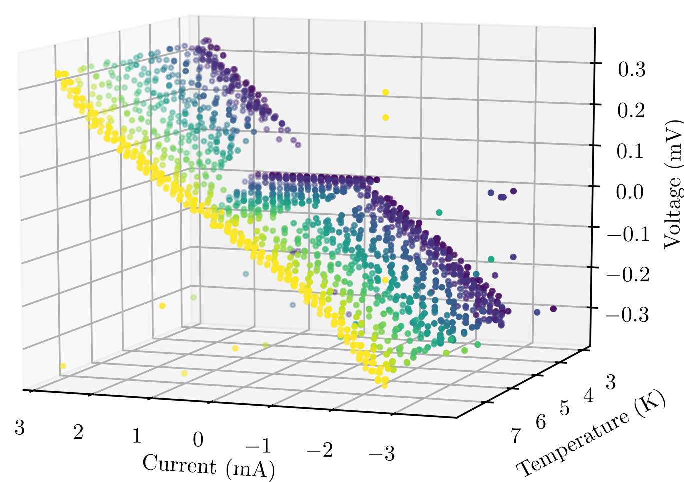

Figure 5.9: Sweeping the current from −3 mA to +3 mA it can be seen that the nanobridge transitions to the superconducting state at the return current, I_R and returns to the normal state once the value of I_c is reached. As the temperature is reduced the value of both I_R and I_c increase at different rates, which can result in hysteretic behaviour.

To realise large scale SFQ circuits requires the capability to consistently produce Josephson junctions where the junction critical current, I_c and normal state resistance, R_n, are fabricated to the same specifications each time.

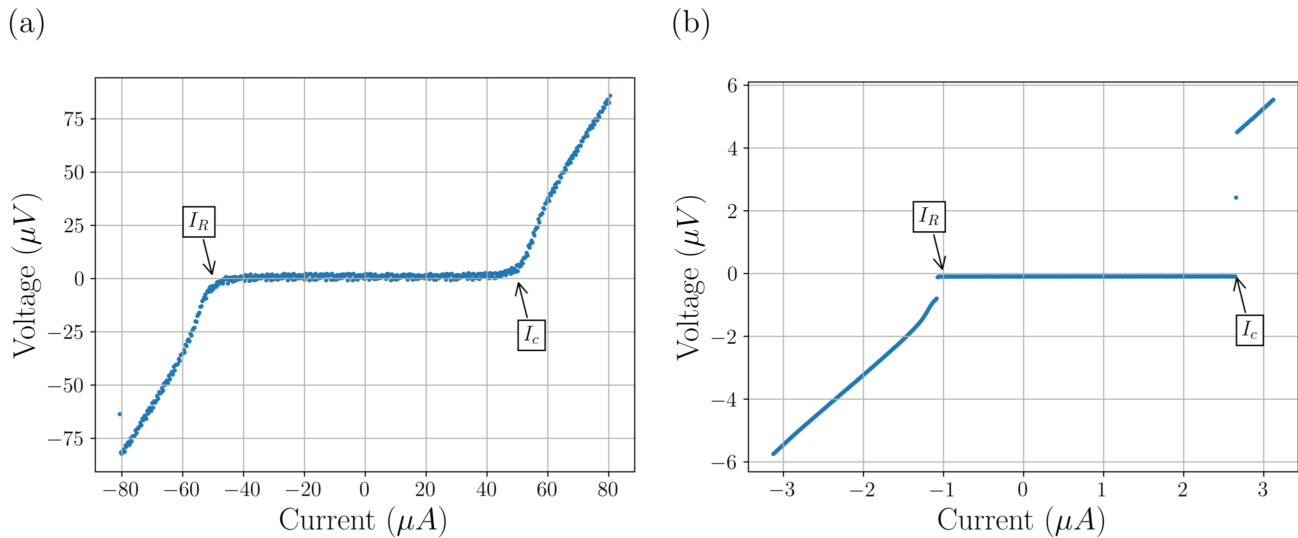

Figure 5.10: Two examples of IVC of the same nanobridge at different temperatures, where T_c = 8.65 K. (a) The non-hysteretic behaviour which can be seen at temperature 8.6 K. (b) When the temperature is reduced to 7.2 K the hysteretic behaviour of the nanobridge can be seen, where $I_R < I_c$.

This requires Josephson junctions which operate in the non-hysteretic regime, unlike the latching Josephson logic which was developed in the 1970s [94]. In STJs this is achieved by the addition of a shunt resistor which reduces the Stewart-McCumber parameter to operate in the overdamped regime, $\beta_c < 1$. Due to their small intrinsic capacitance, nanobridges operate in the strongly damped regime where $\beta_c << 1$.

As in all Josephson junctions the IVC of a nanobridge is dependent on temperature, in Figure 5.9 I_c can be seen to increase as T is reduced. At temperatures close to T_c the nanobridge will typically produce a non-hysteretic IVC, and as the temperature is reduced the nanobridge can begin to exhibit hysteretic behaviour. This change from the non-hysteretic to the hysteretic regime occurs at a thermal hysteretic crossover temperature, T_H, which is the temperature below which $I_R < I_c$. Examples of the hysteretic and non-hysteretic IVCs of a single nanobridge are shown in Figure 5.10.

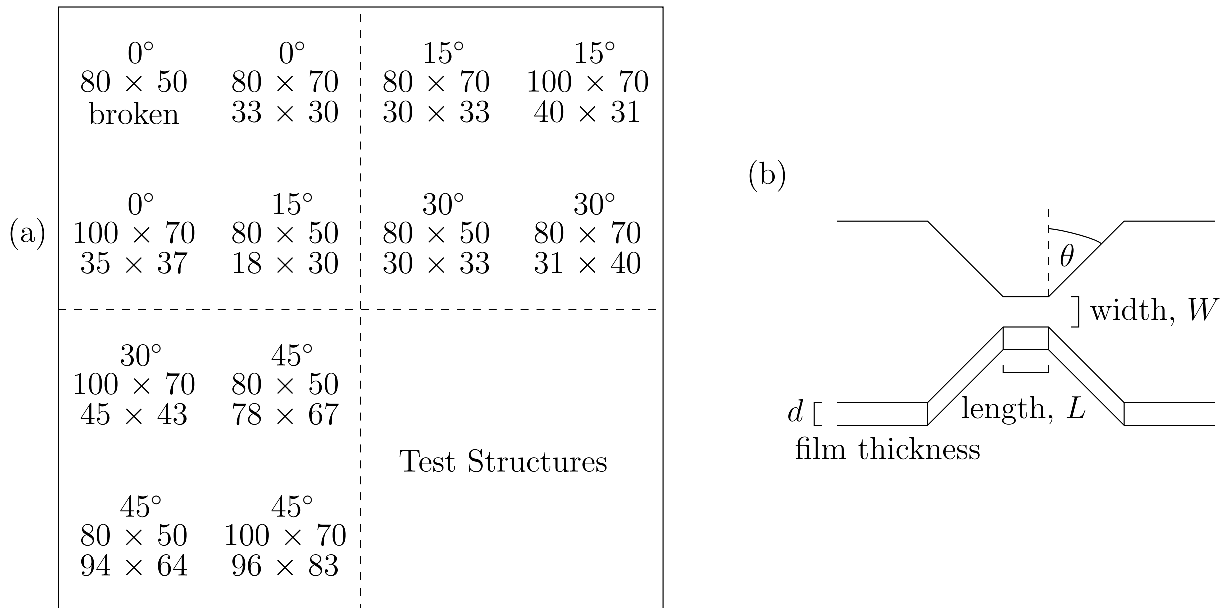

Figure 5.11: The layout of the sample, showing the electrode angle, the designed dimensions and the average physical dimensions of the array in nanometres. Four arrays were placed on each 5 mm × 5 mm segment. The sample was fabricated as a single piece and then cleaved along the dashed lines.

It has been demonstrated in Chapter 4 that the fabrication process developed over the course of the project allows the production of nanobridges with reproducible physical dimensions. This section examines the results of measurements into the repeatability of the fabrication process, followed by an examination of how the physical geometry of the nanobridge can be used to influence the behaviour of the self-consistent thermal hotspot generated in the resistive regime.

To investigate the repeatability of the fabrication process the critical current of identically fabricated nanobridges were measured.

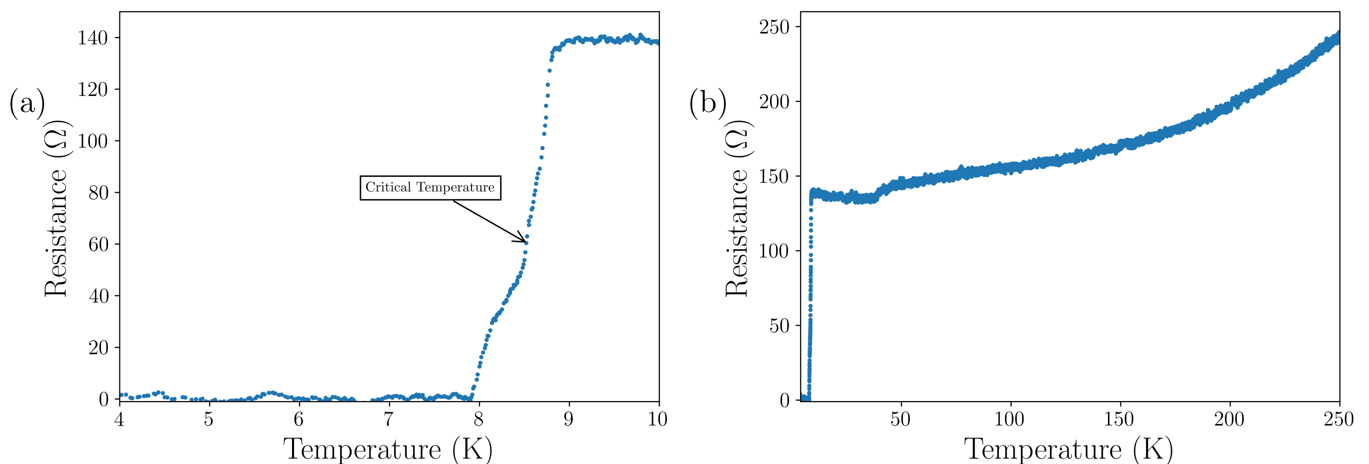

Figure 5.12: Measuring the T_c of the sample it was found that the $T_c \approx 8.6$ K, which was defined as being the point at which the resistance reached $1/2R_n$. R_n is the point at which the gradient of $R(T) \approx 0$, shown here at 140 Ω.

Nanobridge samples were prepared for measurement in arrays of ten identically designed nanobridges,

the physical dimensions and layout of the sample is shown in Figure 5.11. Three arrays were fabricated for angles of the electrode 0° to 45° in increments of 15°. For each angle each array was fabricated with lengths and widths of 80 nm × 50 nm, 80 nm × 70 nm and 100 nm × 70 nm. This allowed a comparison to be made between similar widths and similar lengths of nanobridge.

The film was deposited by DC magnetron sputter deposition, as described in Section 4.1 to a film thickness of 150 nm, the critical temperature of the film was found to be ∼ 8.6 K as shown in Figure 5.12.

5.2.1 Effect of Physical Geometry on Critical Current

The effect of the length and width of the nanobridge is described in Section 3.3.2.1. The nanobridge arrays were designed in such a way that the lengths and widths of arrays could be compared. The average critical current of each array is used to compare between arrays with different physical properties.

The physical dimensions of the nanobridge were measured through different means. The film thickness, d, was measured by a Dektak height profilometer after the etching process. The electrode angle, θ, was measured by measuring the x and y position during SEM inspection, and calculating the angle. Similarly, the nanobridge length and width was measured using the SEM, although the beam spot size is greater than measured variance of the physical dimensions of the nanobridges.

To determine a estimation of the nanobridge critical current the experimentally measured values are fitted to the Bardeen equation [146],

$$I_c(T) = I_c(0)\left[1 - \left(\frac{T}{T_c}\right)^2\right]^{3/2} . \tag{5.2}$$

The values of the nanobridge critical current at $T = 0$ K, $I_c(0)$, and the T_c were used as fitting parameters to determine $I_c(T)$.

5.2.1.1 Nanobridges with $\theta = 0°$

Two arrays of ten nanobridges were fabricated. The arrays had length and width of 33 nm × 30 nm, with $\sigma_L = 1.6$ nm and $\sigma_W = 0.8$nm, and 35 nm × 37 nm with $\sigma_L = 2.1$ nm and $\sigma_W = 3.4$ nm. The third array, which had the smallest designed nanobridge length and width, was damaged during the fabrication process resulting in the loss of all ten nanobridges. The results of measuring the critical current of the nanobridges over the temperature range are shown in Figure 5.13. From each array, nine nanobridges were measured.

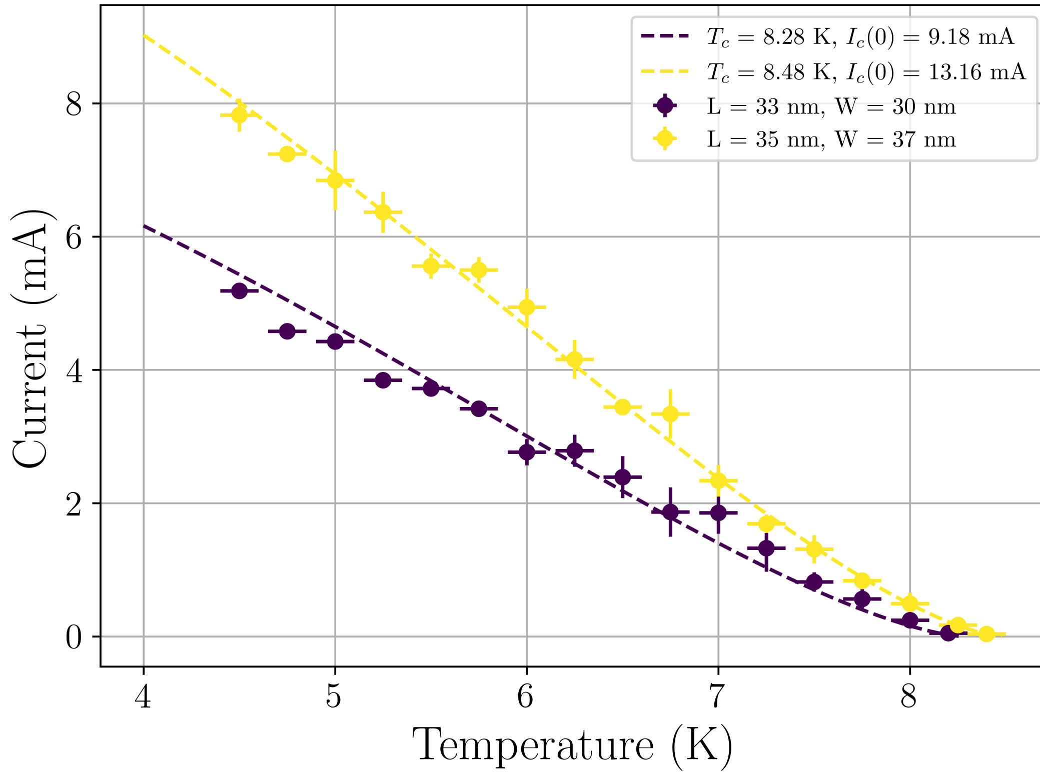

Figure 5.13: The average critical current plotted over a range of temperatures from 4.2 K to T_c of the sample, which occured at 8.5 K for nanobridges with $\theta = 0°$. The Y-axis error bars shown represent the standard deviation in the critical currents across the sample for each temperature,. The dashed line shows the best fit achieved using Equation 5.2, the fitting parameters are shown in the legend.

It can be seen that increasing the width of the nanobridge produces an associated increase in the critical current of the nanobridge for a given temperature. This is consistent with the view of the nanobridge as allowing the current to flow directly, in that increasing the cross sectional area will allow a greater current to flow. For nanobridges with identical W, L and d it has been shown that the critical current will vary over temperature with θ in the way that it varies with length.

5.2.1.2 Nanobridges with $\theta = 15°$

The arrays were fabricated which had $\theta = 15°$. The physical dimensions and standard deviation of each of these arrays, as measured by SEM, can be seen in Table 5.1.

Table 5.1: The average physical dimensions of the nine measured nanobridges for each of the three arrays which were fabricated with $\theta = 15°$.

Average Length (nm)	σ_L (nm)	Average Width (nm)	σ_W (nm)
18	1.5	30	3.4
30	0.8	33	1.8
31	0.8	41	1.2

The physical measurements allow a comparison between the widths and lengths of the nanobridges to be made. The measured average critical current across each of the arrays is shown in Figure 5.14.

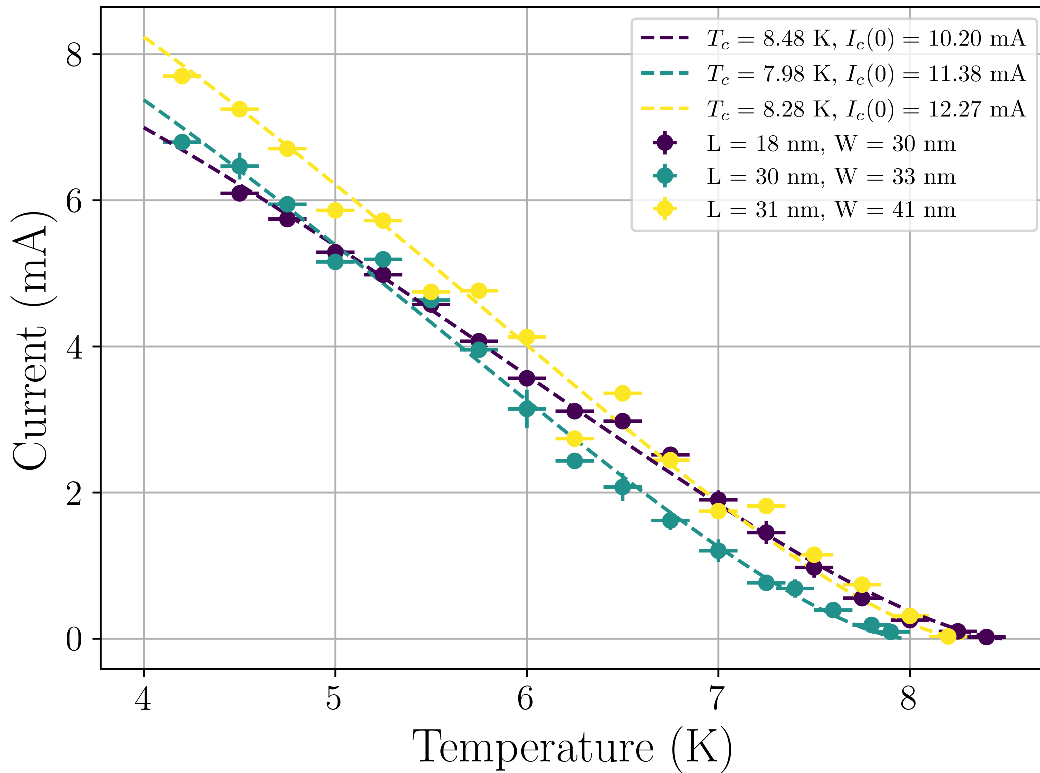

Figure 5.14: The critical current against temperature for arrays with nanobridges fabricated with $\theta = 15°$ over the temperature range 4.2 K to T_c, which occured at $\sim$ 8.4 K. Equation 5.2 was used to determine the values of $I_c(0)$ and T_c, and the fitting parameters used in each case are included in the legend.

Over the temperature range at which the samples were measured it can be seen that the samples with similar widths take similar values of the critical current. The array with L = 31 nm and W = 41 nm was found to have the greatest I_c over the measured temperature range. The array with L = 18 nm and W = 30 nm was found to show a similar T_c, but I_c was increased less rapidly as the temperature was reduced. In the array with L = 30 nm and W = 33 nm the T_c was reduced, but increased at a similar rate to the array with similar width as the temperature was reduced.

The differences in T_c of the samples can be explained by the changing nanobridge physical dimensions. It is expected that the T_c is dependent on the overlapping of Δ from each of the electrodes, which will occur at a higher temperature where the physical distance between them is reduced and the nanobridge length shorter. A greater value of T_c is also expected for nanobridges with a larger cross sectional area, which for nanobridges fabricated in the same film corresponds to a greater width.

The changes in I_c over the measured temperature range suggest that for nanobridges with similar widths the rate of increase with reducing temperature is constant. This can be seen from the shortest nanobridges, which have the greatest T_c and lowest value of $I_c(0)$. This suggests that at temperatures

close to T_c the variation of the coherence length ξ in the nanobridge greatly influences the I_c. As the temperature is reduced and $\xi \to L_{\text{eff}}$, then the cross sectional area begins to dominate the I_c.

5.2.1.3 Nanobridges with $\theta = 30°$

In the nanobridge arrays fabricated with $\theta = 30°$ there were three arrays which were fabricated, with nine nanobridges measured on each array. The physical dimensions of these are shown in Table 5.2.

Table 5.2: The average physical dimensions of each of the three arrays which were fabricated with $\theta = 30°$.

Average Length (nm)	σ_L (nm)	Average Width (nm)	σ_W (nm)
30	1.2	33	1.5
41	2.0	31	1.4
45	1.0	43	1.0

As in the case of the arrays with $\theta = 15°$, there are arrays with lengths which are similar enough that allows direct comparison. The results of measurement of the critical current over the temperature range for these arrays are shown in Figure 5.15.

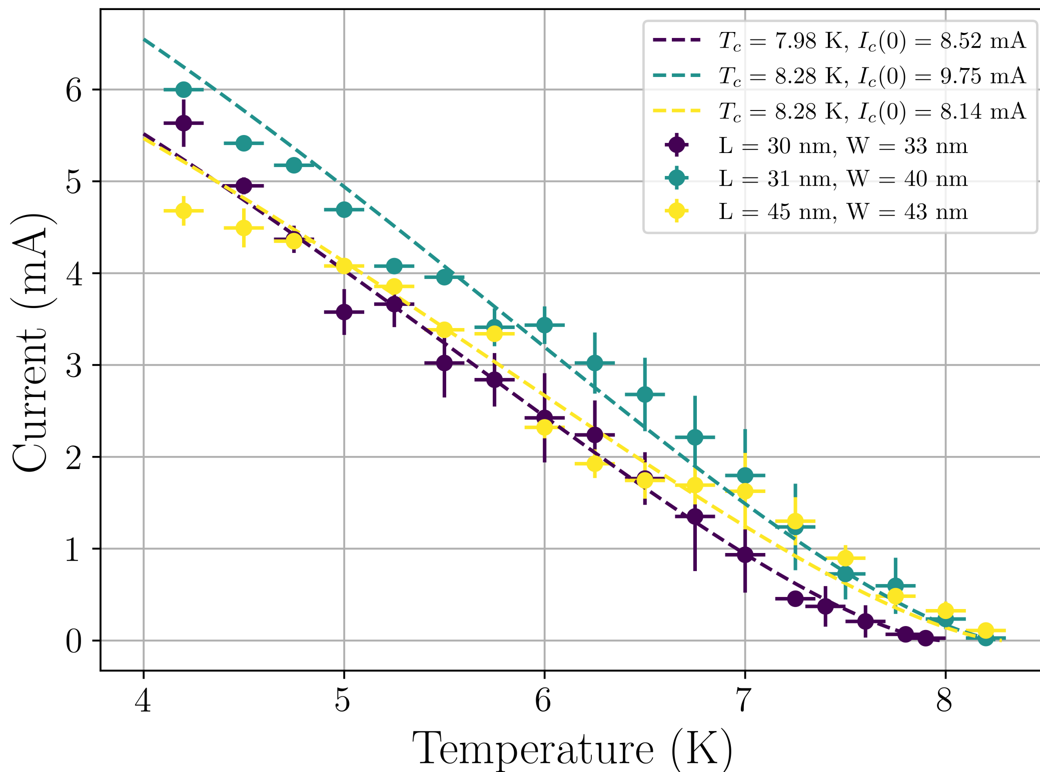

Figure 5.15: The critical current against temperature for nanobridge arrays with $\theta = 30°$,

A similar result is found in this case as was found for the nanobridges with $\theta = 15°$. The value of T_c is similar for the nanobridges with $W \approx 40$ nm, and the shorter nanobridges have a greater

increase in I_c as the temperature is reduced. It can be seen that the increased nanobridge width and reduced nanobridge length results in a greater value of I_c.

5.2.2 Effect of Electrode Angle on Critical Current

The electrode angle influences the behaviour of the nanobridge by changing the effective length, L_{eff}, which is the length scale at which the Josephson behaviour extends into the electrodes. This affects the nanobridge by causing the CPR to deviate from the $I_s = I_c \sin(\varphi)$ found in STJ [147].

In the nanobridges fabricated for this project there were three arrays with comparable nanobridge length and width, which had different values of θ. The results of measuring $I_c(T)$ can be seen in Figure 5.16.

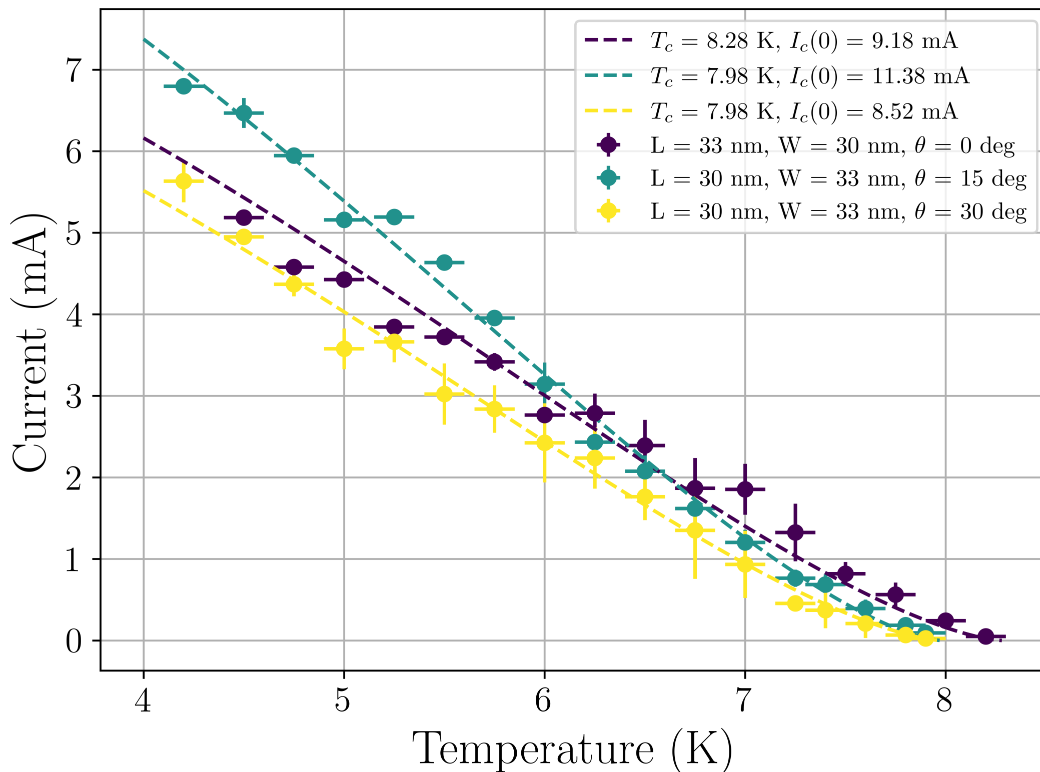

Figure 5.16: Three arrays of nanobridges for which L and W are similar, with varying θ. The average critical current over the temperature range from 4.2 K to $T_c = 8.4$ K is plotted.

It can be seen that in this example, nanobridges with identical physical W and L will diverge as the temperature is reduced. This behaviour is similar to that seen in the previous sections for nanobridges with varying lengths, and is the result of the increasing L_{eff} as θ is increased.

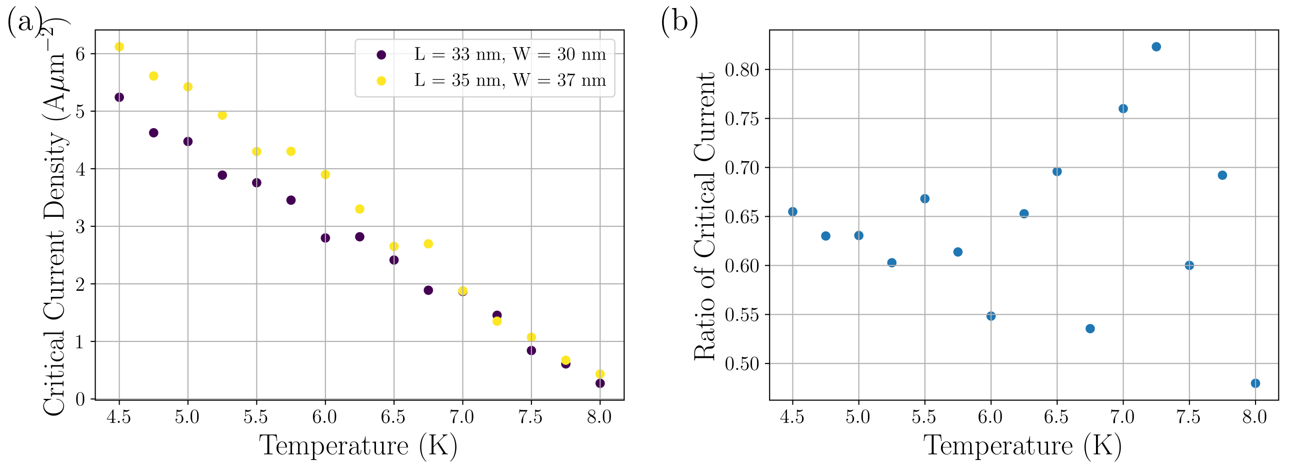

Figure 5.17: (a) The calculated critical current densities in the arrays with nanobridges where $\theta = 0°$, assuming uniform current density throughout the cross sectional area. (b) The ratio of the current densities shown in (a) which at low temperature takes on a value close to the average value, 0.64, where the standard deviation of the I_c in the array is $\sigma = 0.08$.

The behaviour described can be explained due to the physical geometry. For the width, the current will flow in one direction through the nanobridge which is determined primarily by the cross-sectional area. This is not a linear process, as demonstrated by the critical current density for the two arrays with $\theta = 0°$ shown in Figure 5.17, as this is influenced by the magnetic penetration depth λ. However, over a range of temperature two similar cross-sectional areas which can be considered to have the same rate of change in the critical current, regardless of the other physical parameters. As the nanobridge operates in the regime $W < \lambda(T)$, it is expected that this will vary linearly, as shown in Figure 5.17.

The effect of L on the critical current of the nanobridge is dependent on the ratio of $L/\xi(T)$ [155]. It can be seen then how as the temperature varies the rate at which the critical current changes depends on the length of the nanobridge. As described in Section 3.3.2 for bridges where the length is $L/\xi(T) \lesssim 3.49$, the rate at which I_c is increased as the temperature is reduced is much less than for short nanobridges. At low temperature it can be expected that nanobridges with varying L will show approximately the same value of I_c.

Where the electrode angle was varied, while physical length was similar, the same phenomena occured for L_{eff}. Nanobridges which have greater L_{eff} were found to have smaller values of I_c, at $T \lesssim T_c$ the critical currents in both cases became similar as $L/\xi(T)$ becomes large.

It has been shown that L, W and θ influence the critical current of the nanobridge. With the level of control of physical parameters due to the fabrication process, as shown in Chapter 4, the nanobridge critical current can be tuned to the required value for a given operating temperature. The critical current was found to vary approximately linearly with nanobridge W, but not wth L.

5.2.3 Comparison with Theoretical Models for Critical Current

There are three theoretical models which can be used to describe the behaviour of weak links as described in Section 3.3.2. The Ambegaokar-Baratoff (AB) model [33] is based on the theoretical description of the STJ, while the Kulik-Omelyanchuk I (KO-I) [112] and Kulik-Omelyanchuk II (KO-II) [113] describe weak links in the dirty case and clean case, respectively.

The experimentally obtained data for the nanobridge arrays where $\theta = 15°$ is plotted with the calculated values for each of the AB, KO-I and KO-II models in Figure 5.18.

It was found that the calculated values for each of the three theories does not describe the critical current in nanobridges.

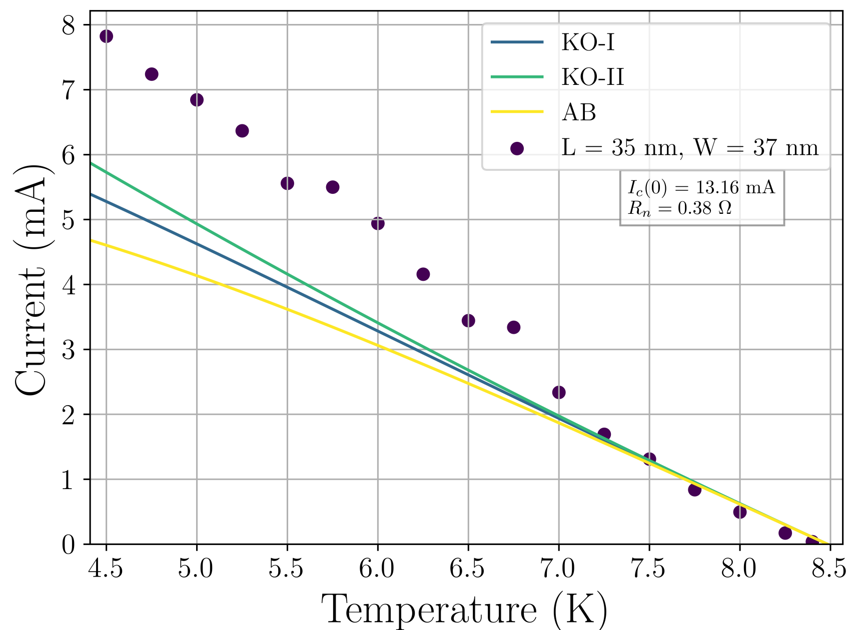

Figure 5.18: Fitting the measured critical current for an array with d = 150 nm, $\theta = 15°$, L = 18 nm and W = 30 nm to the calculated theoretical values for AB, KO-I and KO-II. The fitting parameters used are shown in the legend, $I_c(0)$ was found by fitting Equation 5.2, while R_n was determined from the measured IVC of the nanobridge.

The AB model uses the theoretical description of the STJ, and least accurately fits the experimentally obtained data. The KO-I and KO-II models require that order parameter variation is restricted to the physical dimensions of the bridge, while in nanobridges the order parameter variation will extend beyond the physical limits of a the nanobridge into the surrounding electrodes. In our nanobridges it is expected that only at $T \lesssim T_c$ will $L/\xi(T) < 1$ be satisfied, it can be seen from Figure 5.18 that at $T = 7.5$ K $= 0.88T_c$ the measured critical current deviates from the fitted values.

It has been demonstrated that the theoretical descriptions of the KO-I and KO-II models are not applicable in the measured nanobridges. In the KO-I theory the nanobridge effective length is assumed to be the exact physical length of the nanobridge, that is to say that the nanobridge

behaviour does not extend into the superconducting electrodes. For the KO-II theory, where ξ, $\ell >> L$, and the non-linear processes of the nanobridge extend into the superconducting electrodes, better agreement is found between the experimental data and the calculated values. However the measured values of I_c cannot be suitably described by either theory. To fully describe the microscopic behaviour of the nanobridge requires that the Usadel equations [111] be solved for the specific geometry found in nanobridges.

5.2.4 Effect of Film Thickness on Critical Current

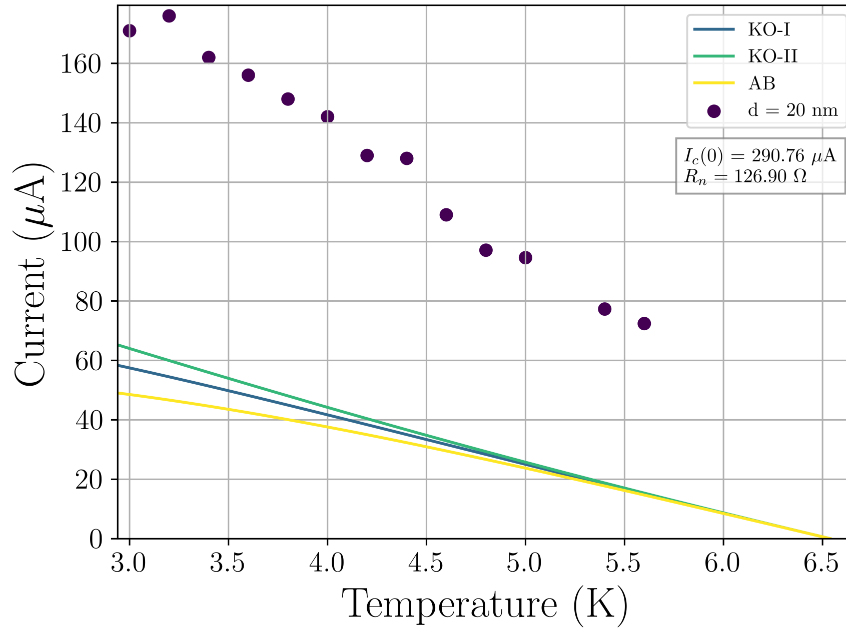

Figure 5.19: Fitting the measured critical current for an array with $d = 20$ nm, $\theta = 0°$, $L = 70$ nm and $W = 50$ nm to the calculated theoretical values for AB, KO-I and KO-II. The fitting parameters are shown in the legend.

Nanobridges with $d = 50$ nm and $d = 20$ nm were fabricated, and the critical current measured. Generally it was found that as the film thickness is reduced that I_c is reduced, and the R_n of the nanobridge is increased. A table of some typical values of the I_cR_n product are shown in Table 5.3. It can be seen that as the film thickness is reduced the I_cR_n product is increased.

Table 5.3: A comparison of values of the I_cR_n product for nanobridges which were fabricated in each of the three film thicknesses used over the course of the project. The values of I_c and R_n were determined from a four point contact IVC measurement to negate the lead resistance.

Film Thickness (nm)	I_c (mA)	R_n (Ω)	I_cR_n (mV)
150	5	0.37	2.7
50	0.8	6.7	5.36
20	0.13	127	16.51

In Figure 5.19 the critical current of a nanobridge with d = 20 nm plotted against the fitted values according to the AB, KO-I and KO-II theories. The experimentally measured values show less agreement with the theoretically derived values than in the case where d = 150 nm.

It has been shown by Vijay et al [147] that for thinner films the order parameter varies slowly in thin films, and as a result the bridge processes can extend far into the electrodes. This is in contrast to the requirement that the variation of the order parameter is restricted to within the physical dimensions of the bridge made in the theoretical models.

5.2.5 Nanobridge Switching Characteristics

On measuring the critical current of the nanobridges it was found that the magnitude of the difference between individual nanobridges in the array was comparable to the digitisation of the current source. To overcome this and investigate the nanobridge switching from the superconducting state to the normal state a measurement scheme was devised to increase the current resolution of the measurement set up, and increase the number of measurements which could be made. Using the measurement scheme described in Figure 5.3 an array of nanobridges were cooled and measured, taking $50,000$ measurements at each value of temperature.

Examples of the switching distributions are shown in Figure 5.20. The curve fitting was achieved using the "norm.fit" function of the Python SciPy package [148], using 250 bins.

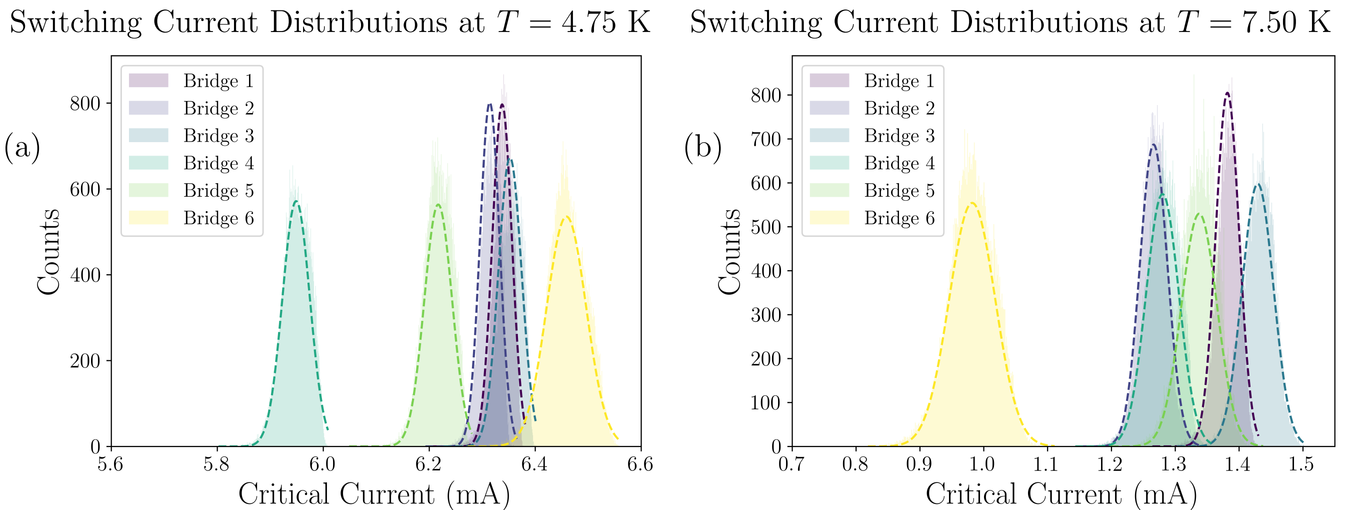

Figure 5.20: The switching currents of six identically fabricated nanobridges were each measured fifty thousand times at temperatures from 4.2 K to the critical temperature, shown at (a) T = 4.75 K and (b) T = 7.50 K. It can be seen that the switching current forms a Gaussian curve. It can be seen that as the temperature changes the critical current distributions vary at different rates. For example, it can be seen that Bridge 6, which has the greatest critical current at 4.75 K has the lowest critical current at 7.50 K.

It can be seen from Figure 5.20 that the variation of the critical current distribution over the

temperature range varies between nanobridges. The difference between Bridge 4 and the remaining nanobridges can be explained by the length: this bridge was found to have a length of 37 nm while the average length of the nanobridges in the array was found to be 33 nm. For Bridge 6 it can be seen that as the temperature is increased from 4.2 K that the nanobridge reduces in I_c. The value of L in this nanobridge was measured at 32 nm.

The differences between I_c for each nanobridge at the varying temperatures is likely the result of differences in the physical dimensions of the nanobridges. Without a precise measurement of the nanobridges it is difficult to determine if this is the case, or if these differences arise due to internal defects, such as grain boundaries of the Nb think film in the nanobridges or due to thermal cycling.

It can also be seen that the full-width half maximum (FWHM) of the switching current curve differs between nanobridges. Again, it is difficult to determine a reason for this, there is no apparent difference between the nanobridges and each measurement was made using the same setup, and recorded on a single cooldown.

What was determined from these measurements however is that the switching current distribution is small, as was seen in the IVC measurements. This confirms that these nanobridges can be fabricated to reliably and repeatable produce a desired value of I_c for use in superconducting digital electronics.

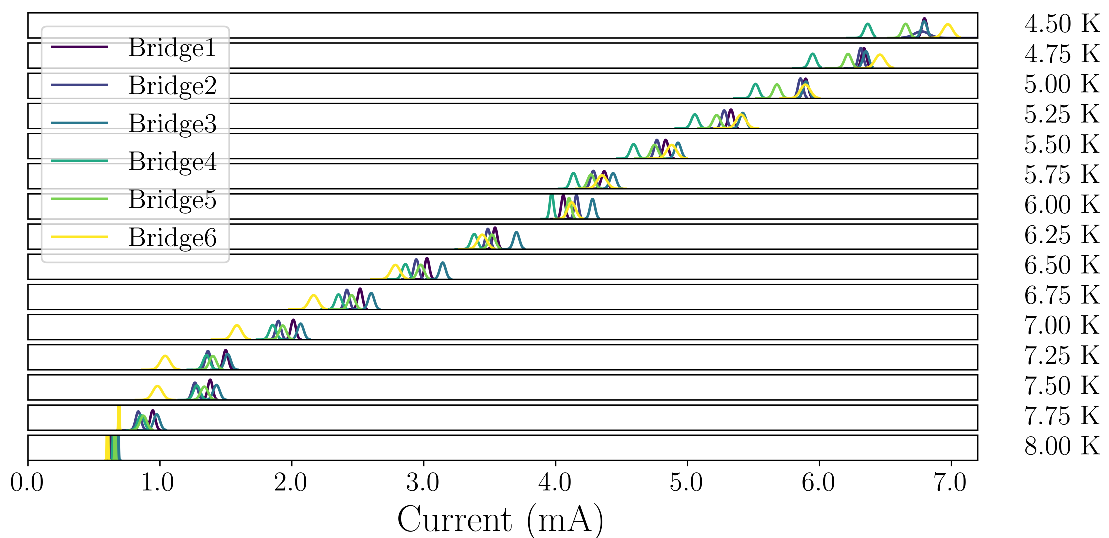

Figure 5.21: The switching distributions across the range of temperatures, where each distribution curve corresponds to a single nanobridge. It can be seen that the switching currents vary at different rates over the temperature range.

At higher temperatures, seen at 8.00 K, where the transition between the superconducting and normal states becomes less clear this method breaks down. In this regime there is significant noise seen in the IVC and it is difficult to correctly determine a point at which the transition occurs.

5.2.6 Nanobridge Repeatability

To scale up to circuitry which includes large numbers of Josephson junctions it is required that for identically fabricated nanobridges that the operating parameters fall within some tolerance. For SFQ electronics this can be as large as 60 % [73], and has been targeted at 15 % for SFQ electronics made with nanobridges [149].

To measure this the standard deviation of identically fabricated nanobridges across each array was measured. Across all eight tested arrays the standard deviation as a function of temperature was calculated. Shown in Figure 5.22 is the standard deviation across the array as a percentage of the critical current for a given temperature.

The switching current is determined from the time difference between the start and stop pulses registered by the counter, this time can be converted to current due to the rate at which the bias current is ramped. The measurement was repeated 10,000 times to produce a probability curve for the switching events in each of eight identically designed nanobridges across the array. The nanobridges in the array had length and width 30 nm × 33 nm, and an electrode angle of 15°.

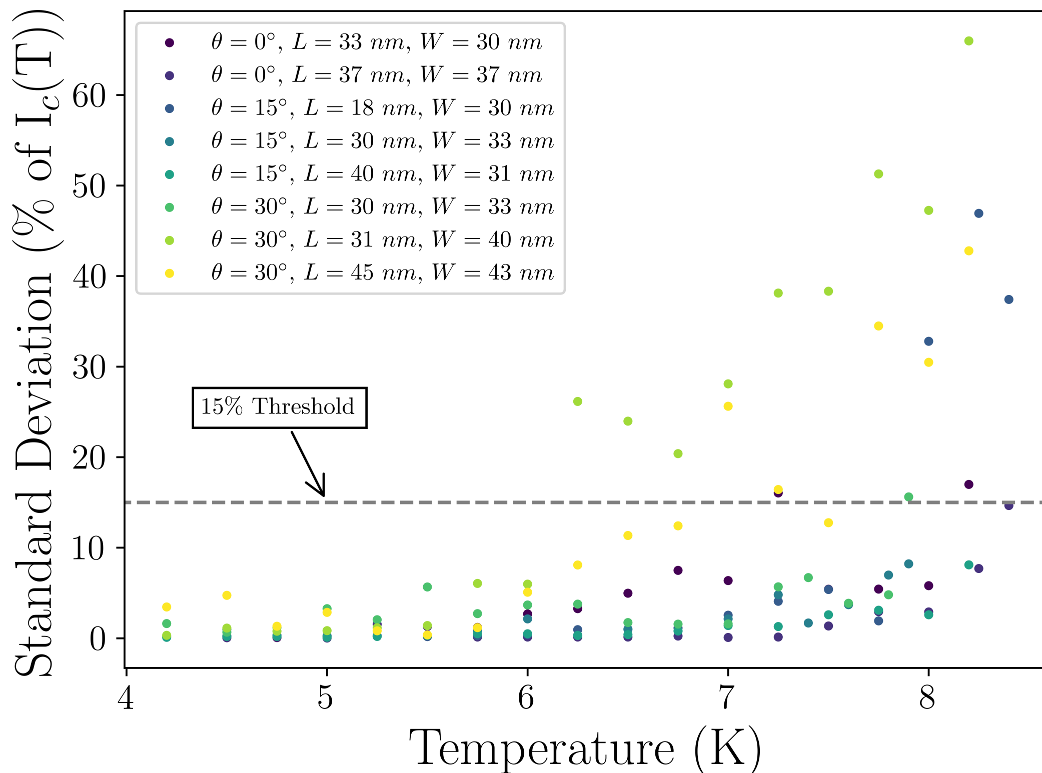

Figure 5.22: Looking at the standard deviation of nanobridges in all arrays as a percentage of the average switching current it can be seen that as the temperature is reduced the variation between the switching currents in the nanobridges is also reduced. Below 6 K the standard deviation of all arrays has reduced to less than 15 %. At higher temperatures the instability of the temperature creates larger variations in the I_c, at lower temperature where the I_c becomes more stable the variation across the nanobridge becomes significantly smaller.

It was found that the standard deviation across the array is reduced as the temperature is reduced. The large standard deviation is caused by the fluctuations in the temperature, which result in relatively large changes for the reduced I_c at temperatures close to T_c. At $T \lesssim 6$ K the standard deviation in each array has reduced below the 15 % level discussed for use in SFQ electronics.

The array which was used for this measurement was made using the a PMMA process described in Chapter 4. With the improvements made to the fabrication process the standard deviation would be expected to improve further.

5.3 Thermal Hysteresis in Nanobridges

As described in Section 3.3.2.2, the hysteretic behaviour in nanobridges is caused by a hotspot which is self-generating in the normal state. In this section, the thermal hysteresis of our nanobridges is investigated. Measurements were undertaken to confirm that the Skocpol theoretical model can be used to describe the nanobridge behaviour. An Al layer was then added in an attempt to reduce the Joule heating which produces the self-generating hotspot. Finally, the nanobridges with different physical geometries to investigate the effect this has on the thermal hotspot.

5.3.1 Effect of Film thickness on the return current in nanobridges

Nanobridges were fabricated using Nb films of thicknesses 150 nm, 50 nm and 20 nm. The return current in each case was measured from 4.2 K to T_c at NPL, and from 3 K to T_c at UoG. Samples with film thickness 50 nm and 150 nm were measured in a He dip dewar, where the critical temperature was found to be 8.4 K and 8.55 K, respectively. The 20 nm sample was measured with a cryogen-free system which reached a base temperature of 3 K, and the critical temperature of the sample was found to be 5.7 K. An additional sample which was fabricated in a film of thickness 50 nm was measured in the cryogen free system, and the critical temperature was determined to be 6.8 K.

To measure the resistivity of the Nb film a nanowire was fabricated in a 150 nm film, with a length of 16 μm and a width of 2 μm. The resistance of this wire at room temperature was measured to be 8.1 Ω. The resistivity of the film could then be determined as

$$\rho = R\frac{Wd}{l} \tag{5.3}$$

$$= 8.1\frac{2\mathrm{E}-6 \cdot 150\mathrm{E}-9}{16\mathrm{E}-6} \tag{5.4}$$

$$= 0.0152\ \mu\Omega\mathrm{cm}\ . \tag{5.5}$$

During the cooldown the residual resistivity ratio (RRR) of the film was measured, from room temperature to just before the transition at 8.4 K. This was calculated to be $RRR = 0.634$, and so the corrected resistivity at the critical temperature was calculated to be $\rho_{8.4\ \mathrm{K}} = 96.36$ nΩm. It was assumed that this value was consistent with the resistivity of each of the films independent of thickness.

The thermal conductivity of the film was calculated from the Wiedemann-Franz law,

$$\kappa = \frac{LT_c}{\rho} \tag{5.6}$$

$$= \frac{2.44\mathrm{E}-8}{96.36\mathrm{E}-9} T_c \tag{5.7}$$

$$= 0.253 T_c \ \mathrm{Wm^{-1}K^{-1}} \ , \tag{5.8}$$

and the T_c which was measured for each sample.

The results of I_R over temperature is seen in Figure 5.23, for the two samples which were measured in a cryogen-free system at UoG, where the two channels of heat-flow are through the substrate and through the film and there is no additional cryogenic liquid. A 20 nm sample, which showed no hysteresis at any measured temperature, and a 50 nm sample which showed hysteresis at 5.7 K corresponding to around $0.86T_c$. The calculated values from Equation 3.72 were found to theoretically validate the experimental data for both the 20 nm and 50 nm films.

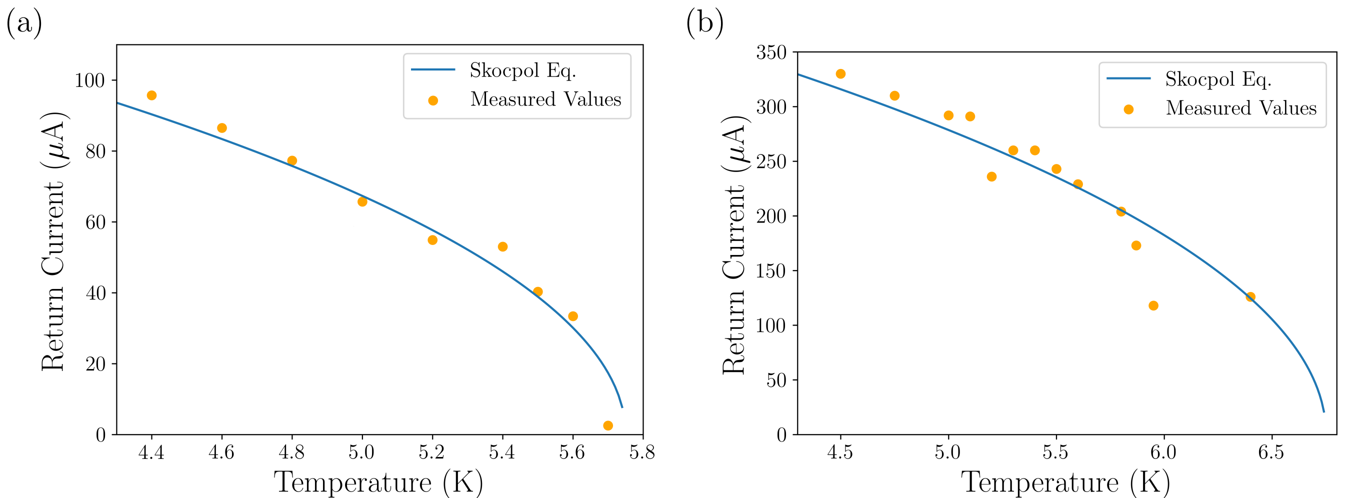

Figure 5.23: The averaged values of the return current across an entire array. In (a) the film thickness was 20 nm, while in (b) the film thickness was 50 nm. The calculated line shown in blue was calculated using Equation 3.72, using the measured parameters for the nanobridge.

A second set of two samples was measured in a He dip dewar, which in addition to the two channels of heat flow has an additional heat channel due to the Helium vapour, the results of these

measurements are shown in Figure 5.24.

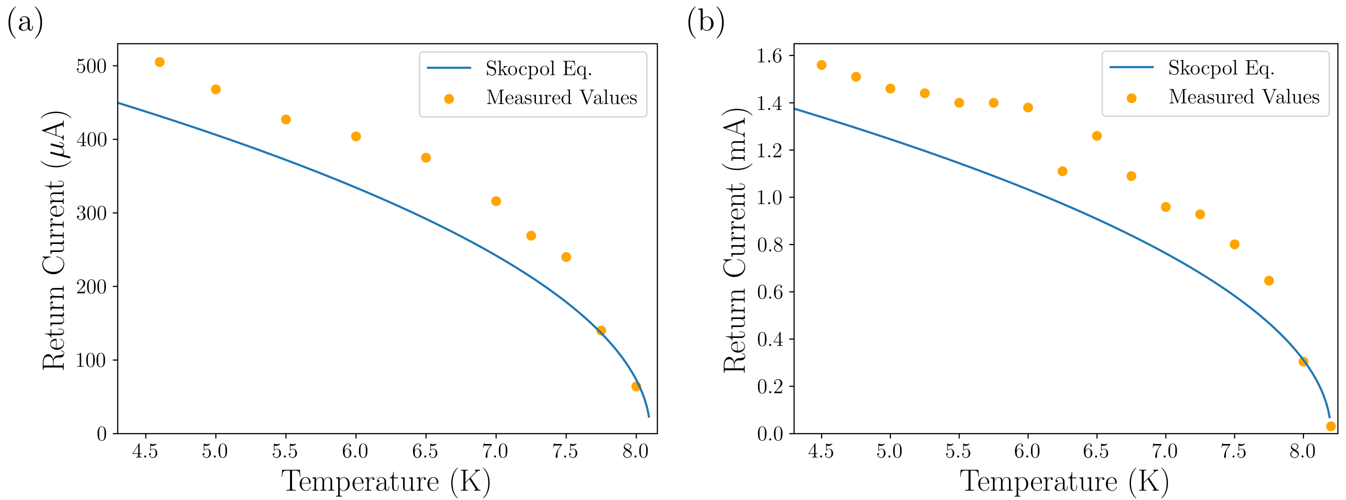

Figure 5.24: When measured in a He dip dewar, where heat can flow into the He as an additional thermal channel, it was found that the values of the return current were consistently greater than predicted by Equation 3.72. For both films with thicknesses 50 nm, shown in (a), and 150 nm, shown in (b), the measured values of the return current were consistently greater than expected.

In the samples measured in the cryogen-free system the measured values show good agreement with Equation 3.72. The samples measured in the He dip dewar show a higher than expected value for I_R. This is caused by heat flow into the cryogen which allows the hotspot to dissipate, and for the nanobridge to switch from the normal to the superconducting state at a greater value of I_R.

5.3.2 Effect of the addition of Al Thermal Channel on Nanobridge Behaviour

Close to the critical temperature of the nanobridge, where $I_c << I_c(0)$, the nanobridge will exhibit non-hysteretic behaviour. As the temperature is reduced, and the critical current becomes larger, the nanobridge can move into the hysteretic regime. The temperature at which this crossover occurs is the hystertic temperature, T_H.

To investigate if T_H could be influenced by modifying the mechanics of the heat flow in the nanobridge an additional heat channel was added to allow heat flow through a layer of Al added on top the thin film material. This was achieved by testing the samples before stripping the 40 nm thick Al hard mask used in the etching step. It was hypothesised that the Al layer will remain as a normal metal and allow heat to flow away from the hotspot, similar to the effect of the cryogen which resulted in an increase of the measured value of I_R. After testing of the sample, the Al layer was wet etched using a TMAH based photodeveloper, and the samples were tested a second time. Table 5.4 shows the effect this had on T_H when testing the sample before and after stripping the Al

layer. Although the temperature at which the nanobridges crossed into the hysteretic regime was reduced, the critical temperature was also reduced. The relative values in comparison to the critical temperature showed a slightly reduced value of T_H.

Table 5.4: The calculated values of the T_H, for two arrays, where the sample was measured with the normal metal Al layer added on top, and again after the Al layer had been stripped.

Array number	Without Al	T_H/T_c	Added Al	T_H/T_c
A2	7.66 K	0.93	8.05 K	0.94
B1	7.55 K	0.93	8.06 K	0.94

The small reduction in T_H suggests that the addition of an Al layer adds a negligible heat carrying channel. The ratio of T_H/T_c was consistent when measured with and without the added Al layer in both cases. In Figure 5.25 the average I_c and I_R values for all devices in both arrays are shown, and at temperatures below T_H these values are approximately the same in both cases suggesting that there is no change in the current density due to the thermal cycling of measurement and the wet etch process of removing the Al layer.

It was found that the critical current was reduced in the second measurement. This is consistent with the results described in 5.2, if it is assumed that the superconducting Nb causes the Al layer to become fully proximitised as the temperature is reduced. The value of the coherence length is much greater than the Al layer thickness.

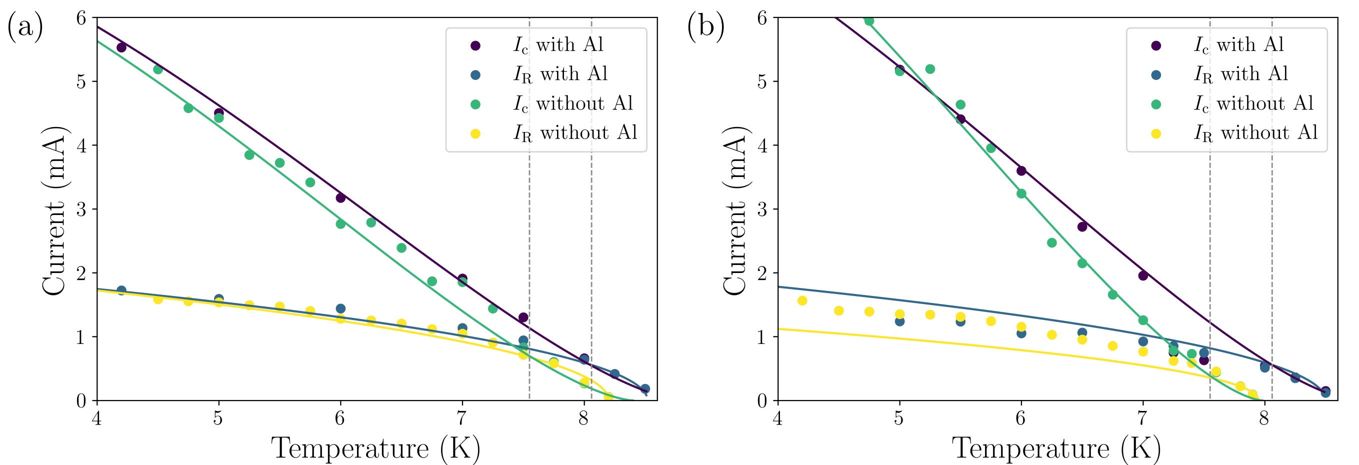

Figure 5.25: The average values of I_c and I_R for eight nanobridges in two arrays, where in (a) the electrode angle is 0°, and in (b) the electrode angle is 15°. In both cases, the value of T_H showed minimal change due to the additional Al layer, and the critical temperature appeared to be reduced when the Al was removed. The values of I_c were fitted using Equation 5.2, and the values of I_R were fitted with 3.72. T_H was calculated as the point of intersect between these two fitted curves.

The reduction in T_c between the measurements is similar to that seen in the case where the width, and therefore the cross-sectional area of the nanobridge, is reduced. To reduce this effect in future

measurements a thick oxide barrier layer could be included at the interface between the Al and Nb to prevent the proximitisation of the normal metal layer.

When comparing the I_c and I_R in two arrays of nanobridges with differing electrode angles measured with and without the added Al layer, shown in Figure 5.25, it can be seen that the values of the return current are greater than the values estimated by Equation 3.72. The measured values of the return current with and without the additional Al layer are approximately the same, suggesting that the effect of the Helium cooling channel is much greater than the heat flowing through the Al.

5.3.3 Effects of Nanobridge Geometry on Thermal Hysteresis

Measuring arrays of nanobridges which have differing electrode angles was thought to change the terms in Equation 3.68, by reducing the volume of the material which is driven into the normal state the power dissipated by Joule heating is reduced and provides a greater temperature range for non-hysteretic behaviour. This would lead to an increase in I_R for a given temperature, and in turn reduce the temperature at which T_H occurs. The measured values of T_H for three arrays of nanobridges with comparable bridge geometries and varying electrode angles is shown in Table 5.5.

Table 5.5: The hysteretic crossover temperature, T_H, occurs at approximately the same point independent of the electrode angle.

Electrode Angle	T_H	T/T_c	R_n (Ω)
0°	7.66 K	0.93	0.31
15°	7.55 K	0.93	0.37
30°	7.51 K	0.91	0.44

While the relative values of T_H compared to T_c are similar, T_H is reduced as θ is increased. It can be seen that the reduction in the cross sectional area from the increased angle θ results in a larger value of R_n and an increase in Joule heating. For each array L and W are similar, so it is expected that the effective length of the nanobridge will scale with θ, which is shown to be the case in Section 5.2.

It can be seen from Figure 5.26 that increasing the value of θ will result in a reduced value of I_R for a given temperature. The dissipated power corresponds to $P_{\text{Joule}} = I_R^2 R_n$, and it follows that the effect of variations in the current would be more significant than variations in the resistance.

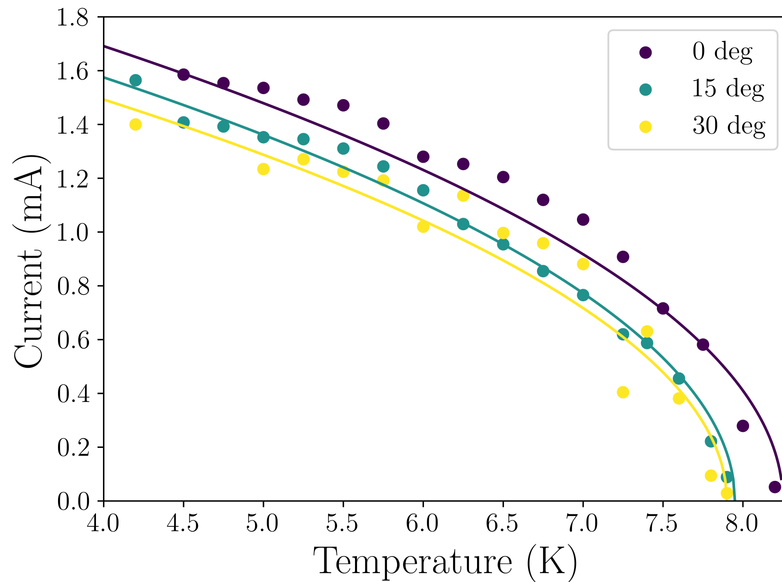

Figure 5.26: The measured values of I_R for three arrays with similar values of L, W and d, and the value of θ is varied.

The Skocpol model assumes radial propogation of the hotspot into the electrode, without any consideration for the geometry of the electrodes. For our measurements it is shown that variations in θ can influence the self-consistent hotspot.

5.4 Investigations of the Current-Phase Relationship in Nanobridge type weak links

From Equation 3.4 it is evident that to produce an SFQ pulse the Josephson junction must undergo a phase transition of 2π. A condition of the current-phase relationship (CPR) is that it must be 2π-periodic [110], and in the simplest case corresponds to Equation 3.1. In STJs the CPR can be approximately described by Equation 3.1 at all temperatures, however in bridge-type weak links the CPR can deviate significantly from a simple sinusoidal relation.

Directly proving the existence of SFQ pulses is a challenging task, although this has been achieved in STJs [150], by optoelectronically reconstructing the pulse shape. Alternatively, the CPR can be directly measured and there are several means of achieving this, although these are outside the scope of this project.

Some of the methods with which direct measurement of the CPR have been achieved are:

- A DC measurement, incorporating a Josephson junction into a single junction RF-SQUID. The flux in the loop is measured from which the CPR is derived [151, 152, 153].

- An RF measurement, where the Josephson junction is incorporated into an RF-SQUID, which is then coupled to an LC resonator. The CPR is then constructed by measuring the inductance of the RF-SQUID [154].

To determine an approximate expression for the CPR in our nanobridge we followed the model developed by Deaver and Pierce [101] to describe the differences which were observed between the behaviour of the STJ, for which the RCSJ model was developed, and bridge type weak-links. The RCSJ model typically uses a barrier with a sinusoidal CPR to represent the superconducting current branch of the Josephson junction. It can be seen from Section 5.2 that the CPR of the nanobridge is clearly different from that found in the STJ, as the CPR of the STJ can be approximately described by the AB model.

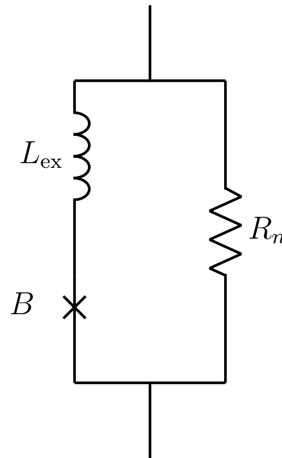

Figure 5.27: The equivalent circuit for constant thickness bridges used by Deaver and Pierce [101]. The bridge capacitance is considered to be small such that the displacement current is negligible, and the nanobridge can be represented by only the superconducting branch composed of an in-series inductance L_{ex} and constriction B, with a purely sinusoidal CPR, and a resistive branch composed of the normal state resistance R_n.

In this work the Josephson junction is modelled as a set of parallel current channels, where the superconducting current channel includes an in-series inductance, shown in Figure 5.27 as L_{ex}, which is used to describe the intrinsic inductance of the weak link. Jackel et al. [109, 151], experimentally verified this using continuous thickness bridge type weak links.

5.4.1 Derivation of Current Phase Relationship in Nanobridges

In the model described by Jackel [151] the junction voltage is described by the equation

$$V_J = -\frac{2\pi R_n I_c}{\varphi_c} \ln\left(\frac{I/I_c - 1}{I/I_c - 1 + 2\pi\varphi_c}\right)^{-1} , \tag{5.9}$$

where I is the current flowing through the junction, and φ_c is the point of inflection in the CPR, as described in Section 3.3.2. Using this expression we can substitute the sinusoidal voltage term from Equation 3.91, which results in

$$V = \frac{V_c}{I_n\sqrt{2\pi}}\left(\int_{I_c}^{\infty} V_J \exp\left[-\frac{(I - I_{\text{app}})^2}{2I_n^2}\right] dI - \int_{-\infty}^{-I_c} V_J \exp\left[-\frac{(I - I_{\text{app}})^2}{2I_n^2}\right] dI\right) , \tag{5.10}$$

which can be used to describe the voltage in the Jackel model, with the inclusion of the low-frequency voltage noise seen. This calculated voltage was then fitted to nanobridges with $d = 150$ nm and $d = 50$ nm, as shown in Figure 5.28.

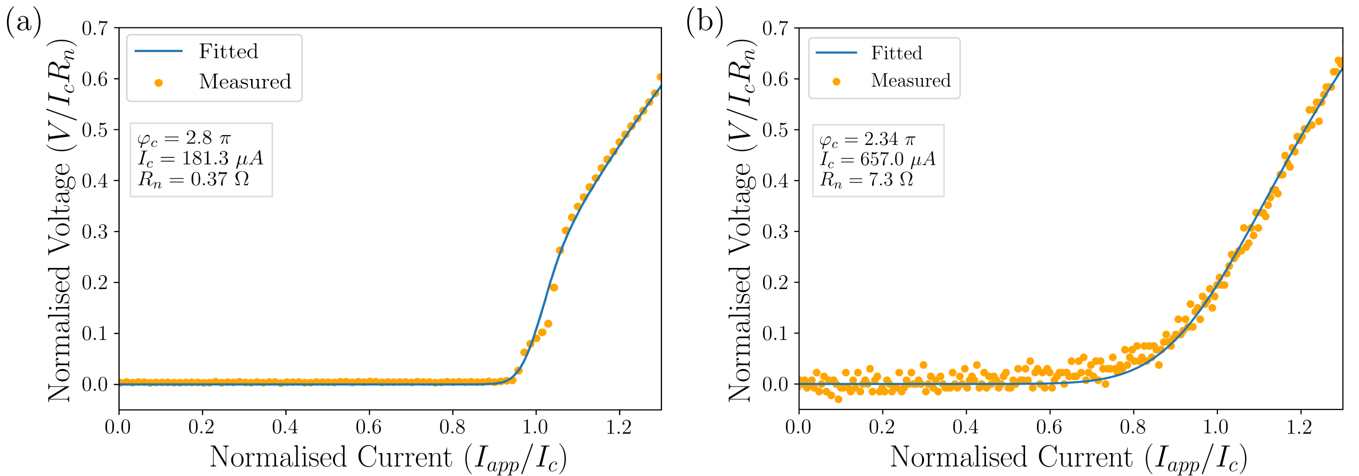

Figure 5.28: In (a) the experimental data from a nanobridge with parameters $d = 150$ nm, $L = 30$ nm, $W = 33$ nm and $\theta = 15°$, measured at $T = 7.8$ K $= 0.92T_c$. In (b) the experimental data from a nanobridge with parameters $d = 50$ nm, $L = 65$ nm, $W = 60$ nm and $\theta = 0°$, measured at $T = 4.5$ K $= 0.89T_c$.

In both the nanobridges with $d = 50$ nm and $d = 150$ nm it can be seen that the value of φ_c corresponds to a multivalued CPR. It is expected that at $I_s = I_c$ these nanobridges a phase-slip occurs in the nanobridge [75].

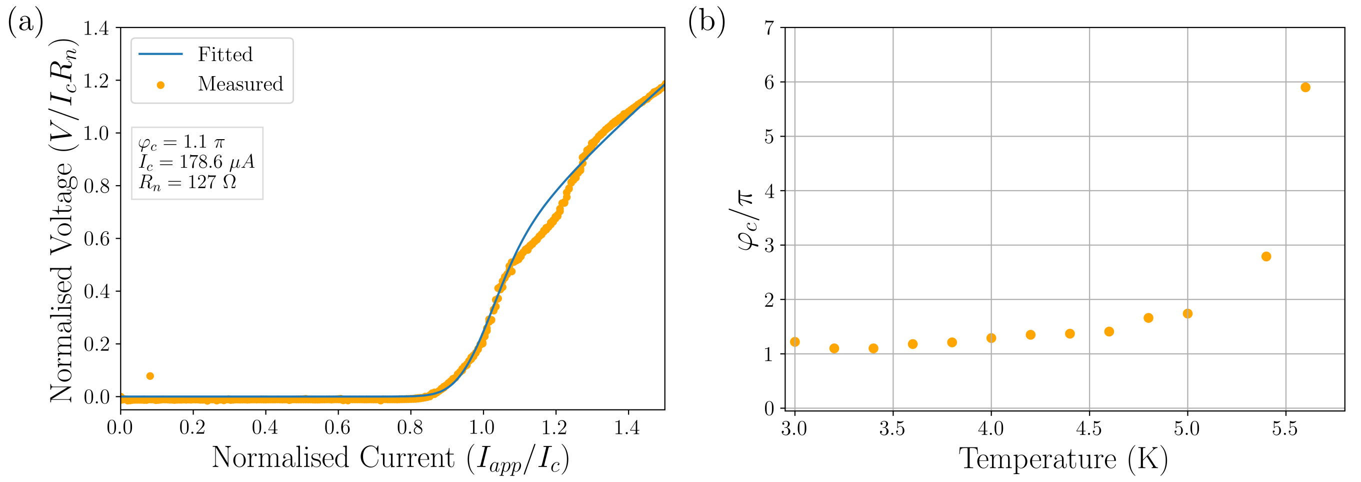

Figure 5.29: (a) The IVC of a nanobridge with parameters $d = 20$ nm, $L = 70$ nm, $W = 50$ nm at $T = 3.2$ K $= 0.52T_c$. (b) The derived values of φ_c at temperatures 3 K to 5.6 K.

In the case of the nanobridge with $d = 20$ nm, shown in Figure 5.29, it was found that at all temperatures the value of $\varphi_c > 1$, and that the CPR was in the multivalued regime. Close to T_c the values of φ_c rapidly increase, which is consistent with the increase in inductance close to T_c [102, 155].

At temperatures less than $T = 5.1$ K $= 0.88T_c$ it can be seen that $\varphi_c < 2\pi$, which results in a multivalued, non-sinusoidal CPR.

Using the equation for the Jackel model, with an in-series inductance L_{ex}, the phase of the nanobridge can be described as

$$\varphi = \arcsin\left(\frac{I\text{s}}{I_\text{c}}\right) + \left(\frac{2\pi L_{\text{ex}}}{\Phi_0} I\right) \tag{5.11}$$

$$\text{where } L_{\text{ex}} = \frac{\Phi_0 \varphi_c}{2\pi I_c}\ . \tag{5.12}$$

An example of the CPR was calculated from the derived values of φ_c for this nanobridge, which is shown in Figure 5.30. This CPR was achieved by determining the value of L_{ex} and, and then solving for a range of values of φ to calculate I_s. The resulting CPRs over the measured temperature range can be seen in Figure 5.30.

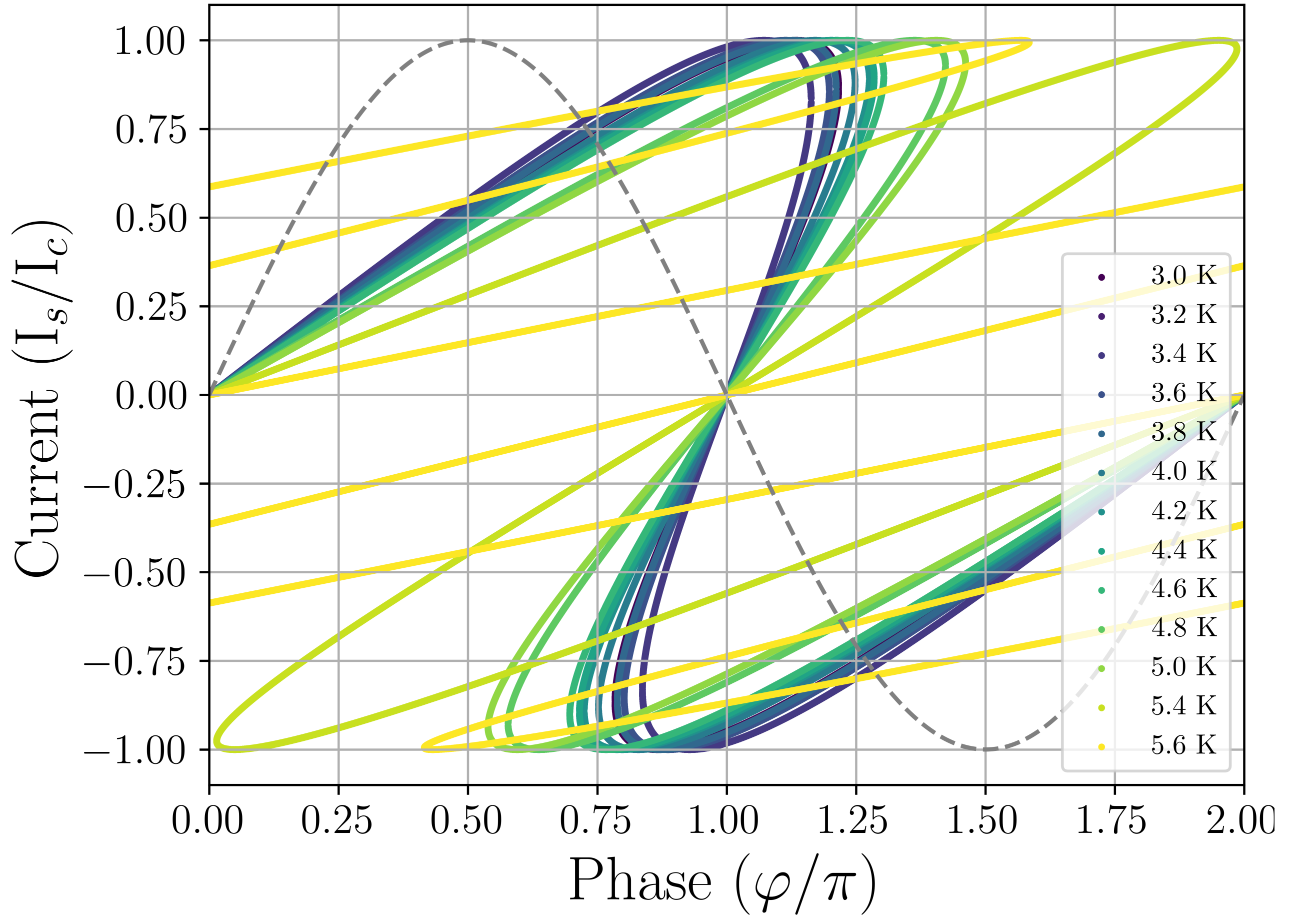

Figure 5.30: By fitting the measured IV data to the Jackel model the CPR was determined for a range of temperatures. It was expected that the CPR would be approximately sinusoidal at temperatures close to T_c and deviate with reduced temperature, however it was found that the smallest φ_c occurred at the lowest temperature. This can be explained by the inductance of the nanobridge increasing as the temperature approaches T_c.

It can be seen that the CPR of the nanobridge approaches a value of $\varphi_c \sim 1.1\pi$ at $T = 3.0$ K, which is consistent with the mathematical derivation of Likharev [75] and the experimental measurements of Jackel [156, 157]. It remains unclear if it is possible to use a nanobridge with a CPR where $\varphi_c > 1$ to generate pulses, SFQ or otherwise, which can be used for digital electronics applications.

5.5 Evidence of Josephson Effect in Nanobridges based on Shapiro Steps

Shapiro steps occur in Josephson junctions which are driven by a RF source, as described in Section 3.1.3.3. The steps occur in the IVC at voltages corresponding to voltages

$$V_n = n\frac{hf}{2e} \ , \tag{5.13}$$

where f is the frequency of the driving RF source.

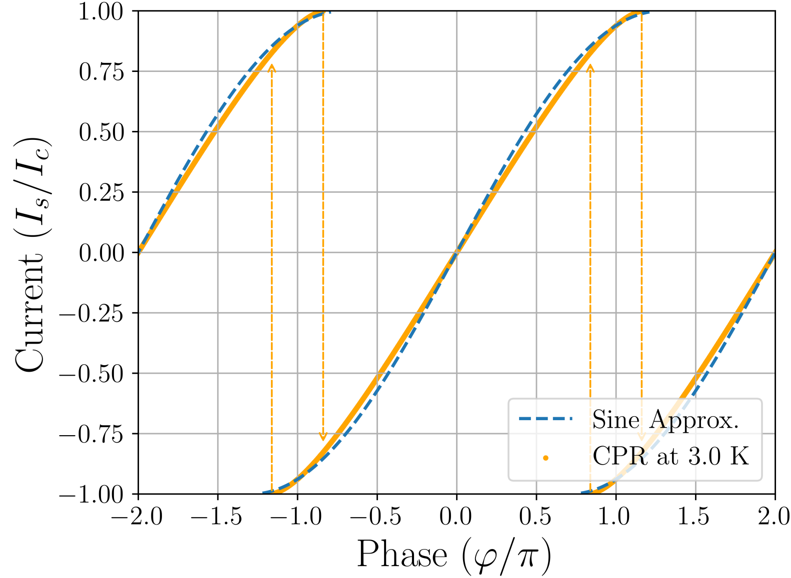

Figure 5.31: The derived CPR of the nanobridge was calculated using Equation 5.11, however this is not suitable to mathematically describe the CPR in the JSim software. Instead, an approximation was made, shown in blue, where the CPR could be described using 5.16. It was assumed that at $\varphi > \varphi_c$ a phase slip would occur, and the system would jump to the curve which was offset by 2π, which is represented here by the dashed arrows.

According to the RCSJ model, when driven by a current source the nanobridge can be described by the equations

$$\frac{\hbar}{2eR_n}\frac{d\varphi}{dt} + I_s(\varphi) = I_{\mathrm{dc}} + I_{\mathrm{rf}}\sin(2\pi f t), \tag{5.14}$$

$$V = \frac{h}{2e}\frac{d\varphi}{dt}, \tag{5.15}$$

where R_n is the normal state resistance, I_{dc} and I_{rf} are the amplitude of the DC and RF sources, and f is the frequency of the RF source. $I_s(\varphi)$ is the CPR of the Josephson junction, which typically is considered to be sinusoidal as described in Equation 3.1. The IVC is determined by the time-average of the solution of these equations [158, 159].

To accurately describe the behaviour of the nanobridges the CPR determined from Equation 5.11 must be described mathematically in a way that can be easily used in simulation. This is difficult to calculate, due to the multivalued nature of the CPR, so this was approximated with a sine function

$$I_s(\varphi) = I_c \sin(\varphi_c \varphi) \ , \tag{5.16}$$

where φ_c is the critical angle as determined in Section 5.4.1, resulting in a CPR that was applicable in the range $-\varphi_c < \varphi < \varphi_c$. It was assumed that at $\varphi > |\varphi_c|$ the current would go an instantaneous transition and the phase was shifted by 2π, and when φ was driven to a value greater than $|\varphi_c|$ it was set to

$$\varphi_{t+1} = \varphi_t - 2\pi \ , \tag{5.17}$$

where t represents the time step used in the calculation. In this way the $2-\pi$ periodicity of the CPR was preserved.

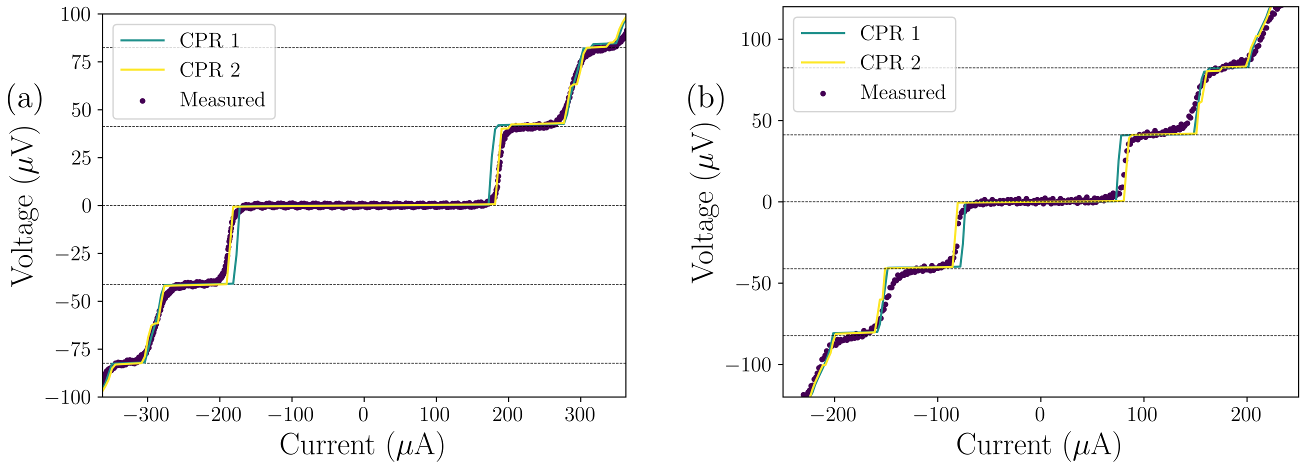

Figure 5.32: (a) The parameters of the nanobridge $d = 50$ nm, $\theta = 0°$, $L = 65$ nm and $W = 60$ nm. The applied RF frequency was 20 GHz, and the sample was measured at 5.4 K. From the fitting function the nanobridge was found to have $I_c = 226.75$ µA, $I_{\text{rf}} = 58$ µA and $R_n = 6.2$ Ω. In (b) the parameters of the nanobridge $d = 150$ nm, $\theta = 0°$, $L = 50$ nm and $W = 35$ nm. The applied RF frequency was 20 GHz, and the sample was measured at $T = 8.1$ K. From the fitting function the nanobridge was found to have $I_c = 251.6$ µA, $I_{\text{rf}} = 86$ µA and $R_n = 0.35$ Ω.

To investigate the difference that the non-sinusoidal CPR had on the nanobridge IV under RF two separate CPRs were used to calculate the IVC. In CPR 1 the standard sinusoidal equation, $I_s = I_c \sin(\varphi)$ was used to describe the CPR, while for CPR 2 this was replaced with Equation 5.16. In both of these cases the calculated IVC was plotted against the measured IVC of nanobridges with $d = 50$ nm and $d = 150$ nm. The IVC of nanobridges of these nanobridges when biased with an RF signal are shown in Figure 5.32. In both cases the nanobridge was measured while in the non-hysteretic regime. It can be seen that for both cases the steps occur at the expected values of

V_n. The fitted curves were found by solving Equation 5.14 with CPR 1 set as $I_s(\varphi) = I_c \sin(\varphi)$.

Upon comparing the experimentally obtained data with the values calculated from CPR 1 and CPR 2, which was determined by applying the experimentally measured parameters of I_c at zero applied RF bias, R_n and the amplitude of the RF bias, it was found that the analytically derived CPR fitted the experimental data more closely in both cases.

It can be seen that from Figure 5.32 the IVC calculated with CPR 2 predicts the existence of anharmonic steps which have been shown to occur at $V_n = n/2hf/2e$ and $V_n = n/3hf/2e$ in bridge type weak links [83], these have not been observed in any of the nanobridges measured over the course of this project. Due to the small size of the step predicted by Equation 5.14 it is possible that anharmonic steps are present in the IVC and are not recorded. This is likely a combination of rounding caused by noise currents in the Shapiro steps, and that the magnitude of the step is on the order of the resolution of the measurement device.

A nanobridge with $d = 150$ nm was also measured in the hysteretic regime, at $T < T_H$. To prevent heating which would drive the sample into the non-hysteretic regime the sample was held at a constant temperature with the use of a heater and PID controller. Before the measurement the sample was lowered into the He vapour, and heated

To ensure that the local temperature of the sample was not increased by the RF bias the sample temperature was controlled by PID with a large heater supply current, as the sample was locally heated the heater current was reduced to maintain a consistent temperature.

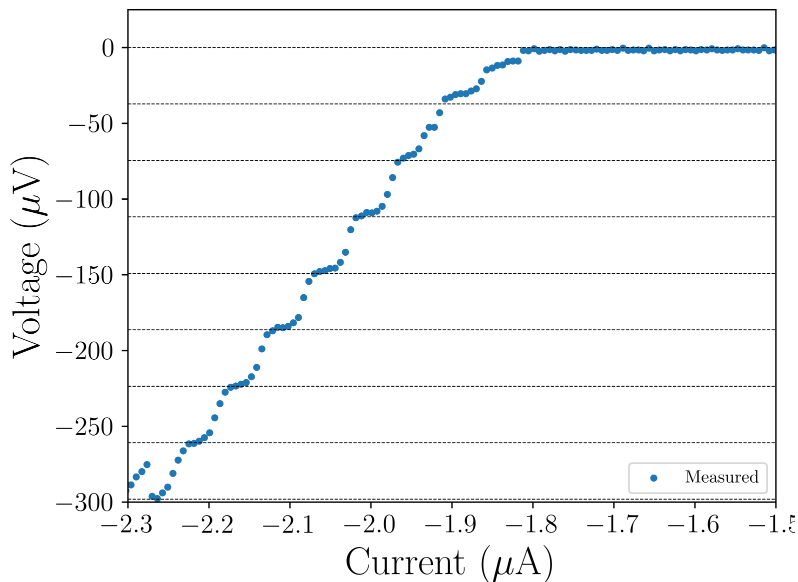

Figure 5.33: In the return current branch of the IVC in a nanobridge with parameters $L = 80$ nm, $W = 55$ nm, $d = 150$ nm and $\theta = 0$ Shapiro steps can be observed. The measurement was made at $T = 7.75$ K with $f = 18.1$ GHz.

Shown in Figure 5.33 it can be seen that the nanobridge exhibits Shapiro steps in the I_R branch.

In the I_c branch of the IVC the Shapiro steps cannot be seen, as the observable steps occur at values of $V_n < V_c$. The nanobridge remains in the superconducting state at the expected values of bias current.

5.5.1 IVC Response to Increasing RF Power

As described in Section 3.1.3.3, the IVC of a Josephson will change with increasing RF power, where steps which occur at voltages corresponding to $V_{\text{step}} = hf/2e$, where f is the applied RF frequency are formed. For a voltage biased junction with a sinusoidal CPR the variation in step amplitude in current at increasing RF bias can be described by as a Bessel function, by solving Equation 3.53. The current step size in weak links can be found by solving the equation

$$\alpha_{\text{dc}} + \alpha_{\text{rf}} \sin \xi\tau = \frac{d\varphi}{d\tau} + \sin\varphi \tag{5.18}$$

where $\alpha_{\text{dc}} = I_{\text{dc}}/I_{\text{c}}$ and $\alpha_{\text{rf}} = I_{\text{rf}}/I_{\text{c}}$, $\xi = \hbar 2\pi f/2eI_{\text{c}}R_{\text{n}}$, and $\tau = 2eI_{\text{c}}R_{\text{n}}t/\hbar$. Once solved the current step amplitude can be extracted from the IVC. This equation was solved using the parameters measured for nanobridges for each of the three film thicknesses: 20 nm, 50 nm and 150 nm.

Table 5.6: The parameters used for each thickness of film to numerically calculate the step size. The values of I_{c} and R_{n} were obtained from measurement, the values of ξ were calculated for $f = 20$ GHz and φ_{c} was obtained from the IVC fitting described in Section 5.4.

Film Thickness (nm)	I_{c} (µA)	R_{n} (Ω)	ξ	φ_{c}
20	187.0	127.1	0.002	1.1π
50	70.9	6.2	0.094	2.85π
150	27.5	0.3	0.467	3.15π

These parameters were used to numerically determine the IVC of each of the three nanobridges for values $0 < \alpha_{\text{rf}} < 4.0$. This was calculated for both CPR 1 and CPR 2, where CPR 1 is described by the equation for a typical STJ , and CPR 2 used the values of φ_{c} found in Table 5.6, $I_{\text{s}} = I_{\text{c}} \sin(\varphi)$. The approximated CPRs used to calculate the step amplitude for each film thickness are shown in Figure 5.34.

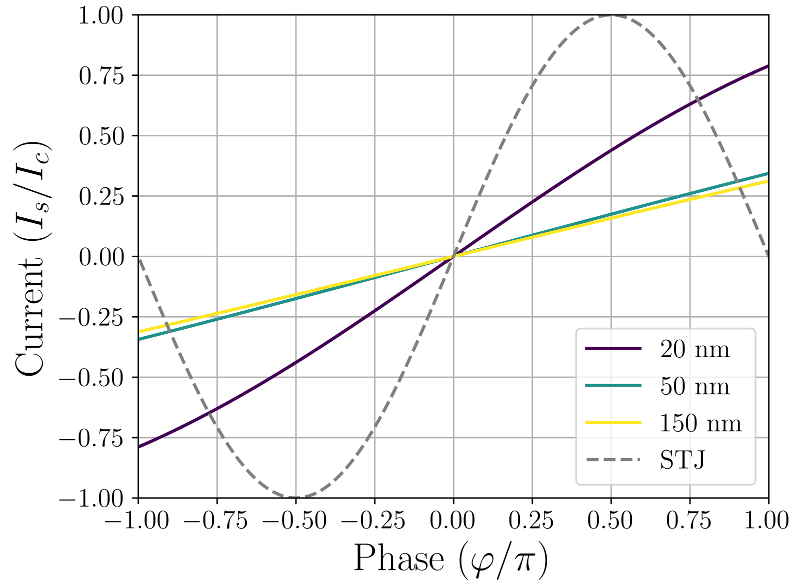

Figure 5.34: The approximated functions used as CPR 2 for each film thickness are shown, with the associated colour corresponding to the function used for each film thickness. The sinusoidal function, shown as a dashed grey line, was used as CPR 1 in each case.

The films with d = 150 nm were found to have the smallest value of the $I_{\text{c}}R_{\text{n}}$ product, and correspondingly the largest value of ξ.

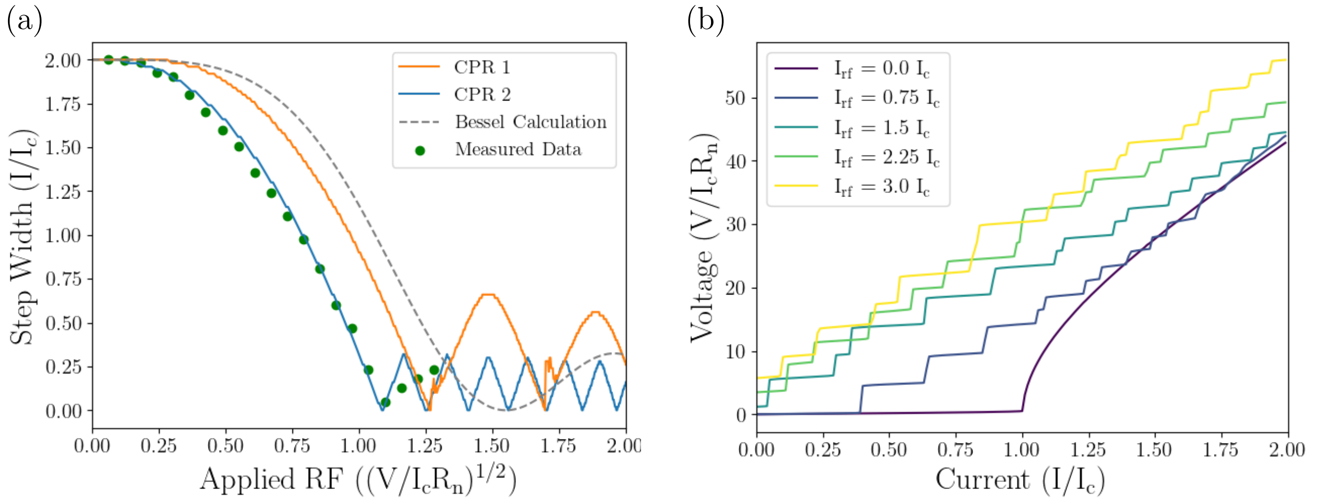

Figure 5.35: (a) The step size of the zeroth step in the current domain, plotted against the applied RF power. (b) The IVC of the nanobridge is shown for several values of the applied RF power.

As the attenuation of the RF line was unknown, the RF power applied to the nanobridge during the measurement was unknown. The step amplitude at no applied RF power, and the first minimum in the step power were therefore used as fixed points,. The measured step amplitude data was fitted to these two points for each of the three numerically calculated values.

The measured step amplitude data for each of the three numerically determined values is shown in Figure 5.35(a) for a nanobridge with film thickness d = 150 nm. It can be seen that the Bessel

calculation does not provide a suitable fit to the experimental data, where at the step amplitude minimum there is a sharp inflection. It can be argued that CPR 1 - the sinusoidal STJ case - provides a better fit to the measured data than the CPR 2, particularly after the first minimum.

In 5.35(b) the Shapiro steps can be seen to form as the RF bias is increased. It can be seen that the numerical simulation predicts non-integer steps to occur in the IVC of the nanobridges.

Looking at the higher order steps, it is clear that the data more accurately fits the numerically calculated values for CPR 2 than for CPR 1. Using the same scaling as in Figure 5.35(a), the onset of the first step occurs where expected when calculated using CPR 1. It can be seen in Figure 5.36(a) that the shape and amplitude of the step height curve are found to be more closely in agreement with the numerically determined values of CPR 2 than CPR 1. This is also the case for the second step, shown in Figure 5.36(b), where despite the onset of the curve occurring at a slightly lower value of the applied RF power, there is a much closer agreement with CPR 2 than with CPR 1.

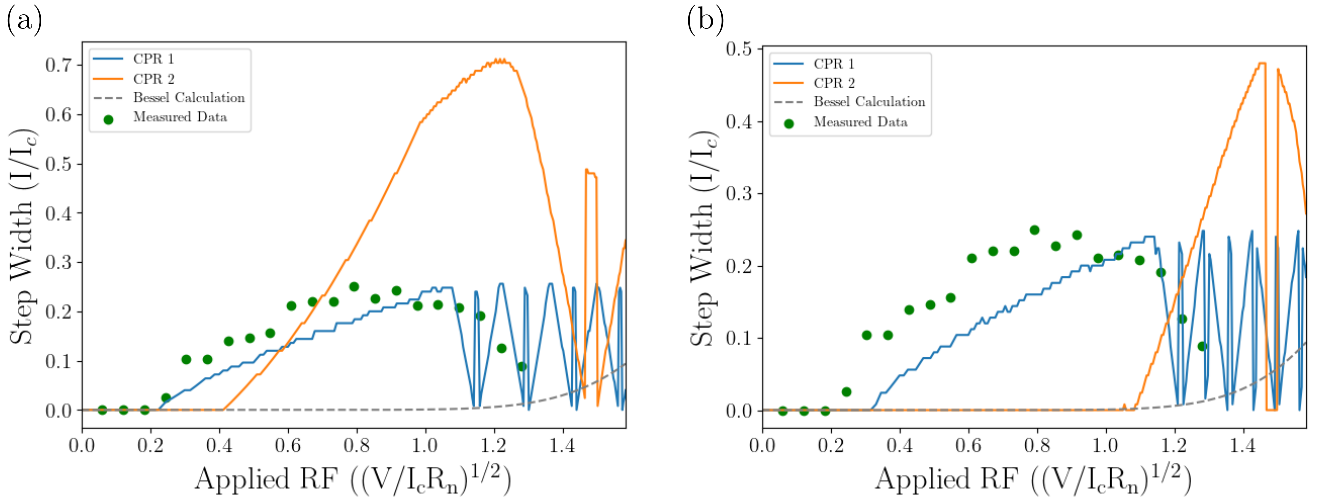

Figure 5.36: The measured values of the step width, shown in green, compared with the values for CPR 1, CPR 2 and the Bessel calculation. In (a) the first step is shown, and in (b) the second step is shown.

The nanobridges with film thickness $d = 50$ nm have a greater value of R_n, corresponding to a reduced value of ξ. It is expected that the amplitude of the step height curves scales with ξ [158].

In Figure 5.37(a) it can be seen that the step amplitude is reduced in comparison to that seen in Figure 5.35, as would be expected. As in the previous example for $d = 150$ nm, the RF power applied to the nanobridge was not known, and so the zero applied RF bias and first minimum were used as fixed points to scale the RF power. Both samples were measured on the same measurement setup, and the RF power was scaled by $C_{150} = 0.193$ for the $d = 150$ nm nanobridge and $C_{50} = 0.212$ for the $d = 50$ nm nanobridge.

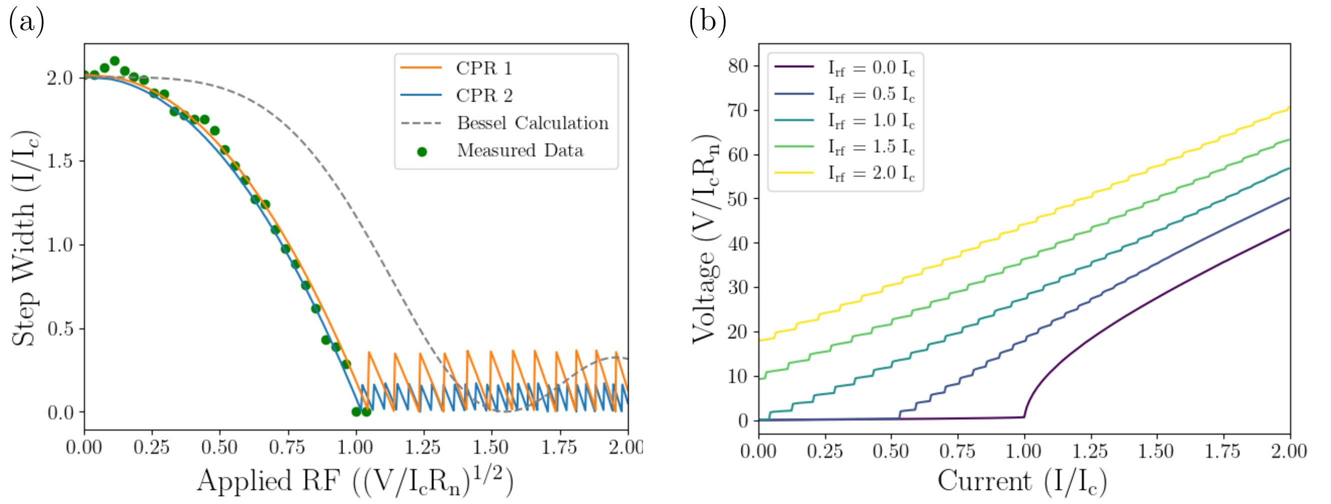

Figure 5.37: (a) The step height with increasing RF power, plotted with the numerically calculated values for CPR 1 and CPR 2, as well as the Bessel calculated values. (b) The IVC for a nanobridge with $d = 50$ nm calculated using CPR 1.

From the IVC shown in 5.37(a) it can be seen that there are no non-integer steps which were found when using the parameters shown in Figure 5.32(a). This is due to a combination of factors: the reduction in the value of φ_c, which results in less excess current than in the $d = 150$ nm; a greater value of ξ than in the sample which was measured in Figure 5.32(a); the current step size used in the simulation is approximately the same as the non-integer step width, which prevents them from appearing in the IVC.

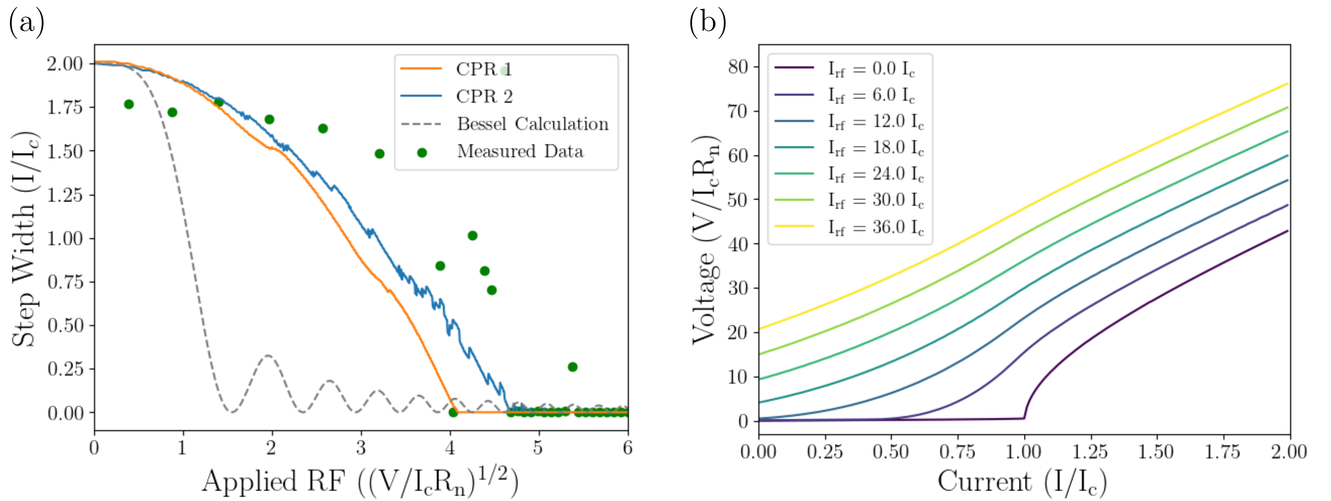

Figure 5.38: In the IVC of nanobridges with film thickness (a) 20 nm and (b) 50 nm it can be seen that the width of the zeroth order step oscillates as the RF power is increased.

For the nanobridge with $d = 20$ nm the scaling in the x-axis was achieved by the same method as the previous examples, by fitting to the zero RF and first minimum. It can be seen from Figure 5.38 (a) that the numerical calculation does not provide a good fit to the measured data. This is likely due to difficulties in scaling in the x-axis, this sample was measured in Glasgow where the

RF attenuation was ~ -80 dB. Additionally, as the value of ξ is small the numerical step width calculated can be drastically changed with a small change in the calculation parameters. However, after the first minima the I_c is completely suppressed on further increasing of the RF power in agreement with the calculated values.

In Figure 5.38 (b), the numerically calculated IVC trace for CPR 2 shows that no higher order steps can be seen. Over several nanobridges which have been measured under RF bias the I_c has been seen to reduce as the applied RF power increases, but no higher order steps have been measured in the IVC of the nanobridges.

5.6 Simulated RSFQ Circuitry with Derived Nanobridge CPR

As described in Section 3.1.2.1, the RCSJ model uses the current flowing through several parallel lumped elements to describe the total current in the junction, including a Josephson junction which has a sinusoidal current phase relationship described by Equation 3.1. As described in Section 5.4, this CPR differs from that which has been estimated for nanobridges, and so to evaluate the suitability of nanobridges for use as SFQ elements the RCSJ model has been modified to use the CPR described.

The CPR used in the simulation is the same as that shown in Figure 5.31 and with the process described in Section 5.5. The JSim code was then modified to include the new form of the CPR. Firstly, to verfy that the modification had worked, and that the non-sinusoidal CPR could generate SFQ pulses, a single junction pulse train generator was used, the circuit diagram of which is shown in Figure 5.39.

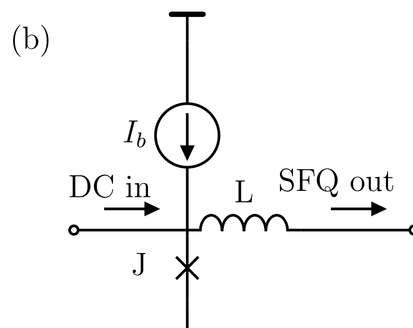

Figure 5.39: The simple circuit which can produce a train of SFQ pulses from a DC input. The parameters were set based on the experimentally obtained parameters for the nanobridge: I_c = 150 µA and biased at $0.7I_c$, the inductance L was set to 8.8 pH which corresponded to $\lambda \approx 4$.

This circuit was simulated for both the sinusoidal and non-sinusoidal CPRs to compare the output. The circuit was driven with a square pulse with amplitude of $1.1I_c$, and a pulse duration of

1000 ps. In Figure 5.40(a) it can be seen for the non-sinusoidal CPR that with the same bias the current flowing through the junction in the steady state is higher than in the sinusoidal junction. The current of the junction during the generation of an SFQ pulse can be seen to take on different shapes, but a similar process occurs for both CPRs. The current in the junction oscillates, and produces a current drop in reponse to the production of an SFQ pulse.

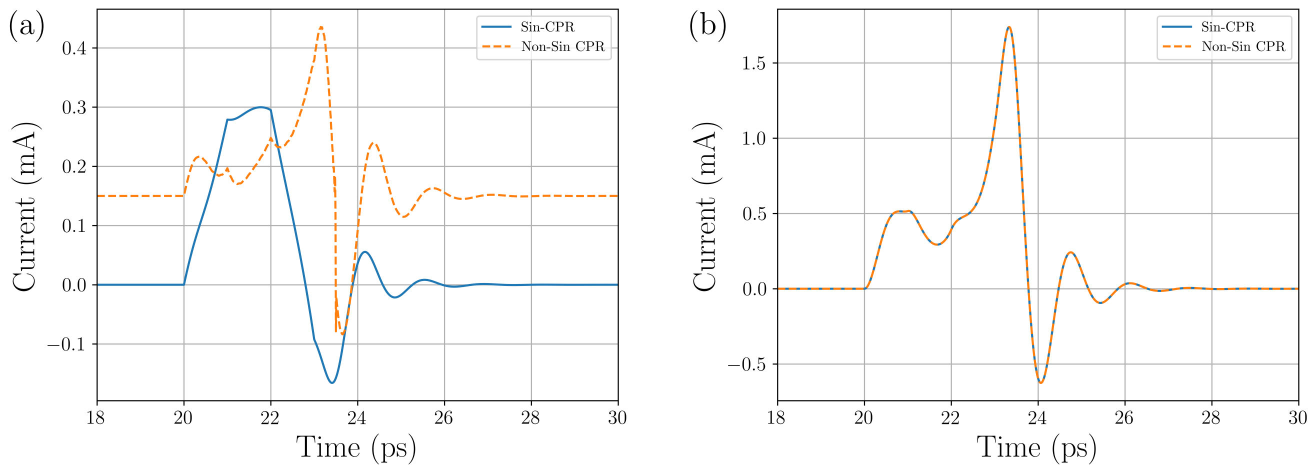

Figure 5.40: It can be seen that when simulating the circuit where the Josephson junctions have a non-sinusoidal CPR that the device operates as intended to. The input pulse produces a single SFQ pulse just as it does in the standard case, with a greater pulse amplitude.

In Figure 5.40(a) the comparison of a the current for a single SFQ pulse generated with both CPRs is shown. The current drop is greater in the non-sinusoidal case, and the time period for both cases is the same. In Figure 5.40(b) the SFQ voltage pulse can be seen. The pulse shapes are identical for both cases, and were found to have a quantised area of 2.07 mV $\cdot\, ps$, corresponding to one SFQ.

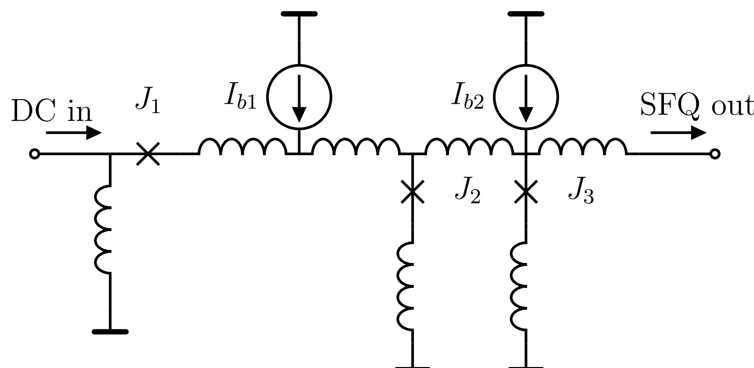

Figure 5.41: The schematic of the DC-SFQ converter which was simulated, showing the parameters of each of the components.

Next, a simple circuit, a DC-SFQ converter, was simulated to assess the suitability of the SFQ pulses produced for electronics purposes. The behaviour of the circuit over a period of 3 ns was simulated, in which time four input pulses would be used to trigger the junction. The parameters

of the circuit, shown in Figure 5.41, are identical to those of Figure 3.10 with the only change being that the CPR of each of the Josephson junctions is described in Figure 5.31.

The device was triggered by input pulses, as shown in Figure 5.42. The rising edge of the input pulse caused the triggering of the J2-J3 loop, which produced a single SFQ pulse at the output. The falling edge produces a pulse in J1 which resets the circuit ready for another input.

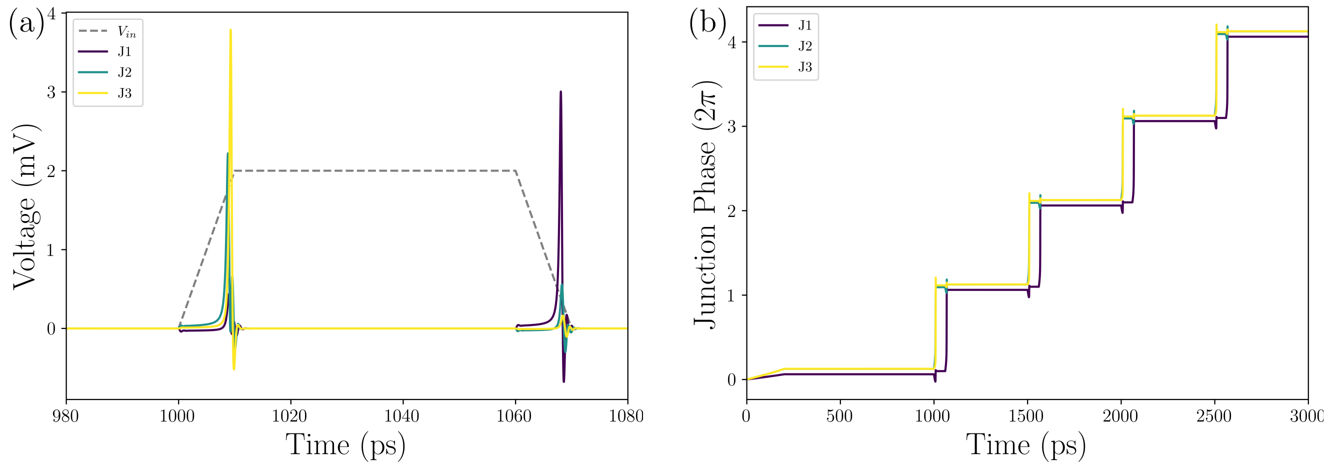

Figure 5.42: (a) The rising edge of the input pulse triggers junctions J2 and J3, as shown in Figure 5.41, and generates a SFQ pulse at the output. The DC-SFQ converter is reset by the falling edge of the input pulse, which triggers J1 and resets the J2 - J3 loop. It is shown in (b) that when driven by a periodic input that J2 and J3 undergo a 2π phase change at the rising edge of the pulse and J1 will be driven by 2π at the falling edge of the pulse.

It can be seen that the behaviour of this circuit is similar to the results shown in Figure 3.11 for the same DC-SFQ converter where the Josephson junction CPR was described by Equation 3.1. The individual pulse shape differs in each case, with the non-sinusoidal CPR producing a greater amplitude, lower period pulse.

The results of these simulations suggest that the 20 nm nanobridges fabricated and tested over the course of this project can be used to realise SFQ circuitry.

Chapter 6

Conclusion and Future Work

6.1 Summary of Results

This research aimed to show the feasibility of using nanobridges as SFQ elements for superconducting digital electronics circuitry.

Based on the measurements of the physical parameters it has been shown that the nanobridge fabrication process is both repeatable and scalable. Nanobridges were fabricated to < 5 nm of the designed dimensions, and were the critical current was shown to vary with L, W and θ with temperature. The physical dimensions of the nanobridge can be controlled to give the required critical current for a given temperature. This variation was found not to agree with AB, KO-I or KO-II theory, which agrees with the work of Vijay et al (2009) [147], in which the Usadel equations were solved for a specific geometry. Statistical measurements of the critical current were made, showing that the distribution of the critical currents for a single nanobridge is small, and that nanobridges which were fabricated with similar physical dimensions show similar critical currents.

The nature of the thermal hysteresis in nanobridge was described by Skocpol et al (1974) [105] as the result of Joule heating generated by a self-consistent thermal hotspot. It was found that the fabricated nanobridges were in agreement with the calculated values for the return current where the sample was cooled in a cryogen free system. Where the sample was cooled by a cryogen it was found that the vapour added an additional channel for the heat to flow away from the hotspot, and as a result the value of I_R was increased. An additional channel was added to the top of the sample to allow heat to flow and increase the value of I_R, but this was found to have a negligible effect. This was likely due to the proximitisation of the Al layer.

The IVC of the nanobridge was fitted using the Jackel model with the addition of a noise current to find a value for the inflection point of the CPR φ_c. From this, a CPR was constructed for the nanobridge which showed that the value of φ_c was inversely proportional to temperature. At the

lowest measured temperature it was found that φ_c, which is in agreement with the derivation of Likharev [75] that the CPR of the nanobridge should be multivalued at all temperatures.

The IVC under RF bias was calculated using the derived CPR, it was found that this provided a better fit to the experimentally measured data than the case where the CPR was described by a the sinusoidal relation $I_s = I_c \sin(\varphi)$. Shapiro steps were also measured in the return current branch of the IVC, showing that in the regime of thermal hysteresis the Josephson effect can occur in the nanobridge. The current width of the Shapiro steps was fitted to a Bessel function, which showed that the sinusoidal description did not fit the measured data.

Finally, using an approximation of the derived CPR to calculate the behaviour of the Josephson junction, SFQ circuitry was simulated. Firstly, a single junction DC-SFQ converter was simulated to investigate the nature of the SFQ pulses produced when the junction CPR was described by the sinusoidal and non-sinusoidal functions. Then a more complete DC-SFQ converter was simulated, where a square input pulse will produce a single SFQ output pulse. With junctions using the non-sinusoidal CPR this circuit was found to produce a single SFQ pulse at the output as expected. This suggests that Josephson junctions with a multivalued CPR are capable of generation SFQ pulses which can be used in superconducting digital electronics.

6.2 Outlook and Future Work

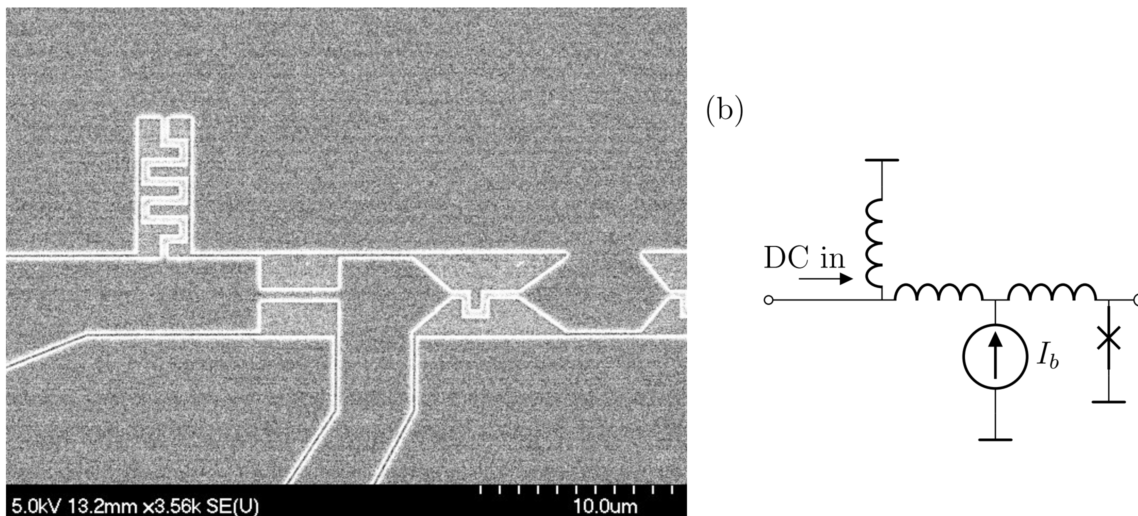

Figure 6.1: An example SEM image of the fabricated SFQ circuit, which makes use of nanobridges as the active element. The first stages of the fabrication process were completed in February 2020, prior to the JWNC closure in March 2020.

Fabrication of a simple SFQ circuit which makes use of nanobridges, an example of which is shown in Figure 6.1, is now underway. This sample includes DC-SFQ generators, and an SFQ logic circuit, which will only produce an output pulse when SFQ pulses are produced at both inputs. The output

signal is produced by a superconducting cascade switch, which will switch to the normal state in the presence of an SFQ pulse and produce an output pulse which is detectable at room temperature. In this way the existence of SFQ pulses can be indirectly confirmed.

After this the next step should be to interface an SNSPD with a nanobridge based SFQ circuit to provide the input which triggers the production of an SFQ pulse. There has been some consideration at Glasgow on how to achieve this, and despite some considerable fabrication challenges this is a realistic goal. From here a small scale SNSPD array with integrated, on-chip nanobridge based SFQ readout scheme.

As a proof of principle device an SNSPD with a simple DC/SFQ converter to SFQ/DC converter which can be used to prove that SFQ pulses can be used as a means of reading out SNSPD pulses. A follow on stage from this would be to build a simple combiner which could be used to multiplex multiple SNSPD pixels without any pixel discrimination information. There are a number of challenges to overcome even for this simple circuit. Integrating SFQ circuitry and an SNSPD onto a single sample requires either fabricating nanobridges in a NbN film, where the maximum length is a factor of $\sim$ eight $\times$ smaller than in Nb due to the shorter coherence length, or to produce a high quality NbN adjacent to a Nb film on a single sample. Furthermore, the output pulse of the SNSPD, which is on the order of ~ 0.5 mV must be integrated in a way which provides a trigger for the SFQ circuitry. The output from the SFQ circuitry must then be detectable at room temperature.

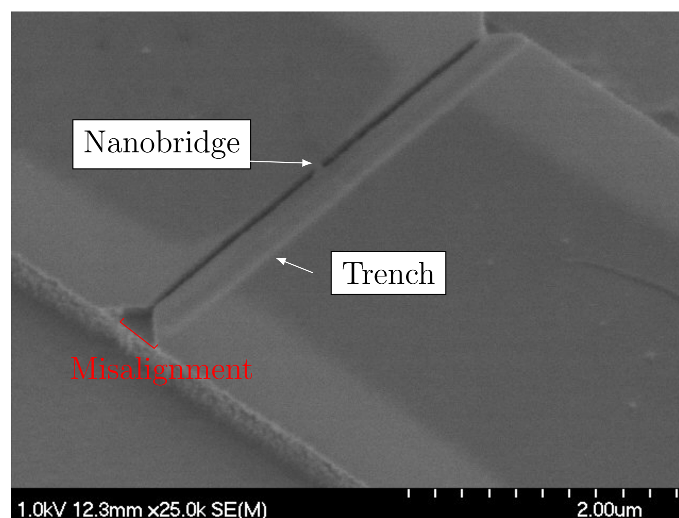

Figure 6.2: An example of a nanobridge which was fabricated as part of an investigation on making variable thickness nanobridges. A trench can be seen in the rightmost electrode showing the misalignment of the final patterning step. The trench etched into the sample should be patterned directly over the gap between the two electrodes, in this case there has been a misalignment of ~ 220 nm in the $x-$direction.

To improve the operating parameters of the nanobridges, and reduce the value of ϕ_c, a variable thickness bridge (VTB) can be used in place of the constant thickness nanobridges which have been

used throughout this project. There has been some recent efforts at Glasgow to fabricate this type of weak link using the existing fabrication process developed over the course of this work, and an example of this can be seen in Figure 6.2, where the final lithography step was misaligned causing the failure of the sample.

Despite the added fabrication challenges in making this type of weak link it would appear that the process is achievable and can be used to produce VTB weak links without significant additional processing.

Nanobridges could also be considered for other applications, for example in Josephson voltage standards [160]. These standards make use of the quantised nature of the Shapiro step, which is depending only on the frequency of the applied RF bias. Over tens of thousands of Josephson junctions this can be summed to provide an accurate volt for reference measurements. With the reliability of the fabrication process demonstrated in this work it could be possible to produce a Josephson standard using nanobridges to provide the quantised voltage steps.

In the work of Likharev [75] on weak links, which is still often used as the defining text on the subject, it was written that he did not expect bridge-type weak links to find any practical applications. This work has demonstrated that the engineering challenges in fabricating bridge-type weak links can be overcome, and that this has meant that the physics of these devices may not be insurmountable.

Appendix A

Fabrication Processes

A.1 Deposition Process

- The number of samples to be deposited at chosen from a diced wafer of (100) orientation Si. Each sample is individually cleaned by placing in acetone in an ultrasonic bath for five minutes, which is then repeated using methanol and isopropanol (IPA). Once cleaned the sample is thoroughly dried with a nitrogen gun and clamped into place on the holder of the deposition system.

- The sample holder is placed inside the loadlock chamber and pumped down to vacuum. The samples are then cleaned using an Ar plasma for two minutes at 100 W, with an Ar flow rate of 15sccm. After completion of the process the samples are held inside the chamber to allow the loadlock to reach a pressure of less than 1×10^{-6} Torr.

- At suitable pressure the samples are transferred to the main deposition chamber, and main chamber pressure is allowed to recover to less than 7×10^{-9} Torr before deposition.

- The samples are spun at 50 rpm to maintain the uniformity of the film growth, at a distance of 100 mm from the Nb target. Ar is flowed into the chamber at 30 sccm to achieve a chamber pressure of 2×10^{-3} Torr and the current is maintained at 0.8 A to ignite the plasma, and the shutter remains closed for three minutes to allow the plasma to stabilise and remove any contamination from the Nb target, before shutter is opened for to achieve the desired film thickness.

- At the end of the deposition the samples remain in the chamber to allow them to cool for several hours under vacuum - typically overnight.

A.2 Fabrication Process

- Samples are cleaned using subsequent steps of acetone and IPA and sonicated for five minutes each, after which the samples are thoroughly dried with a nitrogen gun. The samples are then baked at 120°C for ten minutes in a nitrogen oven to ensure the surface is completely dried.
- A layer of Allresist AR-P 642.12 PMMA, with molecular weight of 200K is spun onto the sample at $4,000$ rpm for 60 s to a thickness of 680 nm. This layer is then baked on a hotplate at 135°C for five minutes to drive off the anisol solvent and harden the PMMA.
- A second layer of Allresist AR-P 679.02 PMMA, with molecular weight of 950K is the spun onto the sample, again at $4,000$ rpm for 60 s to a thickness of 70 nm. This layer is also baked on a hotplate at 135°C for five minutes to drive off the ethyl lactate solvent.
- The sample is patterned using the ebeam to layout the markers, and developed using a mixture of MIBK and IPA at 2:1 heated to 23°C. The sample is developed for $60 mathrm\ s$ and then placed into an IPA stopper for 10 s before being gently dried with a nitrogen gun. At this stage the pattern must be checked under optical microscope.
- Prior to metallisation the samples are exposed to an oxygen plasma at 95 W for 45 s, which will remove the "PMMA scum" from the exposed area and improve the adhesion of the metallic layer to the Nb film. The sample is metallised with 5 nm of Ti as an adhesion layer followed by 70 nm of Au. The PMMA resist is then dissolved using Microposit 1165 resist stripper, which is left for at least two hours (often overnight) in a heated waterbath held at 50°C. The unwanted Ti/Au layer can then simply be washed away with gentle flushing of acetone.
- This process is repeated exactly to layout the microwires and Nb contacts for the sample, until the metallisation stage. At this stage a 20 nm layer of Al is deposited and the lift-off process is repeated to form an Al hard mask. The mask must also cover the gold to protect the alignment markers and contact pads.
- The sample is etched using an Oxford Instruments Plasmalab 100 RIE system. A mixture of CHF_3 and SF_6 gases are flowed at a rate of $35 : 14$ sccm, with a chamber pressure of 20 mTorr and applied rf power of 200 W. The microwires are protected by the Al mask, and measurements show that the etch rate of Al is around 2 nm/min. The Al mask is then removed by being placed in CD-26 photoresist developer (2.4% TMAH) for 90 s and then rinsed in deionised water for 60 s.

- To now produce the nanobridge structure the samples are again cleaned and dried, and a layer of ZEP520A ebeam resist is spun at $4,000$ rpm for 60 s to produce a layer around 180 nm thick. This is baked on a hotplate for five minutes at 180°C.

- The nanobridge trenches are patterned into the ZEP by ebeam and developed using o-Xylene which is heated to 23°C for 60 s and stopped by placing in IPA for 60 s. The ZEP can now be used as the etch mask.

- Trenches are formed by etching the sample using the same process which has been previously outlined. The ZEP is now removed by Microposit 1165 resist stripper and the sample is ready to be tested.

Bibliography

[1] A. D. Semenov, G. N. Gol'tsman, and A. A. Korneev., *Quantum detection by current carrying superconducting film*, Physica C: Superconductivity, 351(4):349–356, (2001).

[2] F. Marsili, F. Bellei, F. Naja, A. E. Dane, E. A. Dauler, R. J. Molnar, and K. K. Berggren, *Efficient single photon detection from 500 nm to 5 m wavelength*, Nano Lett., 12(9):4799-4804, (2012).

[3] F. Marsili, V.B. Verma, J.A. Stern, S. Harrington, A.E. Lita, T. Gerrits, I. Vayshenker, B. Baek, M.D. Shaw, R.P. Mirin and S.W. Nam, *Detecting Single Infrared Photons with 93% System Efficiency*. Nature Photonics 7, 210-214 (2013).

[4] C. Schuck, W. H. Pernice and H. X. Tang, *Waveguide integrated low noise NbTiN nanowire single-photon detectors with milli-Hz dark count rate* Sci. Rep. 3 1893 (2013).

[5] B. A. Korzh, Q-Y. Zhao, S. Frasca1, J. P. Allmaras, T. M. Autry, E. A. Bersin, M. Colangelo, G. M. Crouch, A. E. Dane, T. Gerrits, F. Marsili, G. Moody, E. Ramirez, J. D. Rezac, M. J. Stevens, E. E. Wollman, D. Zhu, P. D. Hale, K. L. Silverman, R. P. Mirin, S. W. Nam, M. D. Shaw and K. K. Berggren *Demonstrating sub-*3 ps *temporal resolution in a superconducting nanowire single-Photon Detector*, arXiv 1804.06839, (2018).

[6] A. J. Annunziata, O. Quaranta, D. F. Santavicca, A. Casaburi, L. Frunzio, M. Ejrnaes, M. J. Rooks, R. Cristiano, S. Pagano, A. Frydman, and D. E. Prober, *Reset dynamics and latching in niobium superconducting nanowire single-photon detectors*, J. Appl. Phys. 108(8), 084507 (2010).

[7] H. Takesue, S. W. Nam, Q. Zhang, R. H. Hadfield, T. Honjo, K. Tamaki, and Y. Yamamoto, *Quantum key distribution over a 40-dB channel loss using superconducting single-photon detectors*, Nat. Photonics 1, 343-348 (2007).

[8] M. Sasaki, M. Fujiwara, H. Ishizuka, W. Klaus, K. Wakui, M. Takeoka, S. Miki, T. Yamashita, Z. Wang, A. Tanaka, K. Yoshino, Y. Nambu, S. Takahashi, A. Tajima, A. Tomita, T. Domeki, T. Hasegawa, Y. Sasaki, H. Kobayashi, T. Asai, K. Shimizu, T. Tokura, T. Tsurumaru, M.

Matsui, T. Honjo, K. Tamaki, H. Takesue, Y. Tokura, J. F. Dynes, A. R. Dixon, A. W. Sharpe, Z. L. Yuan, A. J. Shields, S. Uchikoga, M. Legre, S. Robyr, P. Trinkler, L. Monat, J.-B. Page, G. Ribordy, A. Poppe, A. Allacher, O. Maurhart, T. Langer, M. Peev, and A. Zeilinger, *Field test of quantum key distribution in the Tokyo QKD Network*, Opt. Exp. 19 (11), 10387-10409 (2011).

[9] Z. Wang, S. Miki, M. Fujiwara, *Superconducting nanowire single- photon detectors for quantum information and communications.* IEEE J. Sel. Top. Quantum. Electron. 15, 1741–1747 (2009).

[10] A. McCarthy, N. J. Krichel, N. R. Gemmell, Ximing Ren, M. G. Tanner, S. N. Dorenbos, V. Zwiller, R. H. Hadfield, and G. S. Buller, *Kilometer-range, high resolution depth imaging via 1560 nm wavelength single-photon detection*, Opt. Exp. 21 (7), 8904-8915 (2013).

[11] J. P. Allmaras, A. D. Beyer, R. M. Briggs, F. Marsili, M. D. Shaw, G. V. Resta, J. A. Stern, V. B. Verma, R. P. Mirin, S. W. Nam, and W. H. Farr, *Large-area 64-pixel array of WSi superconducting nanowire single photon detectors* in Conference on Lasers and Electro-Optics, OSA Technical Digest (online) (Optical Society of America), paper JTh3E.7. (2017).

[12] Single Quantum Products. (2020). [online] Available at https://singlequantum.com/products/

[13] Quantum Opus Products. (2020). [online] Available at https://www.quantumopus.com/web/product-info/

[14] Scontel Products. (2020). [online] Available at http://www.scontel.ru/products/sspd/

[15] G. G. Taylor, D. Morozov, N. R. Gemmell, K. Erotokritou, S. Miki, H. Terai, and R. H. Hadfield, *Photon counting LIDAR at 2.3 μm wavelength with superconducting nanowires*, Opt. Express 27, 38147–38158 (2019).

[16] Y. Hochberg, I. Charaev, S.-W. Nam, V. Verma, M. Colangelo, and K. K. Berggren, *Detecting sub-GeV dark matter with superconducting nanowires*, Phys. Rev. Lett. 123(15), 151802 (2019).

[17] The OST mission concept study team, The Origins Space Telescope (OST) mission concept study interim report, https://arxiv.org/abs/1809.09702 (2018).

[18] M. S. Allman, V. B. Verma, M. Stevens, T. Gerrits, R. D. Horansky, A. E. Lita, F. Marsili, A. Beyer, M. D. Shaw, D. Kumor, R. Mirin, and S. W. Nam, *A near-infrared 64-pixel superconducting nanowire single photon detector array with integrated multiplexed readout*, Appl. Phys. Lett. 106(19), 192601 (2015).

[19] A. Gaggero, F. Martini, F. Mattioli, F. Chiarello, R. Cernansky, A. Politi, and R. Leoni, *Amplitude-multiplexed readout of single photon detectors based on superconducting nanowires*, Optica 6(6), 823–828 (2019).

[20] A. McCaughan, F. Bellei, F. Najafi, D. De Fazio, A. Dane, Y. Ivry, Y., and K. K. Berggren, *Superconducting-nanowire single-photon-detector linear array.* Appl. Phys. Lett., 103(14), 142602. doi:10.1063/1.4823542. (2013).

[21] S. Doerner, A. Kuzmin, S. Wuensch, K. Ilin, and M. Siegel, *Operation of Superconducting Nanowire Single-Photon Detectors Embedded in Lumped-Element Resonant Circuits.* IEEE Trans. Appl. Supercond., 26(3), 1–5. doi:10.1109/tasc.2016.2525995 (2016).

[22] E. E. Wollman, V. B. Verma, A. E. Lita, W. H. Farr, M. D. Shaw, R. P. Mirin, and S. Woo Nam, *Kilopixel array of superconducting nanowire single-photon detectors*, Opt. Express 27, 35279 (2019).

[23] K. K. Likharev, and V. K. Semenov, *RSFQ Logic/Memory Family: A New Josephson-Junction Technology for Sub-Terahertz-Clock-Frequency Digital Systems.* IEEE Trans. Appl. Supercond. vol. 1, pp. 3-28 (1991).

[24] D. S. Crankshaw, J. L. Habif, X. Zhou, T. P. Orlando, M. J. Feldman, and M. F. Bocko, *An RSFQ Variable Duty Cycle Oscillator for Driving a Superconductive Qubit* IEEE Trans. Appl. Supercond. 13 966 (2003)

[25] R. McDermott and M. G. Vavilov, *Accurate qubit control with single flux quantum pulses*, Phys. Rev. Appl., vol. 2, no. 1, Art. no. 014007. (2014).

[26] C. Howington, A. Opremcak, R. McDermott, A. Kirichenko, O. Mukhanov, B. L. Plourde, *Interfacing superconducting qubits with cryogenic logic: Readout*, IEEE Trans. Appl. Supercond., vol. 29, 1700305, (2019).

[27] W. Chen, A.V. Rylyakov, V. Patel, J.E. Lukens and K.K. Likharev, *Rapid Single Flux Quantum T-Flip Flop operating up to 770 GHz*, IEEE Trans. Appl. Supercond., 9, pp. 3212–3215 (1999).

[28] O.A. Mukhanov, *Energy-efficient single flux quantum technology* IEEE Trans. Appl. Supercond. 21, 760 (2011).

[29] T. Ortlepp and T. Van Duzer, *Access time and power dissipation of a model 256-bit single flux quantum RAM.* IEEE Trans. Appl. Supercond. 24, 1300307 (2014).

[30] V. V. Ryazanov, V. V. Bol'ginov, D. S. Sobanin, I. V. Vernik, S.K. Tolpygo, A.M. Kadin, O. A. Mukhanov, *Magnetic Josephson junction technology for digital and memory applications* Phys. Procedia, 36, 35–41. doi:10.1016/j.phpro.2012.06.126 (2012).

[31] V. V. Ryazanov; V. A. Oboznov; A. Yu. Rusanov; A. V. Veretennikov; A. A. Golubov; J. Aarts (2001). "Coupling of two superconductors through a ferromagnet: evidence of a π -junction". Physical Review Letters. 86 (11): 2427–30. arXiv:cond-mat/0008364. Bibcode:2001PhRvL..86.2427R. doi:10.1103/PhysRevLett.86.2427. PMID 11289946. (2012).

[32] P.W. Anderson and J.M. Rowell, *Probable Observation of the Josephson Superconducting Tunneling Effect*. Phys. Rev. Lett. 10, 230 (1963).

[33] V. Ambegaokar, and A. Baratoff, *Tunneling Between Superconductors*, Phys. Rev. Lett. M, 486; 11, 104(E). (1963).

[34] N. R. Werthamer, *Nonlinear self-coupling of Josephson radiation in superconducting tunnel junctions*, Phys. Rev. 147, 255. (1966).

[35] A. I. Larkin, and Yu. N. Ovchinnikov, *Decay of the Supercurrent in Tunnel Junctions*, Zh. Eksp. Teor. Fiz. 51, 1535 [Sov. Phys.-JETP 24, 1035 (1966).

[36] M. Gurvitch, M. A. Washington, and H. A. Huggins, *High quality refractory Josephson tunnel junctions utilizing thin aluminum layers*, Appl. Phys. Lett. 42, 472 (1983).

[37] Q. Y. Zhao, A. N. McCaughan, A. E. Dane, K. K. Bergren, T. Ortlepp, *A nanocryotron comparator can connect single-flux-quantum circuits to conventional electronics* Supercond. Sci. Technol. 30 044002 (2017).

[38] N. Takeuchi, F. China, S. Miki, S. Miyajima, M. Yabuno, N. Yoshikawa, and H. Terai, *Scalable readout interface for superconducting nanowire single-photon detectors using aqfp and rsfq logic families*, Opt. Express 28, 15824 (2020).

[39] G. N. Gol'tsman, O. Okunev, G. Chulkova, A. Lipatov, A. Semenov, K. Smirnov, B. Voronov, A. Dzardanov, C. Williams and R. Sobolewski, *Picosecond superconducting single-photon optical detector*, Appl. Phys. Lett. 79, 705–7 (2001).

[40] S. V. Polyakov, *Experimental Methods in the Physical Sciences*, Volume 45, 2013, Pages 69-82 (2013).

[41] R. H. Hadfield. *Single-photon detectors for optical quantum information applications*. Nature Photonics, 3(12):696-705, (2009).

[42] H. Kume, K. Koyama, K. Nakatsugawa, S. Suzuki, and D. Fatlowitz, *Ultrafast microchannel plate photomultipliers*. Applied Optics, 27(6):1170-1178, (1988).

[43] M. Liu, C. Hu, X.Bai, X. Guo, J. C. Campbell, Z. Pan, and M. M. Tashima, *Highperformance InGaAs/InP single-photon avalanche photodiode*. IEEE J. Sel. Topics Quantum Electron., vol. 13, no. 4, pp. 887–894, (2007).

[44] A. Restelli, J. C. Bienfang, and A. L. Migdall, *Single-photon detection efficiency up to 50% at 1310 nm with an InGaAs/InP avalanche diode gated at 1.25 GHz*, Appl. Phys. Lett., 102(14):141104, (2013).

[45] Z. Lu, W. Sun, J. Campbell, X. Jiang, and M. A. Itzler,*Common-mode cancellation in sinusoidal gating with balanced InGaAs/InP single photon avalanche diodes*, J. Sel. Top. Quant. Phys., IEEE Trans 48(12), 1505–1511 (2012).

[46] M. D. Eisaman, J. Fan, A. Migdall, and S. V. Polyakov. *Invited review article: Single-photon sources and detectors,*. Rev. Sci. Instrum. 82, 071101 (2011).

[47] A. Peacock, P. Verhoeve, N. Rando, A. van Dordrecht, B. G. Taylor, C. Erd, M. A. C. Perryman, R. Venn, J. Howlett, D. J. Goldie, J. Lumley and M. Wallis, *Single optical photon detection with a superconducting tunnel junction*, Nature, 381:135, (1996)

[48] B. Cabrera, R. M. Clarke, P. Colling, A. J. Miller, S. Nam, and R. W. Romani, *Detection of single infrared, optical, and ultraviolet photons using superconducting transition edge sensors*, Appl. Phys. Lett., 73:735, (1998)

[49] A. E. Lita, A. J. Miller, and S. W. Nam. *Counting near-infrared single-photons with 95% efficiency*. Optics Express, 16(5):3032-3040, (2008)

[50] D. Fukuda, G. Fujii, T. Numata, A. Yoshizawa, H. Tsuchida, S. Inoue, and T. Zama, *Titanium TES based photon number resolving detectors with 1 MHz counting rate and 65% quantum efficiency*, In SPIE OPTO: Integrated Opto-electronic Devices, pages 72360C-72360C. International Society for Optics and Photonics, (2009)

[51] D. Fukuda, G. Fujii, T. Numata, A. Yoshizawa, H. Tsuchida, H. Fujino, H. Ishii, T. Itatani, S. Inoue, and T. Zama, *Photon number resolving detection with high speed and high quantum efficiency*, Metrologia, 46(4):S288, (2009)

[52] A. Pearlman, A. Cross, W. Slysz, J. Zhang, A. Verevkin, M. Currie, A. Korneev, P. Kouminov, K. Smirnov, B. Voronov, G. Gol'tsman, and R. Sobolewski, *128 Gigahertz counting rates of NbN*

single-photon detectors for quantum communications, IEEE Trans. Appl. Supercond. 15 579–82 (2005).

[53] R. Meservey and P. M. Tedrow, *Measurements of the Kinetic Inductance of Superconducting Linear Structures*,, J. Appl. Phys. 40, 2028. (1969).

[54] A. J. Kerman, E. A. Dauler, W. E. Keicher, J. K. W. Yang, K. K. Berggren, G. Gol'tsman, G., and B. Voronov, *Kinetic-inductance-limited reset time of superconducting nanowire photon counters.* Appl. Phys. Lett., 88(11), 111116. doi:10.1063/1.2183810 (2006).

[55] H. L. Hortensius, E. F. C. Driessen, T. M. Klapwijk, K. K. Berggren, and J. R. Clem, *Critical-current reduction in thin superconducting wires due to current crowding.* Appl. Phys. Lett., 100(18), 182602. doi:10.1063/1.4711217 (2012).

[56] R. A. Kirkwood, *Superconducting single photon detectors for quantum information processing*, Ph.D. thesis, University of Glasgow, (2017)

[57] C. Natarajan, M. Tanner, and R. Hadfield, *Superconducting nanowire single-photon detectors: physics and applications*, . Supercond. Sci. Technol. 25, 063001 (2012).

[58] R. Santagati, J. W. Silverstone, M. J. Strain, M. Sorel, S. Miki, T. Yamashita, M. G. Thompson, M. G. *Silicon photonic processor of two-qubit entangling quantum logic.* Journal of Optics, 19(11), 114006. doi:10.1088/2040-8986/aa8d56 (2017).

[59] M. Yabuno, S. Miyajima, S. Miki, H. Terai, *Scalable implementation of a superconducting nanowire single-photon detector array with a superconducting digital signal processor*, Opt. Express 28(8), 12047 (2020).

[60] O. Quaranta, S. Marchetti, N. Martucciello, S. Pagano, M. Ejrnaes, R. Cristiano and C. Nappi *Superconductive three-terminal amplifier/discriminator* IEEE Trans. Appl. Supercond. 19 367–70 (2009)

[61] F. Marsili, F. Najafi, E. Dauler, F. Bellei, X. Hu, M. Csete, R. Molnar, K. K. Berggren, *Single-Photon Detectors Based on Ultranarrow Superconducting Nanowires*, Nano Lett. 2011, 11, 5, 2048–2053 (2011)

[62] P.K. Day, H.G. LeDuc, B.A. Mazin, A. Vayonakis, J. Zmuidzinas, *A broadband superconducting detector suitable for use in large arrays.* Nature. 425 (6960): 817–821. Bibcode:2003Natur.425..817D. doi:10.1038/nature02037 (2003).

[63] S. Doerner, A. Kuzmin, S. Wuensch, I. Charaev, F. Boes, T. Zwick, and M. Siegel, *Frequency-multiplexed bias and readout of a 16-pixel superconducting nanowire single-photon detector array*, Appl. Phys. Lett. 111(3), 32603 (2017)

[64] K. Sakai, R. Yamamoto, Y. Takei, K. Mitsuda, N. Y.Yamasaki, M. Hidaka, T. Miyazaki, *Development of Frequency-Division Multiplexing Readout System for Large-Format TES X-ray Microcalorimeter Arrays*, J. Low Temp. Phys., vol. 184, no. 1, pp. 519–526, 2016. [Online]. Available: http://dx.doi.org/10.1007/s10909-016-1564-2 (2016).

[65] D. Zhu, Q-Y. Zhao, H. Choi H, *A scalable multi-photon coincidence detector based on superconducting nanowires.* Nat Nanotechnol 2018;13:596–601. (2018)

[66] H. Terai, S. Miki, and Z. Wang, *Readout electronics using single-flux quantum circuit technology for superconducting single-photon detector array*, IEEE Trans. Appl. Supercond. 19 350–3 (2009).

[67] T. Ortlepp, M. Hofherr, L. Fritzsch, S. Engert, K. Ilin, D. Rall, H. Toepfer, H.-G. Meyer, and M. Siegel, *Demonstration of digital readout circuit for superconducting nanowire single photon detector*, Opt. Express 19(19), 18593–18601 (2011).

[68] M. Hofherr, M. Arndt, K. Il'in, D. Henrich, M. Siegel, J. Toussaint, T.May, and H. Meyer, *Time-Tagged Multiplexing of Serially Biased Superconducting Nanowire Single-Photon Detectors*, IEEE Trans. Appl. Supercond., 23, 2501205, (2013).

[69] T. Yamashita, S. Miki, H. Terai, K. Makise, and Z. Wang, *Crosstalk-free operation of multi-element SSPD array integrated with SFQ circuit in a 0.1 W GM cryocooler*, Opt. Lett. 37(14), 2982–2984 (2012).

[70] S. Miki, T. Yamashita, Z. Wang, and H. Terai, *A 64-pixel NbTiN superconducting nanowire single-photon detector array for spatially resolved photon detection* Opt. Express 22, 7811 (2014).

[71] S. Pagano, N. Martucciello, R. Cristiano, M. Ejrnaes, A. Casaburi, R. Leoni, P. Cavalier, *Nano-Strip Three-Terminal Superconducting Device for Cryogenic Detector Readout.* IEEE Trans. Appl. Supercond., 21(3), 717–720. doi:10.1109/tasc.2010.2085411 (2011).

[72] A. McCaughan, K. Berggren, *A Superconducting-Nanowire Three-Terminal Electrothermal Device* Nano Lett., 14, 10, 5748-5753 (2014).

[73] S. V. Polonsky, V. K.Semenov, P. I. Bunyk, A. F. Kirichenko, A. Yu. Kidiyarova-Shevchenko, O. Mukhanov, P.N. Shevchenko, D.F. Schneider, D. Yu. Zinoviev, and K. K. Likharev, *New RSFQ circuits (Josephson junction digital devices).* IEEE Trans. on Appl. Supercond. 3, (1993).

[74] B.D. Josephson, *Possible new effects in superconductive tunnelling.* Phys. Letters 1, 251 (1962).

[75] K. K. Likharev, *Superconduting weak links.* Rev. Mod. Phys. 51, 101 (1979).

[76] I. Giaever, *Energy gap in superconductors measured by electron tunneling.* Phys. Rev. Letters 5, 147, 464 (1960).

[77] V. L. Ginzburg, L. D. Landau. *On the Theory of Superconductivity*, Zh.Eksp.Teor.Fiz. 20 **20**, 1064-1082 (1950)

[78] J. Bardeen, L.N. Cooper, and J.R. Schrieffer, *Theory of superconductivity* Phys. Rev. 108, 1175 (1957).

[79] Larkin, A.I., and Ovchinnikov, Yu.N. Zh. Eksp. Teor. Fiz. (Sov.Phys.-JETP) 53: 2159. (1967).

[80] W.C. Stewart, *Current-voltage characteristics of Josephson junctions.* Appl. Phys. Lett. 12, 277 (1968).

[81] D.E. McCumber, *Effect of ac impedance on dc voltage-current characteristics of superconductor weak-link junctions.* J. Appl. Phys. 39, 3113 (1968).

[82] A. Barone, and G. Paterno, *Physics and Application of the Josephson Effect.* Wiley, New York (1982).

[83] P. E. Gregers-Hansen, M. T. Levinsen, L. Pederson, and C. L. Siostrom *A sinusoidal current-phase relation for superconducting thin-film microbridges*, Proceedings of the Applied Superconductor Conference (IEEE, New York), IEEE Pub. No. 72-CH0682-5-TABSC, p. 597. (1972)

[84] C. Enss and S. Hunklinger, *Low-Temperature Physics.* Springer (2005).

[85] S. Shapiro, *Josephson currents in superconducting tunneling: The effect of microwaves and other observations.* Phys. Rev. Lett. 11, 80. (1963).

[86] K. K. Likharev, O. A. Mukhanov, and V. K. Semenov, *SQUID'85, W. de Gruyter, Berlin, pp. 1103-1108.* (1985).

[87] O. A. Mukhanov, V. K. Semenov, and K. K. Likharev, *Ultimate performance of the RSFQ logic circuits* IEEE Trans. on Magn. 23, 759-762. (1987)

[88] O. A. Mukhanov, S. V. Rylov, V. K. Semenov, and S. V. Vyshenskii, *RSQ Logic Arithmetic* IEEE Trans. on Magn. 25, 857-860. (1989)

[89] V.K. Kaplunenko, M.I. Khabipov, V.P. Koshelets, K.K. Likharev, O.A. Mukhanov, V.K. Semenov, I.L. Serpuchenko, and A.N. Vystavkin, *Experimental study of the RSFQ logic elements* IEEE Trans. on Magn. 25, 861-864. (1989).

[90] O. A. Mukhanov, S. V. Rylov, V. K. Semenov, and S. V. Vyshenskii, *Recent development of rapid single flux quantum (RSFQ) logic digital devices*, in Ext. Abstr. of ISEC'89, Tokyo, pp. 557-560. (1989).

[91] K. K. Likharev, Pis'ma Zh. Eksp. Teor. Fiz. 20, 730 (1974); JETPLett. 20, 338 (1974).

[92] K. K. Likharev. *Rapid single-flux-quantum logic*. [online] Available at http://pavel.physics.-sunysb.edu/RSFQ/Research/WhatIs/rsfqre2m.html, (1992).

[93] E. S. Fang and T. Van Duzer, *A Josephson Integrated Circuit Simulator (JSIM) for Superconductive Electronics Appliction*. Extend Abstract 1989 International Superconductive Electronics Conference, Japan, pp. 407-410 Jun. 1989.

[94] W. Anacker, *Josephson computer technology: An IBM research project*, IBM J. Res. Develop., vol. 24, (1980).

[95] A. Fujimaki and M. Tanaka *Impact of recent advancement in cryogenic circuit technology* Superconductivity News Forum IEEE CSC 11 n.41 STP591 (2017)

[96] O. A. Mukhanov, S. Sarwana, D. Gupta, A. F. Kirichenko, and S. V. Rylov, *Rapid single flux quantum technology for SQUID applications*. Physica C: Superconductivity, 368(1-4), 196–202. doi:10.1016/s0921-4534(01)01166-2 (2002).

[97] P. E. Gregers-Hansen, M. T. Levinsen, L. Pederson, and C. L. Siostrom, *Variation with microwave power of the current steps of superconducting microbridges*. Solid State Commun. g, 661. (1971)

[98] F. Paolucci, G. De Simoni, E. Strambini, P. Solinias F. Giazotto, *Ultra-Efficient Superconducting Dayem Bridge Field-Effect Transistor*. Nano Lett. 2018, 18, 7, 4195–4199 Publication Date:June 12, (2018)

[99] F. Paolucci, G. De Simoni, E. Strambini, P. Solinas, N. Ligato, P. Virtanen, F. Giazotto, *Magnetotransport Experiments on Fully Metallic Superconducting Dayem-Bridge Field-Effect Transistors*, Phys. Rev. Appl. 11, 024061 (2019).

[100] W. H. Keller, and J. E. Nordman, *Niobium thin-film Josephson junctions using a semiconductor barrier*. J. Appl. Phys.,vol. 44, p. 4732, (1973).

[101] B.S. Deaver and J.M. Pierce, *Relaxation oscillator model for superconducting bridges*. Phys. Lett. A 38,81 (1972).

[102] K. K. Likharev, and L. A. Yakobson, *Steady-State Properties of Superconducting Bridges*, Zh. Tekh. Fiz. 45, 1503 Sov. Phys. -Tech. Phys. 20, 950 (1975).

[103] A. F. Volkov., *Critical Current in Narrow Superconducting Links*, Fiz. Tverd. Tela 15 1364 (Sou. Phys.-Solid St. 15 925), (1973).

[104] Kuprianov MY, Likharev KK and Maslova LA 1975 Proc. LT-14 vol4, ed M Krusius and M Vuorio Lett. 22 1416 conductivity Conf. IEEE Con hTo CIXI dS2-5-TABASC (New York: IEEE) pp597-602 Phys.-JETP Lett. 21 226) PhyS.-JETP 41 11 50) 14 819) Lett. 28 353 Sweden, 3-12 June (Amsterdam: North-Holland) pp104-7

[105] W. J. Skocpol, M. R. Beasley, and M. Tinkham, *Self-heating hotspots in superconducting thin-film microbridges* J. Appl. Phys. 45, 4054 (1974).

[106] P. H. Kes, J. G. A. Rolfes, and D. de Klerk. *Thermal Conductivity of Niobium in the Purely Superconducting and Normal States*. J. Low Temp. Phys. 17, 341 (1974).

[107] J. W. Yang, A. J. Kerman, E. A. Dauler, V. Anant, K. M. Rosfjord, K. K. Berggren, *Modeling the Electrical and Thermal Response of Superconducting Nanowire Single-Photon Detectors.* , IEEE Trans. Appl. Supercond. 17, 581 (2007).

[108] T. J. Rieger, D. J. Scalapino, and J. E. Mercereau, *Time-dependent superconductivity and quantum dissipation*. Phys. Rev. B 6, 1734 (1972).

[109] Jackel, L. D., J. M. Warlaumont, T. D. Clark, J. C. Brown, R. A. Buhrman, and M. T. Levinsen, *Superconducting weak-link current-phase relations.* App. Phys. Lett. 28, 353 (1976).

[110] A. A. Golubov, M. Y. Kupriyanov, and E. Il'Ichev, *The current-phase relation in Josephson junctions*. Rev. Mod. Phys. 76, 411 (2004).

[111] Usadel, K. D., *Generalized diffusion equation for superconducting alloys* Phys. Rev. Lett. 25, 507. (1970).

[112] I. O. Kulik, and A. N. Omelyanchuk, *Zh. Eksp. Teor. Fiz. Pis'ma Bed. 21, 216 [JETP Lett. 21, 96 (1975)]*. (1975).

[113] I. O. Kulik, and A. N. Omelyanchuk, *Fiz. Nizk. Temp. 3, 945 [Sov. J. Low Temp. Phys.]*. (1977).

[114] F. Kohlraush, Praktische Physik Zl (Stuttgart: B G Teubner Verlag) p305, 335 (1962).

[115] V. Ambegaokar, and B. I. Halperin, *Voltage Due to Thermal Noise in the dc Josephson Effect.* Phys. Rev. Lett. 22, 1364(1969).

[116] Yu. M. Ivanchenko, L. A. Zil'bermann. *Destruction of Josephon Current by Fluctuations.*Pis'ma Zh. Eksp. Teor. Fiz. 8, 189 (1968).

[117] C. M. Falco *Effect of the Quasiparticle-Pair Interference Current on Thermal Fluctuations in Weakly Coupled Superconductors and on the Operation of Rf-Biased Squids.* Ph.D. thesis, Harvard University, (1974).

[118] H. Kanter and F. L. Vernon, Jr., *Response of Highly Damped Josephson Junctions to External, Low-Frequency Noise Currents* Phys. Rev. B 2, 4694 (1970).

[119] S.K. Tolpygo, *Superconductor digital electronics: scalability and energy efficiency issues*, Low Temp. Phys. 42 361–79 (2016).

[120] A. Brinkman, D. Veldhuis, D. Mijatovic, G. Rijnders, D.H.A. Blank, H. Hilgenkamp, H. Rogalla. *Superconducting quantum interference device based on nanobridges*, Appl. Phys. Lett., 79, p. 2420 (2001).

[121] J. George, *Preparation of thin films*, M. Dekker, (1992).

[122] A. R. Wildes, J. Mayer, K. Their-Broehl, *The growth and structure of epitaxial niobium on sapphire.* Thin Solid Films, 401 7 (2001).

[123] A. Anders, *A structure zone diagram including plasma-based deposition and ion etching.* Thin Solid Films, Volume 518, Issue 15, Pages 4087-4090 (2010).

[124] M. Murakami and T. Yogi, *Strain in evaporated Nb thin films.* Journal of Applied Physics 57, 211 (1985).

[125] V. Lacquaniti, S. Maggi, E. Monticone, R. Steni, *Thickness dependence of electrical and structural properties of Nb thin films.* Phys. Status Solidi A 151 (1995).

[126] M. Altissimo, *E-beam lithography for micro-/nanofabrication*, Biomicrofluidics, vol. 4, pp. 3-6, (2010).

[127] T. H. P. Chang, *Proximity effect in electron-beam lithography.* J. Vac. Sci. Technol., 12, 1271 (1975).

[128] Allresist PMMA data sheet (2020). [online] Available at https://www.allresist.com/wp-content/uploads/sites/2/2015/12/allresist_produktinfos_arp630-670_englisch.pdf

[129] HSQ data sheet (2020). [online] Available at https://ebeam.mff.uw.edu/ebeamweb/process/process/hsq_files/11-1547e-01.pdf

[130] ZEP data sheet (2020). [online] Available at https://www.nanophys.kth.se/nanolab/resists/zep520a-7-2.pdf

[131] W. Hu, K. Serverwaran, M. Lieberman and G. H. Bernstein, *Sub-10 nm electron beam lithography using cold development of poly (methyl methacrylate)* J. Vac. Sci. Technol. B 22, 1711 (2004).

[132] A. Gangnaik, Y. M. Georgiev, B. McCarthy, N. Petkov, V. Djara, and J. D. Holmes,*Characterisation of a novel electron beam lithography resist, SML and its comparison to PMMA and ZEP resists.* Microelectronic Engineering, 123, 126–130. doi:10.1016/j.mee.2014.06.013 (2007).

[133] A. Meisters, G. Moad, E. Rizzardo, and D. H. Solomon, *Thermal stability of poly(methyl methacrylate).* Polymer Bulletin, 20(5), 499–503. doi:10.1007/bf01153444 (1988).

[134] Reinspach, M Lindblom, O. V. Hofsten, M. Bertilson, H. M. Hertz and A. Holmberg, *Cold developed electron-beam-patterned ZEP 7000 for fabrication of 13 nm nickel zone plates* J. Vac. Sci. Technol. B 27, 2593 (2009).

[135] T. Nishida, M. Notomi, R. Iga, and T. Tamamura, *Quantum Wire Fabrication by E-Beam Elithography Using High-Resolution and High-Sensitivity E-Beam Resist ZEP-520.* Jpn. J. Appl. Phys. 31 , 4508 (1992).

[136] D. S. MacIntyre and S. Thoms, *Comparison of hydrogen silsesquioxane development methods for sub-10 nm electron beam lithography using accurate linewidth inspection* J. Vac. Sci. Technol. B 29, 06F307 (2011).

[137] Washington Nanofabrication Facility, HSQ Resist Process Information (2020). [online] Available at https://ebeam.mff.uw.edu/ebeamweb/process/process/hsq.html

[138] T. Chang, M. Chou, Y. Mei, J. Tsang, F. Pan, W. Wu, and H. Huangc, *Enhancing the thermal stability of low dielectric constant hydrogen silsesquioxane by ion implantation.* Thin Solid Films, 332(1-2), 351–355. doi:10.1016/s0040-6090(98)01036-0 (1998).

[139] J. Bausells, Instituto de Microelectronica de Barcelona, (2020) [online] available at http://nanonems.imb-cnm.csic.es/index.php?option=com_content&view=article&id=25%3Aeiss-electron-beam-monte-carlo-simulator&catid=2%3Ananofabrication&Itemid=9&lang=en

[140] B. Cord, J. Yang, H. Duan, *Limiting factors in sub-10nm scanning-electron-beam lithography.* Journal of Vacuum Science & Technology B: Microelectronics and Nanometer Structures Processing, Measurement, and Phenomena 27, 2616 (2009).

[141] D. Rio, C. Constancias, M. Saied, B. Icard and L. Pain, *Study on line edge roughness for electron beam acceleration voltages from 50 to 5 kV.* Journal of Vacuum Science & Technology B: Microelectronics and Nanometer Structures Processing, Measurement, and Phenomena 27, 2512 (2009).

[142] P. Li, *A Review of Proximity Effect Correction in Electron-beam Lithography* https://arxiv.org/pdf/1509.05169.pdf (2015).

[143] Private communication with Dr. Haiping Zhou

[144] J. M. Williams, D. R. Smith, D. Georgakopoulos, P. D. Patel, and J. R. Pickering, *Design and metrological applications of a low noise, high electrical isolation measurement unit* IET Sci. Meas. Technol. 3, 165–174 (2009).

[145] Isabellenhutte (2020), [online] Available at https://www.isabellenhuette.de/en/precision-alloys/products/manganinr/

[146] J. Bardeen, *Critical fields and currents in superconductors.* Rev. Mod. Phys. 34, 667 (1962).

[147] R. Vijay, J. D. Sau, M. L. Cohen, and I. Siddiqi, *Optimizing Anharmonicity in Nanoscale Weak Link Josephson Junction Oscillators*, Phys. Rev. Lett. 103, 087003 (2009).

[148] P. Virtanen, R. Gommers, T.E. Oliphant, M. Haberland, T. Reddy, D. Cournapeau, E. Burovski, P. Peterson, W. Weckesser, J. Bright, S.J. van der Walt, M. Brett, J. Wilson, K. J. Millman, N. Mayorov, A. R. J. Nelson, E. Jones, R. Kern, E. Larson, C. J. Carey, İ Polat, Y. Feng, E. W. Moore, J. VanderPlas, D. Laxalde, J. Perktold, R. Cimrman, I. Henriksen, E. A. Quintero, C. R. Harris, A. M. Archibald, A. H. Ribeiro, F. Pedregosa, P. van Mulbregt, and SciPy 1.0 Contributors, *SciPy 1.0: Fundamental Algorithms for Scientific Computing in Python*, Nat. Methods, 17, 261-272, https://rdcu.be/b08Wh, 10.1038/s41592-019-0686-2, (2020).

[149] C. D. Shelly, P. See, J. Ireland, E. J. Romans, and J. M. Williams, *Weak link nanobridges as single flux quantum elements*, , Supercond. Sci. Technol. 30, 095013 (2017).

[150] C.-C. Wang, M. Currie, D. Jacobs-Perkins, M. J. Feldman, R. Sobolewski, and T. Y. Hsiang, *Optoelectronic generation and detection of single-flux-quantum pulses*. Appl. Phys. Lett. 66, 3325 (1995).

[151] L.D. Jackel, R.A. Buhrman, W.W. Webb, *Direct measurement of current-phase relations in superconducting weak links*. Phys. Rev. B 10, 2782 (1975).

[152] Waldram, J. R., and J. M. Lumley, *Direct measurements of the current-phase relation in superconducting weak links*, Rev. Phys. Appl. 10, 7. (1975).

[153] E. de Wolff and R. deBrup Oubder, *The Josephson supercurrent-phase relation*. Physica B,v. 176,pp. 133-153, (1992).

[154] R. Rifkin, B. S. Deaver, *Current-phase relation and phase-dependent conductance of superconducting point contacts from rf impedance measurements*. Phys. Rev. B 13, 3894. (1976).

[155] K. K. Likharev and L. A. Yakobson, *Dynamical properties of superconducting filaments of finite length*, Zh. Tekh. Fiz. 45,1503 (1975).

[156] Jackel, L. D., T. D. Clark, and R. A. Buhrman, *Current-phase relations and noise in rf biased squids*. IEEE Trans. Magn. 11, 732 (1975).

[157] Jackel, L. D., W. H. Henkels, J. M. Warlaumont, and R. A.Buhrman, *Current-phase relations as determinants of superconducting thin-film weak-link I-V characteristics*. Appl. Phys. Lett. 29, 214 (1976).

[158] P. Russer, *Studies on AC Current Josephson Effect*. Acta Physica Austriaca 32, 373 (1970).

[159] H. Fack and V. Kose, *Maximal Output PowEr of Point-Contact Josephson Junctions*. J. Appl. Phys. 42, 320 (1971).

[160] Hamilton, C. A. *Josephson voltage standards*. Rev. Sci. Instrum. 71, 3611. (2000).